Measurement of angular correlations between D^0 mesons and charged particles in pPb collisions at $\sqrt{s_{\mathrm{NN}}} = 5.02$ TeV with ALICE at the LHC

By

Somnath Kar

Enrollment No. PHYS04201104006

Variable Energy Cyclotron Centre, Kolkata

A thesis submitted to

The Board of Studies in Physical Sciences

In partial fulfillment of requirements for the Degree of

DOCTOR OF PHILOSOPHY

of

HOMI BHABHA NATIONAL INSTITUTE

July, 2017

Homi Bhabha National Institute[1]

Recommendations of the Viva Voce Committee

As members of the Viva Voce Committee, we certify that we have read the dissertation prepared by **Somnath Kar** entitled "**Measurement of angular correlations between D^0 mesons and charged particles in pPb collisions at $\sqrt{s_{NN}}$ = 5.02 TeV with ALICE at the LHC**" and recommend that it may be accepted as fulfilling the thesis requirement for the award of Degree of Doctor of Philosophy.

Chairman – Prof. Tapan Kumar Nayak	**Date:** 30/6/2017
Guide / Convener – Prof. Premomoy Ghosh	**Date:** 30.06.2017
Co-guide - <Name> (if any)	**Date:**
Examiner – Prof. Arghya Deb	**Date:** 30.6.17
Member 1- Prof. Subhasish Chattopadhyay	**Date:** 30/6/17
Member 2- Prof. Munshi Golam Mustafa	**Date:** 30/06/17

Final approval and acceptance of this thesis is contingent upon the candidate's submission of the final copies of the thesis to HBNI.

I/We hereby certify that I/we have read this thesis prepared under my/our direction and recommend that it may be accepted as fulfilling the thesis requirement.

Date: 30.06.2017

Place: VECC, KOLKATA

Co-guide (if applicable) **Guide**

[1] This page is to be included only for final submission after successful completion of viva voce.

Statement by Author

This dissertation has been submitted in partial fulfilment of requirements for an advanced degree at Homi Bhabha National Institute (HBNI) and is deposited in the Library to be made available to borrowers under rules of the HBNI.

Brief quotations from this dissertation are allowable without special permission, provided that accurate acknowledgement of source is made. Requests for permission for extended quotation from or reproduction of this manuscript in whole or in part may be granted by the Competent Authority of HBNI when in his or her judgment the proposed use of the material is in the interests of scholarship. In all other instances, however, permission must be obtained from the author.

Somnath Kar

Somnath Kar

Declaration

I, hereby declare that the investigation presented in the thesis has been carried out by me. The work is original and has not been submitted earlier as a whole or in part for a degree / diploma at this or any other Institution / University.

Somnath Kar

Somnath Kar

List of Publications arising from the thesis

In peer-reviewed Journal:

1. *"Measurement of azimuthal correlations of D mesons and charged particles in pp collisions at* $\sqrt{s}$ *= 7 TeV and p–Pb collisions at* $\sqrt{s_{\mathrm{NN}}}$ *= 5.02 TeV."*
   Andrea Rossi, Sandro Bjelogrlic, Elena Bruna, **Somnath Kar** **(as primary author)**, Fabio Filippo Colamaria, Jitendra Kumar, ALICE Collaboration (J. Adam et al.).
   Eur. Phys. J. C 77 (2017), 245, arXiv:1605.06963v1 [nucl-ex]
2. *"Multiple parton interactions and production of charged particles up to the intermediate-*p_{T} *range in high multiplicity pp events at the LHC."*
   Somnath Kar, Subikash Choudhury, Sanjib Muhuri, and Premomoy Ghosh.
   Phys. Rev. D95 (2017) 014016.

Conference Proceedings:

1. *"Measurement of* D^0*-hadron azimuthal correlations in p–Pb collisions at* $\sqrt{s_{\mathrm{NN}}}$ *= 5.02 TeV with ALICE."*
   Somnath Kar for the ALICE collaboration.
   Proceedings of the DAE Symp. on Nucl. Phys. 58 (2013).

2. *"Study of angular correlations between D mesons and charged particles in pp and p–Pb collisions with ALICE at the LHC."*

   Somnath Kar on behalf of the ALICE Collaboration.

   Proceedings of the DAE-BRNS Symp. on Nucl. Phys. 60 (2015)

Other publications:

List of publication related to this thesis (as a part of ALICE Collaboration):

1. *"Suppression of high transverse momentum D mesons in central Pb–Pb collisions at $\sqrt{s_{\rm NN}}$ = 2.76 TeV."*

   B. Abelev et al., ALICE Collaboration, JHEP09 (2012) 112.

2. *"Measurement of electrons from heavy-flavour hadron decays in p–Pb collisions at $\sqrt{s_{\rm NN}}$ = 5.02 TeV."*

   J. Adam et al., ALICE Collaboration, Phys. Lett. **B754** (2016) 81-93.

3. *"Elliptic flow of muons from heavy-flavour hadron decays at forward rapidity in Pb–Pb collisions at $\sqrt{s_{\rm NN}}$ = 2.76 TeV."*

   J. Adam et al., ALICE Collaboration, Phys. Lett. **B753** (2016) 41-56.

4. *"Measurement of charm and beauty production at central rapidity versus charged-particle multiplicity in proton-proton collisions at $\sqrt{s}$ = 7 TeV."*

   J. Adam et al., ALICE Collaboration, JHEP09 (2015) 148.

5. *"Measurement of electrons from semi-leptonic heavy-flavor hadron decays in pp collisions at $\sqrt{s_{\rm NN}}$ = 2.76 TeV."*

   B. Abelev et al., ALICE Collaboration, Phys. Rev. **D91** (2015) 012001.

6. *"Measurement of prompt D-meson production in p–Pb collisions at $\sqrt{s_{\rm NN}}$ =*

5.02 TeV."

B. Abelev et al., ALICE Collaboration, Phys. Rev. Lett. **113** (2014) 232301.

7. *"Azimuthal anisotropy of D meson production in Pb–Pb collisions at* $\sqrt{s_{\rm NN}}$ = *2.76 TeV."*

   B. Abelev et al., ALICE Collaboration, Phys. Rev. **C90** (2014) 034904.

8. *"D meson elliptic flow in non-central Pb–Pb collisions at* $\sqrt{s_{\rm NN}}$ = *2.76 TeV."*

   B. Abelev et al., ALICE Collaboration, Phys. Rev. Lett. **111** (2013) 102301.

Somnath Kar

Somnath Kar

Dedicated to

my parents and brother

Acknowledgements

First and foremost, I would like to express my sincere gratitude to my supervisor, ***Prof. Premomoy Ghosh*** for his constant guidance, motivation, support and supervision for accomplishing my thesis. It is my privilege to work with you, Sir, for more than 4 years at VECC.

I would like to thank the other members of my Doctoral Committee: Prof. Tapan K. Nayak, Prof. Subhasish Chattopadhyay, and Prof. Munshi Golam Mustafa, for their insightful comments, encouragement and advices which helped me to widen my research experience in experimental higher energy physics, data analysis, detector systems and in related theory. My sincere thanks also goes to Prof. Bedangdas Mohanty, Prof. Jan-e Alam, Prof. Sourav Sarkar for their advices, useful discussion and guidance during my course work at VECC. I would like to thank Prof. Raghava Varma of IIT Bombay and Dr. Prithwish Tribedy, Dr. Parth Pratim Bhaduri and Mr. Sanjib Muhuri from VECC for their intense support and discussion on various part of physics throughout my PhD tenure.

Very very special thanks to ***Dr. Jitendra Kumar*** (IIT Bombay) with whom I spent most valuable time during data analysis at CERN, Geneva, Switzerland. Thanks for all the help throughout those toughest beginning of data analysis in ALICE framework. We became very good friends and we finished our Ph.D. work almost at the same time. Thanks for those memorable days we spent together. Special gratitude to other ALICE collaborators Dr. Andrea Rossi, Dr. Fabio Colamaria, Dr. Sandro Bjelogrlic, Dr. Elena Bruna, Dr. Zaida Conesa del Valle. It was almost impossible for me to crack the analysis codes without their constant help.

Special thanks to my senior colleague ***Dr. Subikash Choudhury*** for his constant support and help in both, technicalities in data analysis and physics discussions. I also take this opportunity to thank my colleagues Debojit Sarkar, Abhirup Chaudhuri and Tanmoy Roy with whom I spent lots of unforgettable moments over the years. I would like to thank also my seniors and juniors of VECC for their cooperation and providing beautiful environment at VECC. Heartily thanks to ***Shreyasi***, Nachiketa and Samrangy for all the beautiful moments we shared during last two years of my Ph.D. tenure.

I acknowledge Dr. Klaus Werner for providing me the EPOS 3 code and for constant guidance in installing and running the code. I acknowledge the support of VECC GRID peer team in maintaining the computational facilities during my work. Thanks to all the hostel staff for providing good food and nice accommodation at VECC over the years.

Last but not the least, I would like to thank my family: ***my parents and brother*** for continuing with the moral support, as always. Without your immense love, sacrifice, patience and motivation this work would have not been possibly completed.

Somnath Kar

Somnath Kar

Contents

SYNOPSIS xv

List of Figures xxx

List of Tables xlviii

1 Introduction **1**

1.1 Overall organization 1

1.2 Preliminaries 4

1.2.1 The Standard Model 4

1.2.2 Quantum Chromodynamics: The theory of Strong Interactions 7

1.2.3 QCD phase diagram & Quark-Gluon Plasma 9

1.3 Discovery and Study of QGP 13

1.3.1 A Brief Overview 13

1.3.2 Heavy-ion collisions and relevant QGP-signals 16

1.3.2.1 Facilities 16

1.3.2.2 Geometry and Dynamics 17

1.3.2.3 Relevant QGP-signals 21

1.3.2.3.1 Collective Phenomena 22

1.3.2.3.2 High-p_{T} suppression: Jet quenching 27

1.3.3 The baselines: proton-proton (pp) and proton-nucleus (pA) collisions 29
1.3.3.1 The elementary pp collisions 29
1.3.3.2 pA collisions: the CNM effects 35
1.3.3.2.1 Nuclear modification of PDFs: shadowing and anti-shadowing 36
1.3.3.2.2 k_T broadening and Cronin enhancement . . 37
1.3.3.2.3 Isospin effect 39
1.3.3.2.4 Cold Nuclear Matter energy loss 40
1.4 High-multiplicity events of small systems 41
1.4.1 Hydrodynamic-like features in high-multiplicity pp and pPb events at the LHC 41
1.4.2 Non-hydrodynamic approaches in understanding the high-multiplicity pp and pPb events at the LHC 50

2 Two-particle angular correlations: the analysis tool 64
2.1 Different correlation sources 65
2.2 Construction of two-particle angular correlation 68
2.2.1 Jets and ridge 69
2.3 Observations in heavy-ion collisions 72

3 Open Heavy-flavor as probe 79
3.1 Basics of heavy-flavour quarks and mesons 80
3.2 Heavy-flavor production in high energy collisions 82
3.2.1 Experimental results in pp ($\bar{p}$) from CDF to LHC 84
3.3 Heavy-flavour in heavy-ion collisions 87

3.3.1 The QGP medium effect on HF 88
3.3.1.1 Collisional Energy Loss 90
3.3.1.2 Medium-induced radiative energy loss 91
3.3.2 Experimental results from heavy-ion data 94
3.4 Heavy-flavour in pPb 98
3.4.1 Results: Initial state effects on Heavy-flavor 99

4 Experimental Set-up **106**
4.1 The Large Hadron Collider 106
4.1.1 General Overview of ALICE and its Sub-detectors 110
4.1.1.1 Central barrel detectors 112
4.1.1.2 Forward detectors 114
4.1.1.3 ALICE Coordinate Systems 116
4.1.1.4 Inner Tracking System 117
4.1.1.5 Time Projection Chamber 119
4.1.1.6 Time of Flight (TOF) 122
4.1.1.7 VZERO detector 125
4.1.2 ALICE data taking model: Online 126
4.1.2.1 Detector Control System (DCS) 127
4.1.2.2 Trigger system (TRG) 127
4.1.2.3 Data Acquisition (DAQ) 127
4.1.2.4 High Level Trigger (HLT) 128
4.1.3 ALICE data taking model: Offline 128
4.1.3.1 Raw data flow 130

4.1.3.2 ALICE AliEn: the ALICE Analysis Framework on the Grid . . . 130
4.1.3.3 The AliRoot Framework . . . 131
4.1.3.4 ALICE upgrade . . . 135

5 Angular correlations between D^0 mesons and charged particles in *pPb* with ALICE 141

5.1 Data, Kinematic cuts & D^0 meson reconstruction . . . 142
5.1.1 Data set and Kinematic cuts . . . 142
5.1.2 Reconstruction of D^0 mesons . . . 143
5.1.2.1 Event selection and Secondary Vertex . . . 145
5.1.2.2 Topological cuts . . . 146
5.1.2.3 PID selection on the daughters . . . 152
5.1.3 Raw signal extraction . . . 154
5.1.4 Acceptance and efficiency correction . . . 157
5.1.5 Associated charged particle selection . . . 159
5.2 Analysis Details . . . 160
5.2.1 Correlations between D^0 mesons and charged particles . . . 162
5.2.2 Signal region background subtraction (Side-Band method) . . 163
5.2.3 Corrections to the correlation distributions . . . 165
5.2.3.1 Correction via Event Mixing technique . . . 165
5.2.3.2 D^0 meson efficiency correction . . . 169
5.2.3.3 Efficiency correction for associated charged particles 171
5.2.3.4 Beauty feed-down subtraction . . . 172

5.2.3.5 Correction for the contamination due to secondary particles (purity check) . . . 173
5.2.4 Evaluation of systematic uncertainties . . . 175
5.2.4.1 Uncertainty related to D^0 meson yield extraction . . 175
5.2.4.2 Uncertainty related to background subtraction . . . 176
5.2.4.3 Uncertainty related to D^0 topological cut efficiency . 178
5.2.4.4 Uncertainty related to associated track efficiency . . 179
5.2.4.5 Uncertainty related to beauty feed-down subtraction 181
5.2.4.6 Uncertainty related to residual contamination from secondary tracks . . . 182
5.2.4.7 Uncertainty related to soft-pions from D^* decays . . 183
5.2.5 Monte Carlo simulations: Closure test . . . 184
5.2.6 Summary of systematic uncertainties . . . 188
5.2.7 Fitting of correlation distribution . . . 189
5.2.8 Systematic uncertainty related to fit procedure . . . 190
5.3 Results . . . 191
5.3.1 $\Delta\eta - \Delta\varphi$ correlations between D^0 mesons and charged particles 192
5.3.2 Comparing three D mesons (D^0, D^+ and D^{*+}) correlation distributions . . . 193
5.3.3 Average of D^0, D^+ and D^{*+} . . . 194
5.3.3.1 Computation of near-side yields, near-side widths and baselines as a function of D meson p_T . . . 200
5.3.3.2 Comparison of data and Monte Carlo simulations . . 202
5.3.3.3 Comparison of *pp* and *pPb* data results . . . 205
5.3.4 Summary and Conclusion . . . 207

6 Study of small systems with simulated events 213

6.1 Study of high-multiplicity *pPb* events using EPOS 3 model 214

6.1.1 Heavy-flavor mesons: The probe 216

6.1.2 Two-particle angular correlations: The analysis tool 217

6.1.3 Event generation by EPOS 3 221

6.1.4 Centrality estimation 224

6.1.5 Relative yields of D-meson as a function of relative charged particle multiplicity 225

6.1.6 Multiplicity dependent invariant yields of identified charged particles 226

6.1.7 Short-range jet-like correlations 227

6.1.8 Long-range ridge-like correlations 230

6.1.9 Summary and Conclusion 236

6.2 Study of high-multiplicity *pp* events at the LHC energies up to the intermediate-p_{T} range 239

6.2.1 Results and Discussions: PYTHIA 8 simulated events for *pp* collisions at $\sqrt{s} = 7$ TeV 240

6.2.2 Transverse Momentum (p_{T}) / Mass (m_{T}) 241

6.2.2.1 $< N_{ch} >$ dependent $< p_{\mathrm{T}} >$ for identified charged particles up to intermediate-p_{T} 241

6.2.2.2 Identified charged particle spectra 242

6.2.3 Two-particle angular correlations 246

6.2.3.1 The correlation function 246

6.2.3.2 Extraction of long-range near-side correlated yields . 248

6.2.4 Summary and Conclusion 252

7 Outlook **256**

7.1 Angular correlations between D^0 mesons and charged particles using ALICE data: Outlook and future perspectives 256

7.2 Study of small systems with simulated events: Outlook and future perspectives 258

8 Appendix **261**

8.1 Event generators 261

8.1.1 PYTHIA 262

8.1.1.1 PYTHIA 8 tune 4C and Color Reconnection 264

8.1.2 HIJING 265

8.1.3 POWHEG 266

8.1.4 EPOS 267

SYNOPSIS

The Quark-Gluon Plasma (QGP) [1, 2], a thermalized state made up of partonic degrees of freedom, can be envisaged as a natural consequence of asymptotic freedom [3], one of the key features of Quantum Chromodynamics (QCD). It is now well established that the QGP is formed in relativistic heavy-ion collisions in the laboratory. The experimental search for the QGP witnessed the first important signal at the Super Proton Synchrotron (SPS) at CERN that led to the declaration [4] of indications of formation of the QGP-like new state of matter. In 2005, the experiments at the Relativistic Heavy-Ion Collider (RHIC) at the Brookhaven National Laboratory (BNL), confirmed [5–8] the formation of QGP in the ultra-relativistic heavy-ion collisions. ALICE (A Large Ion Collider Experiment) [9] is a dedicated experiment for studying the properties of QGP at the Large Hadron Collider (LHC), that became operational at CERN effectively in the year 2009. The recently recorded heavy-ion data with heavier nuclei at higher energy, as compared to the RHIC data, by ALICE and other LHC experiments corroborate most of the RHIC findings and provide opportunity to characterize the QGP in further detail.

Of several probes for characterizing the QGP, formed in relativistic heavy-ion collisions, the hadrons with constituent heavy quarks are unique ones. The heavy quarks (i.e charm and beauty quarks), because of their large masses ($m_c \approx 1.3$ GeV/c^2 and $m_b \approx 4.5$ GeV/c^2), are primarily produced in the initial stage of the collisions in the hard (large momentum transfer) parton-parton scattering [10]. Hence, their production cross-sections are calculable using perturbative QCD (pQCD). At the

LHC energy, the gluon-gluon fusion is the dominant source of the production of heavy quarks. The heavy quarks experience the full evolution of the medium by propagating through it. The heavy-flavour in-medium energy loss in heavy-ion collisions is studied by measuring the invariant yield of the produced particles in the heavy-ion collisions with respect to the corresponding yield in the proton-proton (pp) collisions at the same colliding energy, scaled by the number of incoherent binary nucleon-nucleon collisions, obtained from Glauber Model calculations [11, 12]. To extract more precise measurement of the final state effects of the hot nuclear matter (QGP), formed in relativistic nucleus-nucleus collisions, the initial state effects due to the cold nuclear matter (CNM) need to be properly estimated. The usual experimental method of disentangling the CNM effects from the hot nuclear matter effects is to normalize the nucleus-nucleus collision data with the respective proton-nucleus collision data. The analysis of the RHIC heavy-ion data, leading to the discovery of the QGP, also followed similar procedure (at RHIC, the CNM effect was actually studied with deuteron-gold (dAu) collisions instead of proton-gold (pAu) collisions, because of technical reasons).

At the LHC, however, beside providing the baseline for the study of QGP in heavy-ion collisions, the data of high-multiplicity events of pp and pPb collisions exhibit some unexpected features which resemble the signals for the formation of hydrodynamic medium in the heavy-ion collisions. Because of this reason, both the pp and pPb collisions at the LHC have generated new interest in the study of high multiplicity events. In fact, for construction of more realistic baselines for the study of the QGP in $PbPb$ collisions, it is imperative to understand the as yet unresolved features of the high multiplicity pp and pPb events. However, because of the non-availability of reasonably high statistics of high multiplicity events, these systems could not yet be thoroughly studied in the experiments to compare different contradicting models, proposed as explanations to the unexpected features. In these cases, for a better understanding of the particle production dynamics, one depends on simulation based studies.

In the analysis of heavy-ion data collected at RHIC and LHC, the two-particle angular correlations has been a powerful tool to study numerous properties, such as collective behaviour of the medium, jet-fragmentations, decays of resonances etc. The two-particle angular correlations is the prime analysis tool for the work related to this thesis. The **first part** of the thesis reports analysis of *pPb* data at $\sqrt{s_{\rm NN}} =$ 5.02 TeV in terms of angular correlations between D^0-mesons and primary charged particles produced in the collisions as recorded by the ALICE detector. In the **second part**, the thesis addresses some of the aspects of newly observed phenomena in the small systems (formed in high-multiplicity *pp* and *pPb* collisions at LHC energy) by analyzing events from the Monte Carlo event generators, primarily in terms of two-particle angular correlations.

First Part:

The angular correlation analysis (between the D-mesons and the primary charged particles) using the ALICE data is performed by associating D-mesons (D^0, D^+, D^{*+} mesons and their antiparticles), defined as "trigger" particles, with charged primary particles, defined as "associated particles" in the same event, excluding the daughters of the trigger D-mesons. The D-mesons and their charge conjugates are reconstructed via their hadronic decay channels. The thesis focuses mainly on D^0-meson as a trigger particle which is reconstructed from the decay channel $D^0 \to K^-\pi^+$ with a branching ratio 3.88±0.05%. For this study, about 100 million minimum bias events of *pPb* collisions at $\sqrt{s_{NN}} = 5.02$ TeV, as recorded by ALICE in 2013, and corresponding Monte Carlo productions have been analysed. The ALICE sub-detectors used for this analysis are the Inner Tracking System (ITS), the Time Projection Chamber (TPC) and the Time Of Flight (TOF). The charged particle tracks are reconstructed using the ITS and the TPC. The Particle Identification (PID) is based on the specific energy loss (dE/dx) in the TPC gas and on the time of flight from the interaction vertex to the TOF detector. The trigger for the minimum bias events has been the V0 scintillator detectors which is used as the multiplicity estimator also. The results of the data analysis are compared with the model estimations provided by Monte Carlo simulations.

The extraction of the D^0-meson signal is based on the reconstruction of decay vertices displaced from the primary vertex by a few hundred microns and on the identification of the decay-particle species [13]. To reconstruct D^0-mesons, several topological cuts are applied on the daughter tracks. The topological cuts help to reduce the combinatorial background during signal extraction. The main variables used to reject the combinatorial background are the separation between primary and secondary vertices, the distance of closest approach (DCA) of the decay tracks to the primary vertex, and the angle between the reconstructed D^0-meson momentum and the flight line defined by the primary and secondary vertices. Further reduction of background to the signal is obtained by identification of charged kaons and pions (daughter particles) using the TPC and TOF detectors. The raw D^0 yields or the D^0-candidates are extracted by fitting the distributions of invariant mass with a function, composed of a Gaussian term for the signal and an exponential term that models the combinatorial background. The D^0-candidates or the "triggers" are then correlated with other charged primary particles, referred to as the "associated particles" in the same event in the given kinematic range. In the analysis, relatively wide p_T intervals for D^0-meson ($3 < p_T < 5$ GeV/c, $5 < p_T < 8$ GeV/c, $8 < p_T < 16$ GeV/c) and associated charged tracks ($p_T > 0.3$ GeV/c, 0.5 GeV/c, 1 GeV/c) are chosen in order to reduce the statistical fluctuations in the angular correlation distributions. The ALICE detector set-up facilitates the study with the pseudo-rapidity cut, $|\eta| < 0.8$. The daughter particles from D^0-candidates and particles coming from other weak decays or originating from interactions with the detector material are excluded from the associated particle sample.

The difference in the azimuthal angle ($\Delta\phi$) and in pseudo-rapidity ($\Delta\eta$) for D^0-candidates and the associated particles are computed over different mass windows in the D^0 invariant mass distribution around the signal mass peak containing the signal and background candidates. In order to correct for the acceptance and reconstruction efficiency of the associated tracks and the D^0-candidates inside a given p_T interval, the correlation distributions are weighted with appropriate efficiency factor, obtained from simulation. In order to take into account the limited acceptance of detectors and spacial inhomoginities between the charged particles, a mixed event approach is used. The same-event correlations are divided by the normalized mixed event correlations. The obtained correlation distributions contain the angular correlations due to background also. A "**side-band**" approach has been adopted to get rid of the correlations due to the background under the signal mass peak. A correction for the purity of the primary particle sample is applied. Finally the one-dimensional $\Delta\phi$ correlations are obtained by integrating the two-dimensional ($\Delta\eta$-$\Delta\phi$) correlation distributions over a specified $\Delta\eta$-range. The per trigger yield of associated charged particles has been obtained by normalizing the correlation function with the number of triggers in the specific p_{T} intervals. A fraction of the reconstructed D-mesons consists of secondary D-mesons coming from B-meson decays. The B-mesons decay particles result into different angular correlation distribution. The contribution of B-meson decays (feed-down) to the measured angular correlations has been subtracted. Different systematic studies including "signal and background normalization", "background $\Delta\phi$ variation", "trigger and track efficiencies", "primary charged particle purity", "feed-down subtraction" have been carried out. In order to quantify the properties of the measured azimuthal correlations, the fully corrected $\Delta\phi$ correlations are fitted with a fit function, composed of two Gaussian terms (including a periodicity condition) describing the near-side and away-side peaks and a constant term describing the "baseline". A v_2-like modulation of the baseline which could introduce a bias in the quantification of the correlation distributions, is taken into account during the baseline fit. The integrals of the Gaussian functions give the per-trigger associated-particle yields for the near-side (NS) peak and the away-side (AS) peak with their widths (σ_{NS}, σ_{AS}). The systematic uncertainty related to the fit procedure is also estimated. The thesis contains the study on dependence of the near-side yield-related parameters as a function of p_T of the trigger and associated charged particles.

The measurement of angular correlations between D-mesons (focusing on D^0) and charged particles in pPb collisions at $\sqrt{s_{\mathrm{NN}}}$= 5.02 TeV has been compared with the pp data at $\sqrt{s}$ = 7 TeV [14]. The analysis reveals that, for the given statistics, the results from the two-particle angular correlation study for the minimum bias *pp* and *pPb* events are comparable within the calculated uncertainties. This implies that no cold nuclear matter effect is seen in the *pPb* collisions at $\sqrt{s_{\rm NN}} = 5.02$ TeV in terms of two-particle angular correlations. The finding is consistent with the observed absence [15] of the Cronin effect in the *pPb* collisions. The perspectives of the future studies on angular correlations between D-mesons and charged particles have also been highlighted. Particularly, the study of multiplicity dependent correlations between D-mesons and the charged particles will be worth carrying out when higher statistics data will be available.

Second Part:

In an attempt to understand the features of high multiplicity events in small systems, the *pp* and *pPb* events have been generated with the event generators, PYTHIA and EPOS, respectively, and results from analysis of these events constitute the second part of the thesis. The generated events have been analyzed, primarily, in terms of the same analysis tool, the two-particle angular correlations.

The EPOS [16] event generator has been successful in explaining different features of muti-paticle production in *pp*, *pPb* and *PbPb* collisions at the LHC. Particularly, the EPOS event generator, incorporated with the hydrodynamic evolution, have been effective in describing the particle production in small systems. We, therefore, generate events for *pPb* collisions at $\sqrt{s_{\rm NN}} = 5.02$ TeV, using the EPOS event generator, with and without, hydrodynamic evolution, to extend our D-meson and charged particle angular correlation study for high multiplicity *pPb* events.

In case of high-multiplicity *pp* events, while the hydrodynamic models satisfactorily explain some of the new features of the data, indicating possible formation of hydrodynamic medium, we preferred to look into the pQCD-inspired Multi-Parton Interaction (MPI) model, that has been a well accepted model of particle production in pp collisions. The MPI model with a color reconnection scheme, as implemented in PYTHIA8 tune 4C event generator [17], reproduces the dependence of the mean transverse momentum, $< p_{\rm T} >$ on charged particle multiplicity, $\rm N_{\it ch}$ in pp collisions at the LHC, providing an alternate explanation to the new features. A comprehensive study on the comparison between the data and the MPI model, with and without color reconnection, has been presented in this thesis. The analysis demonstrates the limitations of the model in explaining some of the prominent features of the final state charged particles up to the intermediate-$p_{\rm T}$ range ($p_{\rm T} < 2.0$ GeV/c).

Bibliography

[1] James L Nagle et al., New Journal of Physics 13 (2011) 075004.

[2] Ulrich Heinz, Nuclear Physics A721 (2003) 30c-39c.

[3] J. C. Collins and M. J. Perry, Phys. Rev. Lett 34 (1975) 1354.

[4] CERN press release 2000
`http://pressold.web.cern.ch/PressOld/Releases00/PR01.00EQuarkGluonMatter.html`

[5] I. Arsene et al., (BRAHMS Collaboration) 2005 Nucl. Phys. A 757 1.

[6] K. Adcox et al., (PHENIX Collaboration) 2005 Nucl. Phys. A 757 184.

[7] B. B. Back et al., (PHOBOS Collaboration) 2005 Nucl. Phys. A 757 28.

[8] J. Adams et al., (STAR Collaboration) 2005 Nucl. Phys. A 757 (2005) 102.

[9] J. Schukraft (for the ALICE Collaboration), J. Phys. G: Nucl. Part. Phys. 38 (2011) 124003.

[10] P. Braun-Munzinger, J. Phys. G 34 (2007) S471.

[11] Glauber RJ. Nucl. Phys. A 774:3 (2006).

[12] Michael L. Miller et al., Ann.Rev.Nucl.Part.Sci. 57 (2007) 205-243.

[13] B. Abelev et al., (ALICE Collaboration), JHEP 01 (2012) 128.

[14] J. Adam et al., (ALICE Collaboration), Eur. Phys. J. C 77 (2017) 245.

[15] B. Abelev et al., (ALICE Collaboration), Phys. Rev. Lett. 113 no. 23.

[16] K. Werner et al., Phys. Rev. C 89 (2014) 064903.

[17] Torbjorn Sjostrand, Stephen Mrenna, Peter Skands, JHEP 05 (2006) 026.

Publications:

List of publication related to this thesis:

Referred Journals:

1. *"Measurement of azimuthal correlations of D mesons and charged particles in pp collisions at* $\sqrt{s}$ *= 7 TeV and p–Pb collisions at* $\sqrt{s_{\rm NN}}$ *= 5.02 TeV."*

   Andrea Rossi, Sandro Bjelogrlic, Elena Bruna, **Somnath Kar** **(as primary author)**, Fabio Filippo Colamaria, Jitendra Kumar, ALICE Collaboration (J. Adam et al.).

   Eur. Phys. J. C 77 (2017), 245, arXiv:1605.06963v1 [nucl-ex]

2. *"Multiple parton interactions and production of charged particles up to the intermediate-*$p_{\rm T}$ *range in high multiplicity pp events at the LHC."*

   Somnath Kar, Subikash Choudhury, Sanjib Muhuri, and Premomoy Ghosh.

   Phys. Rev. D95 (2017) 014016.

Conference Proceedings:

1. *"Measurement of* $\rm D^0$*-hadron azimuthal correlations in p–Pb collisions at* $\sqrt{s_{\rm NN}}$ *= 5.02 TeV with ALICE."*

   Somnath Kar for the ALICE collaboration.

   Proceedings of the DAE Symp. on Nucl. Phys. 58 (2013).

2. *"Study of angular correlations between D mesons and charged particles in pp and p–Pb collisions with ALICE at the LHC."*

   Somnath Kar on behalf of the ALICE Collaboration.

   Proceedings of the DAE-BRNS Symp. on Nucl. Phys. 60 (2015)

3. *"Measurement of angular correlations between* D *mesons and charged particles in pp and p–Pb collisions with ALICE at the LHC."*

   Somnath Kar for the ALICE Collaboration, **Proceedings of the ICPAQGP, 2015 conference, February 2-6, 2015**

   arXiv:1510.07577v1 [hep-ex] 26 Oct 2015.

Other publications:

List of publication related to this thesis (as a part of ALICE Collaboration):

1. *"Suppression of high transverse momentum D mesons in central Pb–Pb collisions at* $\sqrt{s_{\rm NN}}$ *= 2.76 TeV."*

   B. Abelev et al., ALICE Collaboration, JHEP09 (2012) 112.

2. *"Measurement of electrons from heavy-flavour hadron decays in p–Pb collisions at* $\sqrt{s_{\rm NN}}$ *= 5.02 TeV."*

   J. Adam et al., ALICE Collaboration, Phys. Lett. **B754** (2016) 81-93.

3. *"Elliptic flow of muons from heavy-flavour hadron decays at forward rapidity in Pb–Pb collisions at* $\sqrt{s_{\rm NN}}$ *= 2.76 TeV."*

   J. Adam et al., ALICE Collaboration, Phys. Lett. **B753** (2016) 41-56.

4. *"Measurement of charm and beauty production at central rapidity versus charged-particle multiplicity in proton-proton collisions at* $\sqrt{s}$ *= 7 TeV."*

   J. Adam et al., ALICE Collaboration, JHEP09 (2015) 148.

5. *"Measurement of electrons from semi-leptonic heavy-flavor hadron decays in pp collisions at* $\sqrt{s_{\rm NN}}$ *= 2.76 TeV."*

   B. Abelev et al., ALICE Collaboration, Phys. Rev. **D91** (2015) 012001.

6. *"Measurement of prompt D-meson production in p–Pb collisions at* $\sqrt{s_{\rm NN}} =$ *5.02 TeV."*

   B. Abelev et al., ALICE Collaboration, Phys. Rev. Lett. **113** (2014) 232301.

7. *"Azimuthal anisotropy of D meson production in Pb–Pb collisions at* $\sqrt{s_{\rm NN}} =$ *2.76 TeV."*

   B. Abelev et al., ALICE Collaboration, Phys. Rev. **C90** (2014) 034904.

8. *"D meson elliptic flow in non-central Pb–Pb collisions at* $\sqrt{s_{\rm NN}} = 2.76$ *TeV."*

   B. Abelev et al., ALICE Collaboration, Phys. Rev. Lett. **111** (2013) 102301.

Signature of Student: Somnath Kar

Date: 20.12.2016

Doctoral Committee:

S. No.	Name	Designation	Signature	Date
1.	Prof. Tapan Kumar Nayak	Chairman	T K Nayak	20/12/2016
2.	Prof. Premomoy Ghosh	Guide/ Convener	Premomoy Ghosh	20.12.2016
3.	NA	Co-guide (if any)		
4.	Prof. Subhasish Chattopadhyay	Member	S Chattopadhyay	20/12/16
5.	Prof. Munshi Golam Mustafa	Member	M Mustafa	20/12/16
6.		Member		

List of Figures

1.1 The standard model and its constituents. 6

1.2 Quark structure of baryons and mesons. 6

1.3 Potential due to strong interactions (left) and variation of running coupling constant (α_s) with momentum transfer [8] (right). 8

1.4 A schematic diagram of the QCD phase diagram of nuclear matter in terms of the temperature (T) and baryonic chemical potential (μ_B) [10]. 11

1.5 Energy density as function of the temperature T from lattice QCD calculations. The calculations are performed for two massless quarks (2), three massless quarks (3) and two massless quark and one (s) with its real mass (2+1) [15]. 12

1.6 Schematic representation of the evolution of relativistic heavy-ion collision [54]. 18

1.7 Schematic representation of space-time evolution of relativistic heavy-ion collision. 19

1.8 A collision between two heavy nuclei in the spectator-participant model. (a) The two Lorentz contracted nuclei before the collision. The centrality is determined by the impact parameter b. (b) Participant region with high temperature and density is created after the collision. 19

1.9 Schematic diagram of elliptic flow in a non-central heavy-ion collisions [69]. 24

1.11 p_{T} integrated elliptic flow for charged hadron as a function of centrality by ALICE compared with STAR results (left) [70]. Elliptic flow as a fucntion of transverse kinematic energy scaled by the number of constituent quarks for identified hadrons (right) [71]. 24

1.10 Elliptic flow (v_2) as a function of p_{T} and comparison between different experiments [70, 72, 73]. 25

1.12 Particle ratios as a function of p_{T} measured in the most central, 0–5%, *PbPb* and in minimum bias *pp* collisions. [61]. 26

1.13 Particle ratios as a function of p_{T} measured in the most central, 0–10%, *PbPb* collisions at $\sqrt{s_{\mathrm{NN}}} = 2.76$ TeV [61] by ALICE and at $\sqrt{s_{\mathrm{NN}}}$ = 200 GeV by STAR (0-12%) and PHENIX (0-10%). 26

1.14 Back-to-back jets in heavy-ion collisions. The one is produced near the surface of the hot and dense medium and the other deep inside. These are called the near-side and away-side jets. 27

1.15 Nuclear modification factor in most central (0–5%) and peripheral (70–80%) $PbPb$ collisions at $\sqrt{s_{\rm NN}}$ = 2.76 TeV (left), measured by ALICE and a comparison with the RHIC results [77] (right) in most central case only. 29

1.16 Schematic diagrams of (a) non- (b) single- and (c) double-diffractive processes, respectively. 30

1.17 Sketch of a hadronic collision (in different colors): hard scattering between two partons (red), the initial- and the final-state showers (blue), a multiparton interaction (purple), beam remnants of the incoming protons (brown), the particles produced after the hadronization (light and dark green) [80]. 32

1.18 Comparison of charged particle multiplicity for data (ATLAS) and PYTHIA with and without MPI model. 34

1.19 (Left) Schematic behaviour of nuclear modification factor ($R^A_{F_2}(x, Q^2)$) as a function of x for a given Q^2 [37]. (Right) The ratio of the structure functions F_2^{Ca} and F_2^d in calcium Ca nuclei and deuterium from EMC and SLAC. 37

1.20 (Left) Cronin effect on pion production at Fermilab [36] and (middle and right) at RHIC with GE computation (solid line). 38

1.21 Nuclear modification factor to account the isospin effect as a function of Q_t, transverse momentum [93]. 39

1.22 Two-particle angular correlations in pp collisions at $\sqrt{s}$ = 7 TeV minimum bias and high-multiplicity events using different trigger momentum cuts. 42

1.23 Long-range near-side associated yield for two-particle correlations in $1 < p_{\mathrm{T}} < 2$ GeV/c in pp collisions at $\sqrt{s} = 7$ TeV as function of multiplicity, measured by CMS experiment. 43

1.24 Charged particle 2-dimensional $(\Delta\eta, \Delta\varphi)$ correlations in high-multiplicity pp collisions at $\sqrt{s}$ =7 TeV with $1 < p_{\mathrm{T}} < 3$ GeV/c using EPOS LHC model. (a) without hydrodynamic evolution and (b) with hydrodynamic evolution. 44

1.25 2-dimensional $(\Delta\eta, \Delta\varphi)$ two-particle correlation functions in pPb collisions at $\sqrt{s_{\mathrm{NN}}} = 5.02$ TeV for pairs of charged particles in $1 < p_{\mathrm{T}} < 3$ GeV/c (CMS) and $1 < p_{\mathrm{T}} < 2$ GeV/c (LHCb). Results are shown for high-multiplicity classes ($\mathrm{N}_{trck}^{offline} > 110$ for CMS and 0-3% event class for LHCb). 45

1.26 (Top) 2-dimensional $(\Delta\eta, \Delta\varphi)$ di-hadron correlation function taking pion and proton as trigger particles measured by ALICE, for high-multiplicity (0–20%) events, after subtraction of the results for the 60–80% centrality class [99]. (Bottom) $\Delta\varphi$ projection of top panel averaged over $0.8 < |\Delta\eta| < 1.6$ on the near side and $|\Delta\eta| < 1.6$ on the away side. 46

1.27 The measured Fourier coefficient v_2 for identified hadrons as a function of p_{T} from the correlation in the 0–20% multiplicity class after subtraction of two-particle correlation from the 60–100% multiplicity class. The mass ordering of the flow coefficient is successfully addressed by EPOS 3 model including hydrodynamical calculations. . 47

1.28 (Left) 2-dimensional $(\Delta\eta, \Delta\varphi)$ di-hadron correlation function calculated using EPOS 3 simulations, for high-multiplicity (0–20%) events, after subtraction of the result for the 60–80% class [103]. (Right) Comparison of one dimensional $(\Delta\varphi)$ per-trigger di-hadron correlations between the Glasma graphs computation from CGC model and the ALICE data [104]. 48

1.29 Charged particle ratios K/π (top) and p/π(bottom) measured by ALICE for most central (0–5%) and peripheral (60–80%) events in pPb and $PbPb$ collisions at $\sqrt{s_{\rm NN}} = 5.02$ TeV and 2.76 TeV respectively [105]. 49

1.30 The average transverse momentum $< p_{\rm T} >$, as a function of charged particle multiplicity, N_{ch}, as measured by ALICE in pp (up), pPb (middle) and $PbPb$ (bottom) collisions. The data are compared with different model calculations [115]. 52

2.1 Contributions from different correlation sources to the $\Delta\eta, \Delta\varphi$ correlation function. Figure taken from [3]. 67

2.2 (Left) sample representation of $\Delta\eta, \Delta\varphi$ correlation distributions obtained via same-event, mixed-events and same/mixed-events. (Right) schematic diagram of 1-dimensional two-particle angular correlations projected on $\Delta\varphi$. 70

2.3 ALICE measurements of two-particle angular correlations in central $PbPb$ collisions at $\sqrt{s_{\rm NN}} = 2.76$ TeV (left) [14]. Di-hadron azimuthal correlations ($\Delta\varphi$ distribution) measured by STAR in three collision systems pp, $AuAu$ and dAu (right) [15]. 73

2.4 (top) Per-trigger corrected di-hadron azimuthal ($\Delta\varphi$) correlation distributions for $8 < p_{\mathrm{T}} < 15$ GeV/c and $4 < p_{\mathrm{T}}^{assoc} < 6$ GeV/c for central and peripheral $PbPb$ events and pp events measured by the ALICE detector. a) azimuthal correlation; b) zoom on the region where the pedestal values (horizontal lines) and the v_2 component are indicated; c) background-subtracted $\Delta\varphi$ distributions using the flat pedestal. (bottom) I_{AA} for near-side (left panel) and away side (right panel) for most central (0-5% $PbPb/pp$) and peripheral (60-90% $PbPb/pp$) events measured by ALICE. 74

2.5 2-dimensional two-particle angular correlation function for two unidentified hadrons in $PbPb$ collisions at the LHC, reported by the CMS Collaboration [17]. 76

3.1 Feynman diagrams of pair creation (left), flavour excitation (middle) and gluon splitting (right) [2]. 84

3.2 The differential cross section measurements for different D mesons at $\sqrt{s} = 1.96$ TeV at CDF II. The solid and dashed curves represent the theoretical predictions from Cacciari and Nason [7] and the shaded bands indicate uncertainties [5]. For the D_s^+ production there is no theoretical prediction. 85

3.3 p_{T}-differential charm hadron (D^0 and D^*) production cross section in pp collisions at $\sqrt{s_{\mathrm{NN}}} = 200$ GeV at STAR [8]. 86

3.4 (Left) p_{T}-differential cross section of prompt D^0 mesons in pp collisions at $\sqrt{s} = 7$ TeV, compared with theoretical calculations. (Right) Total charm cross section measured in pp collisions by ALICE as a function of $\sqrt{s}$, in comparison with other experimental results and MNR calculations [9, 10]. 86

3.5 Collisional (left) and medium-induced radiative (right) energy loss mechanisms of a quark of energy E traversing in a quark medium and loosing a fraction of energy ΔE [14]. 89

3.6 Collisional energy loss of charm quark in $PbPb$ collision at $\sqrt{s_{\mathrm{NN}}} =$ 2.76 ATeV and 5.5 ATeV at LHC, and 200 AGeV at RHIC [17]. . . . 90

3.7 schematic diagram of dead cone effect for heavy quark [27]. 92

3.8 (Left) Suppression factor for a charm quark as a function of x = ω/ω_c where ω_c is the characteristic gluon frequency. The in-medium path length is considered as L = 5 fm. (Right) Energy loss of charm quarks as a function of charm quark initial energy [28]. 93

3.9 (Left) Heavy-flavor electron nuclear modification factor (R_{AA}) and elliptic flow (v_2) measured by PHENIX in $AuAu$ collisions at RHIC [30]. (Right) R_{AA} for baryons, strange mesons, electrons from heavy-flavor, light quark mesons and direct photons measured by PHENIX in 0-10% most central $AuAu$ collisions at $\sqrt{s_{\mathrm{NN}}} = 200$ GeV [31]. 94

3.10 (top-left) $R_{\mathrm{AA}}(p_{\mathrm{T}})$ for average prompt D mesons (color circles), charged particles (color circles), and charged pions (color squares) in the most central event class [32]. (top-right) Centrality dependent R_{AA} for the heavy-flavor decay muons (color triangles), the average prompt D mesons (color filled circles), charged particles (empty circles) and non-prompt J/ψ from CMS [33]. Average D^0, D^+ and D^{*+} v_2 as a function of p_{T}, compared to charged particle v_2 [35, 36] measured by ALICE using the event-plane (EP) method. 95

3.11 (Left) Angular correlations of $c\bar{c}$ pairs with LO pQCD approximation, used for $c\bar{c}$ pair initialization in central $AuAu$ collisions. (Right) D-$\bar{\mathrm{D}}$ angular correlations in central $AuAu$ collisions at RHIC [37]. 97

3.12 (Left) Azimuthal correlation distributions for heavy-flavour decay electrons and charged hadrons in pp (top panel) and $AuAu$ (bottom panel) collisions at $\sqrt{s_{\mathrm{NN}}} = 200$ GeV measured by the PHENIX experiment. (Right) The near-side I_{AA} for $2 < p_T^e < 3.0$ GeV/c (top panel) and $3 < p_T^e < 4.0$ GeV/c (bottom panel) as a function of the associated hadron p_{T} for heavy-flavour decay electron (solid points) and hadron (open points) triggers in $AuAu$ collisions at $\sqrt{s_{\mathrm{NN}}} = 200$ GeV measured by the PHENIX experiment [40]. 98

3.13 (Left) PHENIX measures the nuclear modification factor in dAu collisions, R_{dA} as a function of $p_{\rm T}$ of heavy-flavor electrons at mid-rapidity in different centrality classes [42]. (Right) ALICE measures R_{pPb} as a function of $p_{\rm T}$ of heavy-flavour electrons from hadron decays for minimum-bias pPb collisions at $\sqrt{s_{\rm NN}}$ = 5.02 TeV, compared with theoretical models [41]. 99

3.14 Comparison of nuclear modification factors ($R_{\rm AA}$ and R_{pPb}) as a function of $p_{\rm T}$ for D meson production in minimum-bias pPb collisions and in two different centrality classes in $PbPb$ collisions by ALICE [43]. . 100

3.15 Angular correlations between HF-electrons and hadrons in 3 multiplicity classes in pPb collisions compared to minimum-bias pp events (Left). 2-dimensional $(\Delta\eta, \Delta\varphi)$ correlation in pPb collisions after subtraction of the lowest multiplicity class from the highest multiplicity class by ALICE [44] (Right). 101

4.1 Schematic diagram of LHC tunnel with the positions of different parts. 108

4.2 Schematic diagram of CERN accelerator complex. 110

4.3 Schematic diagram of ALICE detectors with all its sub-systems. . . . 111

4.4 Schematic layout of Muon spectrometer. 115

4.5 The co-ordinate system of ALICE detector. 117

4.6 Schematic diagram of the Inner Tracking System of the ALICE detector describing different layers [23]. 118

4.7 Layout of the ALICE TPC showing the central electrode, the field cage and the end plates supporting the readout chambers. 120

4.8 Energy loss in the TPC (dE/dx) versus momentum p (GeV/c) with Bethe-Bloch predictions (black lines) for different particles in $PbPb$ collisions (left) and in pPb collisions (right) [24]. 122

4.9 Particle β vs. momentum in $PbPb$ collisions at $\sqrt{s_{\mathrm{NN}}} = 2.76$ TeV (left) and in pPb collisions at $\sqrt{s_{\mathrm{NN}}} = 5.02$ TeV(right) by TOF. . . . 124

4.10 Combined pion, kaon and proton identification with the TOF and the TPC for central pPb collisions. 124

4.11 Position of the two VZERO arrays within the general layout of the ALICE experiment (left). Schematic diagram of VZERO-A and VZERO-C arrays showing their segmentation (right) [28]. 125

4.12 Hierarchy of online systems. 126

4.13 Global view of ALICE data flow [29]. 129

4.14 A snapshot of the ALICE VO sites in Europe. A green circle indicates that jobs are running on the site while red and yellow circles indicate sites with problems. 131

4.15 A schematic view of the AliRoot framework. 132

4.16 Schematic view of the reconstruction framework. 133

5.1 Topology of the D^0 meson decay. 147

5.2 Distance to closest approach (dca, left panel) and $\cos\theta^*$ (right panel) distributions for background (black circles) and signal (red triangles) candidates. 149

5.3 Schematic view of D^0 decay in the D^0 rest frame. 150

5.4 Cosine of pointing angle ($\cos\theta_{point}$, left panel) and $d_0^k \times d_0^\pi$ (right panel) distributions for background (black circles) and signal (red triangles) candidates. 151

5.5 nσ TPC vs nσ TOF for pion (left) and kaon (right). 153

5.6 D^0 invariant mass distributions in pPb collisions. The signal is extracted in 4 p_T intervals in the range $1 < p_T < 24$ GeV/c. 155

5.7 D^0 invariant mass distribution as a function of the transverse momentum (left) compared with the reflection invariant mass distribution as a function of the transverse momentum (right). 156

5.8 Acc $\times\epsilon$ as a function of p_T for prompt and feed-down D^0 mesons in the minimum bias pPb events. 158

5.9 D^0 invariant mass distribution with Gaussian+exponential fit in the Signal (yellow+red in $\pm 2\sigma$) and Sidebands (green in $\pm 4\sigma$) regions [6]. 163

5.10 Signal region (left) and total sideband region (right) correlation distribution for the D^0 candidates correlated with the associated charged primary particles in the same event. 164

5.11 schematic diagram of event mixing. 166

5.12 Examples of 2-dimensional ($\Delta\eta$, $\Delta\varphi$) correlation distributions between D^0 mesons and charged primary particles, for $5 < p_T(D^0) < 8$ GeV/c and $p_T^{assoc} > 0.3$ GeV/c: (top) Mixed-event correlation for signal (left) and sideband (right) regions. (bottom) mix event corrected signal (left) and sideband (right) regions. 168

5.13 Background subtracted and mixed-event corrected 2-dimensional ($\Delta\eta$, $\Delta\varphi$) correlation distribution in the signal region. 169

5.14 Prompt D^0 meson efficiency as a function of p_T and multiplicity (left) and p_T only (right). 170

5.15 Single track efficiency as a function of p_T and η (left) and p_T only (right). 172

5.16 (Left) Number of primary/secondary tracks which are accepted/rejected by the DCA cut, for the integrated D^0 p_T bin. (Right) Ratio of correlations due to all tracks passing the quality cuts and of secondary tracks passing the DCA cut. 174

5.17 Ratio of correlation distributions obtained with standard sideband definition over correlation distributions with different ranges for sidebands, for different D^0 p_T bins and associated tracks $p_T > 0.3$ GeV/c. Other associated track p_T variations can be found here [11]. 177

5.18 D^0 meson efficiency map as a function of multiplicity and p_T for tightened (left) and loosened (right) cut selections. 178

5.19 Comparison of the ratio of azimuthal correlation distributions for different cut selections on D^0 reconstruction, in different D^0 p_T bins and associated tracks $p_T > 0.3$, 0.5, 1.0 GeV/c. Other trigger and associated track p_T variations can be found here [11]. 179

5.20 Associated charged particles efficiency map as a function of p_T for three different filtering selections; standard, TPC-only, ITS+TPC. . . 181

5.21 Ratio of correlation distributions obtained with different associated tracks filtering selections, for different D^0 p_T bins and associated tracks $p_T > 0.3$ GeV/c. 182

5.22 Ratio of azimuthal correlation distributions with tighter DCA cuts over standard one (1 cm) for three D^0 p_T bins with associated track $p_T > 0.3$ GeV/c. 184

5.23 D^0-charged particle azimuthal correlation distributions obtained from Monte Carlo simulations, at kinematic level for 5-8 GeV/c and 8-16 GeV/c trigger ranges and with associated track p_T threshold of 0.3 GeV/c. 186

5.24 D^0-charged particle azimuthal correlation distributions obtained from Monte Carlo simulations, at reconstruction level for 5-8 GeV/c and 8-16 GeV/c trigger p_T ranges and with associated track p_T threshold of 0.3GeV/c. 186

5.25 Ratios of fully corrected azimuthal correlation distributions at reconstructed level over azimuthal correlation distributions at kinematic level, in the two D^0 p_T bin, for the different associated track p_T ranges. Colors of different ratios correspond to different sources of D^0 as stated in the text. 187

5.26 Fully corrected 2-dimensional $(\Delta\eta, \Delta\varphi)$ D^0-charged particle correlation distributions, in different D^0 p_T ranges, Low: $3 < p_T(D^0) < 5$ GeV/c, Mid: $5 < p_T(D^0) < 8$ GeV/c , High: $8 < p_T(D^0) < 16$ GeV/c for associated track p_T threshold of 0.3 GeV/c (upper row), 0.5 GeV/c (middle row) and 1.0 GeV/c (bottom row). 193

5.27 1-dimensional $\Delta\varphi$ correlation distributions between D^0 mesons and charged particles in D^0 p_T bin $8 < p_T(D^0) < 16$ GeV/c and with associated track p_T threshold of 0.3 GeV/c (left) and 1.0 GeV/c (right). The distributions are fitted with standard fit function. The blue and green color dotted lines are the near-side and away-side Gaussian functions respectively. 194

5.28 Fully corrected $\Delta\varphi$ distributions of D^0-charged particle azimuthal correlations, in D^0 p_T bins (Column-Left: $5 < p_T(D^0) < 8$ GeV/c, Column-Right: $8 < p_T(D^0) < 16$ GeV/c) and associated tracks p_T ranges (top-row: > 0.3 GeV/c, middle-row: 0.3 to 1 GeV/c, bottom-row: >1.0 GeV/c). 195

5.29 Example of comparison of full range (0 - 2π) and reflected (0 - π) azimuthal correlation distributions for D^0 p_T range $5 < p_T(D^0) < 8$ GeV/c with associated track p_T threshold of 0.3 GeV/c. 196

5.30 Example of comparison of azimuthal correlation distributions for three D mesons in the p_T range of 8-16 GeV/c with associated track p_T threshold of 0.3 GeV/c in full $\Delta\varphi$ range (left) and in reflected range (right). 196

5.31 Azimuthal correlation distributions between average of D^0, D^+ and D^{*+} and primary charged particles in the D meson p_T ranges $5 < p_T(D) < 8$ GeV/c and $8 < p_T(D) < 16$ GeV/c, with associated track $p_T > 0.3$ GeV/c, $p_T > 1$ GeV/c and $0.3 < p_T < 1$ GeV/c. 198

5.32 Comparison of weighted and arithmetic averages D meson-charged particle azimuthal correlations with associated track $p_{\mathrm{T}} > 0.3$ GeV/c, $0.3 < p_{\mathrm{T}} < 1$ GeV/c in the D meson p_{T} range $8 < p_{\mathrm{T}}(\mathrm{D}) < 16$ GeV/c. 199

5.33 Example of fit to the azimuthal correlation distributions, for the average of the three D-mesons in $5 < p_{\mathrm{T}}(\mathrm{D}) < 8$ GeV/c and $p_{\mathrm{T}}^{assoc} > 1$ GeV/c. 200

5.34 (left column) Near-side yield, near-side width and height of the baseline extracted from fit to the azimuthal correlation distributions for $p_{\mathrm{T}}^{assoc} > 0.3$ GeV/c. (right column) The corresponding systematic uncertainties coming from the variation of the fit procedure. 201

5.35 Comparison of $\Delta\varphi$ azimuthal correlation distribution, obtained from data and simulations (PYTHIA, with three tunes), in the different kinematic ranges analyzed. 203

5.36 Comparison of near-side peak associated yield (top row) and near-side peak width (bottom row) values measured in pPb collisions at $\sqrt{s_{\mathrm{NN}}}$= 5.02 TeV with the expectations from simulations performed with different Monte Carlo event generators. Statistical and systematic uncertainties are shown as error bars and boxes, respectively [7]. 204

5.37 Average of D^0, D^+ and D^{*+} azimuthal correlations in pp (red) and pPb (blue) with D meson p_{T} ranges $5 < p_{\mathrm{T}} < 8$ GeV/c and $8 < p_{\mathrm{T}} < 16$ GeV/c, for the three regions of associated track p_{T} [7]. 206

5.38 Comparison of the near-side peak associated yield (top row) and peak width (bottom row) between pp and pPb collisions as a function of $p_{\mathrm{T}}(\mathrm{D})$, for $p_{\mathrm{T}}^{assoc} > 0.3$ GeV/c (left column), 0.3< $p_{\mathrm{T}}^{assoc} < 1$ GeV/c (middle column), and $p_{\mathrm{T}}^{assoc} > 1$ GeV/c (right column). Statistical and systematic uncertainties are shown as error bars and boxes, respectively [7]. 207

6.1 The multiplicity dependent invariant yields of pions (top), kaons (middle) and protons (bottom) in pPb collisions at $\sqrt{s_{\mathrm{NN}}} = 5.02$ TeV, measured by ALICE [2], are compared with the simulated events from the EPOS 3 without hydrodynamic evolution [1]. 215

6.2 Centrality selection for the EPOS 3 generated events from the VZERO-A acceptance [6] of ALICE set-up. 224

6.3 Average relative D-meson yields as a function of the relative V0A multiplicity ($N_{V0A}/ < N_{V0A} >$) in different $p_{\mathrm{T}}(\mathrm{D})$ intervals. 226

6.4 The multiplicity dependent invariant yields of identified charged particles in pPb collisions at $\sqrt{s_{\mathrm{NN}}} = 5.02$ TeV, measured by ALICE [2], are compared with the simulated events from the EPOS 3 event generator with hydrodynamical evolution. 228

6.5 (Left) Minimum bias per D-meson triggered correlated yields, in $|\Delta\eta|$<1 in different $p_T^{trigger}$ ranges, 3 to 5, 5 to 8 and 8 to 16 GeV/c and in the $p_T^{associated}$ threshold, $p_T^{assoc} > 0.3$ GeV/c. (Right) $\Delta\varphi$ projection in $|\Delta\eta|$<1 for different centrality bins of EPOS 3 generated pPb collisions at $\sqrt{s_{\mathrm{NN}}} = 5.02$ TeV in the $p_T^{trigger}$ range, 3 <p_T< 5 GeV/c and in the $p_T^{associated}$ range, 1<p_T< $p_T^{trigger}$ GeV/c. 229

6.6 Comparison of bulk-subtracted jet-yields obtained from the correlation distributions taking trigger particles as D-mesons and charged hadron in the $p_T^{trigger}$ range, 3 $<p_T<$ 5 GeV/c and in the $p_T^{associated}$ range, 1 $<p_T<$ 3 GeV/c for different centrality bins of EPOS 3 generated pPb collisions at $\sqrt{s_{\rm NN}}$ = 5.02 TeV. The dotted lines connect the points to show the trend of the centrality-dependences. 230

6.7 The centrality dependence of $\Delta\varphi$ distributions in the long-range 2 $<\Delta\eta<$ 4 for two-particle azimuthal correlations taking hadrons (left) and D-mesons (right) as trigger particles, for different centrality classes and in different kinematic ranges of the same $p_T^{trigger}$ and $p_T^{associated}$. . 233

6.8 Two particle $\Delta\eta - \Delta\varphi$ correlation function for 3 $<p_T^{trigger}<$ 5 GeV/c and 1 $<p_T^{associated}<$ 3 GeV/c with D-meson as trigger particles for the hydrodynamic-EPOS 3 generated pPb collisions at $\sqrt{s_{\rm NN}}$ = 5.02 TeV in 0 - 20 (top) and 60 - 100 (bottom) per cent central event classes. . 235

6.9 The centrality dependence of per-trigger $\Delta\varphi$ distributions in the long-range (2 $<\Delta\eta<$ 4) as obtained from D mesons-charged particles azimuthal correlations, for 3 $<p_T^{trigger}<$ 5 GeV/c and 1$<p_T^{associated}<$ 3 GeV/c. 235

6.10 Average transverse momentum, $< p_{\rm T} >$, as a function of charged particle multiplicity, N$_{ch}$, as measured by ALICE [30] is compared with the simulated events from PYTHIA 8 Tune 4C event generator with and without CR. 241

6.11 Average transverse momentum, $< p_{\mathrm{T}} >$ for the identified charged particles in pp collisions at $\sqrt{s} = 7$ TeV, as a function of mean charged particle multiplicity for several event classes. The CMS data [31, 32], have been compared with simulated events from PYTHIA 8 Tune 4C event generator with and without CR [33]. 243

6.12 The inverse slope parameter $\mathrm{T}_{effective}$ as a function of mass of identified charged particles ($\mathrm{m}_{\pi^{\pm}} = 0.14$, $\mathrm{m}_{K^{\pm}} = 0.495$, $\mathrm{m}_{p(\bar{p})} = 0.938$ GeV/c^2) produced in pp collisions [31, 32] at $\sqrt{s} = 7$ TeV. $< N_{ch} >$ is the mean multiplicity of the charged particles representing event classes [33]. 245

6.13 m_T -spectra for identified charged particles as obtained from the CMS data. The data are compared with the simulated events using PYTHIA 8 Tune 4C event generator with and without CR. 246

6.14 (Left) Representation of 2-dimensional $(\Delta\eta, \Delta\varphi)$ two-particle angular correlations using PYTHIA 8 CR scheme. (Right) 1-dimensional $\Delta\varphi$ projection for the region of ridge-like correlations from the data [15] and for the simulated events by PYTHIA with and without CR. . . . 250

6.15 Comparison of multiplicity dependent near-side ridge-like correlated yields for the CMS data and simulated PYTHIA events. 251

7.1 (Left) Estimated D^0-charged particle azimuthal correlation distribution in 0-10% central $PbPb$ collisions from Monte Carlo simulations with the upgraded ALICE detectors for $8 < p_{\mathrm{T}}(D^0) < 16$ GeV/c range with $p_{\mathrm{T}}^{assoc} > 0.3$ GeV/c after the subtraction of the baseline. (Right) Estimates for the statistical uncertainty of the near-side yields as a function of p_{T}^{assoc} in $PbPb$ after the ALICE upgrade 257

8.1 A schematic diagram of PYTHIA event generation with different steps. 263

8.2 The color reconnection mechanism in the string fragmentation model. The outgoing partons which are color connected to the projectile and target remnants (continuous lines) are reconnect with the partons in the second hard scattering (in dashed lines) (a). Color reconnected string (b). 265

List of Tables

1.1 Three generations of elementary matter-particles [2]. 5

1.2 The fundamental forces and force-carrier particles [2]. 5

1.3 Heavy-ion collision facilities. 17

3.1 Properties of hadrons carrying charm quark [1]. 81

4.1 Characteristics of the six ITS layers [22]. 118

5.1 Data Set and Run list. 143

5.2 Topological cut values for the D^0 candidate selection in the three integrated p_T ranges used in the correlation analysis. 152

5.3 Event pool setting. 166

5.4 Different track selection criteria for associated charged particles. . . . 180

5.5 List of systematic uncertainties for the $\Delta\varphi$-correlation distributions between D^0 mesons and charged particles in pPb collisions. 189

5.6 List of systematic uncertainties for near-side (NS) peak associated yield, near-side peak width, and baseline in pPb collisions, for two p_T ranges of D^0 meson and associated charged particles. 191

6.1 The inverse slope parameters of the exponential fits to the m_T-spectra of $\pi^{\pm}$, $K^{\pm}$ and p & $\bar{p}$ for the multiplicity class $\langle N_{ch} \rangle = 131$ for CMS experiment [31, 32] and PYTHIA 8 Tune 4C with and without CR. . 247

6.2 Multiplicity classes and the corresponding number of simulated events used for the correlation analysis. 249

Chapter 1

Introduction

1.1 Overall organization

Chapter - 1 : Introduction

The thesis addresses a frontier topic that falls in the broad category of the subject, the Quark-Gluon Plasma (QGP). The thesis is introduced with the "Overall organization" of its contents. The following section of this chapter is "Preliminaries", which contains very basic information on the topics, considered to be relevant for the presentation of the main work vis-a-vis the subject category. The section includes very brief descriptions of "The Standard Model", "Quantum Chromodynamics: The theory of strong interactions" and "QCD phase diagram and the QGP". The second section, "Discovery and study of QGP", starts with "A Brief Overview", followed by the "Heavy-ion collisions and relevant signals" (relevant to the work of the thesis), "The elementary proton-proton and proton-nucleus collisions" which make the baselines for the QGP signals from heavy-ion collisions and the "High-multiplicity events of small systems".

Chapter - 2: Two-particle angular correlations: the analysis tool

This chapter contains description of the analysis tool, the two-particle angular correlations, and its versatility in extracting correlations among produced particles in high energy proton-proton (pp), proton-nucleus (pA) and the nucleus-nucleus (AA) collisions. This analysis tool forms the basis of all the analyses, included in this thesis. The description on the methodology of construction of the two-particle correlation functions, has been followed by a short overview on the observations revealed through analysis of pp, pA and AA data with this tool.

Chapter - 3 : Open Heavy-flavor as probe

The major portion of the analyses, presented in this thesis, deals with open heavy-flavor particles. This chapter presents the role of the Heavy-Flavor (HF) particles as a probe to identify and characterize the medium formed in the heavy-ion collisions and possibly in the proton-nucleus collisions.

Chapter - 4: Experimental Set-up

The major part of the thesis contains results from D^0-charged particle azimuthal correlation study with the pPb data recorded by "A Large Ion-Collider Experiments" (ALICE) at the Large Hadron Collider (LHC). This chapter contains the details of the ALICE Experimental set-up, On-line and Off-line data taking procedures and the Analysis-framework. It also includes a brief discussion on ALICE Upgrade.

Chapter - 5: Angular correlations between D^0 mesons and charged particles in *pPb* with ALICE

This chapter contains the detailed methodology and results of the analysis of the minimum-bias data of *pPb* collisions at $\sqrt{s_{\mathrm{NN}}} = 5.02$ TeV, in terms of the two-particle angular correlations with the D^0 mesons and primary charged particles. It contains the detail of analysis, including the background subtraction, corrections to the correlation distributions, measurement of systematic uncertainties, fitting procedures and yield calculations. An average result of all the D mesons, including D^+ and D^{*+}, has also been presented. The *pPb* results have been compared with those from the *pp* data. The chapter concludes with the summary of the results.

Chapter - 6: Study of small systems with simulated events

During the thesis work, the revelation of some unexpected results in the high-multiplicity events in small systems, *pp* and *pPb*, at the LHC experiments, prompted us to extend our study in terms of the two-particle angular correlations to the high-multiplicity events of these small systems. In absence of sufficient data statistics for these type of correlation studies, events have been generated by reasonably successful simulation codes to use for the extended studies. This chapter contains the results of these studies with the simulated *pPb* and *pp* events, generated by the EPOS 3 and the PYTHIA 8 models, respectively. The chapter concludes with the summary of the results.

Chapter - 7: Summary and Outlook

This chapter presents an overall findings from the studies presented in the thesis.

1.2 Preliminaries

1.2.1 The Standard Model

The quest for the ultimate constituents of matter and prolonged efforts to understand the Universe, the way it is, culminated into the Standard Model or the Standard Model of Particle Physics [1]. The Standard Model, presently a well structured model of elementary particles and fundamental interactions between them, is actually a collection of several independently developed theoretical models and experimental findings which ultimately consolidated into its present form. In this section, only a few of the salient features of the Standard Model, which are relevant to the thesis topic, are briefly described.

The elementary matter-particles in the standard model are the quark and the leptons which are classified into three generations. The first generation includes two quarks, up (u) & down (d) and two leptons, electron (e) & electron-neutrino (ν_e). The second generation consists of strange (s) & charm (c) quarks and two leptons, muon (μ) & muon-neutrino (ν_μ). The third generation is comprised of beauty (b) & top (t) quarks and tau (τ) & tau-neutrino (ν_τ) as leptons. All these particles have corresponding antiparticles. The table 1.1 shows the basic properties of the three generations of quarks and leptons. In nature, there exists four fundamental forces of interactions - strong, weak, electromagnetic and gravitational. The Standard model, however, includes only first three forces, while the gravitation is not yet included. Each of these forces interact via exchange of certain mediator-particles

	name	symbol	charge	mass (GeV/c^2)	type
first generation	up	u	2/3	4×10^{-3}	quark
	down	d	-1/3	7×10^{-3}	quark
	e-neutrino	ν_e	0	$< 7 \times 10^{-9}$	lepton
	electron	e	-1	5.1×10^{-4}	lepton
second generation	charm	c	2/3	1.5	quark
	strange	s	-1/3	0.2	quark
	μ-neutrino	ν_μ	0	$< 2.7 \times 10^{-4}$	lepton
	muon	μ	-1	0.106	lepton
third generation	top	t	2/3	~ 175	quark
	bottom	b	-1/3	4.7	quark
	τ-neutrino	ν_τ	0	$< 2.7 \times 10^{-2}$	lepton
	tau	τ	-1	1.78	lepton

Table 1.1: Three generations of elementary matter-particles [2].

Force	boson name	symbol	charge	spin	mass (GeV/c^2)
Strong	gluon	g	0	1	0
E.M	photon	γ	0	1	0
Weak	W & Z-boson	$W^\pm$ & Z^0	±1 & 0	1	81 & 92

Table 1.2: The fundamental forces and force-carrier particles [2].

or force-carrier particles – 1) gluons for strong, 2) W, $Z^\pm$ for weak and 3) gamma (γ) for electromagnetic interactions. The table 1.2 lists the fundamental forces, the mediator-particles and their basic properties. The Fig. 1.1 summarizes all the particles, including the "Higgs-bosons", of the standard model.

In 1964, Peter Higgs and few other scientists predicted the existence of a particle that is responsible for the bear masses of the elementary particles [3, 4]. This mass-giving particle, called the Higgs Boson has finally been discovered in 2012, by the ATLAS and the CMS experiments [5, 6] at CERN's Large Hadron Collider (LHC).

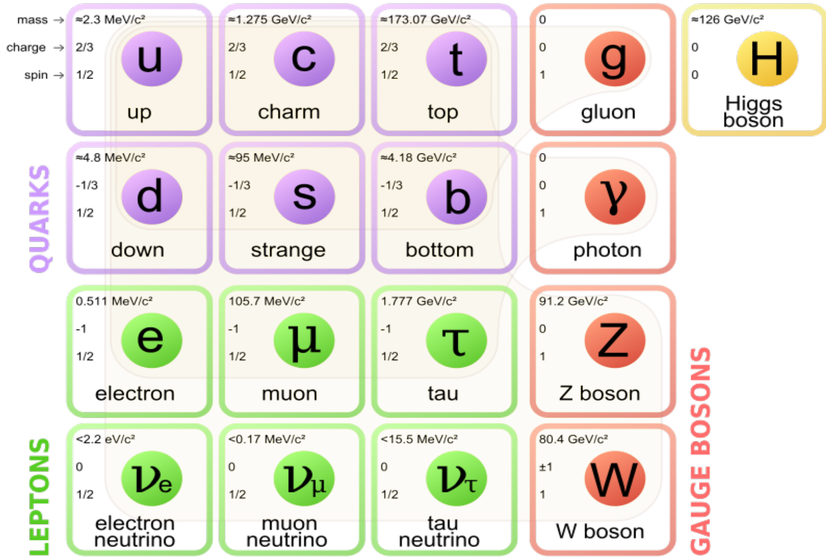

Figure 1.1: The standard model and its constituents.

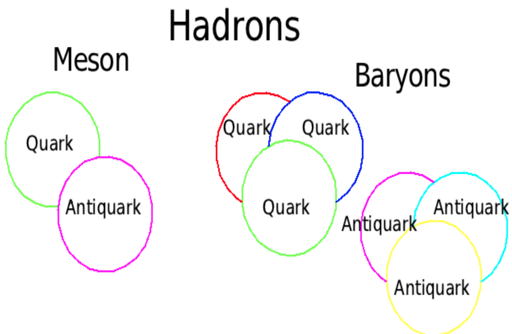

Figure 1.2: Quark structure of baryons and mesons.

In the present day Universe, free quarks or antiquarks are not available. These elementary particles exist as constituent of composite particles, called the hadrons. The hadrons are classified into two groups: baryons and mesons. Baryons (antibaryons) are made of three quarks (antiquarks) whereas mesons are made of one quark and one antiquark. The Fig. 1.2 shows the schematic diagram of simple quark structure of baryons and mesons.

1.2.2 Quantum Chromodynamics: The theory of Strong Interactions

The theory of strong interaction among quarks and gluons is called Quantum Chromodynamics (QCD). The theory is based upon local color gauge symmetry. The full QCD Lagrangian reads as:

$$\mathcal{L}_{QCD} = \bar{\psi}(i\gamma^{\mu}\partial_{\mu} - m_q)\psi - g\bar{\psi}\gamma_{\mu}B_{\mu}\psi - \frac{1}{2}\ \mathrm{Tr}[G_{\mu\nu}G^{\mu\nu}] \tag{1.1}$$

where B_{μ} is the gluon field, g is the gauge coupling, m_q is the mass of the quark. Though QCD calculations are quite similar to QED, there are few basic differences which make the QCD calculations more difficult. In QED electric charge is a single quantity whereas in QCD there are three color charges; red, green and blue. In QED, the mediator, photon is electrically neutral whereas in the QCD the mediator gluon carries color charge. Thus, gluons can interact strongly with other gluons and produce gluons or quarks. Another striking feature of QCD over QED is the coupling constant. Unlike the QED coupling constant ($\alpha \sim 1/137$), the QCD coupling constant does not have a fixed value and hence, it is called as "running coupling" constant (α_s). The α_s, given by the equation (1.2), is determined from different experimental results and are compared with the perturbative QCD prediction.

$$\alpha_s(Q^2) = \frac{1}{b\ln(Q^2/\Lambda^2)} \qquad \text{where, } b = \frac{33 - 2n_f}{12\pi} \tag{1.2}$$

Q^2 is the momentum transfer, with n_f being the number of quark flavours with mass $m < Q$. The value of Λ appears to lie between the range 100 MeV - 500 MeV [7]. The above properties of QCD lead us to two important features: quark confinement and asymptotic freedom.

- ***Confinement*** is the property that does not allow any isolated color charge to exist as a free particle. This is because of the QCD potentials beyond the nucleonic dimension, where the attractive strong force keeps increasing with the distance. Due to this increasing attractive force, the quarks get themselves confined to form colorless composite particles, the hadrons. This property of strong interaction is known as colour confinement.

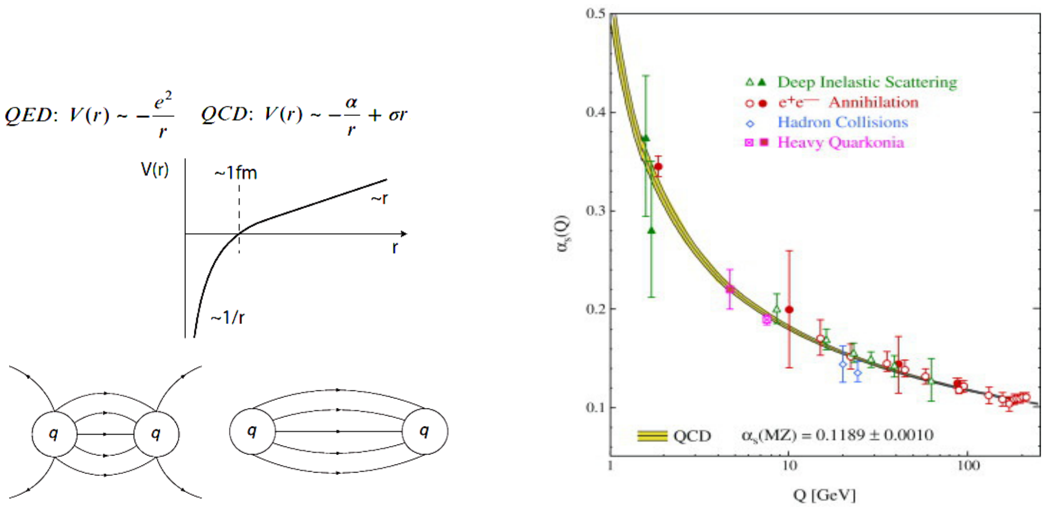

Figure 1.3: Potential due to strong interactions (left) and variation of running coupling constant (α_s) with momentum transfer [8] (right).

- ***Asymptotic freedom*** is the property where the QCD running coupling constant α_s (Eq.1.2) at large momentum transfer or at small distance between two partons (quark or gluon) becomes so weak such that the partons behave as quasi-free (Fig. 1.3) particles. This phenomenon has been confirmed by Deep

Inelastic Scattering (DIS) experiments. The advantage of asymptotic freedom is that, with a very small α_s the QCD interactions are calculable in the perturbative approach, commonly termed as the perturbative-QCD (pQCD).

1.2.3 QCD phase diagram & Quark-Gluon Plasma

De-confinement:

The asymptotic behaviour of strong force leads to the idea that at very high energy the quarks and gluons behave as free particles. In 1975, J. C. Collins and M. J. Perry [9] pointed out that the quarks become free at sufficiently high density. In relativistic heavy-ion collisions, a tiny system of high temperature and density is formed for a very short while. At such a high temperature and / or density, when quarks get much closer to each other, in the range of very small coupling constant (asymptotic freedom), the quarks don't interact much among themselves. A new state of matter is thus formed where quarks and gluons become quasi-free. This phenomenon is called de-confinement (not really confined in a way they are inside hadrons) of quarks. The de-confined quarks and gluons thermalize and form a new state of matter, the quark-gluon plasma (QGP).

Quark-Gluon Plasma: A (locally) thermally equilibrated state of matter in which the quarks and gluons are not confined in hadrons and are relatively free to propagate over a nuclear (rather than hadronic) volume scale.

It is believed that our present universe started with a singularity, the so-called "Big Bang" about 14 billions years ago. A few microseconds after the Big Bang, the tiny Universe was in a quark–gluon plasma state for a very short time. The QGP states ceased to exist as evolution of the Universe continued through fast cooling and the strongly interacting quarks and gluons got themselves confined into composite particles, the hadrons. The QGP state has also been predicted at the core of neutron stars at very high density and zero temperature. The study of quark-gluon soup provides crucial information to understand the early universe. Modern accelerators are powerful enough to produce the micro-universe in the laboratory. This opens up an entire field of research which focuses on mapping the QCD phase diagram and studying the properties of QGP.

In statistical mechanics, the order of phase transition is manifested by how the free energy of the system varies with transition temperature. We call it first order phase transition when the first derivative of the free energy becomes discontinuous and it is accompanied with the presence of latent heat. A second order phase transition is defined by the discontinuity in higher order derivatives of the free energy. When the change of phase occurs with a continuous behaviour of the free energy and its derivatives, it is called a "**cross-over**".

Figure 1.4 shows the basic QCD phase diagram and the phase transition of QCD matter. The phase transition line extends over two extreme conditions of matter, from predominant matter heating (high T and low μ_B) to predominant matter compression (low T and high μ_B). The QCD phase diagram at low temperature (T $\sim$ 0) and at baryonic chemical potential of about $\mu_B \sim 1$ GeV/c, corresponds to nuclear matter in its normal state. Moving along the phase diagram from the high to low baryonic potential (μ_B) direction and with increasing temperature, a first order

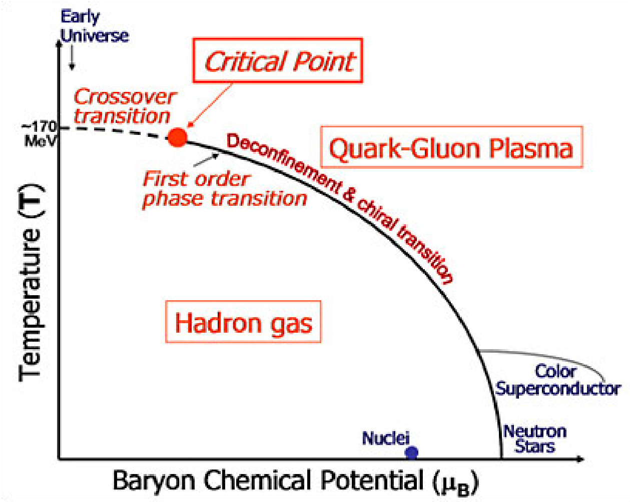

Figure 1.4: A schematic diagram of the QCD phase diagram of nuclear matter in terms of the temperature (T) and baryonic chemical potential (μ_B) [10].

phase transition is expected to occur till QCD critical point is reached. Beyond the critical end-point, with further lowering of μ_B and increasing the temperature, the change of phase takes place through "**cross-over**" i.e without any discontinuities of the thermodynamic quantities which describe the system. The region above the phase diagram curve in the QCD phase diagram corresponds the partonic state of matter or the QGP, while that below the curve represents the hadronic state of matter.

Keeping the temperature low and increasing the μ_B beyond the normal nuclear matter, a state of compressed nuclear matter is formed. Such systems can be found in neutron stars at very low temperature [11]. At ultra-high densities the color-superconducting quark matter is expected to be found in a color-flavor-locked (CFL) phase. Thus, there are two types of phase transition from hadronic to partonic medium and they are connected at a QCD "critical point" whose existence in the phase diagram is still theoretically debated. Significant work has been done in recent time both theoretically and experimentally where the search for the QCD critical point becomes more and more exiting. The first phase of Beam Energy Scan (BES) program at Relativistic Heavy Ion Collider (RHIC) [12] at the BNL provides valuable information about the QCD critical point through the measurements of higher order fluctuations of thermodynamic quantities. Also attempts and progress have been made in theory [13,14] which will be important to connect experimental observables and phase structures of the QCD phase diagram.

The lattice QCD calculations predict that for massless quarks at baryonic potential $\mu_B = 0$, the critical temperature, at which a first order phase transition from hadronic gas to QGP can occur, is $T_c = (173 \pm 15)$ MeV with the critical energy density $\epsilon = 0.7$ [15]

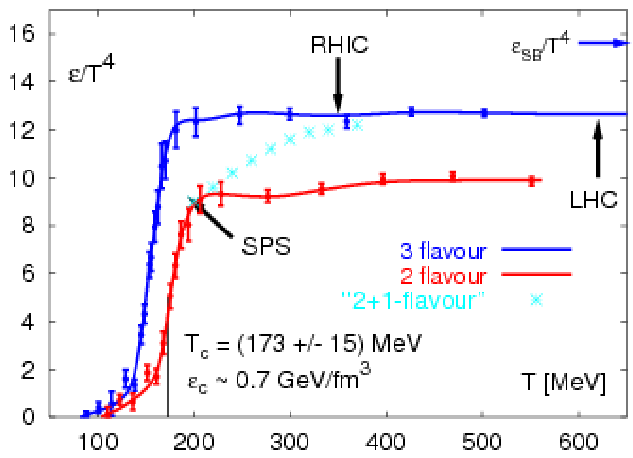

Figure 1.5: Energy density as function of the temperature T from lattice QCD calculations. The calculations are performed for two massless quarks (2), three massless quarks (3) and two massless quark and one (s) with its real mass (2+1) [15].

In Fig. 1.5, ϵ/T^4 shows abrupt changes near to the critical temperature (T_c). The steep trend of this ratio reflects the increase of the degrees of freedom of the system when in the deconfined phase. The lattice QCD calculations show that for massive quarks, the phase transition could fade away, it would become a cross-over and no criticalness would be observed.

1.3 Discovery and Study of QGP

1.3.1 A Brief Overview

The QCD prediction [16,19] of thermalized partonic matter, the Quark-Gluon Plasma (QGP), got the experimental endorsement [17–20] from the ultra-relativistic gold-gold ($AuAu$) collisions at the centre-of-mass energy ($\sqrt{s_{\mathrm{NN}}}$) of 62, 130 and 200 GeV at the Relativistic Heavy Ion Collider (RHIC) at the BNL. Prior to the discovery at the RHIC, there had been efforts in search of the QGP in relativistic heavy-ion collisions at lower [21,22] $\sqrt{s_{\mathrm{NN}}}$ and even in proton-proton (pp) [23–25] collisions. The lack of confirmative signals for the QGP in the lower energy data pushed the requirement of the energy of collisions continually upwards and the heavy-ion collisions, considered to be more conducive to the QGP-thermalization because of the larger volume and longer lifetime, became the system of choice. In the run for the search, the indication of formation of QGP-like new state of matter [26] in lead-lead ($PbPb$) collisions at $\sqrt{s_{\mathrm{NN}}}$ =17.3 GeV at the Super Proton Synchrotron (SPS) at CERN marks a milestone. Finally, the coherent approach of simultaneous measurement of several of predicted signals of the QGP by the state-of-the-art detector-setup of four major experiments at the RHIC helped identifying the QGP-like fluid. Contrary to the prediction, the medium formed at the RHIC is more like a perfect fluid and so, is termed the strongly interacting QGP or the sQGP. Subsequently, the RHIC experiments identified similar partonic medium in $AuAu$ and coper-coper ($CuCu$) collisions at lower energies also [27–29]. The findings motivated further lowering of $\sqrt{s_{\mathrm{NN}}}$ to tens of GeVs and below, in the Beam Energy Scan (BES) program [30], in the search of the critical end-point in the QCD phase diagram [31], implying that the formation of the quark matter might be possible in heavy-ion collisions even in this re-visited lower energy range.

Of the most significant features observed in the RHIC data, the collective flow of the final state particles in the collisions indicates thermalization and the suppression of the high-p_{T} particles or the jets points to the formation of dense partonic medium. To extract the true medium effect on high-p_{T} suppression, the heavy-ion data is studied in terms of the nuclear modification factor, R_{AA} [32], defined as the ratio of the yields in heavy-ion and pp collisions at the same energy in a given p_{T}-bin, normalized with the number of binary nucleon-nucleon collisions. The effect of the hot nuclear matter or the QGP formed in heavy-ion collisions is finally extracted by disentangling the cold nuclear matter (CNM) effects [33–40], experimentally obtained from the proton-nucleus collisions. In the RHIC, however, the CNM effect was studied with deuteron-gold (dAu) collisions because of technical difficulties for pAu collisions.

The Large Hadron Collider (LHC) has extended the domain of the QGP study. The heavy-ion program at the LHC experiments with heavier nuclei ($PbPb$) and at higher $\sqrt{s_{\mathrm{NN}}}$ (2.76 and 5.02 TeV), widens the scope of the understanding the QCD-plasma by creating a hotter partonic matter with increased energy density, volume and the lifetime [41]. It also facilitates the study of properties of the medium with copiously produced unique hard probes, the heavy-flavor (HF) jets. The LHC has also broaden the horizon of the QGP study by unrevealing the formation of collective medium in small systems produced in the high-multiplicity events of pp [42–45] and pPb [46–49] collisions. While the collectivity in the high-multiplicity pp events is not yet unambiguously characterized, there is a general agreement on the formation of QGP-like medium in the high-multiplicity pPb events at the LHC energy. The new analysis of RHIC data on dAu [50] also corroborate the LHC finding. Moreover, the minimum-bias pPb data at the LHC do not exhibit [51] the important Cronin effect [34–36], in contrast to the RHIC results on dAu data. That makes the detail study of the pPb collisions at the LHC energy all the more interesting. This thesis presents the study of the pPb collisions at the LHC energy in terms of HF-meson and charged particles correlations for the first time. While the first part of the thesis contains the analysis of minimum-bias pPb data from ALICE detector at the LHC, the second part contains extension of the analysis further to the high-multiplicity events of the small systems formed in pp and pPb collisions. The study of the high-multiplicity pPb events could not be carried out because of limited statistic of data. So, this study, very much relevant to the thesis topic, has been carried out with the events generated with the EPOS 3 model [52], a successful model in describing most of the features of the pPb data, including the relative multiplicity-dependent yields. The hydrodynamic collectivity in high-multiplicity pPb events prompts us to study high-multiplicity pp events also. The high-multiplicity pp events were generated with PYTHIA 8 [53] using the options with and without color reconnection, as PYTHIA

8 with color reconnection apparently explained the features of the high-multiplicity pp events.

1.3.2 Heavy-ion collisions and relevant QGP-signals

The study of the heavy-ion collisions is not an explicit subject matter of study for this thesis. Nevertheless, as the main topics of the study for this thesis are related to the QGP-study, in general, we briefly describe, in this section, the relativistic heavy-ion collisions and the related experimental signals for the QGP.

1.3.2.1 Facilities

There have been a prolonged efforts in the search of the QGP in the laboratory, giving birth to several facilities / experiments. Here, we mention few of such facilities. During 1980's heavy-ion collision programs started at the Alternating Gradient Synchrotron (AGS) at Brookhaven and at the Super Proton Synchrotron (SPS) at CERN. Those were fixed target experiments using projectile energies of 1 GeV/nucleon up to 158 GeV/nucleon. In the years 2000 and 2009, the Relativistic Heavy Ion Collider (RHIC) at BNL and Large Hadron Collider (LHC) at CERN became operational with a much larger collision energy range. RHIC started with four major experimental setup; PHENIX, STAR, PHOBOS, and BRAHMS. The $\sqrt{s_{\rm NN}}$ energy reached at RHIC was 200 GeV/nucleon. Afterwards, the Beam Energy Scan program [30] in search of the QCD critical point, the energy was reduced to about $\sqrt{s_{\rm NN}} = 7.7$ GeV. The Large Hadron Collider at CERN operates at much higher energy than RHIC. It has already collided Pb-ions up to a centre-of-mass energy of $\sqrt{s_{\mathrm{NN}}} = 5.0$ TeV (the designed top energy being $\sqrt{s_{\mathrm{NN}}} = 5.5$ TeV). The ALICE (A Large Ion Collider Experiment) at the LHC is dedicated for the study of QGP. Other experimental facilities at CERN namely ATLAS, CMS, LHCb have also taken heavy-ion data. Apart from these, many high energy experiments are going to be active in coming decades. Facility for Antiproton and Ion Research (FAIR) is one of the major future experiments which includes the CBM (Compressed Baryonic Matter) experiment, a fixed target experiment that will allow us to study the QCD phase diagram in the high baryonic chemical potential region. The table 1.3 shows different heavy-ion facilities from AGS to LHC.

Facility	Accelerator type	Location	System	Energy (CMS)
AGS	Fixed target	BNL, NewYork	$AuAu$	5 GeV
SPS	Fixed target	CERN, Geneva	$PbPb$	17.3 GeV
RHIC	Collider	BNL, NewYork	$AuAu$	200 GeV
LHC	Collider	CERN, Geneva	$PbPb$	5.5 TeV

Table 1.3: Heavy-ion collision facilities.

1.3.2.2 Geometry and Dynamics

In ultra-relativistic heavy-ion collisions when two nuclei are accelerated to very high velocities, they appear to each other like pan-cakes due to Lorentz contraction. After the collision of the Lorentz contracted nuclei, a substantial amount of kinetic energy is deposited in a very small region of space. The formation of the QCD plasma, in the relativistic heavy-ion collisions, often termed as Little Bangs, necessitates accomplishment of thermodynamic equilibrium. As the system formed in the high energy collision starts expanding almost instantaneously, it remains far from turning to a homogeneous system and so cannot reach the global thermodynamical equilibrium. However, strong interactions of a large number of particles in a small volume, where the mean free path of constituent particles is much smaller than the dimensions of the system, lead to the local thermodynamical equilibrium. In heavy-ion collisions, the local thermodynamic equilibrium is assumed to obtain the equation of state for the space-time evolution of the system in the framework of the relativistic hydrodynamics. Eventually, the formation of QGP in heavy-ion collisions is established mainly by characterizing the system in the hydrodynamic model. Here, we schematically present the dynamical evolution of the system, formed in the heavy-ion collisions, leading to the QGP, followed by the final state particle production.

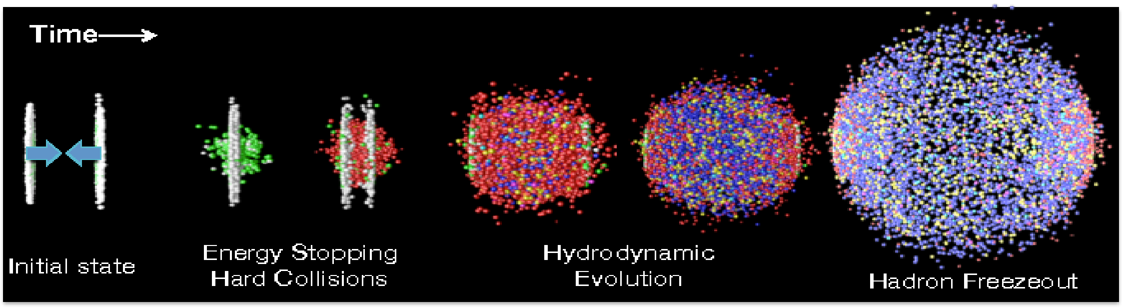

Figure 1.6: Schematic representation of the evolution of relativistic heavy-ion collision [54].

The heavy-ion collision consists of many stages and is shown schematically in Fig. 1.6 along with the space time (z-t) diagram (Fig. 1.7) of the collision phenomenon.

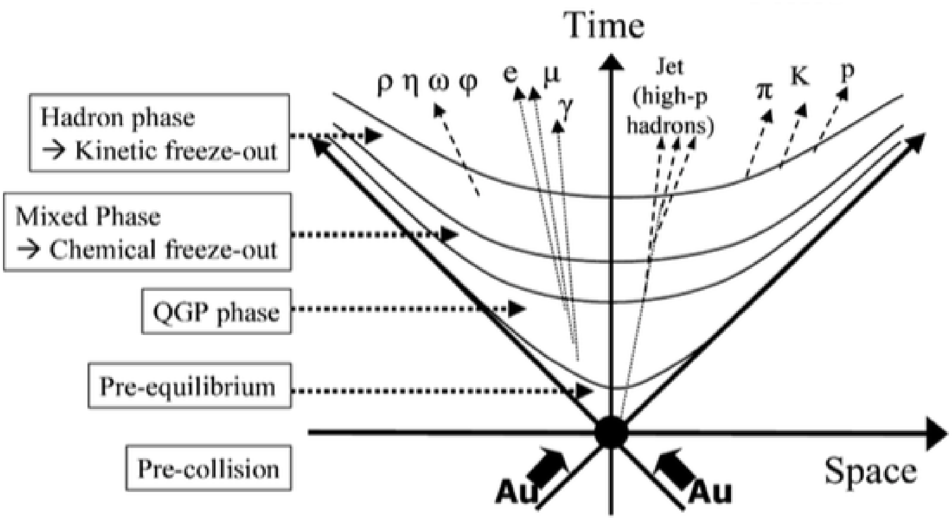

Figure 1.7: Schematic representation of space-time evolution of relativistic heavy-ion collision.

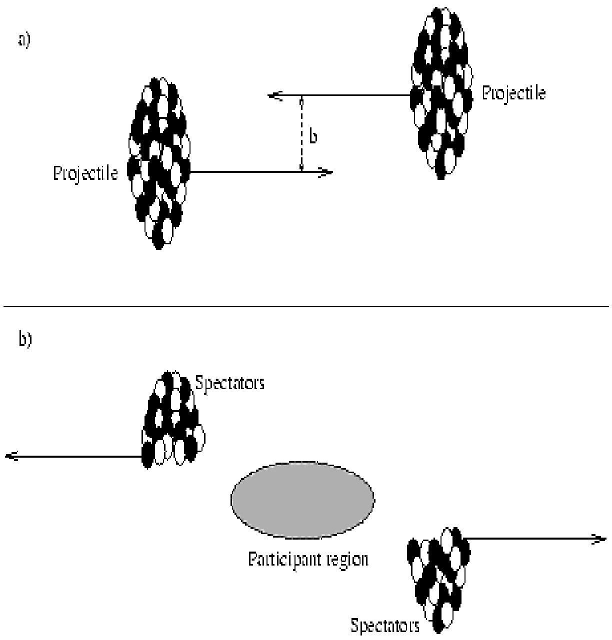

Figure 1.8: A collision between two heavy nuclei in the spectator-participant model. (a) The two Lorentz contracted nuclei before the collision. The centrality is determined by the impact parameter b. (b) Participant region with high temperature and density is created after the collision.

The collision geometry of two nuclei plays an important role in characterizing the experimental results. It is possible to estimate geometrical properties of the heavy-ion collision using Glauber Model [55] with the inputs as nuclear charge density (ρ_0) and inelastic nucleon-nucleon cross section (σ_{inel}^{NN}). Initially partons from two colliding nuclei involve in hard scattering via large momentum transfer. The momentum transfer depends on how two nuclei collide i.e on the centrality of the collision. The centrality is characterised by the impact parameter b (Fig. 1.8) which is the distance between the centres of the nuclei. When the two nuclei collide almost head-on i.e the impact parameter is small, we call it central collision. On the other hand, peripheral collisions are those where impact parameter is large, almost equal to the sum of the radius of the nuclei. It is hard to measure the impact parameter directly from the experiment. Thus, alternative ways are adopted using the information of number of "participants" (N_{part}) and "spectators" ($2A - N_{part}$) in the collision. The participants are defined as the nucleons that participate in the collision whereas the spectators are those which do not participate. The number of participants and spectators depends on the centrality. Number of participants is large in central collisions w.r.t peripheral collisions. At the initial stage of the collision high momentum partons are produced via hard scattering. The inter-inelastic scatterings between the partons lead to the formation of a hot-dense QCD matter which is referred to as *fireball*. The constituent partons of the *fireball* collide among themselves to reach a local equilibrium state of thermalised parton soup, called Quark-Gluon Plasma. The time to reach such a state is called thermalization time. As the system evolves through hydrodynamic expansion, its energy density and temperature decreases and below a certain critical temperature hadronization starts. The partons combine into two (or three) quarks forming meson (or baryons) via parton showering (coalescence or recombination). At this stage the inelastic collisions between the constituent hadrons stop and the particle abundances get fixed. This is called as “chemical freezout”. The system keeps on expanding and the hadrons interact quasi-elastically until “kinetic freezout” is reached. The collisions between the particles stop as soon as the distance between them is larger than the interaction range and they are detected by the detectors.

1.3.2.3 Relevant QGP-signals

The hot and dense partonic medium created in heavy-ion collisions (from RHIC to LHC) can be studied in terms of a number of predicted observables, using different experimental methods and tools. Following are the list of some of the significant observables.

- Energy density estimation [56, 58]
- Collective Phenomena
  - ☐ Identified particle spectra [58, 59]
  - ☐ Anisotropic flow [60]
  - ☐ Particle ratios [61]
  - ☐ Multiplicity dependence of particle production [62]
- Strangeness enhancement [63–65]
- J/ψ suppression [66]
- High p_{T} suppression: Jet quenching [67]
- Two-particle correlations [68]

It is already mentioned in the beginning of this section that since the study of QGP in heavy-ion collisions is not our topic of interest for this thesis, we don't discuss all the QGP-signals. Here, we restrict our discussion to only two of the most prominent signals which helped discovery of the QGP at the RHIC: the non-zero elliptic flow of the final-state particles revealing the collective nature of the medium formed and the suppression of the high-p_{T} particles or jets indicating formation of dense partonic medium. It is also important to note here that the main tool of our analysis, included in the thesis, is the two-particle azimuthal correlations, the generic and versatile analysis tool that addresses several sources of correlations in multiparticle production. This analysis tool provides an useful alternate to the direct jet-reconstruction method for studying the jet properties. Also, the correlated emission of particles from collective medium can be extracted in terms of flow coefficients.

1.3.2.3.1 Collective Phenomena

Since the QGP is expected to exhibit the properties of plasma, it is customary to find any collective behaviour between the produced particles. The space-time correlation between the average momentum particles is described by the collective flow. The average flow velocity $\vec{v}(x)$ at space-time point x of an infinitesimal volume element is obtained by taking the ratio of total 3-momenta ($\vec{P}$) and the associated energy (P^0). The average flow velocity has two components; one along longitudinal beam direction ("longitudinal flow" v_L) and other in the transverse direction ("transverse flow" $v_\perp$). The collective phenomena allows us to study different properties of QGP.

Anisotropic azimuthal flow

At the early stage of the non-central heavy-ion collisions, flow anisotropies are developed as the system does not possess azimuthal symmetry. The azimuthal anisotropy which is originated from spatial anisotropy, transforms into momentum anisotropy. The matter expands faster in the direction where the system size is smaller. The azimuthal distribution of produced particles is customarily expressed as a Fourier series in azimuthal angle φ [60]:

$$E\frac{d^3N}{dp^3} = \frac{d^2N}{2\pi p_T dp_T dy}\Big(1 + 2\sum_{n=1}^{\infty} v_n(p_T, y)\cos[n(\varphi - \Psi_{RP})]\Big) \tag{1.3}$$

where p_{T} is the transverse momentum, y is the rapidity, Ψ_{RP} is the angle that defines the reaction plane, and v_n and n represent the magnitude and direction of the nth-order harmonic respectively. The sine terms in the expansion vanish due to symmetry with respect to the reaction plane, defined as the plane containing the momenta of the beams and the impact parameter b. The $v_n(p_{\mathrm{T}}, y)$ coefficients are computed by averaging the angular difference over the particles, summed over all events in the (p_{T}, y) bin of interest. Each harmonic corresponds to the shape of the flow. The flow coefficients v_1, v_2, v_3 correspond to directed, elliptic, triangular flow and so on. The second order Fourier coefficient, v_2, is defined as $v_2 = <\cos 2(\varphi - \Psi_{RP})>$. A schematic diagram of collision geometry and flow related parameters are shown in Fig.1.9. The elliptic flow has been measured from RHIC ($\sqrt{s_{\mathrm{NN}}}$ = 200 GeV) to LHC ($\sqrt{s_{\mathrm{NN}}}$ = 2.76 TeV) in different heavy-ion collisions at different energies. Figure 1.10 shows elliptic flow for pion, kaon and proton measured by ALICE at $\sqrt{s_{\mathrm{NN}}}$ = 2.76 TeV, STAR and PHENIX at $\sqrt{s_{\mathrm{NN}}}$ = 200 GeV. At low transverse momentum, the observed v_2 is comparable among different experiments.

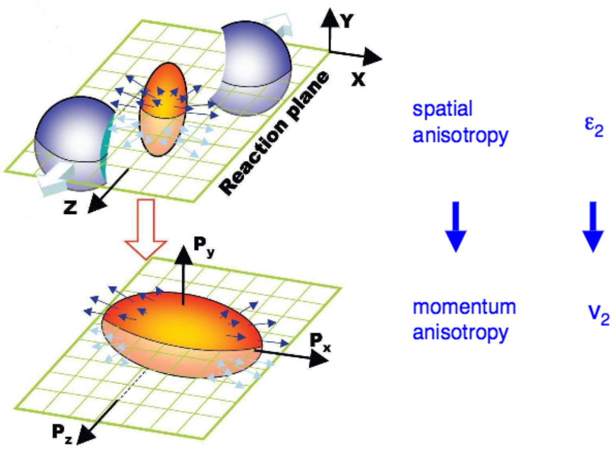

Figure 1.9: Schematic diagram of elliptic flow in a non-central heavy-ion collisions [69].

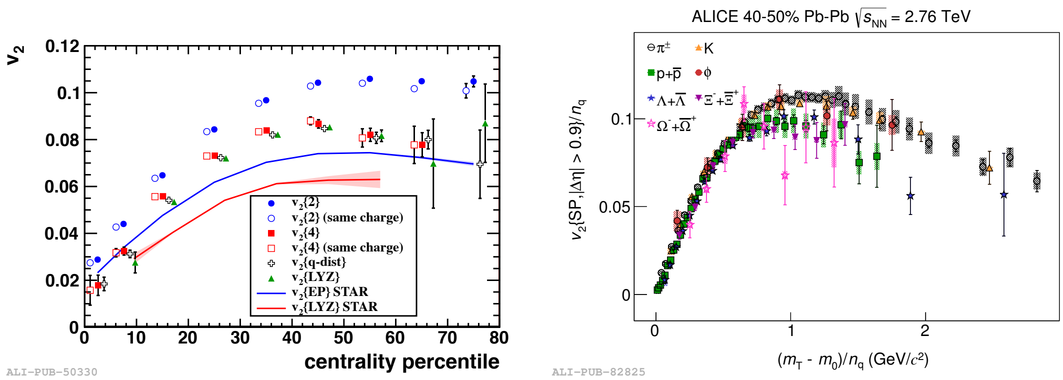

Figure 1.11: p_{T} integrated elliptic flow for charged hadron as a function of centrality by ALICE compared with STAR results (left) [70]. Elliptic flow as a fucntion of transverse kinematic energy scaled by the number of constituent quarks for identified hadrons (right) [71].

Figure 1.11 (left) shows the integrated v_2 as a function of centrality. Blue and red symbols in the figure correspond to two different methods of measuring the correlations between particles in the event. It is found to be 30% higher for LHC data w.r.t RHIC data and this is because of higher radial flow at higher energies. The right

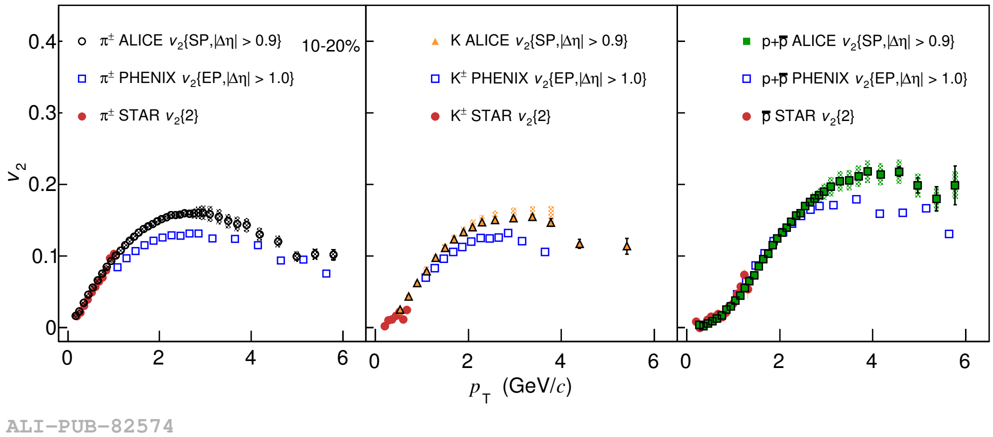

Figure 1.10: Elliptic flow (v_2) as a function of p_{T} and comparison between different experiments [70, 72, 73].

plot of the same figure shows study of elliptic flow with kinematic energy scaled by number of quark constituents. The quark number scaling seems to be valid up to $p_{\mathrm{T}} \sim 2$ GeV [71].

Particle ratios

After the chemical freeze-out, the inelastic collisions stop and the particle abundances can be characterized by using grand canonical approximation of the system. The particle ratios provide necessary information about the collision dynamics as the particle yields get fixed after chemical freeze-out. Figure 1.12 (left) shows ALICE results on the proton to pion ratio measured for most central $PbPb$ collisions and also for pp collisions w.r.t p_{T} and plots on the right side show the same for kaon over pion ratio.

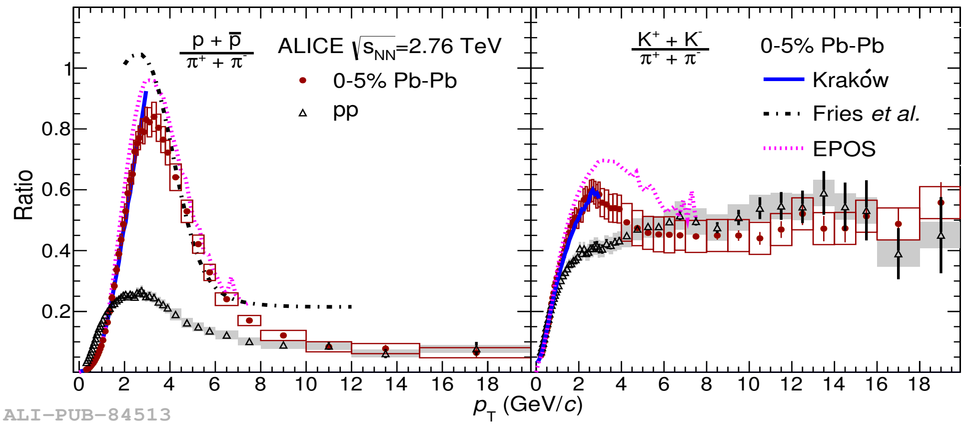

Figure 1.12: Particle ratios as a function of p_{T} measured in the most central, 0–5%, *PbPb* and in minimum bias *pp* collisions. [61].

The Fig.1.13 shows ratios of protons/pions or kaons/pions for different experiments. The values obtained by ALICE are almost 20% higher than the RHIC results [74, 75]. This is because the minijets produced at the LHC energy is larger

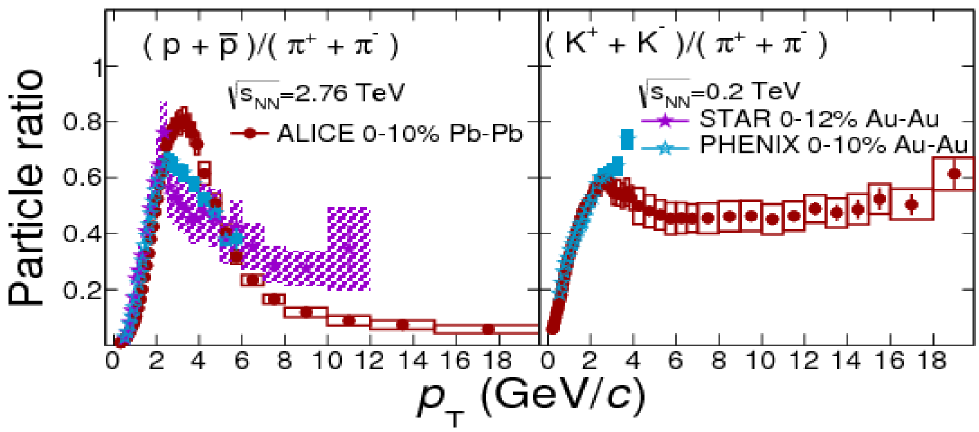

Figure 1.13: Particle ratios as a function of p_{T} measured in the most central, 0–10%, *PbPb* collisions at $\sqrt{s_{\mathrm{NN}}}$ = 2.76 TeV [61] by ALICE and at $\sqrt{s_{\mathrm{NN}}}$ = 200 GeV by STAR (0-12%) and PHENIX (0-10%).

than the RHIC energy and this leads to the recombination of shower partons as predicted by different models. On the other hand the kaon to pion ratio exhibits a bump at $p_{\mathrm{T}} \sim 3$ GeV/c which was absent at RHIC but is observed in the soft coalescence model [76]. Above $p_{\mathrm{T}} = 10$ GeV/c, the heavy-ion data behaves like pp, suggesting that fragmentation dominates the hadron production.

1.3.2.3.2 High-p_{T} suppression: Jet quenching

Jet quenching is one of the major tools to study the QGP formed in high energy heavy-ion collisions. A jet, narrowly collimated final-state particles, is produced via the hadronization of high momentum parton (Fig. 1.14).

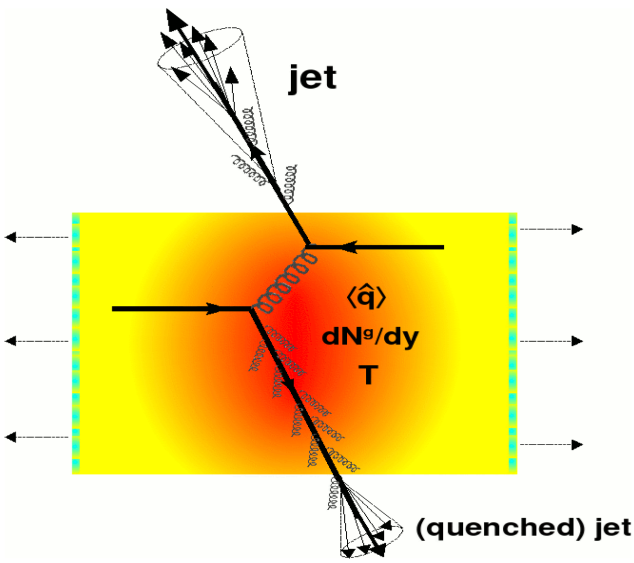

Figure 1.14: Back-to-back jets in heavy-ion collisions. The one is produced near the surface of the hot and dense medium and the other deep inside. These are called the near-side and away-side jets.

In heavy-ion collisions, when the jets pass through the medium, they suffer multiple scattering and lose their energy through interaction with the medium. This attenuation of partons, due to energy loss inside the medium, is referred to as jet quenching [67] or high-p_{T} suppression.

This effect can be evaluated quantitatively with the nuclear modification factor ($R_{\rm AA}$). It is defined as the ratio between the particle yield in heavy-ion collisions relative to the yield in elementary *pp* collisions (the details of particle production in elementary *pp* collisions are described in the following subsection 1.3.3) scaled by the number of binary nucleon-nucleon collisions (i.e. N_{coll}), obtained from Glauber Monte Carlo simulations:

$$R_{AA}(p_T) = \frac{\frac{d^2N}{dp_T dy}|_{AA}}{N_{coll} \times \frac{d^2N}{dp_T dy}|_{pp}} \tag{1.4}$$

where $\frac{d^2N}{dp_T dy}|_{AA}$ and $\frac{d^2N}{dp_T dy}|_{pp}$ are the differential yield in nucleus-nucleus collisions and in *pp* collisions respectively. If there is no effect with respect to a superposition of *pp* collisions (binary scaling), $R_{\rm AA}$ would have been 1. Any deviation from unity spots a specific behaviour of *AA* collisions either due to the QGP or to the presence of the nuclei themselves (cold nuclear matter effects). The latter can be assessed using *pA* collisions. There are experimental measurements of R_{AA} (Fig. 1.15) which suggest that a secondary hot-dense medium is produced after the collisions. The Fig. 1.15 (left) shows the nuclear modification factor R_{AA} of charged hadrons for central and peripheral collisions as a function of $p_{\rm T}$ at $\sqrt{s_{\rm NN}} = 2.76$ TeV in *PbPb* collisions. With respect to central collisions, there is no significant decrease in R_{AA} of peripheral collisions as a function of $p_{\rm T}$. The R_{AA} measured by ALICE, shown in the right plot, is similar to RHIC results. Around $p_{\rm T} \sim 6-7$ GeV/c, the nuclear modification factor measured at LHC energy is smaller than at RHIC energy which suggests an enhanced energy loss at LHC and hence a denser medium.

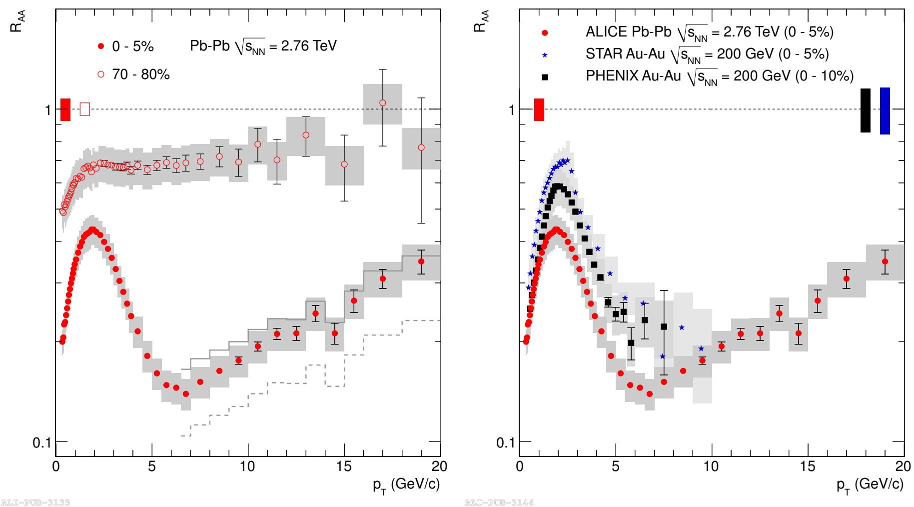

Figure 1.15: Nuclear modification factor in most central (0–5%) and peripheral (70–80%) *PbPb* collisions at $\sqrt{s_{\mathrm{NN}}}$ = 2.76 TeV (left), measured by ALICE and a comparison with the RHIC results [77] (right) in most central case only.

1.3.3 The baselines: proton-proton (pp) and proton-nucleus (pA) collisions

1.3.3.1 The elementary pp collisions

In the QGP-study, conventionally, the proton-proton (pp) collisions are taken as reference measurements in extracting several signals of the heavy-ion collisions. The pp collisions are described as elementary collisions with the implicit assumption that in such small and therefore short-lived systems, a medium cannot be formed [78]. Therefore, deviations in measured quantities in heavy-ion collisions w.r.t pp collisions provide valuable information for the medium created in heavy-ion collisions. The methodology of normalization nucleus-nucleus results with pp results is termed as the nuclear modification factor (R_{AA}) (described above). Here, we briefly describe the multiparticle production mechanisms in high energy pp collisions, as has been adopted by different simulation codes, keeping aside their minor differences.

There can be two types of pp collisions: elastic and inelastic. The elastic processes comprise of identical initial and final states with no new particles produced and thus, out of our physics interests for this thesis. The inelastic processes can be classified into 3 categories: Non-Diffractive (ND), Single-Diffractive (SD), and Double-Diffractive (DD) events.

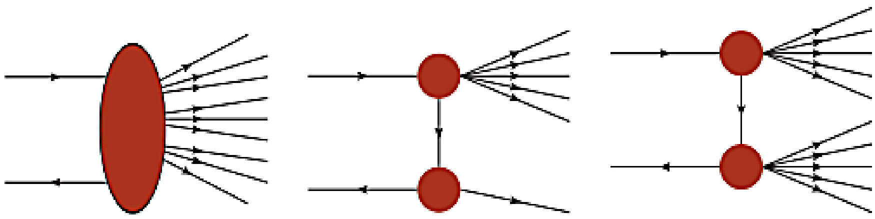

(a) Non-diffractive (b) Single-diffractive (c) Double-diffractive

Figure 1.16: Schematic diagrams of (a) non- (b) single- and (c) double-diffractive processes, respectively.

In diffractive events, the colliding particles are excited. Such excitation of incoming particles creates a diffractive system which carries the quantum number of the original particles. The excitation of the incoming particles (nucleons) are assumed to be from gluons exchanging, a so-called “Pomeron” [79].

In an SD event only one of the colliding particles becomes a diffractive system and dissociates, whereas both the particles become diffractive systems in the case of DD events. In case of ND events, both the particles collide head-on resulting in their complete dissociation. The Fig. 1.16 shows different diffractive events. Thus, the total cross section becomes:

$$\sigma_{tot}^{pp} = \sigma_{el}^{pp} + \sigma_{ND}^{pp} + \sigma_{SD}^{pp} + \sigma_{DD}^{pp} \tag{1.5}$$

At the LHC energy, the main contribution comes from σ_{ND}^{pp}. However, ALICE is incapable of distinguishing different diffractive process types on an event-by-event basis. Thus, results produced by ALICE are based on an event selection referred as non-single-diffractive (NSD) which combines both the ND and DD events.

There are many elementary subprocesses involved in the collision process. This can include both hard (large momentum transfers) and soft (less momentum Monte transfers) scatterings of partons. Perturbative QCD (pQCD) offers precise and detailed study of hard processes. In case of soft interactions, the perturbative calculations are not valid as the coupling constant α_s approaches to unity. Such processes can only be modelled phenomenologically. The Monte Carlo event generators like PYTHIA, HERWIG, Sherpa etc. have successfully generated the LHC events for pp collisions at different centre-of-mass energies. A simulated pp event consists of several stages of collisions: soft & hard subprocesses, parton distribution functions, Multiple Parton Interactions (MPIs), Initial-State Radiation (ISR), Final-State Radiation (FSR), non-perturbative & secondary interactions, beam remnants, hadronization and decays. A complete sketch of a hadronic collision is shown in Fig. 1.17. In an event generator the soft and hard processes are separately considered using the tuneable parameter $p_{T,min}$ where p_{T} is the momentum transfer in the interaction processes. In PYTHIA a hard interaction is defined with a momentum transfer larger than $p_{T,min}$.

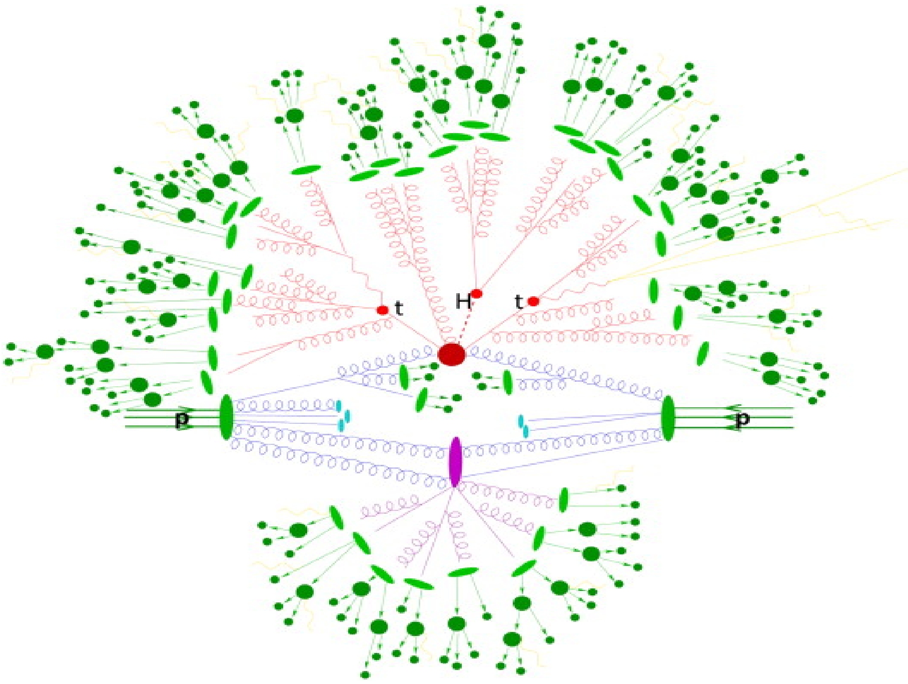

Figure 1.17: Sketch of a hadronic collision (in different colors): hard scattering between two partons (red), the initial- and the final-state showers (blue), a multiparton interaction (purple), beam remnants of the incoming protons (brown), the particles produced after the hadronization (light and dark green) [80].

A brief description of subsequent steps in pp collisions as described in Monte Carlo simulation is following:

- When two particles from the opposite beams move towards each other, they appear to be a point-like strongly-interacting partons. Each of the beam particles consist of partons whose distribution can be characterized by parton distribution functions (PDFs). A PDF $f_i(x, Q^2)$ describes the probability of finding a parton i with the momentum fraction x of the total momentum of the beam particle probed at a scale Q^2.
- Before the physical collisions, partons from each of the beams may branch (e.g. $q \to qg$), loosing their energy by emitting further partons. Such showering is

called **Initial-state showers** and it ends when the particles interact.

- As the beam particles collide, the **hard interaction** (e.g. qg $\rightarrow$ qg or qg $\rightarrow$ qγ) occurs between two partons resulting outgoing partons. Hard scattered partons contain only a fraction of the total beam energy. The remaining partons are called the **beam remnants** which may further collide in the same collision. Besides hard subprocess, there could be semi-hard subprocesses. A semi-hard interaction lies between soft and hard interactions with moderate momentum transfer.
- After the collisions, shower or radiation that develops from the outgoing partons, is called **final-state showers**. The outgoing parton may experience a series of branching (e.g q $\rightarrow$ qg, q $\rightarrow$ qγ, and g $\rightarrow$ gg). Produced particles (also called daughters) can undergo further branching. The splitting is initiated at energy of the hard interaction, looses it during the evolution, and aborts when the remaining energy (of parton and all its decedents) is below certain energy scale.
- It is possible that several distinct pairs of partons collide in a single high energy *pp* collision. Also, partons produced from initial parton-parton interactions can take part into interactions with other partons. This process is called **Multiple Parton Interaction (MPI)**. The hardest (primary) partonic interaction in hadronic collisions may be accompanied by softer (secondary) ones between the beam remnants. These multiple interactions produce additional partons throughout the event and affect the final-state activity in a more global way, increasing the multiplicity and summed transverse energy [81]. A comparison of with and without inclusion of MPI in PYTHIA is shown in Fig. 1.18.

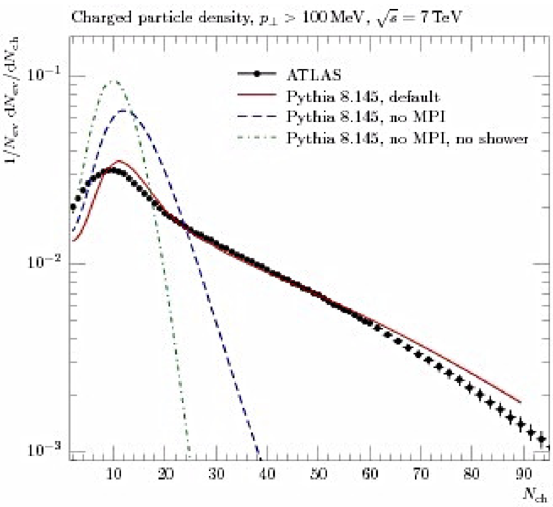

Figure 1.18: Comparison of charged particle multiplicity for data (ATLAS) and PYTHIA with and without MPI model.

It is clear from the comparison of data and simulated events that the MPI model should be included for realistic scenario of soft-inclusive physics.

- With the evaluation of time, the strings span between outgoing partons and energy decreases and finally fragment to colorless hadrons. However, such dynamical processes (**hadronization**) cannot be derived directly from the QCD Lagrangian. Hence, to describe the process of hadronization, the step where hadrons are formed from partons in high energy collisions, string [82] and cluster [83–85] models are used. In PYTHIA, the famous Lund-model of string fragmentation is used. The process of hadronization from strings as described in Lund model is following; for a quark-antiquark pair one can imagine a color flux tube (string) is stretched between them. When the string is stretched further due to the movement of the quark pair, the potential stored in the string increases linearly and ultimately breaks, producing a new pair ($q\bar{q} \rightarrow q\bar{q'} + q'\bar{q}$) via non-perturbative process. In this way mesons are produced. For the baryons, the di-quark production model and the popcorn model [86] are implemented. In di-quark model it is assumed that the strings break into pair of di-quarks, which are loosely bound states of two quarks instead of pairs of single quarks and from that baryons are formed.

- There could be many unstable resonance particles which are produced during fragmentation and undergo further fragmentation into hadrons. Therefore, the event generators include a list of short lived particles and their decays.

An important component of hadronic collisions is the **Underlying Event (UE)**. It includes almost all the physics processes except the "hard scattering". In general, initial- and final-state radiations (soft products), multiple parton interactions and beam remnants can be taken under UE. These processes mostly contribute to the production of hadrons with low transverse momenta.

1.3.3.2 pA collisions: the CNM effects

The signals for the QGP, created in the heavy-ion collisions are likely to carry the initial stage effects due to the cold nuclei (Cold Nuclear Matter (CNM) effects), also. The CNM effects naturally cannot be studied in the relativistic heavy-ion collisions. Experimentally, the CNM effects are disentangled from the hot QGP matter effects in nucleus-nucleus collisions by comparing the results from proton-nucleus (pA) collisions where no medium formation is assumed. Here, we briefly describe several sources of the CNM effects.

1.3.3.2.1 Nuclear modification of PDFs: shadowing and anti-shadowing

The structure function (F_2) for a bound nucleus differs from the superposition of those measured in free constituent nucleons [33]. The ratio of nucleon structure functions $R^A_{F_2}$ is defined as:

$$R^A_{F_2}(x, Q^2) = \frac{{F_2}^A(x, Q^2)}{A\ {F_2}^{nucleon}(x, Q^2)} \tag{1.6}$$

where A is the nuclear mass number and the variables x and Q^2 are defined from leptoproduction or deep inelastic scattering (DIS) experiments.

The left panel of Fig. 1.19 shows a schematic behaviour of $R^A_{F_2}$ for a given Q^2. The European Muon Collaboration (EMC) [87] at CERN and subsequent experiments mapped out the factor $R^A_{F_2}(x, Q^2)$. The ratio of the deep-inelastic cross sections of calcium (Ca) to that of deuterium (D) from EMC (solid circles) and SLAC (open circles) is shown in the right panel of Fig. 1.19. In the range $0.3 < x < 0.7$, EMC data shows a downward slope which is known be the "EMC effect". At lower value of x, the ratio is less than one, where valence quarks should no longer play a significant role. This is known as the shadowing region. From the measurement, the total curve is thus divided into four regions:

- $R^A_{F_2} > 1$ for $x \geq 0.8$: The Fermi motion region.
- $R^A_{F_2} < 1$ for $0.25 - 0.3 \leq x \leq 0.8$: The EMC region.
- $R^A_{F_2} > 1$ for $0.1 \leq x \leq 0.25 - 0.3$: the anti-shadowing region
- $R^A_{F_2} < 1$ for $x \leq 0.1$: the shadowing region.

Since the heavy-flavor study is the one of the main topics of this thesis, here we

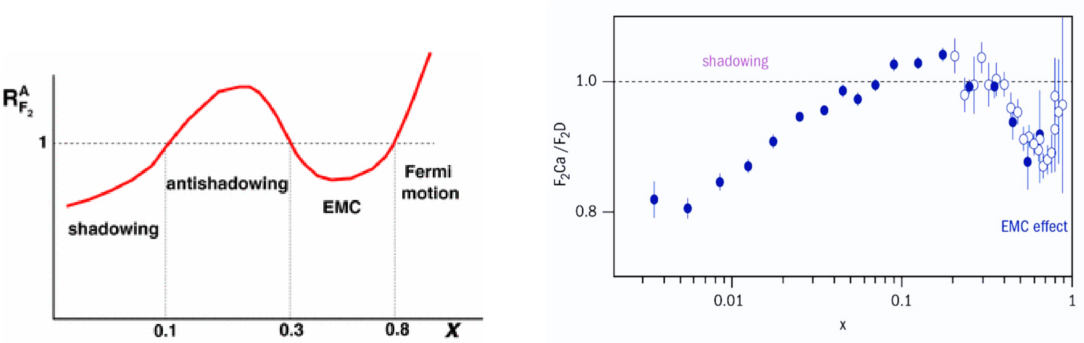

Figure 1.19: (Left) Schematic behaviour of nuclear modification factor ($R^A_{F_2}(x, Q^2)$) as a function of x for a given Q^2 [37]. (Right) The ratio of the structure functions F_2^{Ca} and F_2^d in calcium Ca nuclei and deuterium from EMC and SLAC.

would like to mention that such a modification of nuclear structure function can influence the charm quark production. We can estimate the upper limit of the p_{T}-region affected by the shadowing in $PbPb$ at the LHC. For a back to back charm quark production with p_{T} of 5 GeV/c leads to the EKS98 [88] parameterization giving R_g (for gluon) $\sim$ 90%. The value is already quite small and thus initial state effects should modify the p_{T} distribution of charm quarks only for $p_{\mathrm{T}} < 5-7$ GeV/c.

1.3.3.2.2 k_T broadening and Cronin enhancement

In late 70s' it was first observed that high-p_{T} hadrons were not suppressed in proton-nucleus collisions, rather produced extensively [35, 36]. Also, the hardening of the transverse momentum spectrum was observed in such proton-nucleus collisions relative to proton-proton collisions at transverse momenta of order $k_{\perp} \sim$ 1-2 GeV, and disappeared at much larger $k_{\perp}$. This effect is named after James Cronin [34]. The so-called "Cronin Effect" is interpreted in terms of multiple interactions of the projectile parton in the nucleus prior to the hard scattering [89, 90]. Due to such inelastic interactions, the partons gain an extra quantity of transverse momentum which leads to the broadening of the momentum distributions for the produced particles.

Experimentally, it was observed first via fixed-target experiments at Fermilab and later at RHIC and LHC. The observable related to Cronin effect is the Cronin ratio (R) which is defined as inclusive differential cross sections for proton scattering on two different targets, normalized to the respective atomic numbers A and B [38].

$$R(p_{\mathrm{T}}) = \frac{B}{A}\frac{d\sigma_{pA}/d^2p_{\mathrm{T}}}{d\sigma_{pB}/d^2p_{\mathrm{T}}} \tag{1.7}$$

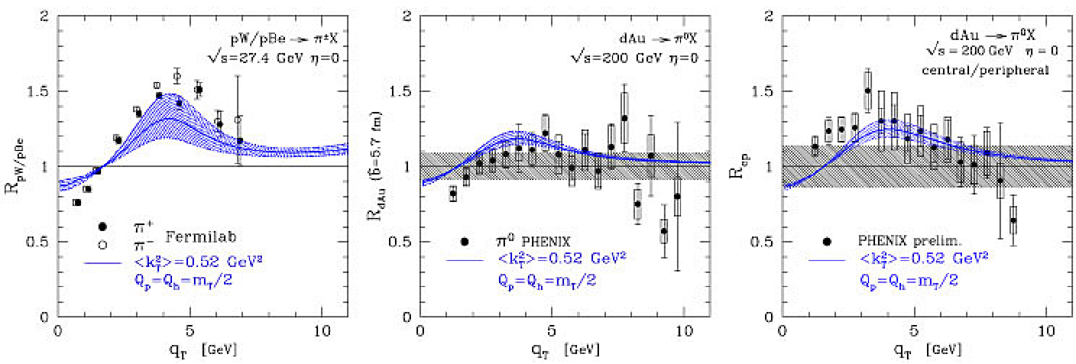

Figure 1.20: (Left) Cronin effect on pion production at Fermilab [36] and (middle and right) at RHIC with GE computation (solid line).

The Fig. 1.20 (left) shows the measurement of the pion (π) nuclear modification factor at mid rapidity in pW collisions relative to the one in pBe collisions by Fermilab and in dAu collisions by PHENIX experiment. The rightmost panel shows the ratio of 0-20% to 60-88% centrality classes for the PHENIX measurement. The data was compared with Glauber-Eikonal (GE) model calculations. The enhancement of the ratio confirms the Cronin effect for both the experiments at intermediate-p_{T} range. This means for more central the collision, the higher the parton density in the nucleus, the larger the non-linear effects as mentioned here [91].

1.3.3.2.3 Isospin effect

The isospin effect is there as the nucleus is composed of neutrons along with protons. The isospin effect can be accounted for, on an average in the PDFs for a nucleus with mass number A and atomic number Z via:

$$f_{a/A}(x) = \frac{z}{A} f_{a/p}(x) + (1 - \frac{z}{A}) f_{a/n}(x) \tag{1.8}$$

where $f_{a/p}$ (x) and $f_{a/n}$ (x) are the PDFs inside a proton and a neutron respectively.

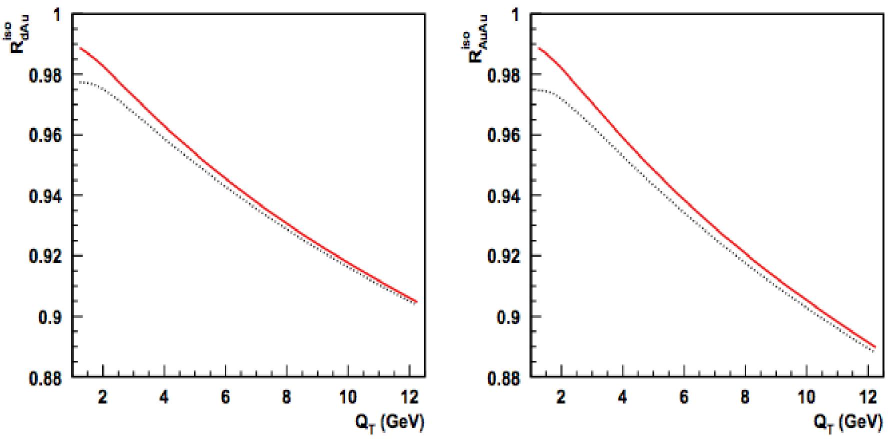

Figure 1.21: Nuclear modification factor to account the isospin effect as a function of Q_t, transverse momentum [93].

The PDFs in the neutron are related to the PDFs in the proton via isospin symmetry [39, 92]. Figure 1.21 shows the nuclear isospin modification factor as defined here [92] with the variation of transverse momentum Q_t for dAu and $AuAu$ collisions at $\sqrt{s_{\rm NN}}$ = 200 GeV. For the integrated mass range of 100-300 MeV isospin effect is significant, giving rise to a reduction of the nuclear modification factor by as much as 10%.

1.3.3.2.4 Cold Nuclear Matter energy loss

Before hard collisions occur, the partons from the protons can lose their energy due to medium induced gluon bremsstrahlung. This effect is reflected in the momentum fraction shift of the PDFs :

$$f_{q/p}(x_a) \rightarrow f_{q/p}\Big(\frac{x_a}{1-\epsilon_{eff}}\Big), \qquad f_{g/p}(x_a) \rightarrow f_{g/p}\Big(\frac{x_a}{1-\epsilon_{eff}}\Big) \tag{1.9}$$

The main effect of the fluctuation due to multiple gluon emission is an effective reduced fraction energy loss relative to mean energy $\langle\epsilon\rangle = \Big\langle \sum_i \frac{\Delta E_i}{E} \Big\rangle$ where the sum runs for all the medium induced gluons. The cold nuclear matter energy loss can be obtained by integrating the initial state medium induced bremsstrahlung spectrum. It also depends on the square of transverse momentum transferred between the parton and the medium (μ^2) per interaction and the gluon mean free path λ_g [39].

1.4 High-multiplicity events of small systems

The experimental measurements in small systems like pp or pPb collisions at the LHC energies generate keen interests due to some unexpected features which resemble the signals of formation of the hydrodynamic medium in the heavy-ion collisions.

1.4.1 Hydrodynamic-like features in high-multiplicity pp and pPb events at the LHC

The idea of hydrodynamic collectivity in high-multiplicity pp and pPb events got triggered with the pronounced signals in long-range two-particle angular correlations (basics of two-particle correlations will be discussed in chapter 2) for multiparticle production in such smaller systems which resemble the results from similar studies in ultra-relativistic heavy-ion collisions, where the formation of collective medium of partonic degrees of freedom is established.

In 2010 CMS collaboration at LHC first published the ridge-like structure in high-multiplicity pp collisions [94]. This observation sparked even more interest in this topic as the ridge-like structure has only been seen in heavy-ion collisions so far from RHIC to LHC (discussion on ridge-like structure in heavy-ion collisions can be found in chapter 2). The ridge structure, a correlation at small $\Delta\varphi$ and large $\Delta\eta$, also commonly referred to as long-range correlation, is produced by the excess particles in the collision along the beam and boosted by transverse flow. The standard explanation of the ridge in heavy-ion collisions is associated with collective

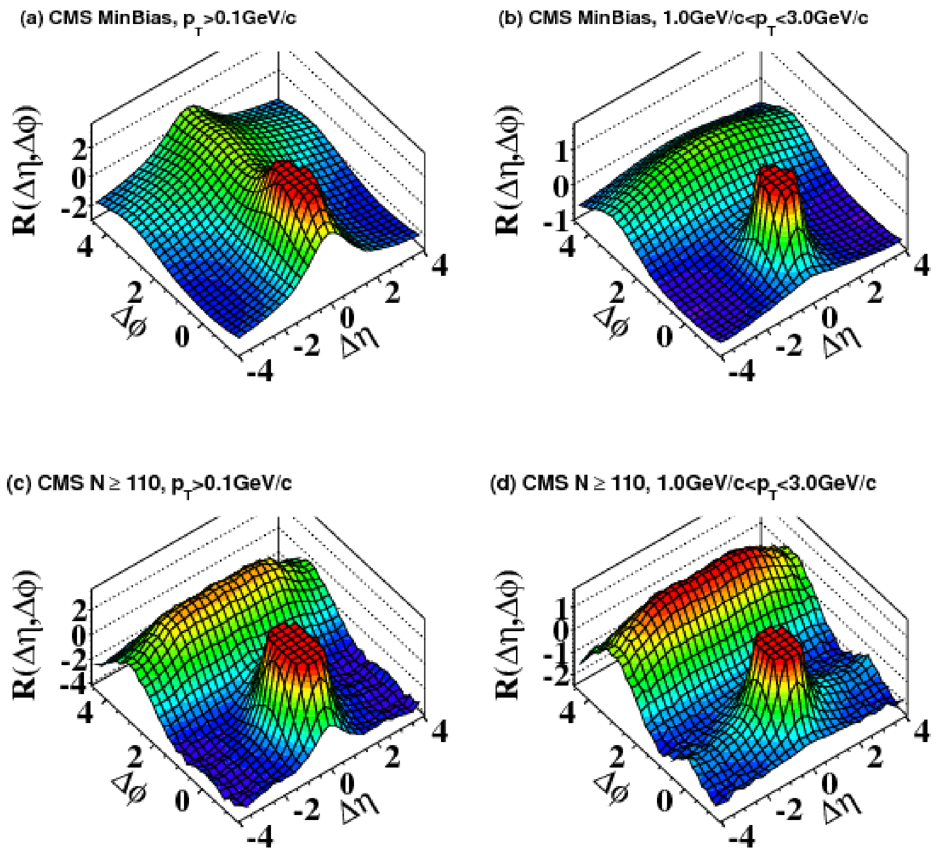

Figure 1.22: Two-particle angular correlations in pp collisions at $\sqrt{s}$ = 7 TeV minimum bias and high-multiplicity events using different trigger momentum cuts.

flow phenomena, characteristic of bulk macroscopic systems. In particular, angular correlations in azimuthal angle φ can be attributed to the radial flow that boosts particles in the radial direction.

Figure 1.22 shows the near-side ridge-like structure obtained from two-particle angular correlations with the trigger particle momenta range 1 – 3 GeV/c at $\sqrt{s}$ = 7 TeV in high-multiplicity pp events. The comparison is shown in the figure for inclusive particles $p_T > 0.1$ GeV/c (top panels) and for particles with $1 < p_T < 3$

GeV/c (bottom panels) for both minimum bias and high-multiplicity events. The minimum bias correlation function is dominated by particle emission from clusters (e.g. resonance decays, string fragmentations) and shows some contribution from jet-like particle production near $\Delta\eta$, $\Delta\varphi \sim (0, 0)$ due to the back-to-back jet fragmentation. It is clear from the figure (a, b) for minimum bias events there is no long-range ridge-like structure in the long-range region $2 < |\Delta\eta| < 4.8$. Even the high-multiplicity events with $p_{\mathrm{T}} > 0.1$ GeV/c (Fig 1.22 [c]) do not show the near-side ridge structure. This suggests that the long-range correlations i.e the collective behaviour of the system is mainly prominent in the intermediate-p_{T} range ($1 < p_{\mathrm{T}} < 3$ GeV/c) and in high-multiplicity events (N $\geq$ 110).

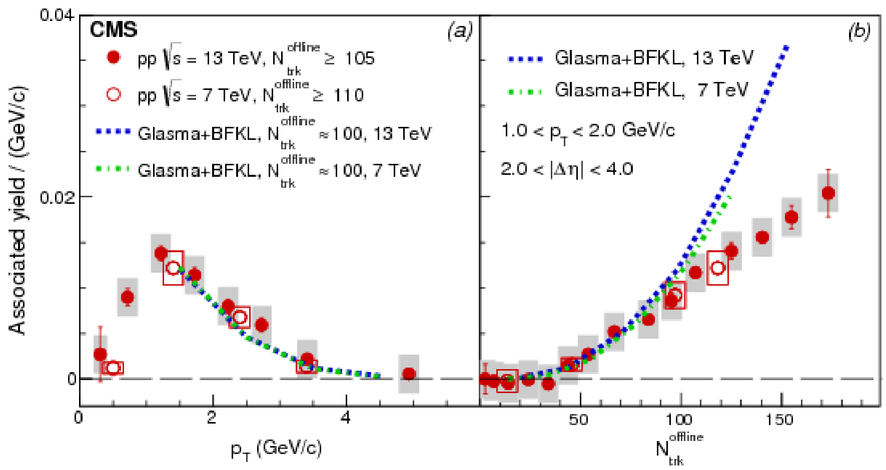

Figure 1.23: Long-range near-side associated yield for two-particle correlations in $1 < p_{\mathrm{T}} < 2$ GeV/c in pp collisions at $\sqrt{s} = 7$ TeV as function of multiplicity, measured by CMS experiment.

Figure 1.23 (right) shows the multiplicity dependent near-side associated yields in long-range ($2 < |\Delta\eta| < 4$) for the intermediate-p_{T} range ($1 < p_{\mathrm{T}} < 2$ GeV/c) where the ridge effect appears to be the strongest [95]. The ridge effect gradually appears with increasing event multiplicity. Since the MPI model does not take into account the angular momentum conservation, hence MPI model with color reconnection as incorporated in PYTHIA fails to explain the long-range correlation in high-multiplicity *pp* collisions. The thesis will survey a test of the MPI model using color reconnection which gave satisfactory results for N_{ch} dependency of mean transverse momentum ($< p_{\mathrm{T}} >$), in order to explain increasing trend of near-side ridge-like associated yields as a function of multiplicity in *pp* collisions at $\sqrt{s} = 7$ TeV.

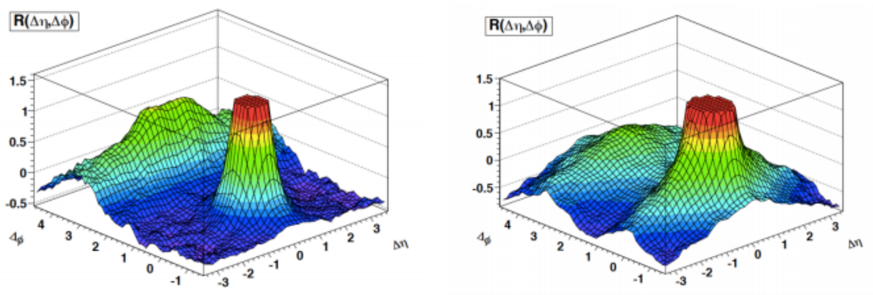

(a) without hydrodynamic evolution (b) with hydrodynamic evolution

Figure 1.24: Charged particle 2-dimensional $(\Delta\eta, \Delta\varphi)$ correlations in high-multiplicity *pp* collisions at $\sqrt{s}$ =7 TeV with $1 < p_{\mathrm{T}} < 3$ GeV/c using EPOS LHC model. (a) without hydrodynamic evolution and (b) with hydrodynamic evolution.

The EPOS model with hydrodynamic evolution successfully reproduced the long-range two-particle correlations in high-multiplicity *pp* events. The Fig. 1.24 shows the two-dimensional $\Delta\eta - \Delta\varphi$ correlations in high-multiplicity *pp* collisions using EPOS-LHC model, based on the hydrodynamic approach [96]. A near-side ridge-like structure is clearly visible with comparable magnitude to the experimental data in Fig. 1.24 (b), while the effect disappears if the hydrodynamic evolution is turned off in the model.

Similar to the pp high-multiplicity events, long-range ridge-like correlations has been found in high-multiplicity pPb collisions. CMS, ALICE, ATLAS and LHCb Collaborations at the LHC show a clear ridge structure in high-multiplicity pPb collisions at $\sqrt{s_{\mathrm{NN}}} = 5.02$ TeV. The Fig. 1.25 shows the two-dimensional $\Delta\eta - \Delta\varphi$ correlations in high-multiplicity pPb events by CMS and LHCb [97, 98] and a clear near-side ridge has been found for both the experiments. Again, it is noteworthy that the long-range or collective like features are only visible in the intermediate-p_{T} range.

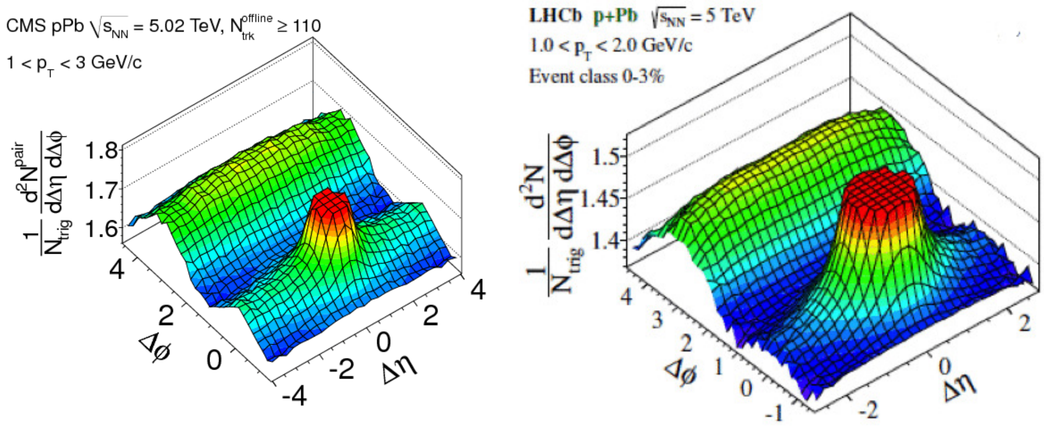

Figure 1.25: 2-dimensional $(\Delta\eta, \Delta\varphi)$ two-particle correlation functions in pPb collisions at $\sqrt{s_{\mathrm{NN}}} = 5.02$ TeV for pairs of charged particles in $1 < p_{\mathrm{T}} < 3$ GeV/c (CMS) and $1 < p_{\mathrm{T}} < 2$ GeV/c (LHCb). Results are shown for high-multiplicity classes ($\mathrm{N}_{trck}^{offline} > 110$ for CMS and 0-3% event class for LHCb).

The ALICE Collaboration put forward the analysis and found a double-ridge (both in near- and away-side of the correlation distributions) structure. To disentangle the jet and ridge structures, the correlation distributions evaluated in low-multiplicity is subtracted from that of high-multiplicity events. It is assumed that the correlation distributions evaluated in low-multiplicity pPb collisions is similar to that obtained in minimum bias pp collisions. Hence, the low-multiplicity collisions are highly jet dominated and the high-multiplicity events contain both the jet and long-range correlations. Therefore, by subtracting the correlation of low-multiplicity events from that of high-multiplicity events would actually cancel out the jet-like correlation. ALICE has measured the correlation distributions with identified particles as trigger particles i.e pion/kaon/proton triggers.

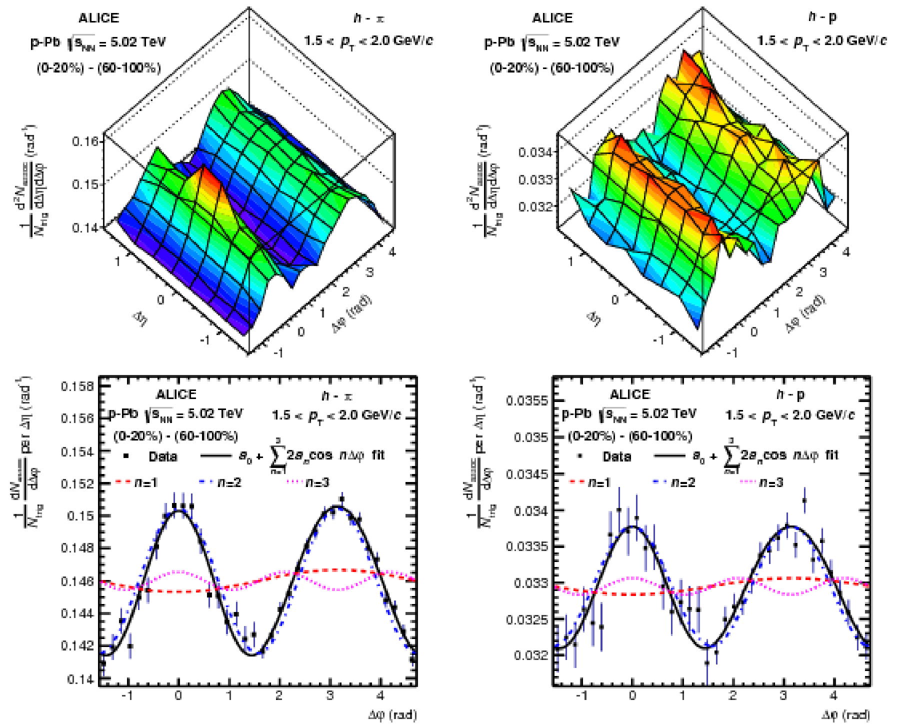

Figure 1.26: (Top) 2-dimensional $(\Delta\eta, \Delta\varphi)$ di-hadron correlation function taking pion and proton as trigger particles measured by ALICE, for high-multiplicity (0–20%) events, after subtraction of the results for the 60–80% centrality class [99]. (Bottom) $\Delta\varphi$ projection of top panel averaged over $0.8 < |\Delta\eta| < 1.6$ on the near side and $|\Delta\eta| < 1.6$ on the away side.

Figure 1.26 (top panel) shows the angular correlations between pions (protons) and unidentified hadrons after the subtraction of low-multiplicity events from high-multiplicity events and the projection on $\Delta\varphi$ is displayed in the bottom panel for the corresponding triggers.

The Fourier coefficients are evaluated by fitting Eq. 2.5 to the measured ridge modulation in $\Delta\varphi$ [99, 100]. The flow coefficient v_2 is evaluated for all the identified triggers and is shown in Fig. 1.27. The surprise comes out with the mass dependence of the flow coefficient which is very similar to the results from $PbPb$ collisions [101, 102].

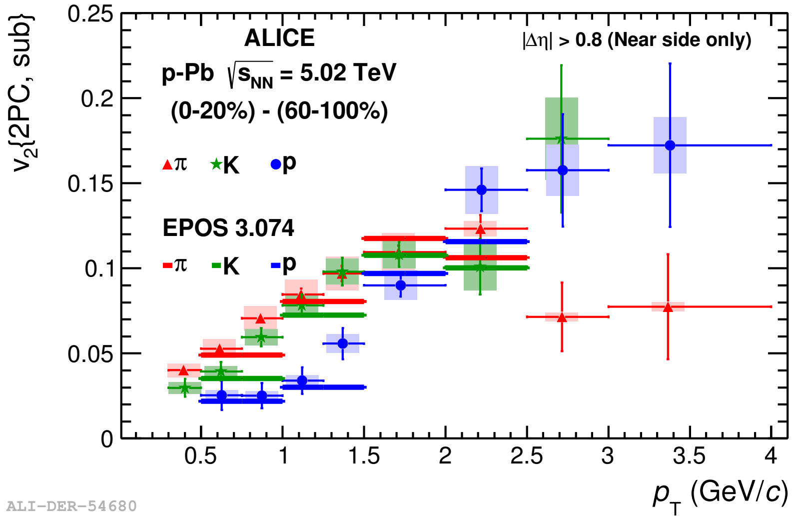

Figure 1.27: The measured Fourier coefficient v_2 for identified hadrons as a function of p_T from the correlation in the 0–20% multiplicity class after subtraction of two-particle correlation from the 60–100% multiplicity class. The mass ordering of the flow coefficient is successfully addressed by EPOS 3 model including hydrodynamical calculations.

The double-ridge structure in pPb collisions creates a big challenge for different theoretical models. The ridge structures on near- and away-side are successfully reproduced by Color-Glass Condensate (CGC) framework or hydrodynamical calculation (e.g. EPOS 3) that assumes collective effects in pPb collisions. The EPOS 3 model calculations reproduce both the double-ridge structure (Fig. 1.28) and mass ordering of flow coefficient v_2 of identified particles (Fig. 1.27) [103]. The CGC model calculations also reproduce a clear double ridge structure [104] with Glasma graph computation to the central ($0-20\%$) minus peripheral ($60-100\%$) yield from ALICE (Fig. 1.28). Though the models using hydrodynamical calculations or initial state color-glass framework successfully reproduce the ALICE data for the double-ridge spectra in pPb collisions, its origin is still unknown. Thus, it creates new scopes towards physics of small systems.

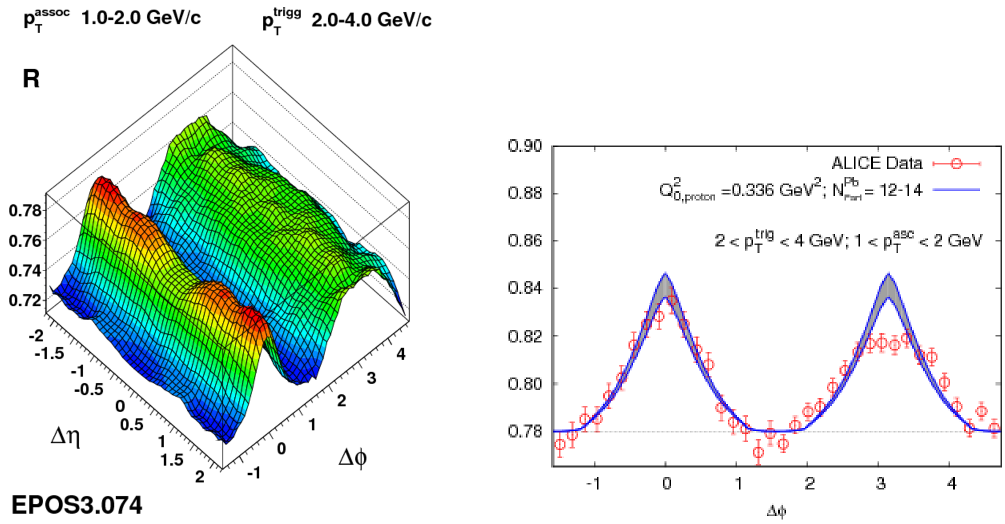

Figure 1.28: (Left) 2-dimensional $(\Delta\eta, \Delta\varphi)$ di-hadron correlation function calculated using EPOS 3 simulations, for high-multiplicity (0–20%) events, after subtraction of the result for the 60–80% class [103]. (Right) Comparison of one dimensional $(\Delta\varphi)$ per-trigger di-hadron correlations between the Glasma graphs computation from CGC model and the ALICE data [104].

As stated in subsubsection 1.3.2.3 that identified charged particle ratio is an important signature for the QGP formation in heavy-ion collisions, such tool can also be equally important for small system like pPb collisions. The charged particle ratios of kaon over pion (K/π) and proton over pion (p/π) are studied as a function of p_{T} for different multiplicity event classes for pPb collisions at $\sqrt{s} = 5.02$ TeV by ALICE as shown in the Fig. 1.29. One can find some similar trends for the particle ratios for both pPb and $PbPb$ collisions (left and right panel of Fig. 1.29 respectively).

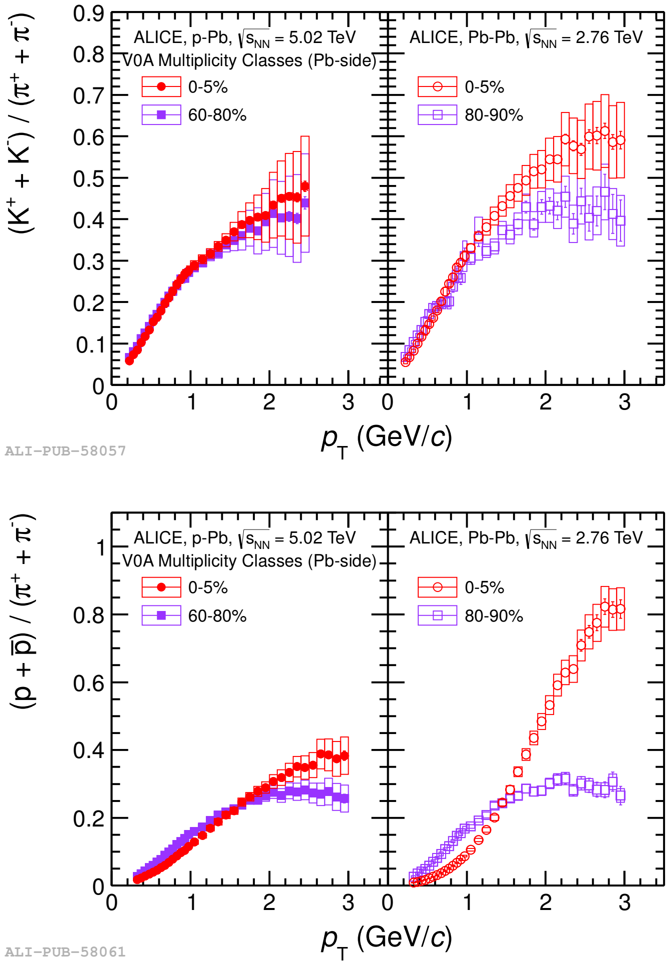

Figure 1.29: Charged particle ratios K/π (top) and p/π(bottom) measured by ALICE for most central (0–5%) and peripheral (60–80%) events in pPb and $PbPb$ collisions at $\sqrt{s_{\mathrm{NN}}} = 5.02$ TeV and 2.76 TeV respectively [105].

In both systems, K/π ratio has only a mild centrality dependence whereas the observed crossing point of p/π ratio of different centralities is roughly at the same position (1.5 and 1.6 GeV/c for $PbPb$ and pPb collisions, respectively). In $PbPb$ collisions such enhancement of baryon over meson in central collisions is attributed to the collectivity of the medium produced in the collision and is explained by hydrodynamical flow [106] and parton coalescence or recombination models [107, 108]. Due to coalescence at low-p_{T}, baryons gain more transverse momentum from flow than mesons and are pushed to higher momentum. The similar behaviour of particle ratios in pPb collisions are reproduced by hydrodynamical models, like EPOS 3 [109].

With the success of EPOS model in explaining flow-like effect in high-multiplicity pPb events we extend the study in heavy-flavor domain taking D mesons as trigger particles. The results will be discussed in section 6.1.

1.4.2 Non-hydrodynamic approaches in understanding the high-multiplicity *pp* and *pPb* events at the LHC

Of the alternate explanations (other than direct hydrodynamic approach) to the flow-like effects, seen in the high-multiplicity pp and pPb events, the MPI model with Color Reconnection (CR), as implemented in the PYTHIA 8 and, the IP-Glasma model have been the most discussed models. Here, we will discuss some of the explanations. It is to be noted here that a comprehensive study on the comparison between the data and the MPI model, with and without CR will be discussed in section 6.2, in terms of several features of the multiparticle production up to the intermediate-p_{T} range in high-multiplicity pp events.

The idea of multiple parton-parton interations provides an alternative theoretical base to understand the flow-like behaviour found in pp and pPb collisions. The understanding of multiple interactions is valuable for the physics involving jets as well as soft part i.e jet-pedestal effect in the underlying event (defined as the region transverse to the leading jet or particle in an event, $\pi/3 < |\Delta\varphi| < 2\pi/3$, where φ is the azimuthal angle of the leading object [110]) in hard scatterings. With the increasing centre-of-mass energy of pp collisions, the MPI becomes more and more important as many observables like the charged particle multiplicity, mean transverse momentum as a function of multiplicity, multi-jet, the jet-pedestal underlying event etc. depend on the number of MPIs [111, 112].

Different experiments at the LHC show a gradual increase of average transverse momentum of the particles ($< p_{\mathrm{T}} >$) as function of charged particle multiplicity. The top panel of Fig. 1.30 shows ALICE measurements of the variation of $< p_{\mathrm{T}} >$ as a function of charged particle multiplicity at different centre-of-mass energies in the kinematic range, $|y| < 0.5$ and $p_{\mathrm{T}} < 10$ GeV/c. The rising trend follows what is obtained in heavy-ion collisions (bottom panel of Fig. 1.30). The trend of $< p_{\mathrm{T}} >$ increasing with centrality in heavy-ion collisions is conventionally interpreted in terms of radial flow [113]. The trend of increasing $< p_{\mathrm{T}} >$ in pp collisions could also be due to some associated radial flow.

The pQCD-inspired multiparton interaction (MPI) model in PYTHIA (see section 8.1) along with the color reconnection (CR) scheme [114] has been proposed as an alternate explanation of the observed flow-like behaviour of charged particles in *pp* collisions. The high-multiplicity events are produced by multiple parton interactions where an incoherent superposition of such interactions would lead to a constant $< p_T >$ at high multiplicities [115]. The MPI with CR [114] between hadronizing strings successfully describes the charged particle multiplicity (N_{ch}) dependence of mean transverse momentum, $< p_{\mathrm{T}} >$, as shown in the top panel of the same figure.

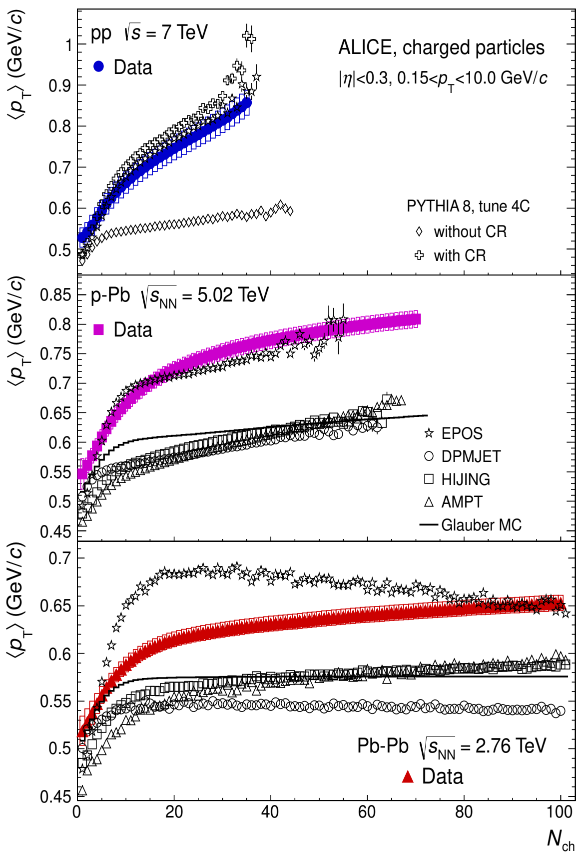

Figure 1.30: The average transverse momentum $< p_{\mathrm{T}} >$, as a function of charged particle multiplicity, N_{ch}, as measured by ALICE in *pp* (up), *pPb* (middle) and *PbPb* (bottom) collisions. The data are compared with different model calculations [115].

It has been assumed that CR mechanism can mimic the collective final-state effects in the high-multiplicity *pp* collisions. According to the CR scheme, the multiparticle production in high-multiplicity events results from a large number of overlapped MPIs. The overlapped partons from individual MPIs get connected by color strings and the partons cannot hadronize independently. The collective hadronization of reconnected partons from the overlapped MPIs takes place through string fragmentation process. The effect of transverse boost of the reconnected partons is manifested in the observed flow-like effect. The CR mechanism could be similar to the string fusion [116] mechanism in heavy-ion collisions.

It is worth noting here that the MPI model with color reconnection explains the data including the high-p_{T} (p_{T} <10 GeV/c) particles, while the signals of hydrodynamic collectivity are seen [117–119] up to the intermediate-p_{T} ($p_{\mathrm{T}} < 2$ GeV/c) range. It is, therefore, important to study the response of color reconnection up to intermediate-p_{T} range only, for a better understanding of the relative effect of the collective hadronization due to color reconnection on the intermediate-p_{T} phenomena in high-multiplicity pp events (discussed in section 6.2).

In pA collisions much larger MPIs occur and the number of MPIs is proportional to the number of binary nucleon-nucleon collisions (N_{coll}). Similar to pp collisions the MPIs overlap in the jet-pedestal region i.e transverse region of collisions. The MPIs in pA collisions also produce such effects as in pp collisions and the color charges may reconnect strongly due to increasing number of MPIs. The mid panel of Fig. 1.30 shows the $< p_{\mathrm{T}} >$ vs N_{ch} for pPb collisions at $\sqrt{s_{\mathrm{NN}}}$ = 5.02 TeV. Since the dependency of average transverse momentum on the collision energy is minimal (Fig 1.30), the 3 collision systems at different centre-of-mass energy can directly be compared. The rise of $< p_{\mathrm{T}} >$ is much faster in pp than in pPb or

$PbPb$ in the multiplicity range of $\mathrm{N}_{ch} \sim 14$. The moderate increase of $< p_{\mathrm{T}} >$ with increasing centrality in $PbPb$ collisions is due to the collective flow as most of the particles take part in the collective motion of the thermalized medium. In pPb collisions, the rise of average transverse momentum with the high-multiplicity events can be attributed to the effects like colour reconnections by a superposition of parton scatterings. The data are compared with different models. None of these models DPMJET (v3.0), HIJING (v1.383), or AMPT (with string-melting) can reproduce the data. However, the EPOS model (see section 8.1) with the hydrodynamical collective effects describes the pPb data successfully.

Bibliography

[1] S. Weinberg, Eur. Phys. J. C. **34**, 5 (2004).

[2] Collider physics, Barger and Phillips.

[3] P. W. Higgs, Phys. Lett. **12**, 132 (1964).

[4] F. Englert and R. Brout, Phys. Rev. Lett. **13**, 321 (1964).

[5] G. Aad et al., ATLAS Collaboration, Phys. Lett. B**716**, 1-29 (2012).

[6] W. Adam et al., CMS Collaboration, Phys. Lett. B**716**, 30-61 (2012).

[7] Yu-Qi Chen and Yu-Ping Kuang, Phys. Rev. D**47**, 350 (1993).

[8] S. Bethke, Prog. Part. Nucl. Phys. **58** (2007) 351.

[9] J. C. Collins and M. J. Perry, Phys. Rev. Lett. **34**, 1353 (1975).

[10] Search for the QCD Critical Point at RHIC: First Experience with $AuAu$ Collisions at 9.2 GeV, T. K. Nayak, RHIC News, April 8, 2008.

[11] S. L. Shapiro and S. Teukolsky, Wiley, New York (1983) 25.

[12] Xiaofeng Luo, Nu Xu, arXiv:1701.02105 [nucl-ex].

[13] Swagato Mukherjee, Raju Venugopalan, Yi Yin, Phys. Rev. Lett. **117**, 222301 (2016).

[14] Swagato Mukherjee, Raju Venugopalan, Yi Yin, Phys. Rev. C**92**, 034912 (2015).

[15] F. Karsch, Lattice QCD at High Temperature and Density. Lecture Notes of Physics, vol. 583, 2002.

[16] E. Shuryak, Phys. Rep. **61**, 71 (1980).

[17] I. Arsene et al., BRAHMS Collaboration, Nucl. Phys. **A757**, 1 (2005).

[18] B. B. Back et al., PHOBOS Collaboration, Nucl. Phys. **A757**, 28 (2005).

[19] J. Adams et al., STAR Collaboration, Nucl. Phys. **A757**, 102 (2005).

[20] K. Adcox et al., PHENIX Collaboration, Nucl. Phys. **A757**, 184 (2005).

[21] S. J. Lindenbaum et al., AIP Conference Proceedings **176**, 778 (1988).

[22] U. Heinz, M. Jacob, arXiv: nucl-th/0002042.

[23] Richard M. Weiner, Int. J. Mod. Phys. **E15**, 37 (2006).

[24] P. Levai and B. Muller, Phys. Rev. Lett. **67**, 1519 (1991).

[25] T. Alexopoulos et al., Phys. Lett. **B528**, 43 (2002).

[26] M. C. Abreu et al., Phys. Lett. **B410**, 337 (1997).

[27] B. B. Back et al., Phys. Rev. Lett. **94**, 122303 (2005).

[28] J. Adams et al., STAR Collaboration, Phys. Rev. **C73**, 034903 (2006).

[29] G. Wang for STAR Collaboration, Nucl. Phys. **A774**, 515 (2006).

[30] X. Luo and N. Xu, arXiv:1701.02105v1 [nucl-ex].

[31] K. Fukushima and T. Hatsuda, Rept. Prog. Phys.**74**, 014001 (2011).

[32] K. Adcox et al., PHENIX Collaboration, Phys. Rev. Lett. **88**, 022301 (2002).

[33] Arneodo M, Phys. Rept. 240 301 (1994).

[34] J. W. Cronin et al., Phys. Rev. **D11**, 3105 (1975).

[35] L. Kluberg et al., Phys. Rev. Lett. **38**, 670 (1977).

[36] D. Antreasyan et al., Phys. Rev. Lett. **38**, 112 (1977).

[37] Nestor Armesto, J. Phys. G: Nucl. Part. Phys. 32 R367 (2006).

[38] A. Accardi, arXiv:hep-ph/0212148v2.

[39] Zhong-Bo Kang, Ivan Vitev, Hongxi Xing, Phys. Lett. **B718**, 482-487 (2012).

[40] Sanghoon Lim for the PHENIX Collaboration, Nuclear Physics **A931**, 525-529 (2014).

[41] B. Muller, J. Schukraft, and B. Wyslouch, Annu. Rev. Nucl. Part. Sci. **62**, 361 (2012).

[42] V. Khachatryan et al., CMS Collaboration, JHEP**09**, 091 (2010).

[43] G. Aad et al., ATLAS Collaboration, Phys. Rev. Lett. **116**, 172301 (2016).

[44] V. Khachatryan et al., CMS Collaboration, Phys. Rev. Lett. **116**, 172302 (2016).

[45] V. Khachatryan et al., CMS Collaboration, arXiv:1606.06198v1 [nucl-ex] (2016).

[46] B. Ablev et al., ALICE Collaboration, Phys. Lett. **B719**, 29 (2013).

[47] S. Chatrchyan, et al., CMS Collaboration, Phys. Lett. **B718**, 795814 (2013).

[48] G. Aad et al., ATLAS Collaboration, Phys. Rev. Lett. **110**, 182302 (2013).

[49] B. Ablev et al., ALICE Collaboration, Phys. Lett. **B728**, 25 (2014).

[50] A. Adare et al., PHENIX Collaboration, Phys. Rev. Lett. **114**, 192301 (2015).

[51] B. Abelev et al., ALICE Collaboration, Phys. Rev. Lett. **110**, 082302 (2013).

[52] H. J. Drescher, M. Hladik, S. Ostapchenko, T. Pierog, and K. Werner, Phys. Rept. 350 93-289 (2001).

[53] T. Sjöstrand, S. Mrenna, and P. Z. Skands, JHEP**05**, 026 (2006).

[54] Nayak, Tapan K. Pramana 79 (2012) 719-735.

[55] R. Glauber, Nucl. Phys. **B21** pp. (1970) 135-157.

[56] J. D. Bjorken, Phys. Rev. **D27**, Number (1983) 1.

[57] B. I. Abelev et al., STAR Collaboration, Phys. Rev. **C79**, 034909 (2009).

[58] M. Floris for the ALICE Collaboration, Quark Matter 2011 proceedings [arXiv:1108.3257].

[59] J. Adams et al., STAR Collaboration, Nucl. Phys. **A757** (2005) 28 and S. Wheaton and J. Cleymans, Comput. Phys. Commun 180 (2009) 84 [hep-ph/0407174].

[60] S. Voloshin and Y. Zhang, Z. Phys. **C70**, 665 (1996).

[61] B. Abelev et al., ALICE Collaboration, Phys. Lett. **B736**, 196-207 (2014).

[62] B. Abelev, et al. ALICE Collaboration, Phys. Lett. **B727**, 371-380 (2013).

[63] K. Fanebust et al., NA57 Collaboration, J. Phys. G: Nucl. Part. Phys. 28 1607 (2002).

[64] R. Hagedorn, CERN Rept. 71 (1971);
E. Shuryak, Phys. Lett. **B42**, 357 (1972);
J. Rafelski, and M. Danos, Phys. Lett. **B97**, 279 (1980);
R. Hagedornetal., Z Phys. **C27**, 541 (1985).

[65] Tounsi A. and Redlich K., arXiv: 0111159[hep-ph] (2001).

[66] T. Matsui and H. Satz, Phys. Lett. **B178**, 416 (1986); T. Matsui, Zeit. Phys. **C38**, 245 (1988).

[67] M. Gyulassy et al., arXiv:nucl-th/ 0302077.

[68] Xiangrong Zhu for the ALICE Collaboration, arXiv:1311.2394v2 [hep-ex] 30 Dec 2013.

[69] Art Poskanzer talk BNL, `http://rnc.lbl.gov/Poskanzer/BonnerTalk/BonnerTalk.pdf`.

[70] K. Aamodt et al., ALICE Collaboration, Phys. Rev. Lett. **105**, 252302 (2010).

[71] B. Abelev et al., ALICE Collaboration, JHEP**06**, 190 (2015).

[72] J. Adams et al., STAR Collaboration, Phys. Rev. **C72**, 014904 (2005).

[73] A. Adare et al., PHENIX Collaboration, Phys. Rev. **C85**, 064914 (2012).

[74] A. Adare et al., PHENIX Collaboration, Phys. Rev. **C88**, 024906 (2013).

[75] B. Abelev et al., STAR Collaboration, Phys. Rev. Lett. **97**, 152301 (2006).

[76] R. J. Fries, B. Müller, C. Nonaka, S. A. Bass, Phys. Rev. **C68**, 044902 (2003).

[77] K. Aamodt et al., ALICE Collaboration, Phys. Lett. **B696**, 30-39 (2011).

[78] GUNTHER ROLAND, PRAMANA journal of physics, Indian Academy of Sciences, Vol. 84, No. 5, May 2015.

[79] A. Kaidalov, REGGE POLES IN QCD, At The Frontier of Particle Physics: pp. 603-636. (2001).

[80] Judith M. Katzy, Progress in Particle and Nuclear Physics 73, 141-187 (2013).

[81] Andy Buckley et al., Phys. Rept. 504, 145-233 (2011).

[82] B. Andersson, G. Gustafson, G. Ingelman, and T. Sjöstrand, Phys. Rept. 97, 31145 (1983).

[83] R. D. Field and S. Wolfram, Nucl. Phys. **B213**, 65 (1983).

[84] T. D. Gottschalk, Nucl. Phys. **B239**, 349 (1984).

[85] B. R. Webber, Nucl. Phys. **B238**, 492 (1984).

[86] T. Sjöstrand, S. Mrenna, and P. Z. Skands, JHEP**05**, 026 (2006).

[87] J. J. Aubert et al., EMC Collaboration, Phys. Lett. **B123**, 275 (1983).

[88] K. J. Eskola, V. J. Kolhinen, C. A. Salgado, Eur. Phys. J. **C9**, 61 (1999).

[89] B. Z. Kopeliovich, J. Nemchik, A. Schäfer, and A. V. Tarasov, Phys Rev Lett. **88**, 232303 (2002).

[90] Jean-Paul Blaizot, Francois Gelis, Raju Venugopalan, Nuclear Physics **A743**, 13-56 (2004).

[91] Alberto Accardi and Miklos Gyulassy, arXiv:nucl-th/0402101v1 27 Feb 2004.

[92] Z. B. Kang, J. W. Qiu, W. Vogelsang, Phys. Rev. **D79**, 054007 (2009).

[93] B. Abelev et al., ALICE Collaboration, Phys. Rev. Lett. **113**, 232301 (2014).

[94] V. Khachatryan et al., CMS Collaboration, JHEP**09**, 091 (2010).

[95] V. Khachatryan et al., CMS Collaboration, Phys. Rev. Lett. **116**, 172302 (2016).

[96] Wei Li, arXiv:1206.0148.

[97] S. Chatrchyan et al., CMS Collaboration, Phys. Lett. **B718**, 795 (2013).

[98] Roel Aaij et al., LHCb Collaboration, Phys. Lett. **B762**, 473-483 (2016).

[99] B. Abelev et al., ALICE Collaboration, Phys. Lett. **B726**, 164-177 (2013).

[100] B. Abelev, et al. ALICE Collaboration, Phys. Lett. **B719**, 29-41 (2013).

[101] B.Abelev et al., ALICECollaboration, arXiv:1205.5761 [nucl-ex] (2012).

[102] Y. Zhou for the ALICE Collaboration. arXiv:1309.3237 [nucl-ex] (2013).

[103] K. Werner et. al., arXiv:1307.4379 [nucl-th] (2013).

[104] K. Dusling and R. Venugopalan, Phys. Rev. **D87**, 094034 (2013).

[105] B. Abelev et al., ALICE Collaboration, Phys. Lett. **B728**, 25-38 (2014).

[106] P. Bozek. Acta Phys. Polon B 43-689, 2012.

[107] V. Minissale, F. Scardina, and V. Greco, arXiv:1502.06213 (2015).

[108] R. Fries et al., Phys. Rev. **C68**, 044902 (2003).

[109] K. Werner et al., arXiv:1405.0664v1[nucl-th] (2014).

[110] Andreas Morsch for the ALICE Collaboration, J. Phys, Conf. Ser. 535 012012 (2014).

[111] T. Sjöstrand and P. Z. Skands, JHEP**03**, 053 (2004).

[112] W. D. Walker, Phys. Rev. **D69**, 034007 (1996).

[113] B. I. Abelev et al., STAR Collaboration, Phys. Rev. **C79**, 034909 (2009).

[114] A. Ortiz Velasquez et al., Phys. Rev. Lett. **111**, 042001 (2013).

[115] B. Abelev et al., ALICE Collaboration, Phys. Lett. **B727**, 371-380 (2013).

[116] N. Amelin, M. Braun and C. Pajares, Phys. Lett. **B306**, 312 (1993).

[117] K. Werner, I. Karpenko and T. Pierog, Phys. Rev. Lett. **106**, 122004 (2011).

[118] E. Shuryak and I. Zahed, Phys. Rev. **C88**, 044915 (2013).

[119] P. Ghosh, S. Muhuri, J. Nayak and R. Varma, J. Phys. **G41**, 035106 (2014).

Chapter 2

Two-particle angular correlations: the analysis tool

Correlations between produced particles in high energy collisions provide valuable information about particle production mechanism and of initial and final state effects of the collisions. Two-particle angular correlation becomes very important tool for different collisions systems (heavy-ion or small systems) at different energies. In this chapter basic details of two-particle angular correlations will be discussed.

The measurement of two-particle azimuthal correlations is a robust tool to explore the properties of QGP created in ultra-relativistic heavy-ion collisions [1]. The tool is equally important in small systems like *pp* and *pPb*. It can exploit both the high-p_{T} suppression as well as collective behaviour of the medium. The angular correlation distributions are sensitive to several properties of the system created in the heavy-ion collisions, such as parton-medium interaction mechanisms, collective expansion, decay kinematics and so on. The property that dominates the angular correlation distribution depends mainly on the kinematic region defined for the trigger and the associated particles. At low-p_{T}, collective phenomena, that are described by hydrodynamic model calculations are dominant, while at high-p_{T}, jet related correlations dominate the distribution structure, as argued in [2].

In high energy collisions, jets are produced back-to-back (as discussed in chapter 1). Jets are supposed to carry the momentum of the parent parton having back-to-back (di-jet) correlations between high-p_{T} hadrons. The two-particle correlation gives most direct evidence for production of jets in high energy collisions and provides information about interaction of hard-scattered partons with the medium. In the long-range (larger $\Delta\eta$ region), one can ignore the jet influence and extract the collective behaviour of produced particles from such correlations.

2.1 Different correlation sources

In general two-particle correlation is sensitive to a number of correlations each of which has its own structure in $\Delta\eta, \Delta\varphi$ space originating from different sources such as:

- **Conservation laws**: The physics processes are governed by the conservation of energy and momentum everywhere. In high energy collisions particle production in different isolated events are maintained via conservation of energy and momentum. The conservation laws influence the shape of the correlation function especially in small systems. The momentum conservation leads to the production of particles in the back-to-back fashion and produces peaks at $\Delta\eta, \Delta\varphi \sim (0,\, 0)$ in the $\eta - \varphi$ phase space.

- **Bose-Einstein correlations:** In high energy collisions, bosons (e.g. pions) are likely to be produced in the same quantum state i.e with similar η or φ as they are obeying the Bose-Einstein statistics. Hence, additional contribution from this kind of correlations is showed up to the near-side peak.

- **Resonance decays:** Resonances i.e short lived particles can produce correlated particles while decaying isotropically. This could give contribute to the near-side peak in the $\Delta\eta, \Delta\varphi$ correlation.

- **Photon conversion:** This is basically refereed as pair production where a photon with certain minimum energy ($>$ 1.02 MeV) produces an electron-positron pair. The lepton pairs produced via photon conversion are tend to move with small azimuthal angle differences and thus they can also contribute to the near-side peak.

- **Coulomb effects:** The final state hadrons interact electrically through Coulomb interactions. The same (opposite) charged particles in close momentum space

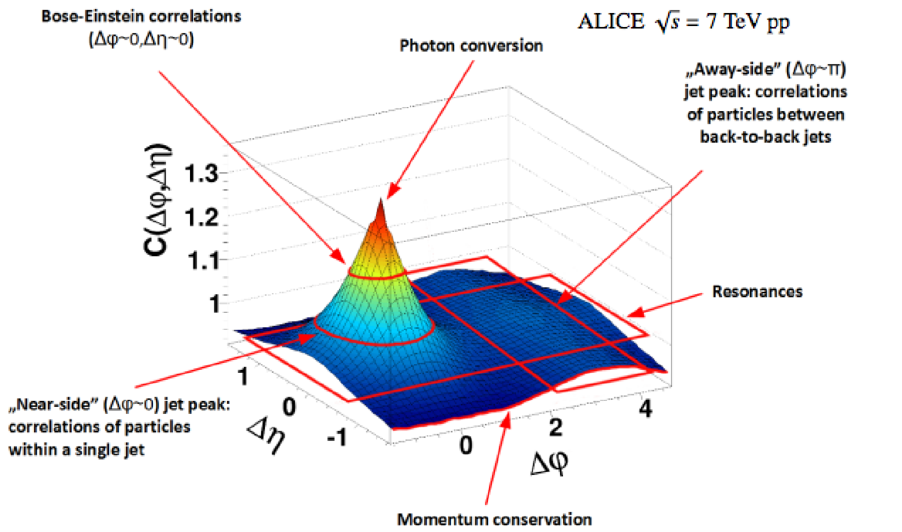

Figure 2.1: Contributions from different correlation sources to the $\Delta\eta, \Delta\varphi$ correlation function. Figure taken from [3].

repel (attract) each. This attraction or repulsion between charged hadrons can contribute to the near-side peak in the $\Delta\eta, \Delta\varphi$ correlation.

Contributions coming from all the above mentioned correlation sources, combine to create one collective distribution of different physical phenomena that are related to the collisions of particles. Figure 2.4 shows the different contributions creating this global picture of the correlation function.

The detail discussions on the other two sources of correlations, the "jets" and the "ridge", having significance for the studies included in this thesis, are given in the subsection 2.2.1.

2.2 Construction of two-particle angular correlation

The two-particle correlation function is constructed by measuring the differences in azimuthal angles $\varphi_{trig} - \varphi_{assoc}$ and/or in pseudorapidities $\eta_{trig} - \eta_{assoc}$ where φ_{trig} and φ_{assoc} (η_{trig} and η_{assoc}) are the azimuthal angle (pseudorapidity) for "trigger" and "associated particles". Taking both variables η and φ, the correlation function can be written as:

$$\frac{1}{N_{trig}}\frac{d^2N^{assoc}}{d\Delta\eta d\Delta\varphi} = B(0,0) \times \frac{S(\Delta\eta,\Delta\varphi)}{B(\Delta\eta,\Delta\varphi)} \tag{2.1}$$

where N_{trig} is the number of trigger particles in the specified $p_T^{trigger}$ range.
The function S$(\Delta\eta, \Delta\varphi)$ is the differential measure of per-trigger distribution of associated hadrons in the same-event, i.e,

$$S(\Delta\eta,\Delta\varphi) = \frac{1}{N_{trig}}\frac{d^2N^{assoc}_{same}}{d\Delta\eta d\Delta\varphi} \tag{2.2}$$

The same-event distribution functions are corrected for the random combinatorial background and effects due to the limited acceptance by dividing the raw same-event distribution function by the mixed-event background distribution, where trigger and associated particles are paired from two different events of similar multiplicity.
The background distribution function B$(\Delta\eta, \Delta\varphi)$ is defined as:

$$B(\Delta\eta,\Delta\varphi) = \frac{d^2N^{mixed}}{d\Delta\eta d\Delta\varphi} \tag{2.3}$$

where N^{mixed} is the number of mixed event pairs.

The factor B(0,0) in Eqn. 6.1 is used to normalize the mixed event correlation function such that it is unity at $(\Delta\eta, \Delta\varphi)$ = (0,0). Finally, the acceptance corrected correlation function is determined by scaling the same event distribution function, $S(\Delta\eta, \Delta\varphi)$ by the inverse of the normalized background distribution function, $B(\Delta\eta, \Delta\varphi)/B(0,0)$.

The two-dimensional correlation distribution is projected in $\Delta\varphi$ by integrating over a specific range of $\Delta\eta$:

$$\hat{C}(\Delta\eta, \Delta\varphi) = \frac{1}{N_{trig}} \frac{dN^{assoc}}{d\Delta\varphi} \tag{2.4}$$

The flowchart of the steps in extracting the two-particle correlation function is pictorially presented in Fig. 2.2.

2.2.1 Jets and ridge

Of the several sources of correlations contributing to the two-particle angular correlations, the two most significant sources that we are interested in for the studies included in this thesis are extracted by choosing appropriate $|\Delta\eta|$ region of the analysis. The "short-range" ($|\Delta\eta| \sim 0$) two-particle azimuthal angle correlations are dominated by high-p_T jets, produced back-to-back in hard QCD scattering. The jet correlations are reflected in $|\Delta\varphi|$ - distribution. The jet-induced per-trigger hadron-pair yields from the same jet populate at $|\Delta\varphi| = (|\varphi_{trigger} - \varphi_{assoc.}|) \sim 0$. The pair yields from away-side jets show up at $|\Delta\varphi| = (|\varphi_{trigger} - \varphi_{assoc.}|) \sim \pi$.

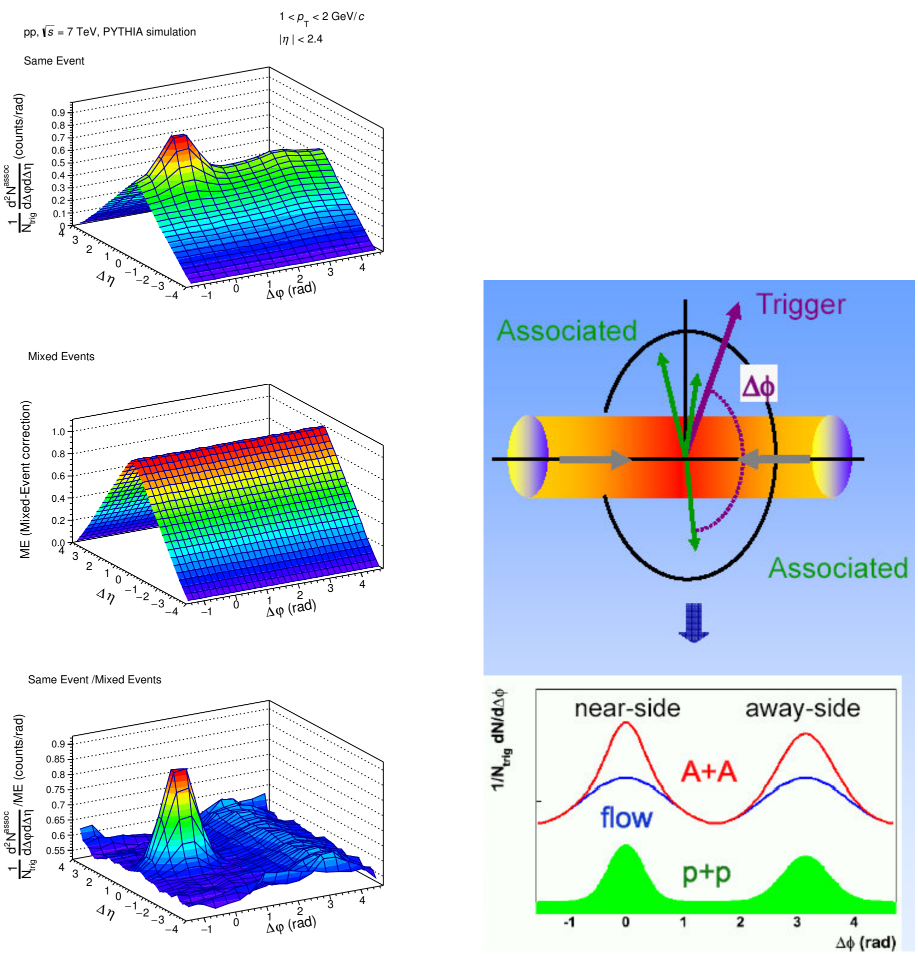

Figure 2.2: (Left) sample representation of $\Delta\eta, \Delta\varphi$ correlation distributions obtained via same-event, mixed-events and same/mixed-events. (Right) schematic diagram of 1-dimensional two-particle angular correlations projected on $\Delta\varphi$.

However, for the fragmentation process and several medium effects, the back-to-back short-range jet correlations get smeared, affecting the away-side structure. On the other hand, for the correlated emission of particles from collective medium, the two-particle azimuthal angle correlations in the "long-range" ($|\Delta\eta| \gg 0$) give rise to structure in both the near-side and the away-side. While the away-side structure may have contribution from correlations due to momentum conservation and other effects, the near-side structure of the two-particle azimuthal angle correlations in the long-range is considered to be free from other effects and attributed to the formation of collective medium.

In relativistic heavy-ion collisions, the per-trigger pair yields with small $|\Delta\varphi|$ over a wide range of $|\Delta\eta|$ (long-range), result a "ridge" structure in the constructed correlation functions. The "ridge" structure also appears in high-multiplicity pp [4–7] and pPb [8–11] collisions at the LHC. In the absence of medium formation, one does not expect significant structure in the near-side of the long-range two-particle angular correlation functions, as the jets and resonance decays contribute in the short-range only. The appearance of "ridge" is primarily a low p_T or soft-particle phenomenon. In the high-multiplicity pPb data [9], the "ridge" structure has been found to be most prominent in the $1<p_T<2$ GeV/c, while the structure diminishes in the higher p_T-range.

To obtain the near-side jet-like yield, the acceptance corrected correlation structure is projected on to the $\Delta\varphi$ axis for $|\Delta\eta| < 1.2$. The Background lying beneath the jet-like peak is modulated by flow correlations dominated by elliptic flow (v_2). In order to subtract the bulk correlations under the jet-peak, the projected $\Delta\varphi$ distributions at larger $\Delta\eta$ (> 1.2) region and subtracted from the short-range region without calculating different orders of flow harmonics and subtracting separately. Such a method of bulk subtraction from the jet peak, called **"η-gap"** method, is validated with the assumption of the correlations other than jet-like are η independent [12].

For the log-range correlations, the acceptance corrected 2-dimensional correlation is projected to $\Delta\varphi$ axis for large $\Delta\eta$ ($>$1.2). The baseline for calculating the correlated yield (jet-like or ridge-like) is evaluated by ZYAM (zero yield at minimum) [13] method or taking average of two or more points near the minimum. The near-side correlated yield above the baseline is calculated by the bincounting method over a range of $|\Delta\varphi| < \pi/2$ or $\pi/3$ of the 1-dimensional $\Delta\varphi$ distribution. It is worth discussing at this point that the calculation of yield above the baseline is very sensitive to the baseline-fluctuations.

2.3 Observations in heavy-ion collisions

The Fig. 2.3 (left) shows two-particle correlations in $\Delta\eta, \Delta\varphi$ as measured by ALICE in central $PbPb$ collisions with trigger $3 < p_{\mathrm{T}}(\mathrm{GeV}/c) < 4$ and associated particle $2 < p_{\mathrm{T}}(\mathrm{GeV}/c) < 2.5$. The near-side peak at $\Delta\varphi = 0$, reflects the near-side jets whereas almost no peak is seen at $\Delta\varphi = \pi$ indicating the suppression of away side jets due to the presence of the medium. The plot of the right panel of Fig. 2.3 shows the per-trigger correlation function $\hat{C}(\Delta\eta, \Delta\varphi)$ of di-hadron correlation as measured by STAR experiment at $\sqrt{s_{\mathrm{NN}}} = 200$ GeV in Au–Au collisions. With respect to pp

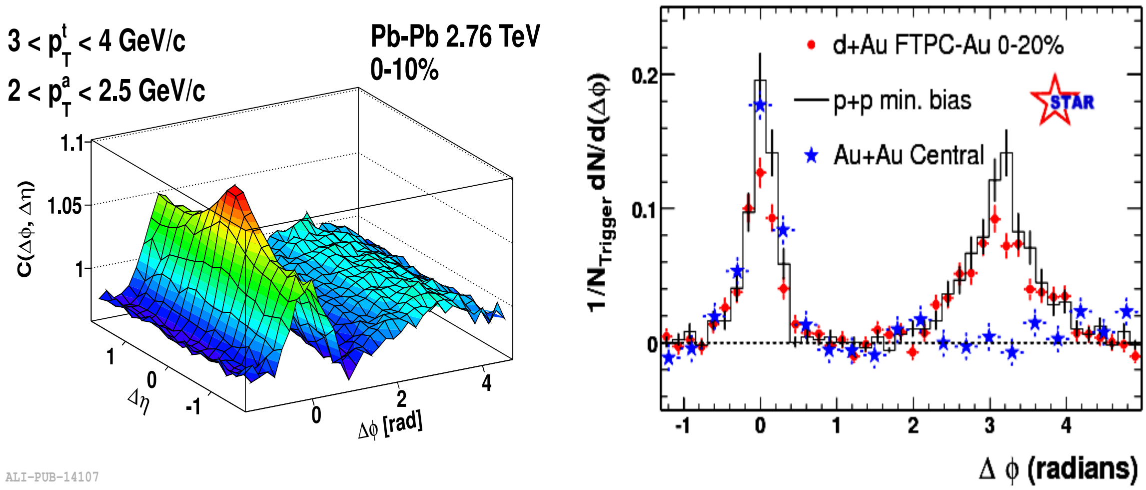

Figure 2.3: ALICE measurements of two-particle angular correlations in central $PbPb$ collisions at $\sqrt{s_{\rm NN}}$ = 2.76 TeV (left) [14]. Di-hadron azimuthal correlations ($\Delta\varphi$ distribution) measured by STAR in three collision systems pp, $AuAu$ and dAu (right) [15].

collisions, the away side peak is suppressed (the blue star points near $\Delta\varphi = \pi$) and this strong suppression is the experimental evidence of jet-quenching.

ALICE continued the di-hadron correlations study in different centrality with much harder trigger particles ($8 < p_{\rm T} <$16 GeV/c) in $PbPb$ collisions at $\sqrt{s_{\rm NN}}$ = 2.76 TeV. The associated particles are taken in the range of transverse momentum less than that of the trigger particle (4< $p_{\rm T}$ <6 GeV/c) [16]. The obtained $\Delta\varphi$ distributions are compared with pp collision. Figure 2.4 (top) shows the per-trigger $\Delta\varphi$ correlation distributions for most central (0-5%) and peripheral (60-90%) events. To measure the observable jet-suppression qualitatively, a variable called I_{AA} is defined as I_{AA}= $\mathrm{Y}_{PbPb}/\mathrm{Y}_{pp}$. The quantity $\mathrm{Y}_{PbPb\ OR\ pp}$ is the ratio of per-trigger yields in heavy-ion to pp. The bottom panel of Fig. 2.4 shows the variation of I_{AA} as a function of associated track $p_{\rm T}$ for the near-side and the away-side. In central

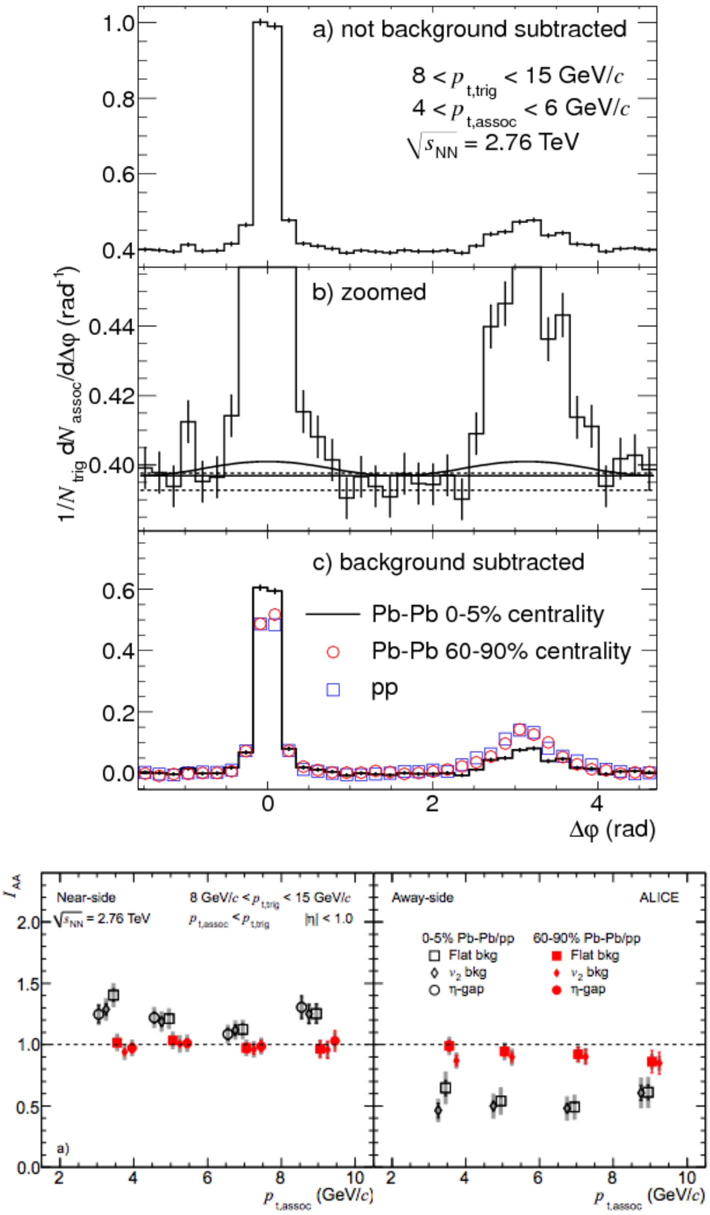

Figure 2.4: (top) Per-trigger corrected di-hadron azimuthal ($\Delta\varphi$) correlation distributions for $8 < p_{\mathrm{T}} < 15$ GeV$/c$ and $4 < p_{\mathrm{T}}^{assoc} < 6$ GeV$/c$ for central and peripheral *PbPb* events and *pp* events measured by the ALICE detector. a) azimuthal correlation; b) zoom on the region where the pedestal values (horizontal lines) and the v_2 component are indicated; c) background-subtracted $\Delta\varphi$ distributions using the flat pedestal. (bottom) I_{AA} for near-side (left panel) and away side (right panel) for most central (0-5% $PbPb/pp$) and peripheral (60-90% $PbPb/pp$) events measured by ALICE.

collisions, an away-side suppression ($I_{AA} \sim 0.6$) is observed whereas about 20–30% enhancement above unity is found in near-side. In away-side the suppression of I_{AA} corresponds to jet quenching. The increase of I_{AA} in near-side could be attributed to various factors, like a change in the fragmentation function, a possible change of the quark/gluon jet ratio in the final state due to their different coupling to the medium or a bias on the parton p_{T} spectrum after energy loss due to the trigger particle spectrum [16].

In the long-range (larger $\Delta\eta$ region), the collective expansion of the medium can be studied from the correlations function, which will present a modulation given by equation 2.5.

$$\hat{C}(\Delta\varphi) \propto 1 + \sum_{n\geq 2} v_n \; cos(n\Delta\varphi) \tag{2.5}$$

where v_n is the nth fourier expnasion coefficient for the associated and trigger particles. Such a modulation leads to the correlations in the long $\Delta\eta$ range, which appears in the 2-dimensional correlations as a ridge-like structure. In Fig. 2.5 a double ridge structure is clearly visible in the two-particle correlation distribution measured in *PbPb* collisions by the CMS Collaboration [17] in the intermediate-p_{T} range $1 < p_{\mathrm{T}} < 3$ GeV/c. In the near-side the jet correlation peak appears on top of the ridge structure while on the away-side the two effects are mixed along the $\Delta\eta$ range.

As already discussed, the two-particle angular correlation function has been thoroughly studied in extracting the correlation structures in *pp* and *pPb* collisions also. The short review on the results, particularly on the appearance of the long-range,

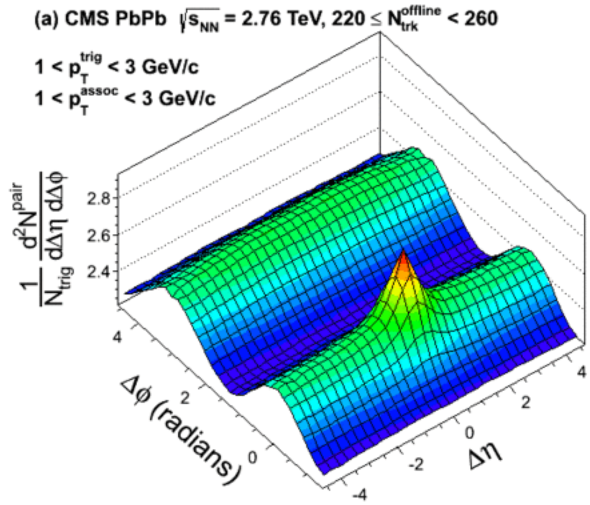

Figure 2.5: 2-dimensional two-particle angular correlation function for two unidentified hadrons in $PbPb$ collisions at the LHC, reported by the CMS Collaboration [17].

"ridge"-like structures in high-multiplicity events of pp and pPb collisions have been included in the section 1.4.

Bibliography

[1] XIANGRONG ZHU for the ALICE Collaboration, arXiv:1311.2394v2 [hep-ex].

[2] B. Abelev et al., ALICECollaboration, Phys. Lett. **B708**, 249-264 (2012).

[3] Lukasz Kamil Graczykowski for the ALICE Collaboration, Nuclear Physics **A926** 205-212 (2014).

[4] K. Fukushima and T. Hatsuda, Rept. Prog. Phys. **74**, 014001 (2011).

[5] K. Adcox et al., PHENIX Collaboration, Phys. Rev. Lett. **88**, 022301 (2002).

[6] Arneodo M, Phys. Rept. 240 301 (1994).

[7] B. Muller, J. Schukraft, and B. Wyslouch, Annu. Rev. Nucl. Part. Sci. **62**, 361 (2012).

[8] V. Khachatryan et al., CMS Collaboration, JHEP**09**, 091 (2010).

[9] G. Aad et al., ATLAS Collaboration, Phys. Rev. Lett. **116**, 172301 (2016).

[10] V. Khachatryan et al., CMS Collaboration, Phys. Rev. Lett. **116**, 172302 (2016).

[11] V. Khachatryan et al., CMS Collaboration, arXiv:1606.06198v1 [nucl-ex] (2016).

[12] X. Zhu for the ALICE Collaboration, arXiv:1311.2394 [hep-ex].

[13] Thomas A. Trainor, Phys. Rev. **C81**, 014905 (2010).

[14] K. Aamodt et al., ALICE Collaboration, Phys. Lett. **B708**, 249-264 (2012).

[15] J. Adams et al., STAR Collaboration, Phys. Rev Lett. **91** 072304 (2003).

[16] K. Aamodt et al., ALICE Collaboration, Phys. Rev. Lett. **108**, 092301 (2012).

[17] S. Chatrchyan et al., CMS Collaboration, Phys. Lett. **B724**, 213 (2013).

Chapter 3

Open Heavy-flavor as probe

Prior to the experiments at the LHC, the study of the QGP with heavy-flavor (HF) particles had been challenging due to lack of sufficient data. The increased production of the massive heavy-flavor (c and b) quarks and so the HF-mesons (D and B) with the available centre-of-mass energy at the LHC, has extended the scope of the study of the QGP. Because of the several favorable properties of HF-quark productions, their passages through QGP-like medium, the (Open) HF-mesons stand out as unique tools for studying the QGP. The majority of the analyses presented in this thesis deals with this unique probe. This chapter is dedicated to the discussion on HF mesons (particularly D mesons) as a probe to study the QGP. A short overview on the experimental activities and findings related to HF-mesons is also presented here.

3.1 Basics of heavy-flavour quarks and mesons

The basic properties of heavy quarks namely, charm (c), beauty (b) and top (t) along with other light quarks were discussed in chapter 1. Among different potential signatures to study the properties of QGP, already discussed in chapter 1, we saw the bound state of charm quark i.e. J/ψ ($c\bar{c}$) production plays significant role. Here we will see how open heavy-flavor acts as a pertinent candidate for probing such deconfined state of hot-dense medium formed in heavy-ion collisions. The same discussion will also be extended for small systems such as proton-proton (pp) and proton-lead (pPb) collisions. In this thesis we will discuss only about charm quark production and related measurements.

Due to their large masses ($m_c \sim 1.3$ GeV/c^2 and $m_b \sim 4.2$ GeV/c^2), heavy quarks are predominantly produced in the initial phase of the collision, unlike the light quarks, which can be produced from a thermal medium (QGP) produced after the collision. Therefore, they experience full evolution of the QGP medium and interact with its constituents and finally hadronize. This makes them a potential probe to study the QGP. Because of the large masses, cross section measurements of heavy quarks are possible using perturbative QCD (pQCD) calculations at LHC energies. The measurements of heavy-flavour production in pp collisions allow for precision tests of perturbative QCD (pQCD) calculations and provide an essential reference for understanding the results from heavy-ion collisions. Several cold nuclear matter (CNM) effects, such as the modification of parton distribution functions and momentum broadening due to parton scattering in the nucleus, can affect heavy quark production and can be accounted for by analysing pPb data. The results which will

Particle	Quark content	I(J^P)	Mass (GeV/c^2)	Decay mode	B.R.(%) hadronic channel	$c\tau$ (μm)
D^+	cd	$\frac{1}{2}(0^-)$	1.8696 ± 0.0002	$K^-\pi^+\pi^+$ and leptonic	9.13 ± 0.19	312 ± 2
D^0	$c\bar{u}$	$\frac{1}{2}(0^-)$	1.8648 ± 0.0001	$K^-\pi^+$ and leptonic	3.87 ± 0.05	123 ± 1
D_s^+	$c\bar{s}$	$0(0^-)$	1.9685 ± 0.0003	$\phi\,\pi^+$ and leptonic	4.5 ± 0.4	150 ± 2
D^{*+}	$c\bar{d}$	$\frac{1}{2}(0^-)$	2.0102 ± 0.0001	$D^0\pi^+$	67.7 ± 0.5	(2.1 ± 0.5)× 10^6
Λ_c	udc	$0(\frac{1}{2}^+)$	2.2865 ± 0.0001	p $K^-\pi^+$	5.0 ± 1.3	60 ± 2

Table 3.1: Properties of hadrons carrying charm quark [1].

be shown in this thesis are related to heavy-flavor studies, focusing on open charm quark measurements.

The study of observables related to heavy-flavor (charm quark) physics can be divided into two categories:

- **Open charm:** The hadrons in which charm or anti-charm quark binds with a light quark are shown in the table 3.1. For the hadronic decay modes, fully reconstructed charmed hadrons are analyzed by identifying the decay vertices and the decay products. Low branching ratios of such hadron decays require large statistics which is the main disadvantage of such studies. In this thesis azimuthal correlations between open charm hadrons (D mesons) with other charged particles will be presented.
- **Hidden charm:** This includes the charm anti-charm bound states (J/ψ, ψ', ψ'' etc.) and are reconstructed via their leptonic channels ($e^{\pm}$ or $\mu^{\pm}$). These hidden charm mesons are useful probes to study the QGP as mentioned

in chapter 1.

3.2 Heavy-flavor production in high energy collisions

As heavy quarks with large bare masses significantly exceed the QCD scale parameter ($\Lambda_{QCD} \sim 0.2$ GeV/c), the production of heavy quarks in ultra-relativistic pp collisions is exclusively through initial hard partonic scattering processes. Their inclusive production can be calculated using perturbative QCD extensively for all momenta since the large quark mass introduces a hard scale even at zero momentum. This is not possible for lighter quarks and gluons except at very high-p_{T}. The inclusive production of a high-p_{T} partons can be computed from the underlying parton-parton processes using the QCD "factorization theorem" with the parton distribution functions ($f_i^p|_i = q, \bar{q}, g$) of the initial protons. According to factorization theorem, at high energy the production cross section for a partonic process can be written as:

$$\begin{aligned}\frac{d\sigma^{NN\rightarrow H_Q X}}{dp_T}(\sqrt{s}_{NN}, M_Q, \mu_F^2, \mu_R^2) = \sum_{i,j=q,\bar{q},g} f_i(x_1, \mu_F^2) \\ \otimes f_j(x_2, \mu_F^2) \\ \otimes d\hat{\sigma}^{i,j\rightarrow Q\bar{Q}\{k\}}(\alpha_s(\mu_R^2)\mu_F^2, M_Q, x_1, x_2, s_{NN}) \\ \otimes D_Q^{H_Q}(z, \mu_F^2)\end{aligned} \tag{3.1}$$

where Q is the heavy quark (either charm or beauty), M_Q is its mass, and p_{T} is the transverse momentum. The sum runs over all possible sub-processes that lead to the heavy-flavour hadron and all the possible combinations of parton pairs participating in the hard scattering. The various terms of equation 5.1 are as follows:

- $d\hat{\sigma}^{i,j\rightarrow Q\bar{Q}}$: perturbative partonic cross section with x_i as the momentum fractions ($x = p_{parton}/p_{nucleon}$).
- $f_i(x_i, \mu_F^2)$: the parton distribution functions (PDFs), encoding the probability of finding a parton i of particular species with momentum fraction x_i inside the hadron.
- $D_Q^{H_Q}(z, \mu_F^2)$: the fragmentation function (FF), describing the probability that the outgoing parton Q fragments into a final hadron H_Q with fractional momentum z = p_{hadron}/p_{parton}.

The cross section is calculated as a power expansion of the strong coupling constant (α_s) using the leading order QCD processes. The lowest order calculation corresponds to the Leading Order (LO) $\mathcal{O}(\alpha_s^2)$ processes. There are several contributions from different heavy flavour production mechanisms to the total cross sections, dominated by the pair production (PP) processes. The pair production process is mostly dominated by $gg \rightarrow Q\bar{Q}$ as shown in Fig. 3.1. There are other Next-to-Leading Order (NLO $\mathcal{O}(\alpha_s^3)$) perturbative processes including gluon splitting (GS) and flavour excitation (FE) as shown in the Fig. 3.1 that can contribute to heavy quark production. A Next-to-Leading order (NLO) process includes more complicated topologies.

The complete calculation only exists up to NLO as the corrections above NLO

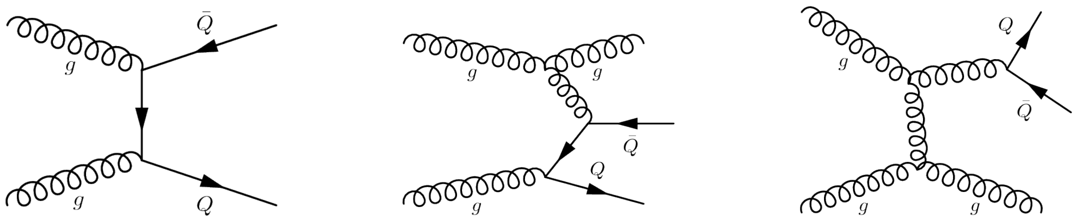

Figure 3.1: Feynman diagrams of pair creation (left), flavour excitation (middle) and gluon splitting (right) [2].

are expected to be small due to large mass (m_Q) of heavy quarks. Renormalization processes are used to remove ultraviolet divergences. Real emission by final state heavy quarks is collinear-safe since the quark mass value prevents gluon emission at small angles. But when the transverse momentum (p_{T}) of the heavy quark is much larger than its mass, large logarithms of the ratio p_{T}/m breaks its convergence which gives rise to all orders in the perturbative expansion of the cross section. Theoretical framework has been advanced to take into account the higher order corrections in perturbative calculations which are; the **FONLL (Fixed Order Next to Leading Log)** calculation [3] and **General-Mass Varaible-Flavour-Number Scheme (GM-VFNS)** [4].

3.2.1 Experimental results in pp ($\bar{p}$) from CDF to LHC

Heavy quark production has been studied at the Tevatron at $\sqrt{s_{\mathrm{NN}}}$ = 1.96 TeV by the CDF and D0 experiments. In 2003, the CDF Collaboration published the measurements of the differential cross sections for the production of charmed mesons as a function of the transverse momentum for $p_{\mathrm{T}} \geq 5.5$ GeV/c at $\sqrt{s} = 1.96$ TeV [5]. Figure 3.2 shows CDF differential cross section measurements for the mesons of the D family [6].

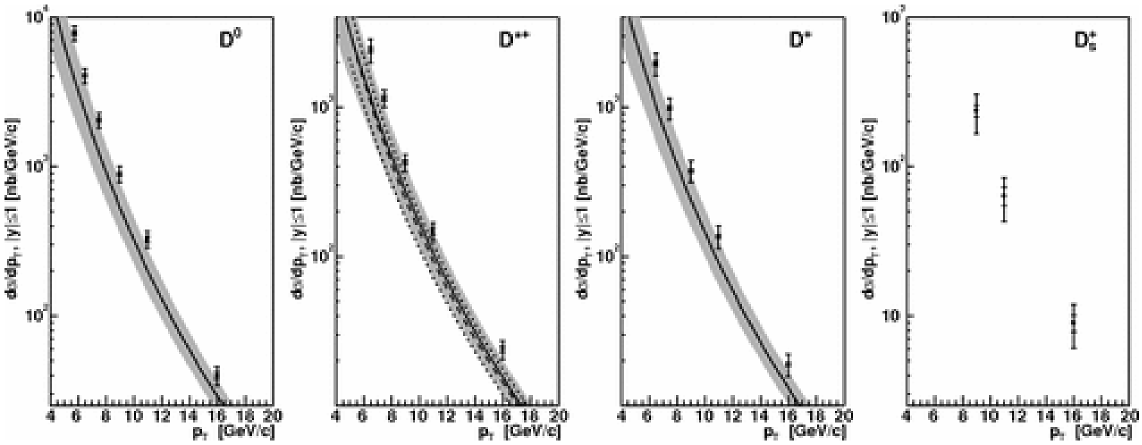

Figure 3.2: The differential cross section measurements for different D mesons at $\sqrt{s}$ = 1.96 TeV at CDF II. The solid and dashed curves represent the theoretical predictions from Cacciari and Nason [7] and the shaded bands indicate uncertainties [5]. For the D_s^+ production there is no theoretical prediction.

The measurements are compared with FONLL and GM-VFNS calculations. The uncertainties are evaluated by varying independently the renormalization and factorization scales. The measured differential cross sections are higher than the theoretical predictions by about 100% at low-p_{T} and 50% at high-p_{T}, though within uncertainty bars, they are in agreement [7]. Figure 3.3 shows the STAR measurements on the charm hadron production cross sections in pp at $\sqrt{s}$ = 200 GeV. Production cross sections are scaled to $c\bar{c}$ pairs and are compared to pQCD FONLL calculation. Measurements are consistent with the upper bound of the FONLL pQCD calculation.

The left panel of Fig. 3.4 shows ALICE measurement on prompt D^0 mesons differential cross section in the p_{T} range $1< p_{\mathrm{T}} < 16\mathrm{GeV}/c$ in pp collisions at $\sqrt{s}$ = 7 TeV. The measured cross section is compared with pQCD calculations such as FONLL [3], GM-VFNS [4] and k_T-factorization at LO [11]. The data are at the

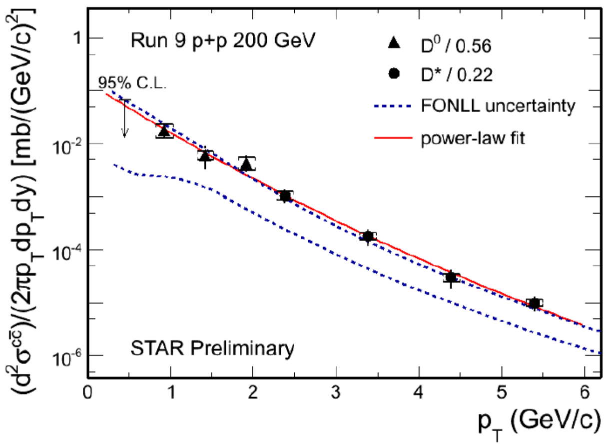

Figure 3.3: $p_{\rm T}$-differential charm hadron ($\rm D^0$ and $\rm D^*$) production cross section in pp collisions at $\sqrt{s_{\rm NN}} = 200$ GeV at STAR [8].

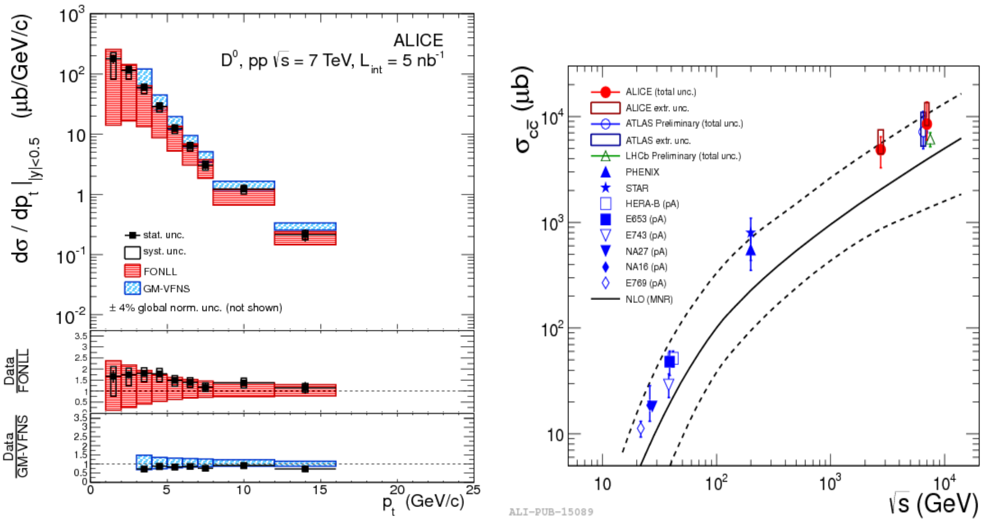

Figure 3.4: (Left) $p_{\rm T}$-differential cross section of prompt $\rm D^0$ mesons in pp collisions at $\sqrt{s} = 7$ TeV, compared with theoretical calculations. (Right) Total charm cross section measured in pp collisions by ALICE as a function of $\sqrt{s}$, in comparison with other experimental results and MNR calculations [9, 10].

upper edge of the uncertainty band for FONLL and k_T-factorization model, but at the lower edge for GM-VFNS.

The total $c\bar{c}$ cross sections are extracted by extrapolating the measured cross sections for pp collisions at $\sqrt{s} = 7$ TeV and 2.76 TeV. The extrapolated results are shown in right panel of Fig. 3.4 along with the results from other experiments and a Next-to-Leading-Order pQCD calculation (MNR). The ALICE result at $\sqrt{s} = 7$ TeV is in agreement with results from the ATLAS [12] and LHCb [13] Collaborations. Both of the ALICE points follow the trend exhibited by the NLO predictions.

3.3 Heavy-flavour in heavy-ion collisions

It has been already mentioned that heavy-flavour particles are effective tool to study the properties of heavy-ion collisions. The production of a heavy quark-antiquark pair (minimum energy $Q_{min} = 2m_Q$) implies a space-time scale in the order of $1/(2m_Q) \sim 0.1$ fm/c for charm (0.02 fm/c for beauty), which is much lower than the expected lifetime of the QGP. This allows us to investigate the charm quark production mechanism and in-medium propagation in heavy-ion collisions.

- They are produced in partonic hard-scatterings as described in pp collisions with large virtuality Q (momentum transfer) unaffected by the properties of the medium. Due to the large virtuality via the hard initial scattering, the production cross sections can be reliably calculated with the perturbative approach for heavy-ion collisions.

- From the equation 5.1 we can say that in heavy-ion collisions the PDFs are, in general, modified due to the nuclear environment. The high virtuality pQCD processes are not affected but the fragmentation functions of the heavy quarks change due to the presence of a QCD medium. Also, there will be interactions of heavy quarks with the medium constituents.

Therefore, we can divide the phenomena influencing heavy-flavour production in heavy-ion collisions in two categories: **Initial state effects or the Cold Nuclear Matter Effects** and **Hot Medium Effects**. Cold Nuclear Matter Effects occur due to presence of "cold" nuclei where the PDFs in nuclei differ from those in free nucleons and influence the heavy quark production kinematic. A general overview of Cold Nuclear Matter Effects are already discussed in chapter 1. Hot Medium Effects are those due to QGP formation after the collisions and they influence the heavy quarks before hadronization. These effects will be discussed in the following sections.

3.3.1 The QGP medium effect on HF

When the heavy quarks pass through the QCD medium, their interactions with the medium constituents modify their dynamical properties. These effects include the parton energy loss inside the medium and thermalization. As already discussed in chapter chapter 1, nuclear modification factor (R_{AA}) is the main observable to study the energy loss of "hard probes" i.e. jets and high-p_{T} hadrons. R_{AA} gives the comparative study of energy loss in heavy-ion and pp collisions for heavy quarks which are produced well before the formation of the medium.

In general, the energy loss (ΔE) of a particle inside the hot medium depends on the medium properties, like temperature (T), particle-medium interaction coupling, thickness (L) and on the characteristics of the particle (energy E, mass m, and charge q). The energy loss experienced by a hard parton depends on the following factors:

- The mean free path $\lambda = 1/(\rho\sigma)$ where ρ is the medium density and σ the integrated cross section of the interaction for the particle in the medium.
- The opacity N = L/λ, or the average number of scatterings experienced by the particle in a medium of thickness L.
- The Debye mass $m_D(T) \sim g_T$ (where g is the coupling parameter) which is the inverse of the screening length of the field in the plasma. m_D is the momenta exchanged between the probe and the medium.
- The transport co-efficient $\hat{q} \equiv m_D^2/\lambda \equiv m_D^2\rho\sigma$ which is the scattering power of the medium linking the thermodynamical and dynamical properties of the medium.
- The diffusion constant D which is related to the momentum drag and diffusion coefficients and is important for heavy non-relativistic particles.

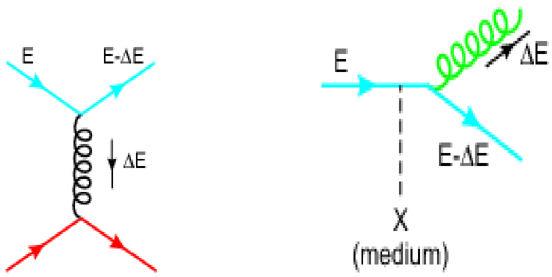

Figure 3.5: Collisional (left) and medium-induced radiative (right) energy loss mechanisms of a quark of energy E traversing in a quark medium and loosing a fraction of energy ΔE [14].

Heavy quarks lose their energy via two processes: induced gluon radiation and elastic collisions via multiple scatterings with other partons inside the medium. The total energy loss is the sum of these two processes ($\Delta E = \Delta E_{coll} + \Delta E_{rad}$) as shown in the Fig. 3.5.

3.3.1.1 Collisional Energy Loss

The collisional energy loss is due to the elastic scatterings of heavy quarks with the medium constituents and it dominates at low-p_{T}. The quantitative calculations were first executed by J. D. Bjorken [15] and a similar formalism was carried out by Peigne in [16].

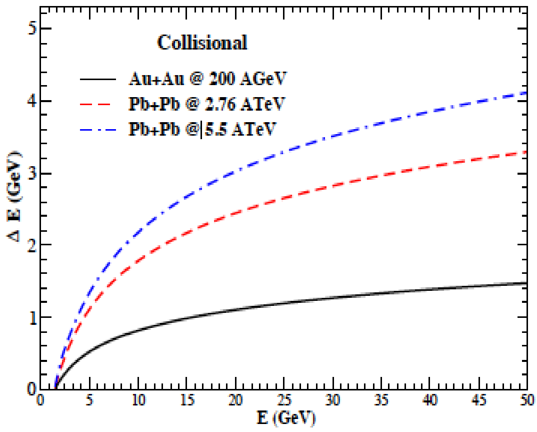

Figure 3.6: Collisional energy loss of charm quark in $PbPb$ collision at $\sqrt{s_{\mathrm{NN}}} = 2.76$ ATeV and 5.5 ATeV at LHC, and 200 AGeV at RHIC [17].

The collisional energy loss is linear with the medium thickness (L) and it depends only logarithmically on the initial parton energy (E). Figure 3.6 shows a theoretical comparison of collisional energy loss of charm quark with medium constituents as calculated by Peigne and Peshier in [16] for RHIC and LHC energies. It seems that the collisional energy loss increases with the increase in centre-of-mass energy.

3.3.1.2 Medium-induced radiative energy loss

Radiative energy loss is due to the inelastic scatterings within the medium and is the most important mechanism of energy loss at higher momenta of partons. This process is analogous to the QED brehmstrahlung i.e., photon emission by an accelerated or decelerated charged particle. That is why it is often called gluon-bremsstrahlung or "gluonstrahlung". When an energetic parton radiates a gluon in the dense QCD medium, the emitted gluon suffers multiple scatterings in a Brownian-like motion with mean free path which decreases as the medium density increases. To estimate the shape of the radiated energy distribution, let us consider that the total number of scattering centres participate coherently to emit the gluon with a given energy. Therefore, at each scattering centre, the standard Bethe-Heitler energy spectrum per unit length gets suppressed. Considering all the scattering centres, we get the average energy loss of the initial parton as discussed in [18]:

$$< \Delta E > \quad \propto \alpha_s C_R \hat{q} L^2 \tag{3.2}$$

Therefore, the average energy loss is proportional to QCD coupling constant (α_s), transport coefficient of the medium ($\hat{q}$), square of the path length traversed (L^2) and colour charge of the parton projectile (C_R, which is 4/3 for quarks, 3 for gluons). From the equation 3.2 we can also see that the average radiated energy loss is independent of the parton initial energy. In general, many model calculations of parton energy loss do not show any dependence on initial energy [19–22]. Other models [23, 24] show explicit dependence of ΔE on the initial energy E assuming that the former cannot be larger than the latter i.e. $\Delta E \leq E$.

Dead cone effect for heavy quarks

It has been studied [25, 26] that due to their large masses, the induced radiative energy loss is lower for heavy quarks compared to light quarks. As a result, the vacuum gluon radiation at a forward angle $\theta < \theta_0$ where $\theta = \frac{M_Q}{E_Q}$ is suppressed by a factor $\left[1 + \frac{\theta_0^2}{\theta^2}\right]^{-2}$ due to destructive interference [25]. This is known as the dead cone effect (Fig. 3.7).

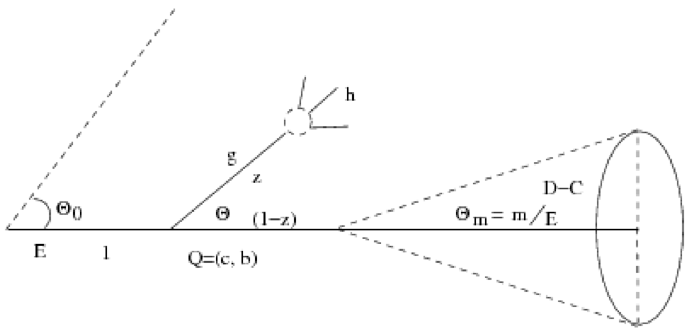

Figure 3.7: schematic diagram of dead cone effect for heavy quark [27].

The energy distribution of the radiated gluons is given by:

$$\frac{dI}{d\omega}_{heavy} \Big/ \frac{dI}{d\omega}_{light} = \left(1+\frac{\theta_0^2}{\theta^2}\right)^{-2} = \left[1+(\frac{m_Q}{E})^2\sqrt{\frac{\omega^3}{\hat{q}}}\right]^{-2} \equiv F_{H/L}(m_Q, E, \hat{q}, \omega) \quad (3.3)$$

where θ is the characteristic angle. The heavy-to-light suppression factor $F_{H/L}$ increases (less suppression) as the heavy quark energy increases (the mass becomes negligible).

Fig. 3.8 (Left) shows the suppression factor for charm quarks as a function of x $= \omega/\omega_c$, where ω_c is the characteristic gluon frequency for different transport coefficients, i.e. different medium densities. The factor $F_{H/L}(\mathrm{x})$ can be interpreted as the decrease of the probability for emitting a gluon with energy E. $F_{H/L}$ decreases at large x, for a given $\hat{q}$ and p_{T} of the charm quark. This indicates that the high energy part of the gluon radiation spectrum is drastically suppressed by the dead cone effect. Right panel of Fig. 3.8 shows an estimate of the average energy loss of charm quarks as a function of their initial energy separating the collisional and radiative contributions. The consequence of the dead cone effect on heavy quarks implies $\Delta E_g > \Delta E_{u,d,s} > \Delta E_c > \Delta E_b$ and experimentally we can expect the nuclear modification factor to be: $R_{\mathrm{AA}}(b) > R_{\mathrm{AA}}(c) > R_{\mathrm{AA}}(g,u,d,s)$ [29].

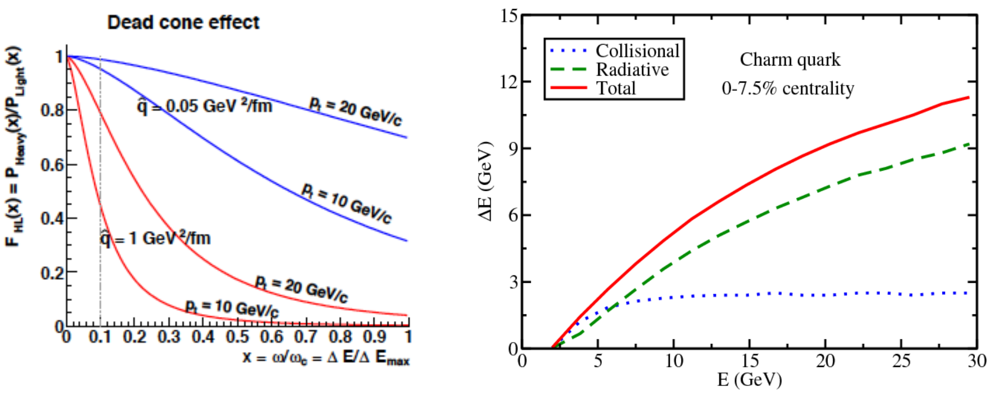

Figure 3.8: (Left) Suppression factor for a charm quark as a function of x $= \omega/\omega_c$ where ω_c is the characteristic gluon frequency. The in-medium path length is considered as L = 5 fm. (Right) Energy loss of charm quarks as a function of charm quark initial energy [28].

3.3.2 Experimental results from heavy-ion data

Left panel of the Fig. 3.9 shows the non-photonic electron R_{AA} vs p_{T} and elliptic flow as measured by PHENIX experiment at $\sqrt{s_{\mathrm{NN}}} = 200$ GeV. The heavy-flavor production at high-p_{T} exhibits a large suppression with respect to the binary scaled cross sections in pp collisions which give the indication of heavy quark energy loss when traversing the medium. A large elliptic flow v_2 is observed for intermediate-p_{T} for heavy quarks as shown in the bottom of the left panel. This shows possible thermalisation of heavy quarks at intermediate-p_{T}.

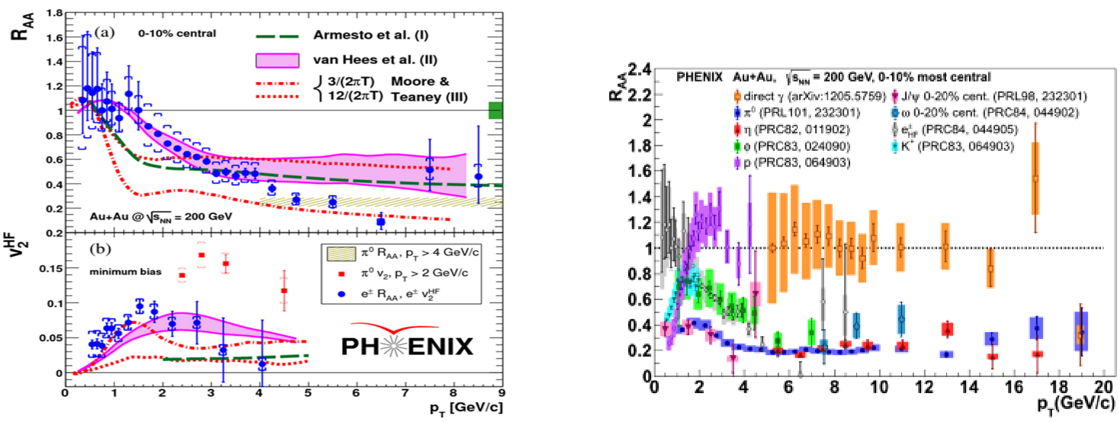

Figure 3.9: (Left) Heavy-flavor electron nuclear modification factor (R_{AA}) and elliptic flow (v_2) measured by PHENIX in $AuAu$ collisions at RHIC [30]. (Right) R_{AA} for baryons, strange mesons, electrons from heavy-flavor, light quark mesons and direct photons measured by PHENIX in 0-10% most central $AuAu$ collisions at $\sqrt{s_{\mathrm{NN}}} = 200$ GeV [31].

Right panel of Fig. 3.9 shows PHENIX R_{AA} measurement for identified particles at $\sqrt{s_{\mathrm{NN}}} = 200$ GeV. The results show an interesting hierarchy in the suppression pattern for different particles at low-p_{T}. Light quark mesons show the largest suppression whereas electrons from heavy-flavor show intermediate suppression. This obeys the energy loss mechanism for different quarks. At very high-p_{T} all the particles show similar suppression.

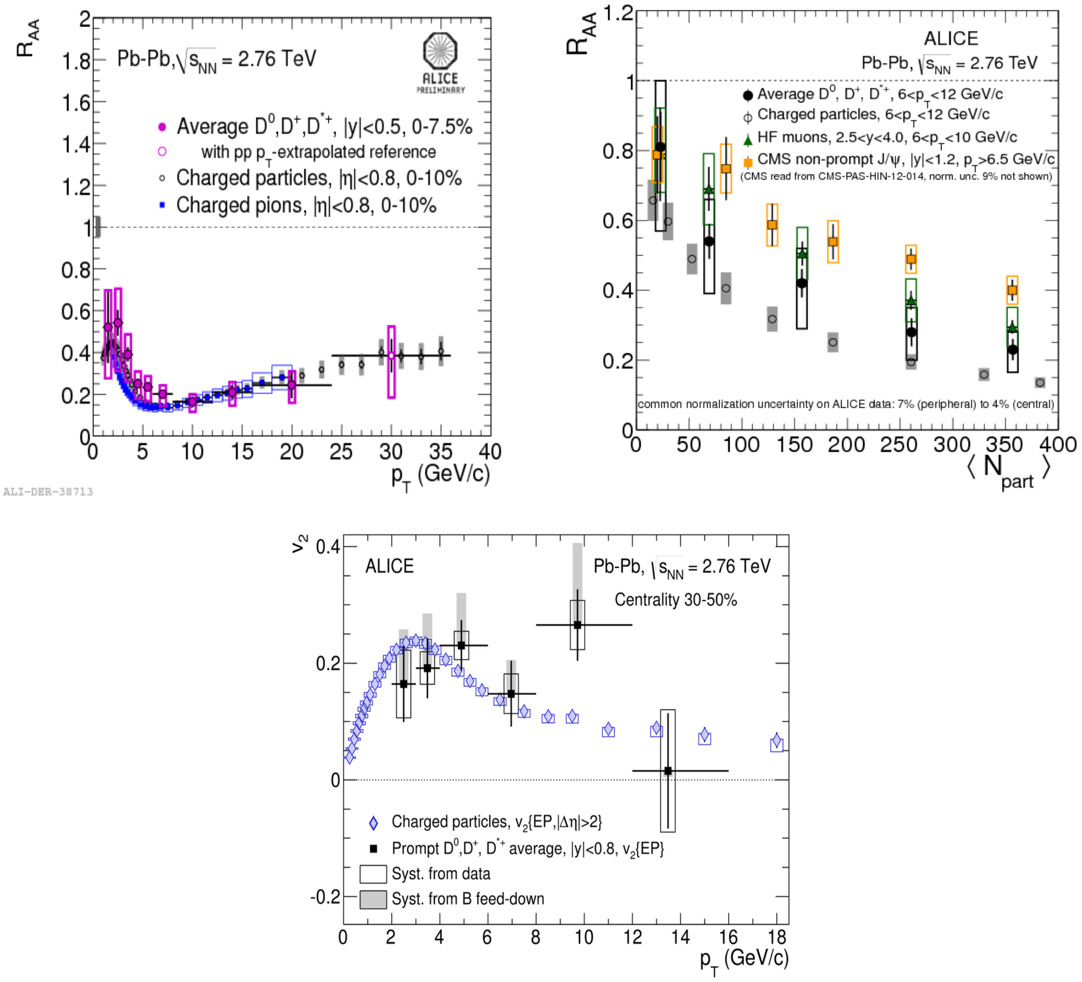

Figure 3.10: (top-left) $R_{\mathrm{AA}}(p_{\mathrm{T}})$ for average prompt D mesons (color circles), charged particles (color circles), and charged pions (color squares) in the most central event class [32]. (top-right) Centrality dependent R_{AA} for the heavy-flavor decay muons (color triangles), the average prompt D mesons (color filled circles), charged particles (empty circles) and non-prompt J/ψ from CMS [33]. Average D^0, D$^+$ and D^{*+} v_2 as a function of p_{T}, compared to charged particle v_2 [35, 36] measured by ALICE using the event-plane (EP) method.

The ALICE and CMS experiments at CERN have also measured the nuclear suppression factor at different p_{T} of charged particles at much higher energy than RHIC. The left panel of Fig. 3.10 shows ALICE measurements of R_{AA} for D mesons, charge particles and pions. It has been mentioned in [32] that within the uncertainties, both light and heavy-flavor measurements are compatible in a large p_{T} range. In the right panel of the same figure, we see prompt D mesons and heavy-flavor decay muons present a similar R_{AA} magnitude and centrality dependence with a caveat of different rapidity range. CMS has measured non-prompt J/ψ [33] in the same centrality class and it is found to be consistent with that of heavy-flavor decay muons. A large elliptic flow v_2 is observed for intermediate-p_{T} (< 6 GeV/c)for average D mesons (bottom panel of Fig. 3.10). It is comparable in magnitude to that of charged particles, dominated by the light-flavour hadrons. The result indicates that the interactions with the medium constituents transfer to charm quarks information on the azimuthal anisotropy of the system, suggesting that low momentum charm quarks take part in the collective motion of the system [34].

The measurements of angular correlation between D mesons (i.e. $\mathrm{D}-\bar{\mathrm{D}}$) was useful at RHIC energies. Though D mesons, both as trigger and associated particles, would give a good outlook at the heavy quark energy loss in a QCD medium, it suffers from combinatorial background of D mesons in data as well as for the reconstruction efficiency. The left panel of Fig. 3.11 shows theoretical calculation of angular correlations between $c\bar{c}$ pairs after they traverse a realistic QGP medium created in central $AuAu$ collisions at RHIC with LO pQCD initialisation for back-to-back production. This shows that the final $c\bar{c}$ correlations peak at $\Delta\varphi = \pi$ if only radiative energy loss of charm quark is included. This implies that the angular correlations of charm quark pairs provide a possibility to distinguish different energy loss mechanisms. The right panel of the same figure shows angular correlations between $D - \bar{D}$ pairs in $AuAu$ collisions at $\sqrt{s_{NN}} = 200$ GeV using PYTHIA 8 simulations keeping the same parameter setting of STAR data [38] with trigger p_T cut of 2 GeV/c. Similar to the $c\bar{c}$ correlations, purely radiative energy loss does not

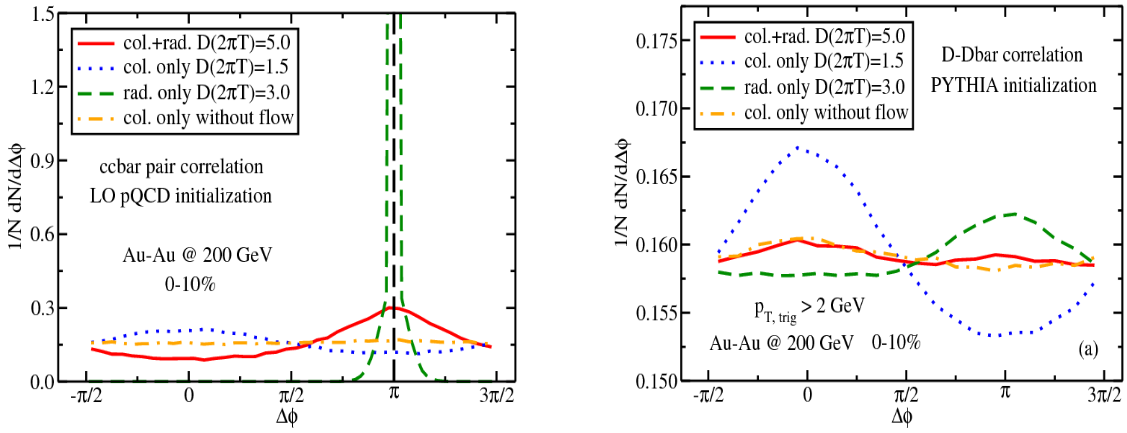

Figure 3.11: (Left) Angular correlations of $c\bar{c}$ pairs with LO pQCD approximation, used for $c\bar{c}$ pair initialization in central $AuAu$ collisions. (Right) D-$\bar{D}$ angular correlations in central $AuAu$ collisions at RHIC [37].

strongly affect the angular correlations of $D - \bar{D}$ pairs. The suppression of the the away-side peak [37] is caused purely due to collisional energy loss.

The Fig. 3.12 (left) shows the measurements the azimuthal correlation between heavy-flavour decay electrons and charged hadrons in $AuAu$ collisions at $\sqrt{s_{NN}} =$ 200 GeV and compared with pp collisions by PHENIX experiment at RHIC. The right panel of Fig. 3.12 describes the ratio of particle yield on the near-side, obtained in $AuAu$ to pp collisions as a function of the associated hadron p_T for e-h and h-h correlations [39]. The I_{AA} (as defined in chapter 2) for e-h correlations is found to be consistent with h-h correlations within the measured uncertainties.

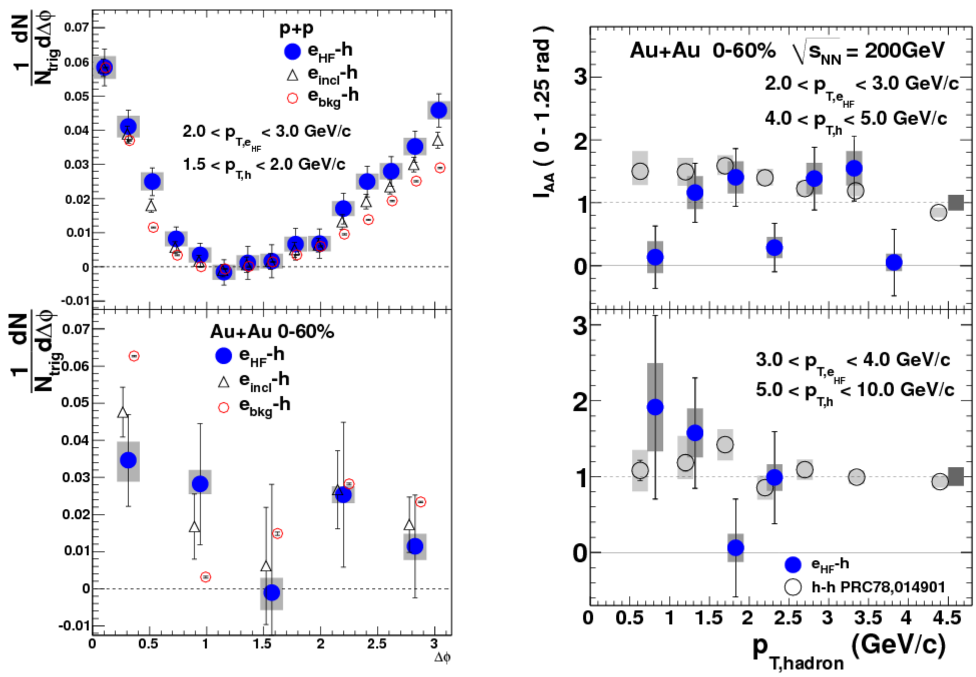

Figure 3.12: (Left) Azimuthal correlation distributions for heavy-flavour decay electrons and charged hadrons in pp (top panel) and $AuAu$ (bottom panel) collisions at $\sqrt{s_{\mathrm{NN}}} = 200$ GeV measured by the PHENIX experiment. (Right) The near-side I_{AA} for $2 < p_T^e < 3.0$ GeV/c (top panel) and $3 < p_T^e < 4.0$ GeV/c (bottom panel) as a function of the associated hadron p_{T} for heavy-flavour decay electron (solid points) and hadron (open points) triggers in $AuAu$ collisions at $\sqrt{s_{\mathrm{NN}}} = 200$ GeV measured by the PHENIX experiment [40].

3.4 Heavy-flavour in pPb

A general overview of different CNM effects are already discussed in chapter 1. Here we will briefly show some results from pA collisions using HF particles as probes.

3.4.1 Results: Initial state effects on Heavy-flavor

Left panel of Fig. 3.13 shows nuclear modification factor (R_{dA}) as a function of p_{T} for heavy-flavor decay electrons in the most central (top) and most peripheral (bottom) centrality classes measured at mid-rapidity in dAu collisions at $\sqrt{s_{\mathrm{NN}}}$= 200 GeV by PHENIX experiment at RHIC. At intermediate-p_{T} the nuclear modification factor shows a clear enhancement over unity in central collisions whereas no modification is seen in peripheral collisions. Right panel of Fig. 3.13 shows the same results for min-bias events at a much higher energy $\sqrt{s_{\mathrm{NN}}}$ = 5.02 TeV measured by ALICE.

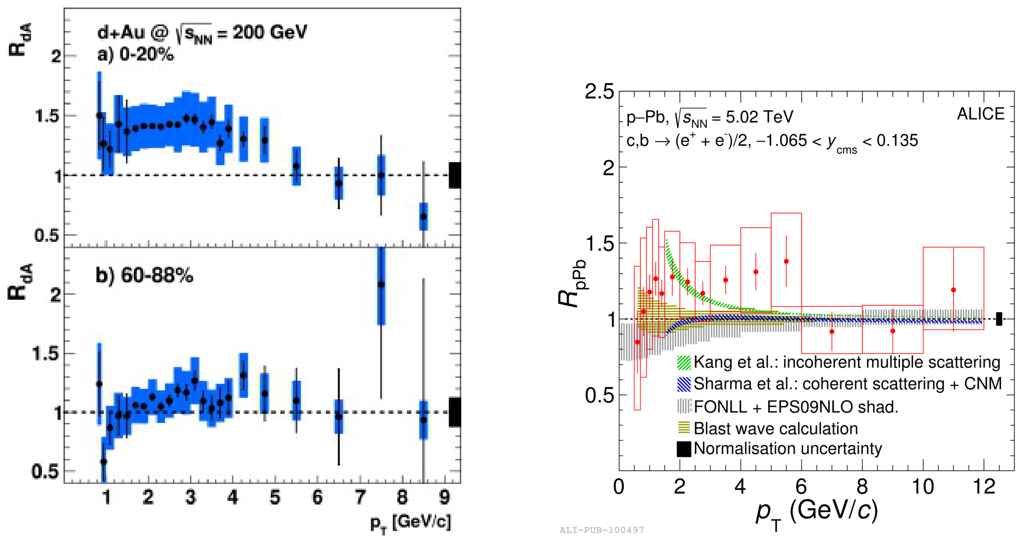

Figure 3.13: (Left) PHENIX measures the nuclear modification factor in dAu collisions, R_{dA} as a function of p_{T} of heavy-flavor electrons at mid-rapidity in different centrality classes [42]. (Right) ALICE measures R_{pPb} as a function of p_{T} of heavy-flavour electrons from hadron decays for minimum-bias pPb collisions at $\sqrt{s_{\mathrm{NN}}}$ = 5.02 TeV, compared with theoretical models [41].

It has been mentioned in [41] that the R_{pPb} is consistent with unity within uncertainties over the whole p_{T} range of the measurement. Hence, the pA result on nuclear

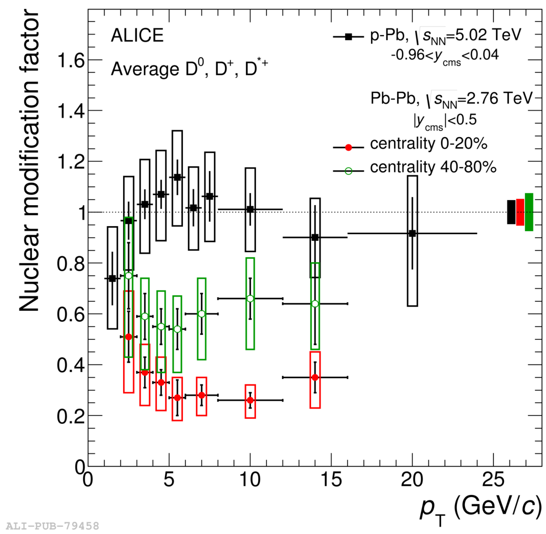

Figure 3.14: Comparison of nuclear modification factors (R_{AA} and R_{pPb}) as a function of p_T for D meson production in minimum-bias pPb collisions and in two different centrality classes in $PbPb$ collisions by ALICE [43].

modification factor suggests that the suppression of yields in $PbPb$ collisions at high-p_T is due to final state effect induced by the hot medium. The data are compared with different theoretical calculations but the uncertainties of the measurement do not allow to discriminate among the theoretical approaches.

Figure 3.14 shows the comparison of the average nuclear modification factor for D mesons (D^0, D^+, D^{*+}) in central (0-20%) and in semiperipheral (40%-80%) $PbPb$ collisions at $\sqrt{s_{NN}} = 2.76$ TeV with the average R_{pPb} of prompt D mesons in pPb collisions at $\sqrt{s_{NN}} = 5.02$ TeV by ALICE experiment at LHC. The interpretation from the comparison infers that the cold nuclear matter effects are smaller than the uncertainties for $p_T \geq 3\text{GeV}/c$ [43]. Therefore, from different experimental results (from Fermilab to LHC), the cold nuclear matter effects are studied extensively and it not straight forward to incorporate them in heavy-ion study. The initial state

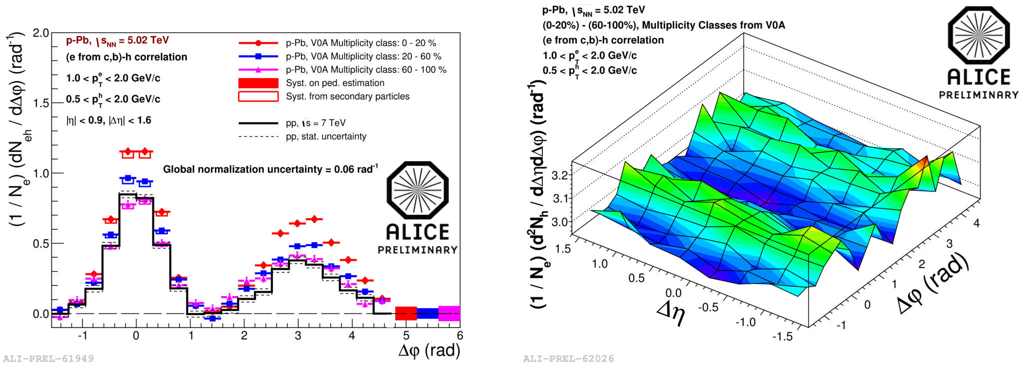

Figure 3.15: Angular correlations between HF-electrons and hadrons in 3 multiplicity classes in pPb collisions compared to minimum-bias pp events (Left). 2-dimensional $(\Delta\eta, \Delta\varphi)$ correlation in pPb collisions after subtraction of the lowest multiplicity class from the highest multiplicity class by ALICE [44] (Right).

effects are not very strong in higher collisional energy as shown by ALICE at $\sqrt{s} =$ 5.02 TeV but are prominent at RHIC energy. Different theoretical calculations also support the experimental results in the measured p_{T} range.

ALICE at the LHC measures the angular correlations in pPb collisions at $\sqrt{s_{\mathrm{NN}}} =$ 5.02 TeV between HF decay electrons and charged hadrons. The angular correlation between trigger particles (HF decay electrons) and associated particles (charged hadrons), performed in three multiplicity classes and compared to pp minimum bias results is shown in the left panel of Fig. 3.15. The highest multiplicity class (0-20%) presents a stronger correlation than the one observed in the multiplicity class 60-100%, which is compatible with pp results [44]. In the right panel of Fig. 3.15, the low-multiplicity correlation is subtracted from the high-multiplicity one, showing a double-ridge structure as observed in hadron-hadron (h-h) correlations [45]. This structure can be interpreted in terms of the hydrodynamical evolution of the system, as well as initial conditions originating from CGC.

Bibliography

[1] K. Nakamura et al., (Particle Data Group), J. Phys. G: Nucl. Part. Phys. **37**, 075021 (2010).

[2] D Souza and N H Brook, J.Phys. **G43**, no.1, 015001 (2016).

[3] M. Cacciari, M. Greco and P. Nason, JHEP**05**, 007 (1998).

[4] B. A. Kniehl et al., Phys. Rev. Lett. **96**, 012001 (2006).

[5] D. Acosta et al., CDF Collaboration, Phys. Rev. Lett. **91**, 241804 (2003).

[6] Thesis by Luigi Marchese, Matr. N94000097, Anno Accademico 2012 -2013.

[7] Matteo Cacciari, Paolo Nason, JHEP**09**, 006 (2003).

[8] Wei Xie for the STAR Collaboration, Pos (DIS 2010)182.

[9] Mangano M, Nason P, and Ridolfi, G Nucl. Phys. **B373**, 295 (1992).

[10] Chitrasen Jena, for the ALICE Collaboration, J. Phys.: Conf. Ser. 535, 012027 (2014).

[11] Maciula R and Szczurek A, Phys. Rev. **D87**, 094022 (2013).

[12] ATLAS Collaboration 2011 ATLAS-CONF-2011-017.

[13] LHCb Collaboration 2010 LHCb-CONF-2010-013.

[14] Rajeev S. Bhalerao, Conference Proceedings, arXiv:1404.3294 [nucl-th].

[15] J. D. Bjorken, FERMILAB-PUB-82-59-THY.

[16] Stephane Peigne, Andre Peshier, Phys. Rev. **D77**, 114017 (2008).

[17] Raktim Abir et. al., Phys. Lett. **B715**, 183-189 (2012).

[18] Carlos A. Salgado and Urs Achim Wiedemann, Phys. Rev. **D68**, 014008 (2003).

[19] M. Gyulassy and X.N. Wang, Nucl. Phys. **B420**, 583 (1994).

[20] B. G. Zakharov, JETP Lett. **63**, 952 (1996).

[21] U. A. Wiedemann, Nucl. Phys. **B588**, 303 (2000).

[22] M. Gyulassy, P. Levai and I. Vitev, Nucl. Phys. **B594**, 371 (2001).

[23] M. Gyulassy and X. N. Wang, Nucl. Phys. **B420**, 583 (1994).

[24] U. A. Wiedemann, Nucl. Phys. **A690**, 731 (2001).

[25] Yu. L. Dokshitzer, D. E. Kharzeev, Phys. Lett. **B519**, 199-206, (2001).

[26] M. G. Mustafa et al., Phys. Lett. **B428**, 234 (1998).

[27] Redamy Perez Ramos (IFIC) et al., JHEP**08**, 047 (2010).

[28] Cao, Qin, Bass, Phys. Rev. **C88**, 044907 (2013).

[29] N. Armesto et al., Phys. Rev. **D71**, 054027 (2005).

[30] Hugo Pereira Da Costa, arXiv:0908.3178v3 [nucl-ex].

[31] Ralf Rapp and Hendrik van Hees, arXiv:0803.0901v2 [hep-ph].

[32] B. Abelev et al., ALICE Collaboration, Phys. Lett. **B720**, 52-62 (2013).

[33] S. Chatrchyan et al., CMS Collaboration, JHEP**05**, 063 (2012).

[34] B. Abelev et al., ALICE Collaboration, Phys. Rev Lett. **111** 102301 (2013).

[35] Zaida Conesa del Valle, for the ALICE Collaboration, Nuclear Physics A 904-905 (2013) .

[36] B. Abelev et al., ALICE Collaboration, Physics Letters **B719**, 18-28 (2013).

[37] Shanshan Cao, Guang-You Qin, and Steffen A. Bass, Phys. Rev. **C92**, 054909 (2015).

[38] L. Adamczyk et al., STAR Collaboration, Phys. Rev. **D86**, 072013 (2012).

[39] A. Adare et al., PHENIX Collaboration, Phys. Rev. **C78**, 014901 (2008).

[40] A. Adare et al., PHENIX Collaboration, Phys. Rev. **C83**, 044912 (2011).

[41] J. Adam et al., ALICE Collaboration, Phys. Lett. **B754**, 81-93 (2016).

[42] Sanghoon Lim for the PHENIX Collaboration, Nuclear Physics **A931**, 525-529 (2014).

[43] B. Abelev et al., ALICE Collaboration, Phys. Rev. Lett. **113**, 232301 (2014).

[44] Sarah Porteboeuf-Houssais for the ALICE Collaboration, PoS Bormio 2014, arXiv:1405.4723 (2014).

[45] B. Abelev et al., ALICE Collaboration, Phys. Lett. **B719**, 29-41 (2013).

Chapter 4

Experimental Set-up

The measurement of angular correlations between D^0 ***mesons and charged particles, presented in this thesis, is based on the data recorded by A Large Ion Collider Experiment (ALICE) at the Large Hadron Collider (LHC). The following sections contain a brief discussion on the LHC machine and the experimental setup regarding ALICE detector.***

4.1 The Large Hadron Collider

In the history of experimental particle physics till date, the Large Hadron Collider (LHC) [1] is the largest and powerful particle accelerator. It is governed by CERN, the "European Organisation for Nuclear Research" and situated in the Franco-Swiss border near Geneva, Switzerland. It is a two ring superconducting accelerator and collider installed in the existing 26.7 km CERN LEP tunnel, constructed between 1984 and 1989, and is 45m to 170m beneath the earth surface. The LHC is designed to collide particle beams circulating in opposite directions in separate beam pipes, kept at ultrahigh-vacuum, at a speed close to the speed of light in vacuum. So far LHC has two types of collision beams, protons and lead nuclei. During 2010-2011, LHC provided proton-proton (pp) collisions with centre-of-mass energy of 7 TeV (3.5 TeV for each proton beam) and in 2012 with higher centre-of-mass energy at 8 TeV. There are heavy-ion collisions at centre-of-mass energy of 2.76 TeV per nucleon-nucleon pair for one month each in 2010 and 2011. In 2013, two months of data were taken for the collisions of proton with lead beams (pPb) at a centre-of-mass energy of 5.02 TeV. After 2013 data taking, LHC was shut down for upgradation. Recently it has started to take data with higher energy. In 2015, LHC started again with pp collisions at centre-of-mass energy of 13 TeV which is almost double of its first pp collisions. The lead-lead ($PbPb$) collisions were taken place during the end of 2015 at a centre-of-mass energy of 5 TeV. In this Run II phase the LHC has planned to take data upto 14 TeV centre-of-mass energy for proton beams.

Since the LHC is mainly conceived as a particle-particle collider, the two beams can not be accelerated in a single ring. The identical bending field in both apertures of the dipole fixes the relation between the momenta of the beams in the two rings. Circulating particles with charges Z_1 and Z_2 in the rings with the magnetic field set to accelerate protons will result in:

$$\sqrt{s_{\mathrm{NN}}} = \sqrt{s_p}\sqrt{\frac{Z_1 Z_2}{A_1 A_2}}, \qquad y_{NN} = \frac{1}{2} log\Big(\frac{Z_1 A_2}{Z_2 A_1}\Big) \tag{4.1}$$

where $\sqrt{s_{\rm NN}}$ is the centre-of-mass energy of collisions, $\sqrt{s_p}$ is the proton highest energy in centre-of-mass frame, A_1, A_2 are the mass numbers and Z_1, Z_2 are the atomic numbers for the two colliding beams. For the proton beam energy of 4 TeV as in the 2012 pp runs and with Pb beam energy as 1.576 TeV per nucleon, one gets the centre mass energy in pPb collisions as $\sqrt{s_{\rm NN}} = 5.02$ TeV. The centre-of-mass frame of the pPb system in the laboratory frame has a rapidity shift of $\Delta y_{cms} = 0.465$ in the proton direction. In this thesis analysis of pPb data at $\sqrt{s_{\rm NN}} = 5.02$ TeV will be the main focus.

The full LHC ring is divided into 8 sectors (Fig. 4.1). Beams are injected through point 2 and point 8 as shown in Fig. 4.1. Beam interactions occurred only in point 1, 2, 5 and 8 where the major detectors are build. The radio frequency system (RF)

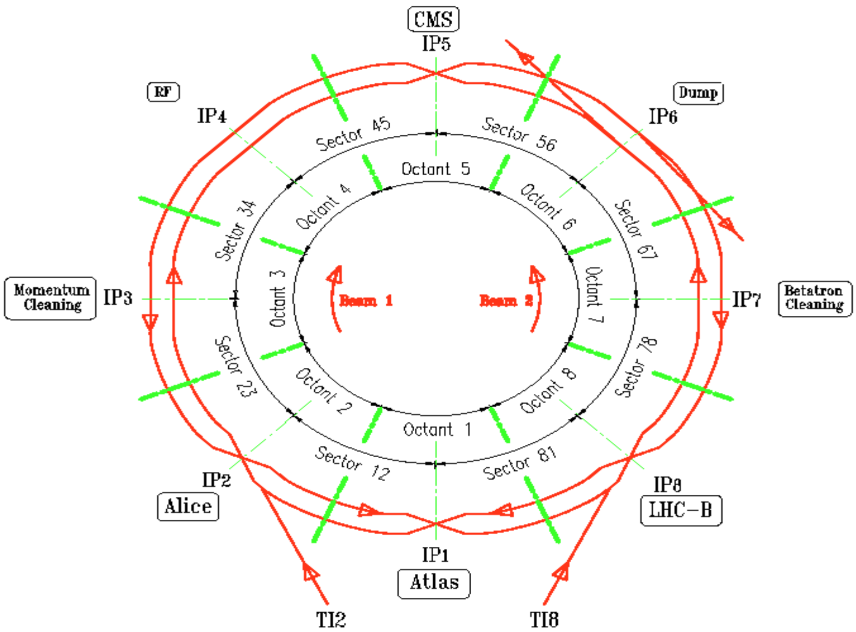

Figure 4.1: Schematic diagram of LHC tunnel with the positions of different parts.

accelerates the beam at the point 4 and at point 6 dumping the beams occurs. The beam cleaning insertions to steer the beam into staggered sets of collimator rather than the super-conducting magnets are in point 3 and 7 [2].

For pp collisions at 7 TeV, first proton beams are produced at LINAC2 with energy 50 MeV. The beams are then injected into the Proton Synchrotron Booster (PSB) which accelerates them to 1.4 GeV for injection into the Proton Synchrotron (PS). The PS pushes the beam energy upto 25 GeV and the beams are passed to Super Proton Synchrotron (SPS), having circumference of 7 Km, where they are accelerated upto 450 GeV. Finally the beams are transferred to the two beam pipes of the LHC at point 2 and Point 1. The beams are then circulated clockwise and anti-clockwise to reach the desire energy of 3.5 TeV (maximum of 4 TeV in Run I). Recently in Run II each proton beam has reached the highest energy of 6.5 TeV (Fig. 4.2). Lead ions from LINAC3 are accelerated in the Low Energy Ion Ring (LEIR) and then follow the same way to reach their maximum energy. Each collision point at LHC ring is referred to a specific experiment with a built in detector facility. There are six detectors, constructed at the LHC's Interaction Points (IPs) where the collision of beams take place. These are A Large Ion Collider Experiment (ALICE) [3] (LHC ring position- point2), A Toroidal LHC ApparatuS (ATLAS) [4] (LHC ring position - point1), Compact Muon Solenoid (CMS) [5] (LHC ring position - point5), Large Hadron Collider beauty (LHCb) [6] (LHC ring position - point8), Large Hadron Collider forward (LHCf) [7] (LHC ring position - in between ALICE and ATLAS), TOTal Elastic and diffractive cross-section Measurement (TOTEM) [8] (LHC ring position - near CMS). CMS and ATLAS experiments are large and are designed to investigate a wide range of physics including Higgs search, extra-dimensional physics and dark matter. LHCb experiment is motivated by the study of matter and anti-

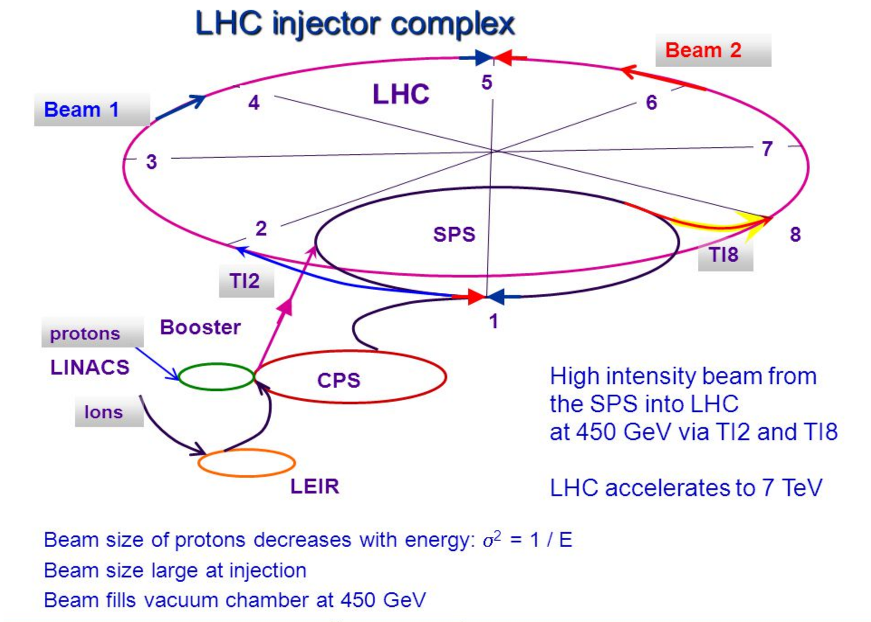

Figure 4.2: Schematic diagram of CERN accelerator complex.

matter through beauty quark. ALICE is dedicated for heavy-ion physics to study Quark Gluon Plasma. The LHCf is designed for forward physics and to calibrate large-scale cosmic-ray experiments. TOTEM is also specialized for forward physics as LHCf.

4.1.1 General Overview of ALICE and its Sub-detectors

ALICE (A Large Ion Collider Experiment), the major heavy-ion detector at the LHC, is dedicated for heavy-ion collisions to study the strongly interacting QCD matter produced at ultra-high energy density and temperature. Beside the heavy-ions, its physics program includes proton-nucleus asymmetric collisions and proton-proton collisions to address several QCD topics, complementary to the physics programme of other LHC detectors. Figure 4.3 shows a schematic diagram of ALICE

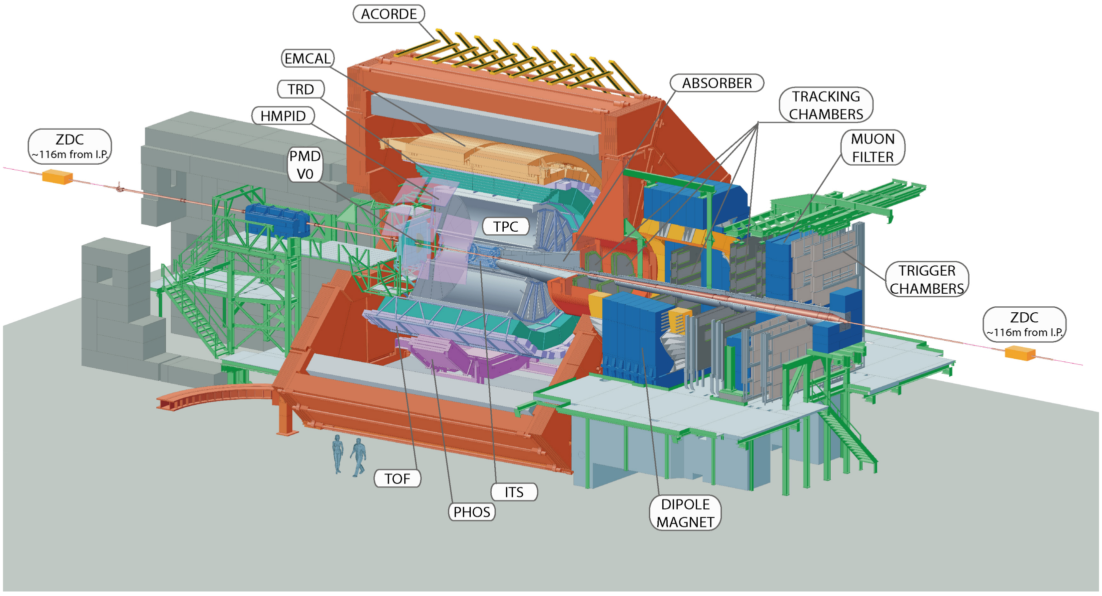

Figure 4.3: Schematic diagram of ALICE detectors with all its sub-systems.

detector setup. Its overall dimension is 26m long, 16m high, and 16m wide with a total weight of approximately 10,000 tonne. The experiment runs with 18 different detector systems. Each sub-detector has its own specific technology choice and design constraints, fulfilling specific physics requirements and the experimental conditions expected at LHC [9]. Different sub-detectors are optimized to deliver high-momentum resolution and excellent Particle Identification (PID) over a broad range of particle momentum.

ALICE consists of a central barrel part, having pseudorapidity coverage of $\pm$ 0.9 over full azimuth, which measures hadrons, electrons, and photons, and a forward muon spectrometer with a coverage $-4.0 < \eta < -2.4$. The central barrel part is embedded inside a large solenoid magnet (L3) of 0.5T magnetic field, optimized between low momentum resolution and particle acceptance. The central barrel consists of an Inner Tracking System (ITS) of six layers of high-resolution silicon detectors, a cylindrical Time Projection Chamber (TPC), three particle identification arrays of Time of Flight (TOF), Ring Imaging Cherenkov (HMPID) and Transition Radiation (TRD) detectors, and two electromagnetic calorimeters (PHOS and EMCal). Among these detectors apart from HMPID, PHOS, and EMCal, all other detectors cover full azimuth. Several smaller detectors (ZDC, PMD, FMD, T0, V0) are located at small angles, parallel to beam direction for global event characterization and triggering. On top of the L3 magnet, An array of scintillators (ACORDE) is used to trigger on cosmic rays. For the thesis work on angular correlations between D^0 mesons and charged particles in *pPb*, the ITS, the TPC, the TOF and the V0 detectors are used. The detail description of these detectors will be discussed in the following sections.

4.1.1.1 Central barrel detectors

- **The Inner Tracking System (ITS)** is consists of six cylindrical layers of coordinate-sensitive silicon detectors, covering the pseudorapidity range of at least $|\eta| < 0.9$. It is a high granularity tracking and vertexing device which is also used for particle identification via energy loss (dE/dx) [10]. More about the ITS detector is discussed later.
- **The Time Projection Chamber (TPC)** is the main tracking detector of ALICE. It is a large gaseous detector utilised for track finding, momentum measurement and particle identification via energy loss (dE/dx) [11]. More details can be found below.

- **The Transition Radiation Detector (TRD)** is placed around the TPC at radial distance of 2.9 to 3.68 m ($|\eta|$ <0.84) over the full azimuthal angle [12]. This contains six layers of multi-wire proportional chambers filled with Xe-CO_2 and a radiator in front of each chamber. The TRD is mainly used to differentiate electrons from charged hadrons via transition radiation and energy loss. It can provide tracking information and also involved in triggering.
- **The Time of Flight Detector (TOF)** is a large area array of Multi-gap Resistive-Plate Chambers (MRPC) surrounding the TRD. It improves the Particle Identification (PID) in the intermediate transverse momentum range from 0.2 to 2.5 GeV/c. More details of TOF is discussed later [13].
- **The High-Momentum Particle Identification Detector (HMPID)** is a Ring Imaging Cherenkov (RICH) counter with a radiator liquid C_6F_{14} (perflurohexane) and CsI photo-catode. The goal of HMPID is to enhance PID capability for hadrons measured by ALICE beyond TOF momentum range. It can provide hadron identification upto 5 GeV/c, mainly pions, kaons, and protons [14].
- **The PHOton Spectrometer (PHOS)** is a high-granularity electromagnetic calorimeter designed to perform photon measurements. It is made up of lead tungsten crystals ($PbWO_4$) with a set of multi-wire proportional chambers in front of it to reject the charged particles. The PHOS detector is at a distance of 4.6 m and covers 100° in the azimuthal angle and pseudorapidity range of -0.12 < η < 0.12. PHOS can measure thermal photons in the energy range between 1 and 10 GeV [15].
- **The ElectroMagnetic CALorimeter (EMCal)** is a large lead scintillator

sampling cylindrical calorimeter, having pseudorapidity range of $-0.7 < \eta < 0.7$ and azimuthal angle coverage of 110°. It enhances the measurement of jets and high momentum photons and electron identification [16].

- **ALICE COsmic Ray DEtector (ACORDE)** is an array of plastic scintillator counters placed on top of L3 magnet having radial distance of 8.5 m ($\eta < 1.3$) over the azimuthal angle ± 60° [17]. In combination with the TPC, TRD and TOF, it detects the atmospheric muons and multi-muon events (cosmic rays).

4.1.1.2 Forward detectors

- **MUON Spectrometer** is optimized for the detection of the particles containing heavy-quark resonances, both the charmonium states (J/ψ and ψ') as well as the bottomonium states (Υ, Υ' and Υ'') via the muonic channel ($\mu^+\mu^-$) [18]. The muon spectrometer is located in the negative z-direction far away from central barrel covering the angular range from 171° to 178° (-4 < η < -2.5). It consists of a passive front absorber to absorb hadrons and photons coming from the interaction vertex, a high-granularity tracking system of 10 detection planes, a large dipole magnet, a passive muon filter wall, followed by four planes of trigger chambers and an inner beam shield to protect the chambers from particles and secondaries produced at large rapidities (Fig. 4.4).
- **Photon Multiplicity Detector (PMD)** is a forward detector (3.67 m from the IP), dedicated to measure the multiplicity and spatial ($\eta - \phi$) distribution

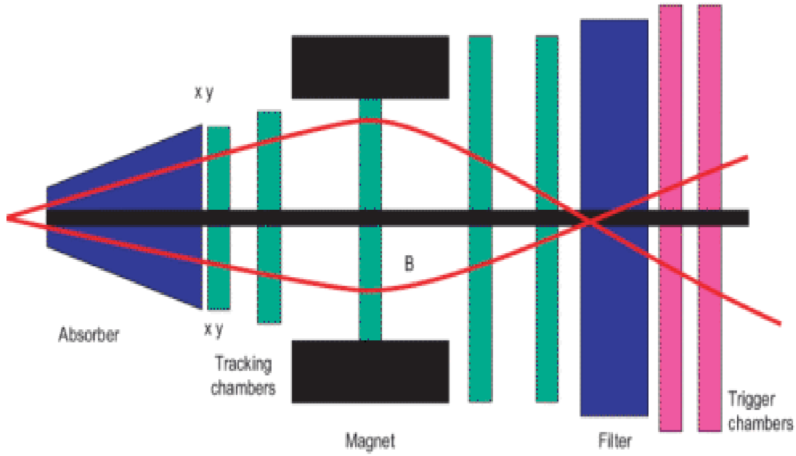

Figure 4.4: Schematic layout of Muon spectrometer.

of photons on an event-by-event basis. It is made up of a preshower detector with a charged particle veto detector in front and covers a pseudorapidity range of $2.3 < \eta < 3.9$ with full azimuth [19].

- **Forward Multiplicity Detector (FMD)** consists of 5 rings of silicon semi-conductor detectors with a total of 51200 individual strips [20]. It is designed to measure the charged particles which are emitted at small angles relative to the beam line direction as it is located in the forward direction having coverage of $-3.4 < \eta < 1.7$ and $1.7 < \eta < 5.03$. It has angular interval of about 0.75 degrees to 21 degrees with respect to the beam direction.
- **VZERO (V0) detector** is a small angle detector consisting of two arrays of scintillator counters, called V0A and V0C, that are installed on either side of the ALICE IP [20]. The V0A is located at 330 cm away from the vertex on the side opposite to the muon spectrometer. The V0C is fixed at the front face of the hadronic absorber at a distance 90 cm from the vertex. They cover the pseudorapidity ranges $2.8 < \eta < 5.1$ (V0A) and $-3.7 < \eta < -1.7$ (V0C) for

collision vertex at the central position. They serve as minimum bias triggers and provide centrality measurements.

- **Time Zero (T0) detector** consists of two arrays of Cherenkov Counters (T0A and T0C) positioned at the opposite sides of the IP at distances of -70 cm and 370 cm. For T0s, the covered pseudorapidity range is 2.9< η <3.3 and 4.5 < η <5 [20]. They serve as trigger and timing detector. They provide main signal to ALICE L0 trigger, an early wake-up trigger to TRD and start-timing to TOF. They can also give approximate vertex position (with a precision $\pm$1.5 cm) and rough estimation of event multiplicity.
- **Zero Degree Calorimeter (ZDC)** is dedicated to measure the centrality of high energy heavy-ion collisions. Two identical sets of calorimeters are located on both sides of the ALICE detector, 116m away from the IP. Each set of detectors consists of three calorimeters: the neutron calorimeter (ZN), proton calorimeter (ZP) and electromagnetic calorimeter (ZEP). The ZDCs are quartz-fiber spaghetti calorimeters, with silica optical fibers as active material embedded in a dense absorber. The principle of operation is based on the detection of of Cherenkov light produced by the charged particles shower [21].

4.1.1.3 ALICE Coordinate Systems

The coordinate system of ALICE setup is a right-handed orthogonal cartesian system having origin at the beam IP (Fig. 4.5). Its x coordinate and y coordinate are perpendicular to the mean beam direction such that the positive x and y coordinates point to the centre and upward of the accelerator respectively. The z coordinate is parallel to the mean beam direction with positive z in the A-side of the detector (RB24, shaft side) and negative z towards the Muon Arm (RB26).

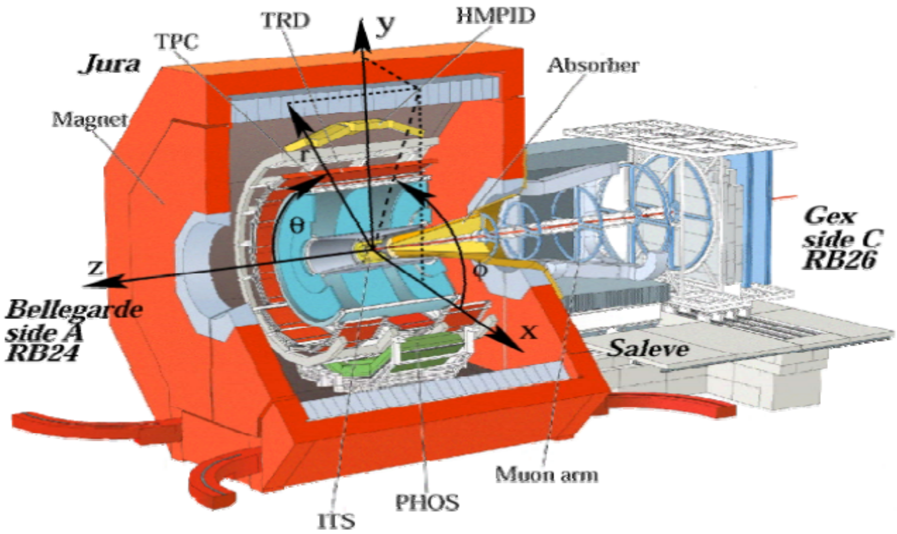

Figure 4.5: The co-ordinate system of ALICE detector.

4.1.1.4 Inner Tracking System

The Inner Tracking System consists of six cylindrical shaped silicon based detectors from inward (IP) to outward. These are two layers of Silicon Pixel Detectors (SPD), two layers of Silicon Drift Detectors (SDD) and two layers of Silicon Strip Detectors (SSD), having radii r = 4, 7, 15, 24, 39 and 44 cm from IP respectively as shown in the Fig. 4.6.

With the fast silicon material, the ITS is used to localize the primary vertex. It has an excellent vertex detection resolution about 100 μm. Also, it has been optimised to detect secondary vertices of shortly lived particles like hyperons, D and B mesons.

Layer/Type	r [cm]	± z [cm]	Number of modules & Intrinsic resolution [μm] $r\phi$	z
1/SPD	3.9	14.1	12	100
2/SPD	7.6	14.1	12	100
3/SDD	15.0	22.2	35	25
4/SDD	23.9	29.7	35	25
5/SSD	38.0	43.1	20	830
6/SSD	43.0	48.9	20	830

Table 4.1: Characteristics of the six ITS layers [22].

It has other goal to reconstruct and identify particles with momentum below 100 MeV. The relative momentum resolution for ITS is better than 2% for pions with 100 MeV/c < p_{T} < 3 GeV/c. It can handle very high track densities about 8000 tracks per unit of rapidity. The main parameters for the three ITS sub-systems are listed in table 4.1

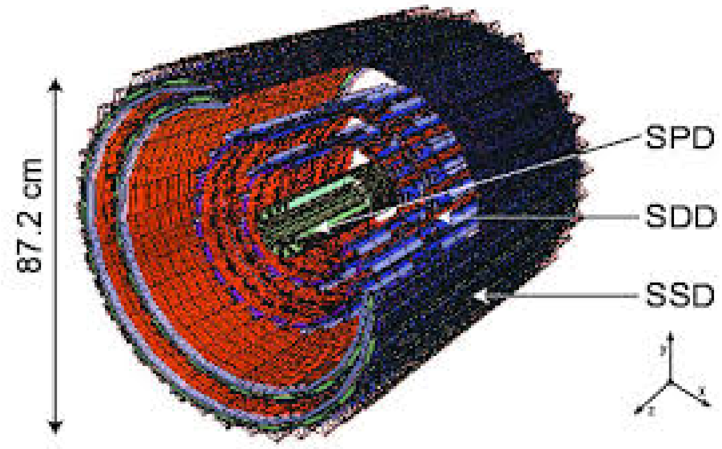

Figure 4.6: Schematic diagram of the Inner Tracking System of the ALICE detector describing different layers [23].

The innermost two layers are Silicon Pixel Detectors (SPD) which consist of reverse-biased silicon diode with a two-dimensional sensor matrix. These are capable of determining the position of the primary vertex, the impact parameter of secondary tracks from various decays of particles. SPDs provide excellent impact parameter resolution accounting up to 80 particles per cm^2 in heavy-ion collisions. The Silicon Drift Detectors (SDD) are situated in the middle of the ITS consisting of two intermediate layers of silicon detectors with drift regions. The SDDs are mounted on linear structures called ladders. There are 14 ladders on layer 3 and 22 on layer 4. Similar to the gaseous drift detectors, SDDs use the transport time of the charge deposited by the tracks to localize the impact point. This enhances the track finding resolution and multi-track capability in heavy-ion collisions with higher multiplicity events. Therefore, it can give position information with high precision and energy loss (dE/dx) of the tracks which help for the particle identification. The outermost two layers are called Silicon Strip Detectors (SSD). These are important as they connect the information between ITS and TPC and provide particle identification for low-momentum particles. Each SSD module consists of a 1536-strip double-sided silicon sensor connected through aluminium-kapton micro-cables [22]. The SSDs can provide good two-dimensional measurement of the track position and reject the fake hits. SSDs use the dE/dx measurements for particle identification in the non-relativistic $(1/\beta^2)$ region, along with the information from the SDDs.

4.1.1.5 Time Projection Chamber

The Time Projection Chamber (TPC) is the main tracking detector of ALICE central barrel [11]. The main task of TPC is to provide charged particle momentum measurements with good two track separation, particle identification, and vertex determination. Along with ITS, it provides information on the flavour composition through the study of hadronic observables.

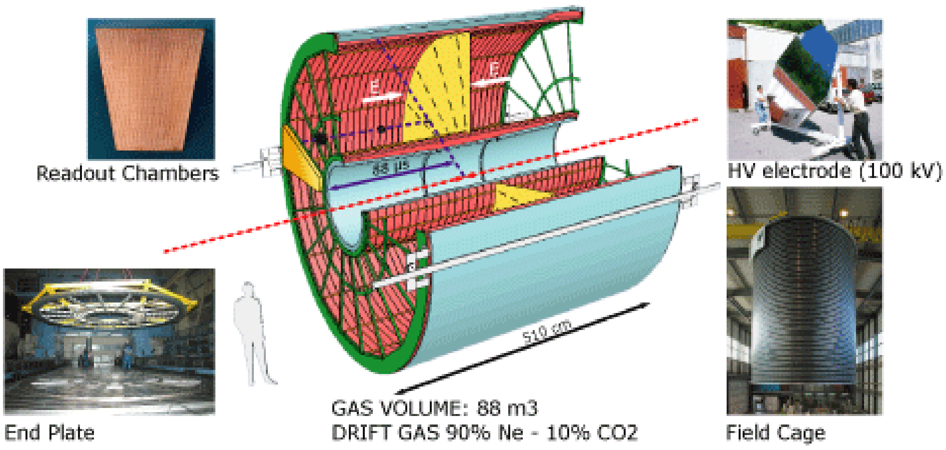

Figure 4.7: Layout of the ALICE TPC showing the central electrode, the field cage and the end plates supporting the readout chambers.

The ALICE TPC covers a phase-space of $|\eta| < 0.9$ and full azimuth. It has a cylindrical volume of $88m^3$ with inner radius of 80cm and outer radius of 250cm and an overall length along the beam direction of 510 cm. A schematic diagram of the TPC is shown in the Fig. 4.7. TPC is a gas detector and a gas mixture of Ne/CO2/N2 (90%/10%/5%) is filled in two cylindrical shape volumes separated by a cathode. Conventional multi-wire proportional chambers with cathode pad readouts are mounted into 18 trapezoidal sectors of each end-plate. A central high voltage (100 kV) electrode creates a highly uniform electrostatic field (400 V/cm). When a charged particle traverses the gas, it ionises the gas molecules. The produced primary electrons are then drifted by the electric filed towards the end cap. The necessary signal amplification is provided through an avalanche effect in the vicinity of the anode wires strung in the read-out. In this way the 3D tracking as well as dE/dx information are stored.

With the three-dimensional space points, TPC is capable of reconstructing the primary tracks for a wide range of transverse momentum. It can provide low momentum track reconstruction (100 MeV/c to 1 GeV/c) with a resolution less than 2%. With ITS and TRD, TPC can extend the track reconstruction with a momentum resolution of 10% for a transverse momentum up to 100 GeV/c at 0.5T magnetic field. Such a large gaseous detector provides dE/dx information for the tracks which helps to identify the tracks. The specific energy loss (dE/dx), described by the Bethe-Bloch formula, is parametrized by a function originally proposed by the ALEPH Collaboration [25].

$$f(\beta\gamma) = \frac{P_1}{\beta^{P_4}}\Big(P_2 - \beta^{P_4} - ln(P_3 + \frac{1}{(\beta\gamma)^{P_5}})\Big) \tag{4.2}$$

where β is the particle velocity, γ the relativistic factor and P_{1-5} are fit parameters. Figure 4.8 shows the energy loss in the TPC as a function of momentum p (GeV/c) for $PbPb$ collisions at $\sqrt{s_{\rm NN}} = 2.76$ TeV and pPb collisions $\sqrt{s_{\rm NN}} = 5.02$ TeV. The background is larger in $PbPb$ collisions than pPb collisions which shows much cleaner distribution. Low momentum particles ($<$ 1 GeV/c) are identified on a track by track basis whereas for higher momenta particles, a statistical based nσ approach is used. nσ cut is defined in terms of resolution as:

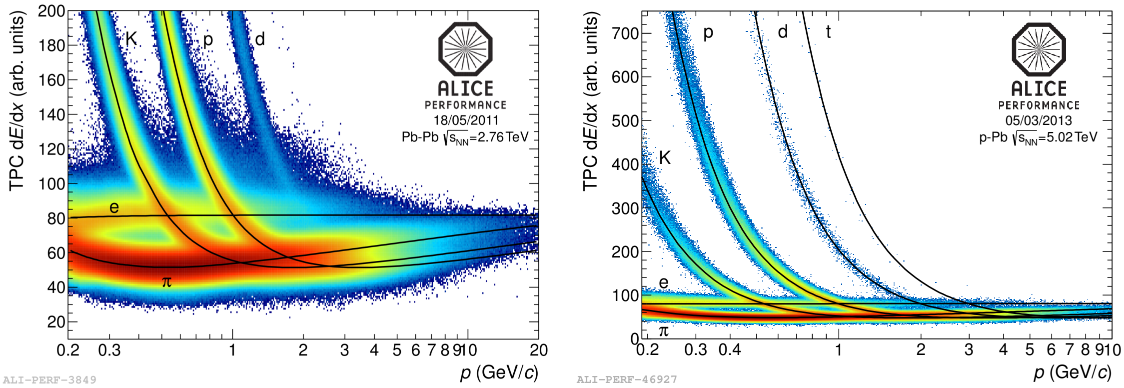

Figure 4.8: Energy loss in the TPC (dE/dx) versus momentum p (GeV/c) with Bethe-Bloch predictions (black lines) for different particles in $PbPb$ collisions (left) and in pPb collisions (right) [24].

$$n\sigma_{TPC} = \frac{dE/dx_{measured} - dE/dx_{expected}}{\sigma_{TPC}} \tag{4.3}$$

where $dE/dx_{measured}$ is the energy loss of the tracks measured in TPC, $dE/dx_{expected}$ is the expected energy loss of the tracks using a parameterzation of modified Bethe-Bloch function and σ_{TPC} is the resolution of the TPC.

4.1.1.6 Time of Flight (TOF)

ALICE Time of Flight (TOF) detector is designed to identify particles produced in high energy collisions. It expands the measurement of particle identification from 1 GeV/c (beyond TPC limit) to a few GeV/c. It is located at 3.7 m from the beam axis. The TOF consists of a large cylindrical array ($\sim 170\ m^2$) of Multi-gap Resistive Plate Chamber (MRPC) strips operated in a $C_2H_2F_4$ (90%), C_4H_{10} (5%), SF_6 (5%) gas in the central region ($-0.9 < \eta < 0.9$) [26].

The working principle of TOF detector is based on the measurement of mass for the particle using its flight time. The particle mass m is calculated using,

$$m^2 = p^2\Big(\frac{t^2}{L^2} - 1\Big) \tag{4.4}$$

where m, p, t, L are the mass of the particle, the momentum, the time-of-flight and the track length respectively. Momentum (p) information is collected from ITS and TPC. The flight time t is $t_{hit} - t_0$ where hit time (t_{hit}) is the time measurement made by the TOF detector while t_0 is the time of the interaction, measured by ALICE T0 detector or TOF itself. L is the particle track length (3.7 m). For two particles of unequal mass m_1 and m_2 having the same momentum p and the same track length L, the time-of-flight difference can be measured as

$$t_1 - t_2 = \frac{L}{2}\Big(\frac{m_1^2 - m_2^2}{p^2}\Big) \tag{4.5}$$

The time-of-flight difference is also related to the standard deviation of the time difference of the two particles. The nσ cut is applied for this

$$n\sigma_{TOF} = \frac{t_1 - t_2}{\delta t} \tag{4.6}$$

where δt is the time resolution. With a global TOF time resolution of 80ps, TOF provides a π/K and K/P separation better than 3σ up to a particle momentum $p \simeq 2.5$ GeV/c and $p \simeq 4$ GeV/c respectively. Below 4 GeV/c the particles are clearly separable [27]. The Fig. 4.9 shows the particle velocity (TOF β) as a function of particle momentum for $PbPb$ collisions at $\sqrt{s_{\rm NN}}$ = 2.76 TeV (left) and in pPb collisions at $\sqrt{s_{\rm NN}}$ = 5.02 TeV (right). Due to less background in pPb collisions the

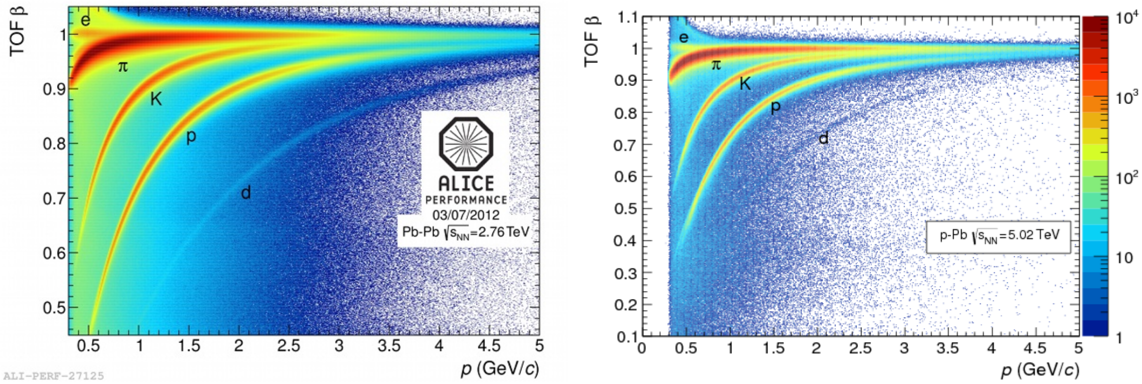

Figure 4.9: Particle β vs. momentum in $PbPb$ collisions at $\sqrt{s_{\rm NN}}$ = 2.76 TeV (left) and in pPb collisions at $\sqrt{s_{\rm NN}}$ = 5.02 TeV(right) by TOF.

distributions are much cleaner w.r.t $PbPb$ case. To improve the particle identifi-

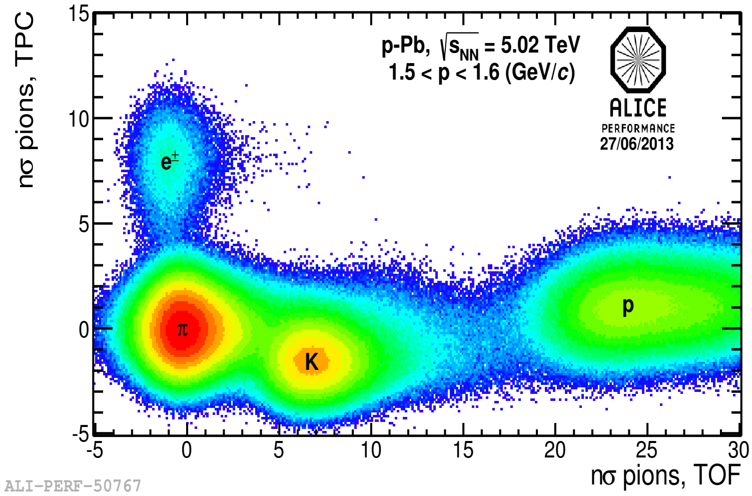

Figure 4.10: Combined pion, kaon and proton identification with the TOF and the TPC for central pPb collisions.

cation, combination of TPC and TOF information is used. This allows a further extension of the momentum range with better precession. The Fig. 4.10 shows the difference between the measured and expected PID signals for TPC and TOF as nσ using pion mass hypothesis. The strategy of combining TPC and TOF clearly enhance the separation between different hadron species. This helps in the secondary vertex reconstruction for D^0 mesons, decaying into kaons and pions, to a reasonable transverse momentum range. Hence the angular correlation analysis between D^0 mesons and other charged particles, get benefited.

4.1.1.7 VZERO detector

The VZERO (V0) detectors are designed to provide :

- minimum bias trigger for central detectors,
- multiplicity or centrality measurement,
- luminosity information,

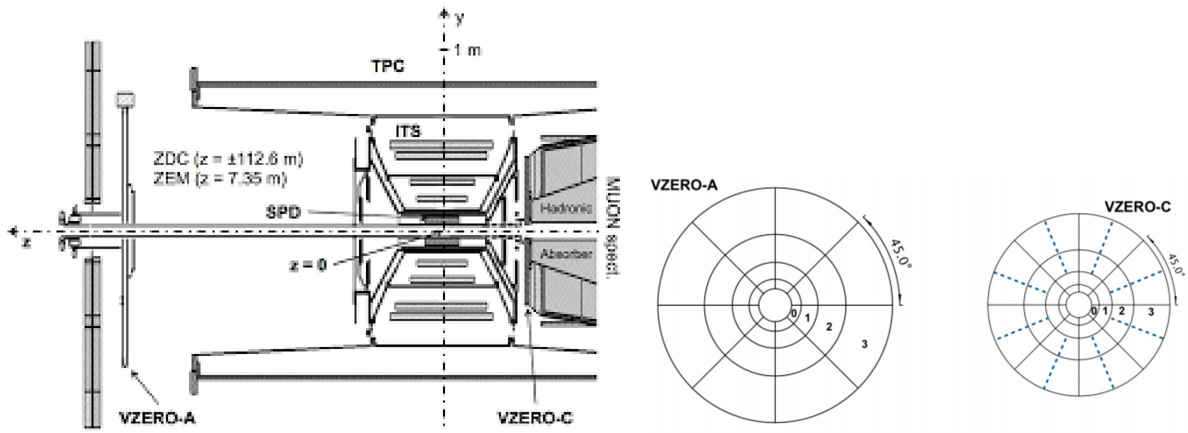

Figure 4.11: Position of the two VZERO arrays within the general layout of the ALICE experiment (left). Schematic diagram of VZERO-A and VZERO-C arrays showing their segmentation (right) [28].

These are small-angle detectors consisting of two arrays of scintillator counters, installed on either side of the ALICE IP. The V0A is located 330 cm away from the vertex and The V0C is at 90 cm from the vertex. They cover the pseudorapidity ranges V0A ($2.8 > \eta > 5.1$) and V0C ($-3.7 < \eta < -1.7$) as shown in the Fig. 4.11.

Each array is segmented into 32 individual counters distributed in 4 rings. Each of these rings are divided into 8 sectors (45°) in azimuth and covers pseudorapidity uint of 0.5 - 0.6. The V0C arrays (rings 3 and 4) are divided into two identical detectors and are optimized for uniform signal [20].

4.1.2 ALICE data taking model: Online

At the time of data taking a set of activities are implied on the detectors and those are grouped into four "Activity Domains":

- Detector Control System (DCS)
- Trigger (TRG)
- Data Acquisition (DAQ)
- High Level Trigger (HLT)

The Experiment Control System (ECS) on top level takes control of all four "Activity Domains" [29, 30] as shown in the Fig. 4.12. These are called online systems of ALICE data taking. ECS activities on the online systems control the operation of the detectors.

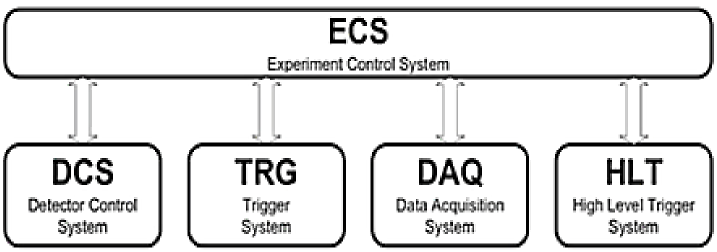

Figure 4.12: Hierarchy of online systems.

4.1.2.1 Detector Control System (DCS)

The Detector Control System (DCS) is the system which controls all the detector services (cooling system, the ventilation system, the magnetic fields, high and low-voltage power supplies, monitoring of the Front-End Electronics etc.). It provides remote control and monitoring for all the detectors from the ALICE Run Control (ARC) room at the LHC point 2.

4.1.2.2 Trigger system (TRG)

Since the interaction rate at the LHC luminosities is much higher than the possible data acquisition rate, we need a trigger system (an electronic system) which makes a decision whether the collision is worth saving or not [31]. With each positive decision, trigger signals are sent to all detectors in order to make them read out synchronously. The trigger system consists two basic parts - Central Trigger Processor (CTP) (the decision maker) and Local Trigger Unit (LTU). LTUs are the same for all detectors and work as an interface between readout detector and CTP. The ALICE trigger system has 3 levels: L0, L1 and L2. L1 and L2 (called L1 message and L2 message) signals have “accept” or “reject” response features. The trigger information is transferred through the LTUs to the Front-End Electronics (FEE) of each sub-detector [32].

4.1.2.3 Data Acquisition (DAQ)

The ALICE Data Acquisition system (DAQ) [33] handles the data flow from the sub-detector electronics to the permanent storage. The readout electronics of all the sub-detector is processed to the Detector Data Links (DDLs). The Local Data Concentrators (LDCs) read the output of the event fragments from DDLs. Several LDCs may be needed to collect the data from a single sub-detector. LDCs ship the sub-events (aggregated of event fragments) to a second layer of computers, the Global Data Collectors (GDCs), where the sub-events are built in a full event retaining the same trigger information. The events are then migrated to the Permanent Data Storage (PDS) and published via the Grid.

4.1.2.4 High Level Trigger (HLT)

The main purpose of the High Level Trigger (HLT) [34] is to reduce the data volume by well over one order of magnitude in order to fit the available storage bandwidth while retaining the physics information. The overall event rate is limited by the Data Acquisition (DAQ) bandwidth to the permanent storage system of 1.25 GB/s. HLT receives the copy of raw data from LDCs. After the full reconstruction of an event, the HLT provides trigger decisions, Regions-of-Interest (RoI), and compressed data to the DAQ in order to reduce the data rate (from 25GB/s to 1.25GB/s) to PDS.

4.1.3 ALICE data taking model: Offline

The ALICE offline project is developed for the sophisticated data processing which includes simulation, reconstruction, calibration, alignment, visualisation and physics analysis. During active runs, ALICE takes huge amount of *pp*, *PbPb* and *pPb* data which are in million, trillion bytes. This requires extensive computing resources. Therefore data processing is distributed onto several computing centres located worldwide [29]. Distribution of the data for reconstruction and analysis needs an automated system; the "ALICE-Grid" [35]. ALICE developed ALICE Environment("AliEn" [36]) system which gives access to the computing Grid. The simulation, reconstruction of ALICE events are performed by the offline framework called "AliRoot" [37], which uses the object oriented programming C++, based on the ROOT framework [38]. ROOT is an object oriented framework used for the data analysis on a large scale. AliRoot package is based on ROOT framework with specific classes and libraries grouped in modules for ALICE purpose. The full software package is developed for event generation, detector simulation, event reconstruction and data analysis. It also makes life easier for analysers with advanced statistical analysis tools of histogramming, random number generation, fitting and many more. ALICE offers its users a system called CERN Analysis Facility (CAF) which enables the parallel use of a computing cluster to perform different analysis.

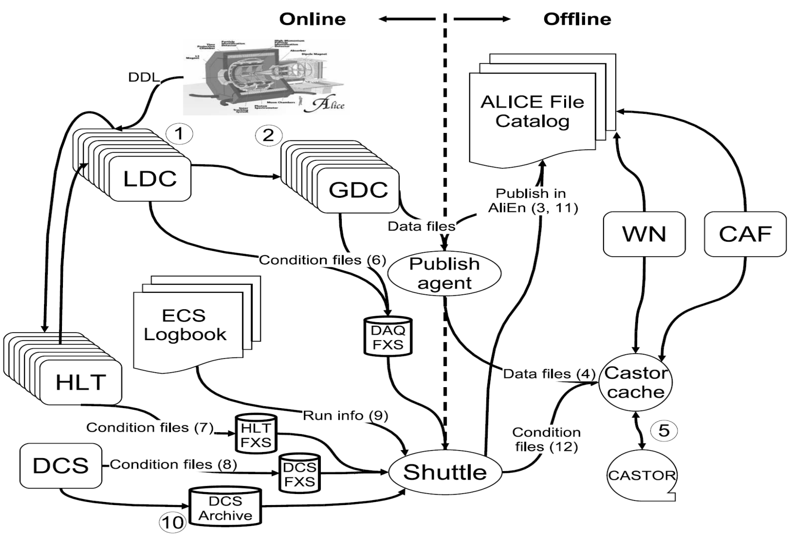

Figure 4.13: Global view of ALICE data flow [29].

4.1.3.1 Raw data flow

The raw data taken by the sub-detectors has to be processed before being available in the form of reconstructed events for further analysis. This happens in several stages as illustrated in Fig. 4.13. Data originating from the sub-detectors (denoted by 1 in Fig. 4.13) are processed by LDCs and global events are built by GDCs (2). The so-called publish agent registers the assembled events into the AliEn system (3) and ships them to the CERN computing centres where events are stored first on disks (4) and then permanently on tapes (5) by the CASTOR system.

4.1.3.2 ALICE AliEn: the ALICE Analysis Framework on the Grid

The Grid facility provides unification of resources of distributed computing centres, computing power and storage, to users all over the world. This works for the resources in large collaborations to be shared. Each year ALICE produces a huge amount of data ($\sim$2 PB per year) which makes almost impossible to handle by single source. This brings the necessity of automatised procedures for the (software) reconstruction of the events with a large mass of computing resources for the physics analysis to the users. One of the main advantage of the Grid is the possibility to analyse a large set of data by splitting a job analysis into many "clone" subjobs running in parallel on different computing nodes. The ALICE VO (Virtual Organisation) is made of more than 80 sites distributed worldwide (in 21 countries) as shown in Fig. 4.14.

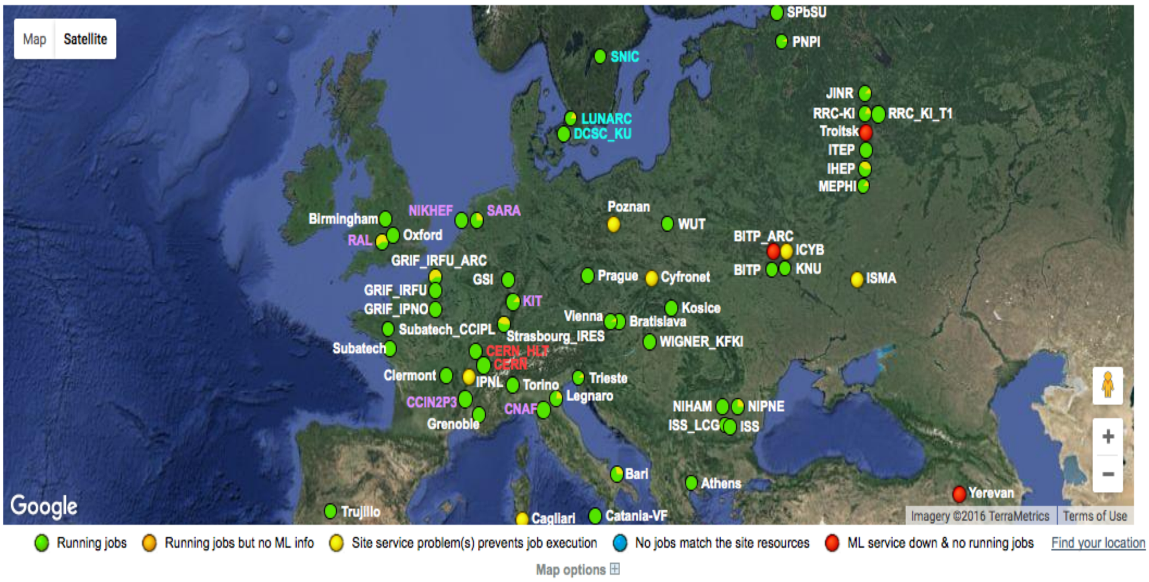

Figure 4.14: A snapshot of the ALICE VO sites in Europe. A green circle indicates that jobs are running on the site while red and yellow circles indicate sites with problems.

4.1.3.3 The AliRoot Framework

As already stated above, AliRoot is the offline framework for simulation, alignment, calibration, reconstruction, visualisation, quality assurance, and analysis of experimental and simulated data. A schematic diagram is shown Fig. 4.15. It is based on the ROOT framework. Most of the codes are written in C++ with some parts in Fortran that are wrapped inside C++ code. The whole framework proceeds as following:

- **Event generation**: Event simulation is performed through events generators, like PYTHIA [39] or HIJING [40] with AliRoot interface. It produces the "Kinematics Tree" containing the full information about the generated particles (type, momentum, charge, production process, originating particle,

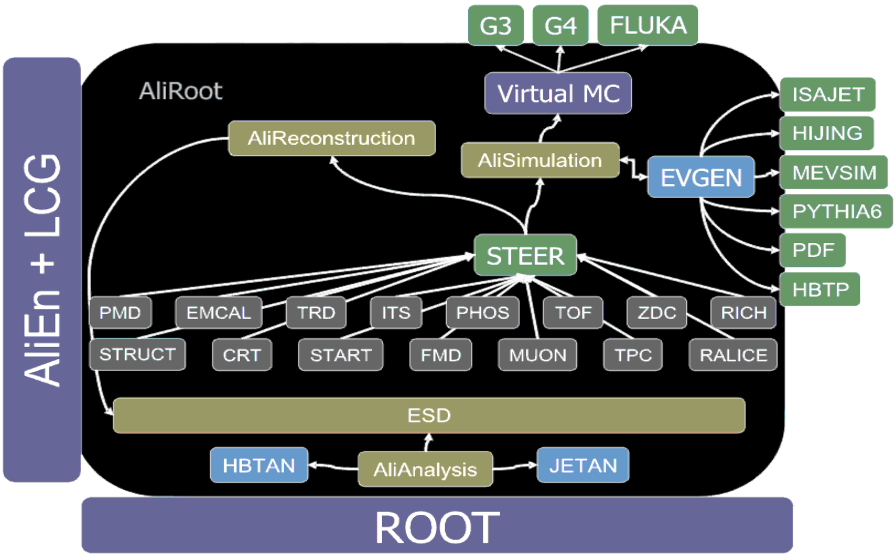

Figure 4.15: A schematic view of the AliRoot framework.

and decay products).

- **Transport:** The particles are propagated through the detector material being realistically as much as possible. Programs that perform the transport for AliRoot framework are Geant3 [41], Geant4 [42], and Fluka [43].

After the transport the digitizations of produced particles are processed and the data are stored as specific hardware format of the detector (raw data). The raw data, representing the response of the detector is reconstructed. For both simulated as well as real events, reconstruction procedure is identical (Fig. 4.16). This is discussed below:

- **Cluster finding:** Particles that interact with the detector usually leave a signal in several adjacent detecting elements or in several time bins of the detector. In this step these signals are combined to form clusters.
- **Primary vertex reconstruction:** The primary vertex reconstruction is done

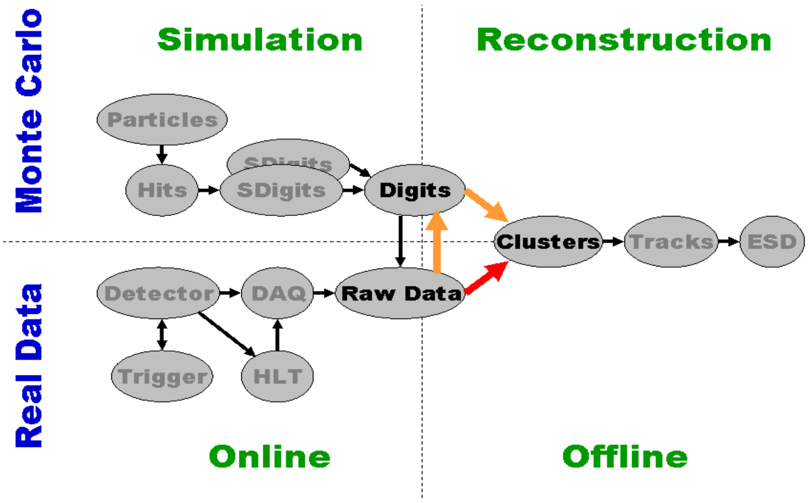

Figure 4.16: Schematic view of the reconstruction framework.

by using the information provided by the silicon pixel detectors of the ITS. Pairs of reconstructed points in the two layers (called tracklets), close in azimuthal angle in the transverse plane, are selected. From their z-coordinate, the z-vertex of the primary vertex is estimated using a linear extrapolation. Finally a similar procedure is performed in the transverse plane. The resolution of the position of the primary vertex depends on the track multiplicity. After track reconstruction, the primary vertex is recalculated using the measured track parameters.

- **Track reconstruction:** The clusters are combined to form tracks that allow the track curvature and energy loss to be calculated with the aim of determining the associated momentum and particle identity. The basic method for track recognition and reconstruction is based on the Kalman Filter, as introduced to this field by P. Billoir [44–46]. In this method for each track, first the tracking is done by using the TPC clusters information. The result, obtained after the full reconstruction process contains information only from the TPC.

These so called “TPC-only tracks” are saved in the reconstruction output. The tracks are then propagated to the outer layers of the ITS. All the reconstructed points associated with the TPC tracks are propagated to the next ITS layer inwards until the inner ITS layer is reached with the best χ^2 for the tracks. The track finding is subsequently repeated for all the TPC tracks. For the very low p_{T}, tracking is repeated inside ITS only, from the reconstructed points not associated to any TPC track. After the ITS inward tracking is completed, the Kalman filter algorithm is repeated again in the opposite direction, starting from the vertex and going outwards through the ITS to the TPC. The tracking follows the track beyond TPC, assigning space points in the TRD, and matching the tracks with hits in the TOF, minimum-ionizing clusters in the HMPID and space points in the CPV (Charged-Particle Veto detector), located in front of the PHOS. In the final step, the Kalman filter is reversed, refitting all tracks from the outside inwards.

- **Secondary vertex reconstruction:** Tracks are combined to find secondary vertices in order to reconstruct decayed particles. Opposite-sign tracks that originate sufficiently far away from the primary vertex are combined. If distance of closest approach (dca) is below some predetermined value and the topology of the two tracks is consistent with a decay, the pair is accepted as a candidate for a secondary decay vertex. Different topological cuts are imposed at different physics analysis level.

The output of the reconstruction is called Event Summary Data (ESD). It contains the information such as the position of the event vertex, parameters of reconstructed charged particles together with their PID information, positions of secondary vertex candidates, parameters of particles reconstructed in the calorimeters, and integrated signals of some sub-detectors. This data is further reduced to Analysis Object Data (AOD) format. These smaller-sized objects contain only information needed for specific analysis. Depending on different physics studies, many AODs can be created for a given event with enriched information.

4.1.3.4 ALICE upgrade

With the success of Run I data analysis, ALICE is going for an upgrade of all its detector systems in order to fully utilise LHC upgrade for Run III [47]. The upgrade will mainly enhance the vertexing and the tracking at low-momentum as well as the ability to collect data at significantly higher rates. For this, the ITS is required to be in an improved state for the measurements of primary or secondary vertices with enhanced resolution. Moreover, the new Time Projection Chamber will use the Gas Electron Multiplier detectors instead of the multiwire proportional chambers. The upgrade will also cover, amongst others, the readout electronics of TRD, TOF and PHOS as well as DAQ system and offline data processing framework to handle the increased rate and number of events coming from the detector.

Bibliography

[1] The CERN Large Hadron Collider: Accelerator and Experiments, Volume1, Breskin, Amos (ed.) and Voss, Rudiger (ed.) (CERN), 2009.

[2] The Large Hadron Collider LHC, E. Keil, LHC Project Report 79, 1996 DPF-DPB Workshop-Snowmass, Colorado, USA.

[3] Technical Proposal for A Large Ion Collider Experiment at the CERN LHC, CERN/LHCC 95-71 (1995).

[4] ATLAS Technical Proposal, CERN/LHCC 94-43 (1994).

[5] The Compact Muon Solenoid Technical Proposal, CERN/LHCC 94-38 (1994).

[6] LHCb Technical Proposal, CERN/LHCC 98-4 (1998).

[7] Technical Proposal for the CERN LHCf Experiment, CERN/LHCC 2005-032 (2005).

[8] TOTEM Technical Proposal, CERN/LHCC 99-7 (1999).

[9] The ALICE experiment at the CERN LHC, 2008 JINST 3 S08002.

[10] Alice Technical Design Report of the Inner Tracking System (ITS), ALICE Collaboration, CERN, 1999.

[11] Technical Design Report of the Time Projection Chamber, ALICE Collaboration, CERN/LHCC 2000-001, 2000.

[12] Technical Design Report of the Transition Radiation Detector, ALICE Collaboration, CERN/LHCC 2001-021, 2001.

[13] Technical Design Report of the Time of Flight System, ALICE Collaboration, CERN/LHCC 2000-012, 2000.

[14] Technical Design Report of the High Momentum Particle Identification Detector, ALICE Collaboration, CERN/LHCC 98-19, 1998.

[15] Technical Design Report of the Photon Spectrometer, ALICE Collaboration, CERN/LHCC 99-4, 1999.

[16] The Electromagnetic Calorimeter Addendum to the Technical Proposal, ALICE Collaboration, CERN-LHCC-2006-014, 2006.

[17] ALICE: Physics Performance Report, ALICE Collaboration, Volume I, J. Phys. **G30**, 1517 (2004).

[18] ALICE Technical Design Report of the Dimuon Forward Spectrometer, ALICE Collaboration, CERN, 1999.

[19] Technical Design Report of the Photon Multiplicity Detector (PMD), ALICE Collaboration, CERN/LHCC 99-32, 1999.

[20] Technical Design Report on Forward Detectors: FMD, T0, V0, ALICE Collaboration, CERN-LHCC-2004-025, 2004.

[21] Technical Design Report of the Zero Degree Calorimeter (ZDC), ALICE Collaboration, CERN/LHCC 99-5, 1999.

[22] G. Contin, 2012 JINST 7 C06007.

[23] K. Aamodt et al., ALICE Collaboration, JINST 5, P03003 (2010).

[24] J. Adam et. al., ALICE Collaboration, Int. J. Mod. Phys. **A29**, 1430044 (2014).

[25] W. Blum, W. Riegler, and L. Rolandi, Springer-Verlag, 2nd edition (2008).

[26] The Time of Flight detector of ALICE at the LHC: construction, test and commissioning with cosmic rays, Thesis by Roberto Preghenella.

[27] A. Alici, for the ALICE Collaboration, Nuclear Instruments and Methods in Physics Research **A706**, 29-32 (2013).

[28] Performance of the ALICE VZERO system, 2013 JINST 8 P10016.

[29] The ALICE experiment at the CERN LHC, JINST 3 S08002 (2008).

[30] THE ALICE EXPERIMENT CONTROL SYSTEM, F. Carena et. al, CERN, Geneva, Switzerland [https://ph-dep-aid.web.cern.ch/ph-dep-aid/DAQ-shifter/TheALICE_ECS.pdf]

[31] ALICE trigger system for newcomers, ALICE twiki: http://www.ep.ph.bham.ac.uk/twiki/bin/view/ALICE/AliceTriggerIntroduction.

[32] M. Krivda et. al., The ALICE trigger electronics.

[33] F. Bergsma et al., CERN ALICE DAQ Group, ALICE DAQ and ECS users guide, ALICE Internal Note ALICE-INT-2005-015, http://cdsweb.cern.ch/record/960457.

[34] V. Lindenstruth et al., for the ALICE Collaboration, Nuclear Instruments and Methods in Physics Research **A534**, 47-52 (2004).

[35] ALICE Environment for Grid, http://alien2.cern.ch/.

[36] AliEn: ALICE Environment Grid Framework, http://alien.web.cern.ch/.

[37] The ALICE experiment Offline project, http://alice-offline.web.cern.ch/.

[38] An object-oriented data analysis framework, http://root.cern.ch.

[39] T. Sjöstrand, S. Mrenna and P. Skands, JHEP**05** (2006).

[40] X. N. Wang and M. Gyulassy, Phys. Rev. **D44**, 3501 (1991).

[41] R. Brun, R. Hagelberg, M. Hansroul and J. C. Lassalle, CERN-DD-78-2-REV (1978).

[42] S. Agostinelli et al., GEANT4 Collaboration, Nucl. Instrum. Meth. **A506**, 250 (2003).

[43] A. Fasso et al., La Jolla, California, arXiv:hep-ph/0306267 (2003).

[44] P. Billoir, Nucl. Instrum. Meth. **A 225**, 352 (1984).

[45] P. Billoir, Nucl. Instrum. Meth. **A241**, 115 (1985).

[46] P. Billoir, Comput. Phys. Commun. 57, 390 (1989).

[47] Upgrade of the Inner Tracking System Conceptual Design Report, ALICE Collaboration, CERN-LHCC-2012-013/LHCC-P-005.

Chapter 5

Angular correlations between D^0 mesons and charged particles in pPb with ALICE

In this chapter the analysis details and results for the correlation study between D^0 mesons and charged primary particles using ALICE pPb data at $\sqrt{s_{\mathrm{NN}}}$ = 5.02 TeV will be discussed. At first, the reconstruction of D^0 mesons from its hadronic decay channel and the selection of charged primary particles (act as associated particles for correlations analysis) will be discussed along with the data set used for the correlation analysis. Then, the details of correlation analysis procedure and ALICE published results as an outcome of this analysis will be discussed.

5.1 Data, Kinematic cuts & D^0 meson reconstruction

5.1.1 Data set and Kinematic cuts

The analysis is performed on the proton-lead data at $\sqrt{s_{\mathrm{NN}}} = 5.02$ TeV taken by ALICE in 2013 (LHC Run I) and on corresponding Monte Carlo samples of same energy. The 2013 pPb run lists with periods are given in table 5.1. The total number of minimum-bias events analysed is ~ 100 million corresponding to an integrated luminosity of about $L_{int} = 50\ \mu b^{-1}$. In this case the minimum-bias trigger requires signals in both the V0 detectors. In pPb collisions, the centre-of-mass reference frame of the nucleon-nucleon collision is shifted in rapidity by $\Delta y_{NN} = 0.465$ in the proton direction with respect to the laboratory frame, due to the different per-nucleon energies of the proton and the lead beams. Only events with a reconstructed primary interaction vertex within ± 10 cm from the centre of the detector along the beam line are considered. The Monte Carlo (MC) production LHC13d3 is used to compute the efficiency & acceptance, feed-down corrections etc. This production is anchored to the two data samples used in order to have the same conditions in terms of detector performance and beam conditions. This MC events are generated using a cocktail of pPb HIJING events and PYTHIA6 signals [1].

D^0 mesons are obtained for ten transverse momentum (p_{T}) ranges in 1-24 GeV/c. Then, they are correlated with associated charged particles and evaluated by integrating the results in three wider $p_{\mathrm{T}}(\mathrm{D})$ intervals to reduce the statistical fluctua-

Type	Production	Run list
Data	LHC13b, pass3/AOD	195483, 195482, 195481, 195480, 195479, 195478,195391, 195390, 195389, 195351,195346, 195344 = [12runs],
	LHC13c, pass2/AOD	195677, 195676, 195675, 195673, 195644,195635, 195633, 195596, 195593, 195592,195568, 195567, 195566, 195532, 195531,195529 = [16 runs]
MonteCarlo	LHC13d3, AOD	195389, 195391, 195478, 195479, 195480, 195481, 195482, 195483, 195529, 195531, 195566, 195567, 195568, 195592, 195593, 195596, 195633, 195635, 195644, 195673, 195675, 195677 = [22 runs]

Table 5.1: Data Set and Run list.

tions: $3 < p_{\mathrm{T}}(\mathrm{D}^0) < 5$ GeV/c, $5 < p_{\mathrm{T}}(\mathrm{D}^0) < 8$ GeV/c and $8 < p_{\mathrm{T}}(\mathrm{D}^0) < 16$ GeV/c. D^0 mesons in each of these $p_{\mathrm{T}}(\mathrm{D}^0)$ intervals are correlated in four p_{T} intervals of associated charged particles: $p_{\mathrm{T}}^{assoc} > 0.3$, 0.5, 1 GeV/c and $0.3 < p_{\mathrm{T}}^{assoc} < 1.0$ GeV/c.

5.1.2 Reconstruction of D^0 mesons

The rest mass of D^0 meson is $m_{\mathrm{D}^0} = 1864.83 \pm 0.14$ MeV and its mean proper decay length $c\tau = 122.9$ μm [2]. D^0 and its anti-particle may decay in hadronic or semi-leptonic channels. In this analysis the hadronic decay channel, $\mathrm{D}^0 \to \mathrm{K}^-\pi^+$ is used which has a branching ratio of $3.88 \pm 0.05\%$ [2].

The yields of prompt D^0 mesons can be calculated from the production cross section. In practice, the cross section for a hard process is given by,

$$\left.\frac{d\sigma^{\mathrm{D}^0}}{dp_{\mathrm{T}}}\right|_{|y|<0.5} = \frac{1}{\Delta y \Delta p_{\mathrm{T}}} \frac{f_{prompt}(p_{\mathrm{T}}) \cdot \frac{1}{2} N_{raw}^{\mathrm{D}^0+\overline{\mathrm{D}^0}}(p_{\mathrm{T}})\Big|_{|y|<y_{fid}} \cdot c_{refl}(p_{\mathrm{T}})}{(Acc \times \epsilon)_{promt}(p_{\mathrm{T}}) \cdot BR \cdot L_{int}} \tag{5.1}$$

The raw yields $N_{raw}^{\mathrm{D}^0+\overline{\mathrm{D}^0}}$ are divided by a factor of two to obtain the average yields (particle and antiparticle). The reflection factor ($c_{refl}(p_{\mathrm{T}})$) is introduced to correct the raw yields for the contribution of signal candidates that are counted both as a particle (D^0) and an antiparticle ($\overline{\mathrm{D}^0}$). To correct for the contribution of B meson decay feed-down, the raw yields are multiplied by the prompt factor (f_{prompt}). Furthermore, they are normalized by the product of prompt D meson acceptance and efficiency [$(Acc \times \epsilon)_{prompt}$], the decay channel branching ratio (BR), the transverse momentum width (Δp_{T}), rapidity interval width ($\Delta y = 2 \cdot y_{fid}$) and integrated luminosity (L_{int}). The normalization by Δy gives the corrected yields in one unity of rapidity ($|y_{lab}| < 0.5$) ($-0.96 < y_{cms} < 0.04$ in pPb collisions). The integrated luminosity L_{int} was computed as $N_{pPb,MB}/\sigma_{pPb,MB}$ where $N_{pPb,MB}$ is the number of pPb collisions passing the minimum-bias trigger condition and $\sigma_{pPb,MB}$ is the cross section of the minimum-bias trigger which was measured with the pPb van der Meer scan [3].

The D^0 meson signal is obtained via an invariant mass analysis of $\mathrm{K}^-\pi^+$ decay topologies. All possible pion and kaon pairs which include actual pairs coming from D^0 meson and fake combinatorial pairs, are considered as "***candidates***" for D^0 mesons. This leads to a very low signal over background, S/B $\sim 10^{-6}$. Therefore, in order to improve the signal over combinatorial background, it is necessary to invoke some topological and kinematical cuts on the decay tracks and on the reconstructed secondary vertices. D^0 meson can come from D^{*+} meson decay as $D^{*+} \rightarrow D^0\pi^+$ with a branching fraction of 68%. This allows a good cross-check and an additional benchmark test of the stand-alone D^0 analysis.

The selection starts with selection of the "good events" as the reconstruction is done via event-by-event analysis. Via secondary vertex reconstruction the D^0 candidates are then selected according to quality and topological cuts and particle identification. The candidates left undergo an invariant mass analysis and raw signals are evaluated.

5.1.2.1 Event selection and Secondary Vertex

The "good events" selection is done via reconstruction of primary vertex with $z_{vtx} <$ 10 cm. Depending on the reconstruction procedure, events can be described in 4 types:

- No vertex events which are at the end discarded
- Global events where the vertex has been reconstructed with global (ITS+TPC and TPC only) tracks
- Events where the vertex has been reconstructed only with SPD tracklets and the 3D (x, y, z) coordinates have been determined (VertexerSPD3D)
- Events reconstructed by SPD tracklets but the z-vetrex information is only extracted (VertexerSPDz)

For better resolution in the transverse plane compared to the vertices reconstructed with only SPD tracklets, events with vertex reconstructed using global tracks are chosen for this analysis. Vertex with $|z_{vtx}| < 10$ cm and tracks reconstructed by ITS and TPC in $\eta < 0.8$ are kept. The pile-up events are rejected by applying a cut on two vertices at a minimum separation of 0.8 cm found by the SPD vertexer. In the pPb minimum bias data sample the pile-up rejected events are low.

Secondary vertices of D mesons are reconstructed from the decay tracks, using the same algorithm as for the primary vertex reconstruction. The implementation and performance of the vertex finding algorithm are described in detail in [4]. Candidate pairs are matched using ITS+TPC tracks having $\eta < 0.8$ and $p_{\mathrm{T}} > 0.3$ GeV/c. Also, the candidate tracks must have at least 70 associated clusters in the TPC with $\chi^2/ndf < 2$ and refitted inwards from TPC to ITS.

5.1.2.2 Topological cuts

In order to gain good signal over background for the D^0, a set of topological cuts on the decay tracks and on the secondary vertex position have been applied. The statistical parameter which tells us how well the signal extraction is performed over statistical fluctuations of background, is the statistical significance. It is defined as:

$$\mathcal{S} = \frac{S}{\sqrt{S+B}} \tag{5.2}$$

where S is the signal and B the combinatorial background calculated from invariant mass spectra. Therefore, the main motivation of application of topological cuts is to optimize the signal and background selections (improvement of significance $\mathcal{S}$).

Figure 5.1 shows a schematic diagram of D^0 meson decaying into kaon and pion.

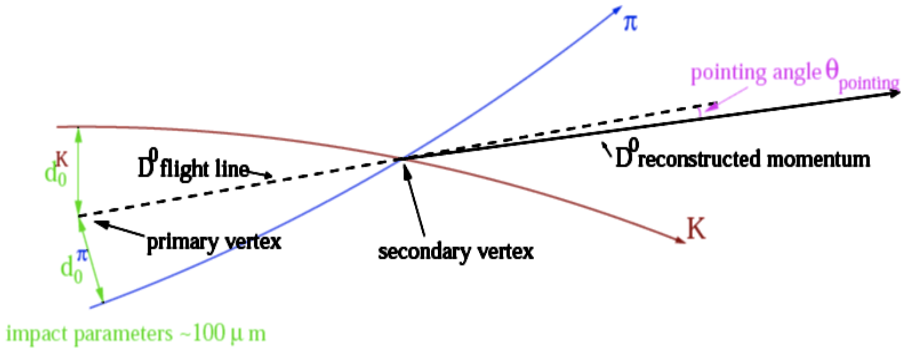

Figure 5.1: Topology of the D^0 meson decay.

There are two kind of variables applied on the selection of secondary vertices: single track variables and pair variables. Single track cuts are applied on daughter track momentums ($p_{\mathrm{T}}^{\mathrm{K}}$, p_{T}^{π}) and on their impact parameters (d_0^K, d_0^{π}). For a pair of tracks (pair variables), cuts are applied on mass window ($|M - M_{\mathrm{D}^0}|$), the distance of closest approach (dca), the cosine of pointing angle (cosθ_{point}), the cosine of decay angle (cosθ^*), the product of impact parameters ($d_0^K \times d_0^{\pi}$), the decay length (L_{XY}) and the normalized decay length (L_{XY}/δ).

Single track variables:

Momentum cuts ($p_{\mathrm{T}}^{\mathrm{K}}$, p_{T}^{π})

A minimum transverse momentum cut is applied on kaons and pions. In pPb, the cut threshold is 0.7 GeV/c. This reduces the contribution of tracks coming from primary vertex and gives better secondary vertex resolution. Also, the momentum cut rejects some background candidates effectively at low-p_{T}.

Impact parameter cuts (d_0^K, d_0^{π})

The impact parameter (d_0) is the distance of closest approach of a particle trajectory to the primary vertex. Quality cuts on the minimum impact parameter could also reduce the background from primary tracks whereas the upper cut could reduce the background coming from strange and bottom hadrons. The determination of impact parameter of D^0 decay products at low-p_T depends mainly on the detector resolution. In this analysis for pPb data, the optimized impact parameters for both kaon and pion are taken as 0.1 cm.

Pair variables:

The pair variables are more powerful in the rejection of background candidates.

Distance of closest approach (dca) between kaon and pion tracks

The distance of closest approach (dca) between the two tracks is the length of the segment minimizing the distance between the two track helices. So, while secondary vertex is reconstructed using the tracks, we can approach to a certain closest distance between the track helices. Ideally this distance between the track helices should be zero if they are coming from a deacy vertex (primary or secondary). But in practice it is non-zero as the the observed dca is determined by the detector spatial resolution on the track position which has some finite value. Left panel of Fig. 5.2 shows the dca for signal (red and more scattered points) and background (black) pairs. The distribution of background candidates which are mostly made of primary track pairs is flatter than the signal pairs. Their dca distribution is strongly correlated to the impact parameter resolution i.e to the tracks transverse momenta. Since the decay products are of higher p_T, the minimum cut on p_T would give similar dca distribution

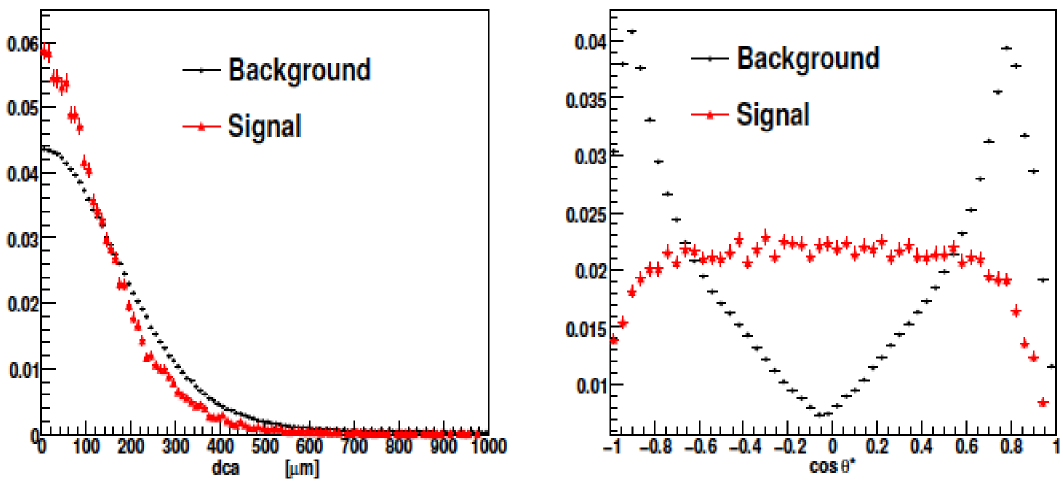

Figure 5.2: Distance to closest approach (dca, left panel) and cosθ^* (right panel) distributions for background (black circles) and signal (red triangles) candidates.

as signal. Therefore, the dca is effective in rejecting background pairs only if a cut on the minimum impact parameter is applied.

Cosine of D^0 decay angle (cosθ^*)

This is defined as the angle between the kaon momentum in the D^0 rest frame and the boost direction (sketch 5.3). Since in D^0 reference frame the daughters decay isotropically, the distribution of cosθ^* would essentially be flat for the signal candidates while the background distribution peaks at $|cos\theta^*| = 1$. This has been illustrated in the right panel of Fig. 5.2.

The depletion at $|cos\theta^*| \sim 1$ is related to the cuts applied in the candidate reconstruction ($p_{\mathrm{T}} > 0.7$ GeV/c and cos$\theta_{point} > 0$) and detector effects. This leads to the fact that if particles are emitted parallel to the mother particle momentum direction, one or two may go out of the geometrical acceptance with low momenta. In the analysis $|cos\theta^*| < 0.8$ is used for pPb, as within this range the signal dominates

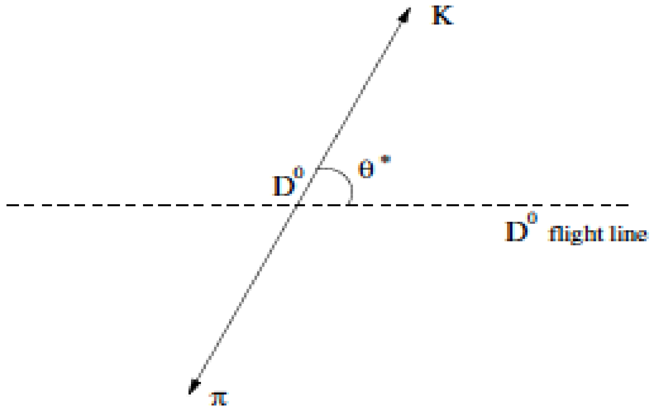

Figure 5.3: Schematic view of D^0 decay in the D^0 rest frame.

over the background candidates.

Cosine of the pointing angle (cosθ_{point}) and $d_0^K \times d_0^\pi$

The pointing angle is defined as the angle between the D^0 flight line and the total momentum of the two daughter tracks. Therefore, for signal candidates, the pointing angle should be very close to 0° (zero degree) and hence cosine will be ~ 1. For background pairs there is no correlation between the momentum directions, formed by random association of tracks and the reconstructed flight line. This is because most of the pairs are composed of primary tracks and the secondary vertex position is determined only by the finite spatial tracking resolution. Hence, the distribution of the cosine of the polar angle with respect to the flight line for the background candidates is flat as shown in left panel of Fig. 5.4

The daughters, pions and kaons, coming from a D^0 candidate have the impact parameter (d_0) of the order of $\sim 100\ \mu m$ and have opposite signs. Therefore, the product of them (d_0^K *and* d_0^π) would be a negative. Due to detector resolution, the observed distribution shows both positive and negative values, but it is strongly

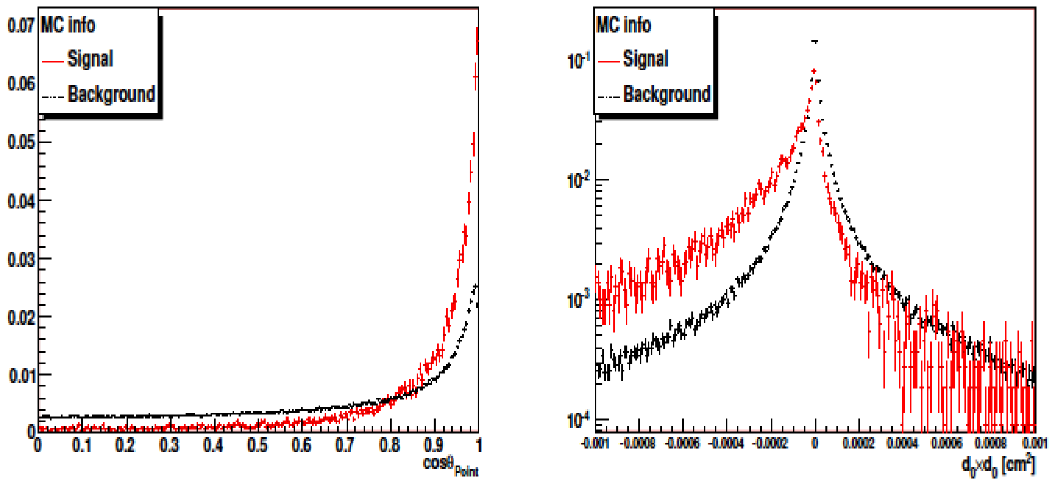

Figure 5.4: Cosine of pointing angle ($\cos\theta_{point}$, left panel) and $d_0^k \times d_0^\pi$ (right panel) distributions for background (black circles) and signal (red triangles) candidates.

asymmetric with respect to zero. Background pairs which are composed of randomly associated primary tracks with opposite charges must have a symmetric distribution. This is shown in the right panel of Fig. 5.4. So the cut value is taken as negative for lower and intermediate p_{T} of candidate. If we assign negative value of $d_0^K \times d_0^\pi$ for higher momentum, we may loss the signal candidates to a large extent.

The decay length (L_{XY})

This is defined as the distance between the primary and the secondary vertex and measured in XY plane. Since the background pairs are mainly composed by primary tracks and the separation of reconstructed secondary vertex from the primary vertex is determined only by the finite spatial tracking resolution, the value of decay length for such pairs is smaller than signal pairs. The decay length, normalized by its error, (L_{XY}/δ) is also useful for signal selection. In this analysis, we do not apply any cut on these two parameters (L_{XY} and L_{XY}/δ) to keep the statistics higher by

Topological cut	Low pT 3–5 GeV/c	Mid pT 5–8 GeV/c	High pT 8–16 GeV/c
DCA (μm)	$<$ 300	$<$ 300	$<$ 300
$\lvert cos\theta^{*}\rvert$	$<$ 0.8	$<$ 0.8	$<$ 0.9
$p_{\mathrm{T}}^{\mathrm{K}}$ (GeV/c)	$>$ 0.7	$>$ 0.7	$>$ 0.7
p_{T}^{π} (GeV/c)	$>$ 0.7	$>$ 0.7	$>$ 0.7
$d_0^K \times d_0^\pi$ (cm^2)	$<$ -3.5 $\times$ 10^{-4}	$<$ -0.8 $\times$ 10^{-4}	$<$ 1 $\times$ 10^{-4}
cosθ_{point}	$>$ 0.90	$>$ 0.85	$>$ 0.85

Table 5.2: Topological cut values for the D^0 candidate selection in the three integrated p_{T} ranges used in the correlation analysis.

compromising a little in the significance values.

The topological cut variables are tuned to maximise the value of significance which is a semi-automatic procedure using different Monte Carlo samples at LHC energies. The set of cuts used for this analysis is listed in the table 5.2

5.1.2.3 PID selection on the daughters

Additional background rejection has been achieved by using particle identification of D^0 daughters. The identification of kaons and pions is done via the energy loss deposited in the TPC and velocity measurements in the TOF detector, which helps in rejection of all candidates which are of type $\pi\pi$, KK, or contain protons or electrons. With the combination of both the detectors TPC and TOF, the D^0 daughters are identified by applying two mass hypothesis: kaon and pion hypothesis for $\mathrm{D}^0/\overline{\mathrm{D}^0}$. For example, in kaon hypothesis, +1 is assigned if the particle is identified as kaon, -1 if it is identified as non-kaon, and 0 if it is not identified. This is done by consulting both detectors and their exit codes (±1, 0) are summed. The decoded answer will be: a kaon if +2, not a kaon if -2, compatible with a kaon if ±1 or 0. The same applies for the pion-hypothesis. The D^0 or $\overline{D^0}$ is identified when positive daughter is identified as K (π) and the negative one as π (K).

Now, for both the detectors the identification is done in units of resolution of the difference between the measured and expected signals (nσ cut). Depending on the p_T, each track has its own resolution σ as measured in TPC or TOF.

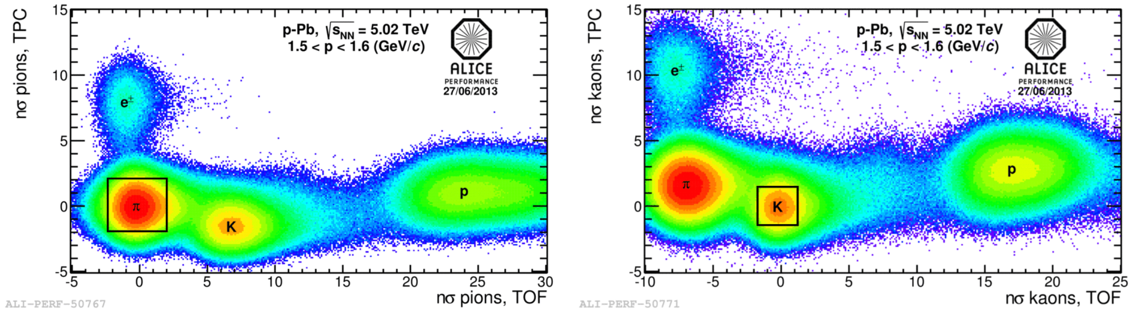

Figure 5.5: nσ TPC vs nσ TOF for pion (left) and kaon (right).

The Fig. 5.5 shows the the distribution of nσ^{TOF} vs nσ^{TPC} for pion (left) and kaon (right). The box-highlighted area near (0,0) is close to the expected pion or kaon. In the TPC, a 2σ selection was applied to identify both pions and kaons. If the TPC dE/dx signal is between 2σ and 3σ from the expected value, it is kept as unidentified and both the kaon and pion mass hypotheses is assigned to it when building the D^0 candidate pairs. For the low momentum candidates ($0.6 < p_T < 0.8$ GeV/c), a cut of 1σ is applied and above 3σ, the tracks are discarded as a kaons (pions).

A 3σ cut is applied to select the kaons detected by the TOF. For momentum $p_T > 2$ GeV/c, particles are considered as non-identified and both mass hypotheses are used. Above 4 GeV/c, PID is less important as the candidates acquire high momentum with smaller background.

5.1.3 Raw signal extraction

After passing the topological cuts and PID selection, the selected candidate pairs are used to get D^0 meson via invariant mass calculation:

$$\begin{aligned} P_K &= (E_K, \vec{p_K}), \qquad P_\pi = (E_\pi, \vec{p_\pi}) \\ P^2_{D^0} &= M^2_{D^0} = (P_K + P_\pi)^2 \\ &= (E_K + E_\pi)^2 - (p^2_K + p^2_\pi + 2p_K p_\pi cos\alpha)^2 \\ &= m^2_K + m^2_\pi + 2(E_K E_\pi - p_k p_\pi cos\alpha) \end{aligned} \tag{5.3}$$

where P is used to indicate four-momenta, $\vec{p}$ stands of the three-momenta and α is the angle between the pion and kaon three-momenta. In the relativistic limit (p $\simeq$ E), the invariant mass is approximated as:

$$M^2_{D^0} \simeq 2p_K p_\pi (1 - cos\alpha) \tag{5.4}$$

The expected error on the invariant mass can be estimated as:

$$\frac{\sigma(M)}{M} \sim \frac{1}{\sqrt{2}} \frac{\sigma(p)}{p} \tag{5.5}$$

where the error related to the angle is neglected and relative uncertainty on momentum is taken as constant. Using a reference value $\sigma(p)/p = \sigma(p_T)/p_T \sim 0.7\%$,

$\sigma(M) \sim 1865 \times 0.005 \sim 9.3$ MeV is expected in the D^0 mass region. A topological cut on $|M - M_{D^0}|$ is applied to take into account the expected mass resolution.

The invariant mass is evaluated for D^0 transverse momentum range of 1 to 24 GeV/c. To extract the signal, the mass distributions are fitted with the sum of a Gaussian function for the signal and an exponential for the combinatorial background. The procedure followed in this thesis is same as described here [5]. Figure 5.6 shows the fitted invariant mass distribution of D^0 in different p_T ranges for pPb minimum bias events. Signal values from the fit function in a 3σ range around the mean value can be extracted. The signal (S), background (B) and significance values ($\mathcal{S}$) are written for each distribution along with mean and σ from the Gaussian function. The D^0 mesons are selected in the rapidity range varying from $|y|$ <0.5 at low-p_T to $|y|$ <0.8 for p_T >5 GeV/c.

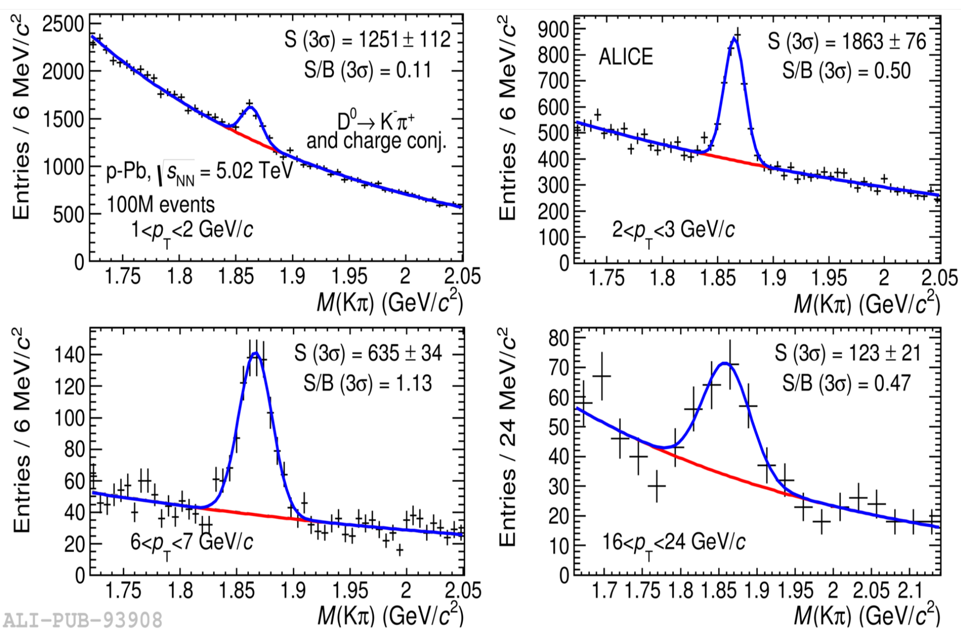

Figure 5.6: D^0 invariant mass distributions in pPb collisions. The signal is extracted in 4 p_T intervals in the range $1 < p_T < 24$ GeV/c.

Reflected D^0 signal

The invariant mass spectra is build with both D^0 and $\overline{D^0}$ candidates. But it may happen that the due to wrong kaon or pion hypothesis, the kaon is misidentified as a pion and vice versa. With this wrong evaluation of candidates, a broader invariant mass distribution will be centred at the D^0 peak. This is called reflected signal of D^0 meson. The width of the reflected distribution depends on momentum which is absent in case of D^0 obtained from proper kaon and pion identification. Figure 5.7 shows the transverse momentum dependence of the width of the reconstructed D^0 (left panel) compared to the width of the reflected signal (right panel). The contribution of the reflection to the D^0 signal varies with the transverse momentum.

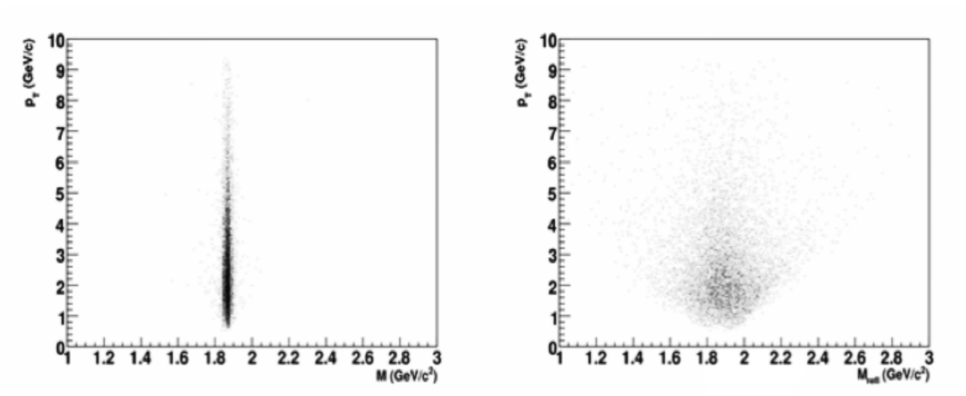

Figure 5.7: D^0 invariant mass distribution as a function of the transverse momentum (left) compared with the reflection invariant mass distribution as a function of the transverse momentum (right).

5.1.4 Acceptance and efficiency correction

From the invariant mass fit, the raw yield is extracted. This is only a small fraction of the total number of D^0 mesons produced in the collisions. D^0 signal may be lost due to the limited detector acceptance, the primary vertex and track reconstruction efficiency and the topological cuts applied on the candidates. Therefore, in order to get the total yield, the raw yield must be corrected and for which Monte Carlo samples are used. The charm enriched samples are used where D mesons are forced to decay in the preferred decay channels.

Efficiency and acceptance correction has been done by using "Correction Framework" (CF) build by ALICE–PWGHF group. The Correction Framework includes a number of "Containers" to store candidates at specific stages (steps). The efficiency is computed both for prompt D (both D^0 and $\overline{D^0}$) mesons and feed-down D mesons from B meson decays. In the CF, the efficiency is calculated in following steps:

- **Step-Generated:** Container includes the generated $D^0/\overline{D^0}$ coming from a charm quark for $|z_{vtx}| < 10$ cm.
- **Step-Generated in Limited Acceptance:** In this step Container stores the generated $D^0/\overline{D^0}$ which are within the limited detector acceptance $|y| < 0.5$.
- **Step-Acceptance:** Container takes the $D^0/\overline{D^0}$, generated with the the acceptance conditions $|\eta| < 0.9$ and $p_{\mathrm{T}} > 0.1$ GeV/c.
- **Step-Reconstructed:** The candidates are selected after passing the track quality cuts.

- **Step-RecoCuts:** Container stores the candidates which pass the topological cuts.
- **Step-RecoPID:** Finally the candidates pass through PID selection after passing topological cuts.

The acceptance correction factor is obtained as the ratio of the "Step-Acceptance" and "Step-Generated in Limited Acceptance" Containers. The efficiency correction factor is obtained as the ratio of the "Step-RecoPID" and "Step-Acceptance" Containers.

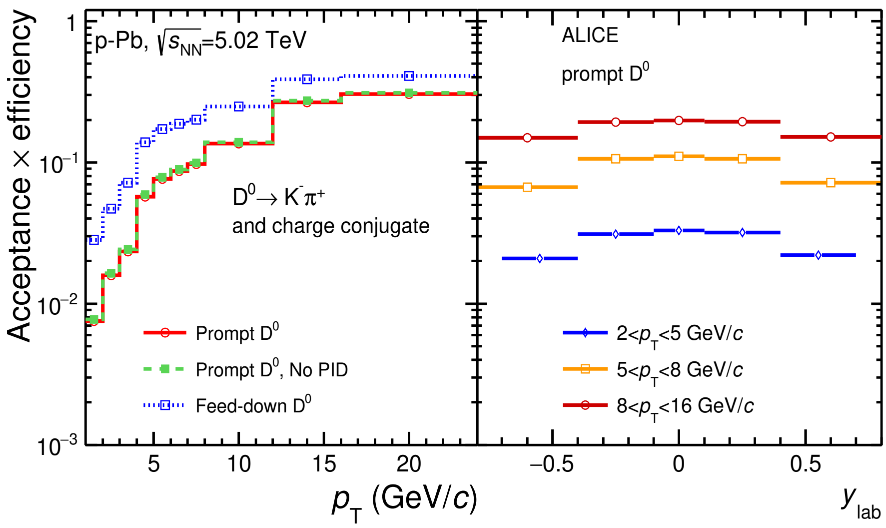

Figure 5.8: Acc $\times\epsilon$ as a function of p_{T} for prompt and feed-down D^0 mesons in the minimum bias pPb events.

The left panel of Fig. 5.8 shows the D^0 meson acceptance times efficiency (Acc $\times\epsilon$) for the minimum bias pPb events as a function of p_{T} in the rapidity range $|y_{lab}| < y_{fid}(p_{\mathrm{T}})$. The feed-down (D coming from B meson decay) efficiency is higher than the prompt one because the D mesons coming from B feed-down are more displaced from the primary vertex and they are therefore preferentially selected by the cuts based on track/vertex displacement. Also, the efficiency without PID selection, shown for comparison, is the same as that with PID selection. The right panel of Fig. 5.8 shows the Acc$\times\epsilon$ as a function of rapidity (y_{lab}) for different D^0 p_{T} bins.

5.1.5 Associated charged particle selection

Associated particles are defined as all charged primary particles with $p_{\mathrm{T}}^{assoc} > 0.3$ GeV/c and within $|\eta| < 0.8$, except for the decay products of the trigger D^0 mesons. Also, particles coming from weak decays or originating from interactions with the detector material are defined as secondary particles and are discarded. The associated tracks are chosen by applying the following criteria:

- TPC refit but no ITS refit
- a minimum of 3 and 70 clusters in the ITS and TPC respectively
- a χ^2/NDF = 4 of the momentum fit in the TPC
- DCA to primary vertex along z: $\mathrm{DC}A_z < 1$ cm
- DCA to primary vertex along xy: $\mathrm{DC}A_{xy} < 0.25$ cm

These selection cuts identify the primary particles with a purity (p_{prim}) of approximately 96%. Low-p_{T} pions may come from $\mathrm{D}^{*+} \rightarrow \mathrm{D}^0\pi^+$ decay which is named as "soft-pions" and are removed from the sample of associated particles by rejecting tracks that yield a ΔM compatible within 3σ with the value expected for D^{*+} mesons.

In the following sections the analysis procedure for the angular correlations between D^0 meson and unidentified charged particles in pPb collisions at $\sqrt{s_{\mathrm{NN}}} = 5.02$ TeV energy will be discussed in details. D^0 is taken as trigger charmed meson and is reconstructed via $\mathrm{D}^0 \rightarrow \mathrm{K}^-\pi^+$ hadronic channel. The associated particles are the unidentified charged tracks excluding D^0-daughters and other resonance decays.

5.2 Analysis Details

The basic analysis strategy is adopted from di-hadron angular correlations but it is different in various aspects and technicalities in order to reach the final correlations results. The fully corrected angular correlations are build with trigger charmed meson (D^0) and unidentified charged primary particles. The basic difference between conventional di-hadron correlations approach and this analysis is based on the trigger and associated particle selection. Apart from the trigger origin, in this analysis the trigger particle is selected by its identity, not by kinematic cuts over associated charged particles (conventional correlations approach would give $p_{\mathrm{T}}(\mathrm{D}^0) > p_{\mathrm{T}}^{assoc}$ as discussed in chapter 1). As the heavy-flavor study suffers from statistics and precessional measurements in Run-I LHC data, the momentum range of the associated particles is not bounded, rather we apply only a minimum transverse momentum cut on associated charged particles. This selection is worthy as the trigger particle here has a different origin than the associated charged particles. The analysis is performed over 3 different p_{T} ranges of trigger; $3 < p_{\mathrm{T}}(\mathrm{D}^0) < 5$ GeV/c, $5 < p_{\mathrm{T}}(\mathrm{D}^0) < 8$ GeV/c, $8 < p_{\mathrm{T}}(\mathrm{D}^0) < 16$ GeV/c and each D^0 meson in each of these $p_{\mathrm{T}}(\mathrm{D}^0)$ intervals is correlated in 4 p_{T} intervals of associated charged particle: $p_{\mathrm{T}}^{assoc} > 0.3$, 0.5, 1 GeV/c and $0.3 < p_{\mathrm{T}}^{assoc} < 1.0$ GeV/c.

The analysis steps are the following:

- Reconstruction and signal extraction of D^0 meson (discussed in previous sections)
- Charged particle selection (discussed in previous sections)
- Correlation of D candidates with associated charged particles
- Subtraction of correlations due to background candidates using SideBand method
- Corrections for:
    1. Detector effects (local inhomogeneities and limited acceptance) via Event Mixing
    2. D^0 meson reconstruction and selection efficiency
    3. Associated track reconstruction efficiency
    4. Contamination from secondary tracks
    5. Contribution due to feed-down from beauty hadron decays
- Evaluation of systematic uncertainties
- Fit to the azimuthal correlation distributions
- Comparison with models
- Average D mesons-charged particle angular correlations and average scale uncertainties

5.2.1 Correlations between D^0 mesons and charged particles

Particle pairs are formed by associating each trigger particle (D^0 candidates) with the remaining charged primary particles (after passing the track selection cuts and excluding the D^0 daughters) in each event (called same event analysis, SE) in the above mentioned trigger p_T intervals and associated charged particle p_T ranges. The pseudrapidity difference $\Delta\eta = \eta_{trig} - \eta_{assoc}$ and azimuthal angle difference $\Delta\varphi = \varphi_{trig} - \varphi_{assoc}$ are used to build the two-dimensional correlations. Though the $\Delta\varphi$ values vary from 0 to 2π, for a good view of correlation distributions, $-\pi/2$ to $3\pi/2$ interval is chosen. Again to reduce the statistical fluctuations the correlation distributions are reflected in the range 0 to π. The definition of the same event correlation function is same as mentioned in chapter 2:

$$C(\Delta\eta, \Delta\varphi) = \frac{d^2N^{pairs}}{d\Delta\varphi d\Delta\eta} \tag{5.6}$$

Since the D^0 candidates are reconstructed using kaon and pion pairs (as discussed in previous sections), the trigger sample contains both the fake pairs (background candidates) and genuine pairs (signal candidates). During the building of two-dimensional correlations, all the D^0 candidates are correlated with the associated charged particles. Each correlation entry in the two-dimensional correlation distributions is weighted by trigger selection & reconstruction efficiency and associated track selection efficiency (efficiency correction).

The efficiency weighted correlations are built for 3 mass regions of trigger D^0 mesons as:

- Signal region: $\pm\, 2\sigma$ (σ from the Gaussian fit) band where the mass peak lies.
- Left Sideband region: 4σ band on the left side of mass peak
- Right Sideband region: 4σ band on the right side of mass peak

The regions are shown in the Fig. 5.9 by different colors. The signal region ($C^{peak}(\Delta\eta, \Delta\varphi)$) [red+yellow band] or Sidebands ($C^{SB}(\Delta\eta, \Delta\varphi)$) (left+right) [green bands] correlations are evaluated by pairing the candidates from that region with associated charged particles.

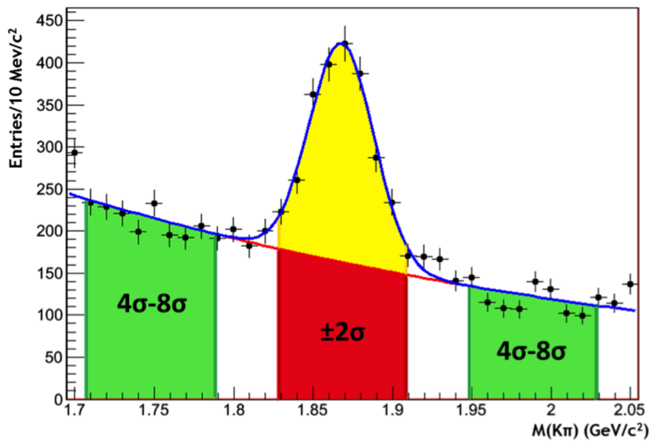

Figure 5.9: D^0 invariant mass distribution with Gaussian+exponential fit in the Signal (yellow+red in $\pm 2\sigma$) and Sidebands (green in $\pm 4\sigma$) regions [6].

5.2.2 Signal region background subtraction (Side-Band method)

The signal region correlations also contain correlations due to background candidates (below the mass peak) which passed the D^0 selection cuts. In order to subtract the background correlations due to those background candidates, we use the correlations from sidebands. At first the total sideband correlation ($C^{SB}(\Delta\eta, \Delta\varphi)$) distributions are normalised by a factor which is the ratio of the background integral in the signal region (B^{peak}) over the integral in the sidebands ($B^{sidebands}$). The normalised background contribution is then subtracted from signal $C^{peak}(\Delta\eta, \Delta\varphi)$ region correlation distributions.

$$C^{signal}(\Delta\eta, \Delta\varphi) = p_{prim} \cdot C^{peak}(\Delta\eta, \Delta\varphi) - \frac{B^{peak}}{B^{sidebands}} \times C^{SB}(\Delta\eta, \Delta\varphi) \tag{5.7}$$

where p_{prim} is the purity of the primary particle sample (see later section). Fig-

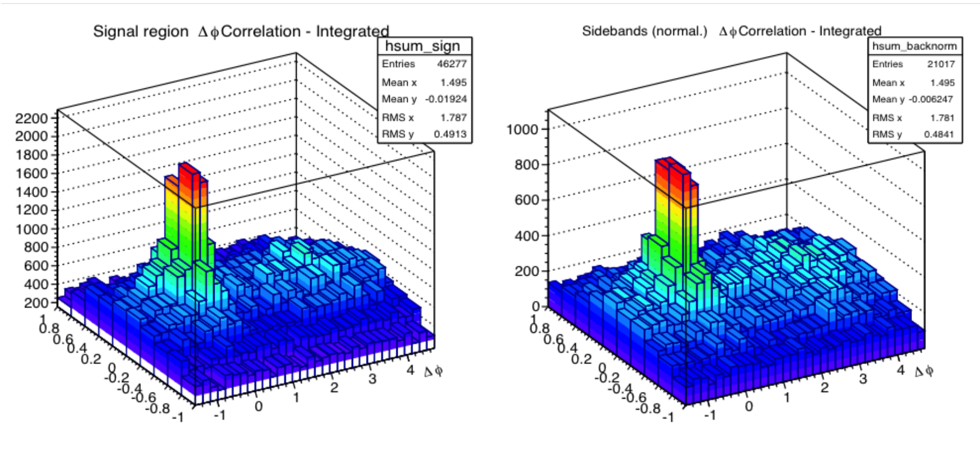

Figure 5.10: Signal region (left) and total sideband region (right) correlation distribution for the D^0 candidates correlated with the associated charged primary particles in the same event.

ure 5.10 shows the two-dimensional sample correlations of signal region (signal+background) on the left panel and total sideband correlation (left+right sideband) on the right panel. Interestingly the sideband candidates also gives the same kind of correlation as the original signal candidates. This is because, the background D^0s are built by one of their two daughters, decay tracks from a real D^0. Also high-p_T tracks belonging to jets, can be misidentified as D^0 daughters. Therefore those candidates can produce the same correlations structure as the real D^0s do.

One should take a note that, the "side-band correction" is applied on the two-dimensional correlation distribution after the Event-Mixing correction (see next section) along with efficiency correction.

5.2.3 Corrections to the correlation distributions

The correlation distributions need to be corrected for different reasons. We apply mixed-event correction to take care of the detector inhomoginities and pair acceptance. They are also corrected for trigger and associated charged particle efficiencies. The side-band subtraction method is applied to the two-dimensional correlation after these two corrections. Then the corrected two-dimensional correlation distribution is projected over $\Delta\varphi$ integrating over the particular $\Delta\eta$ range and is normalised by number of triggers. The additional corrections applied are the residual contaminations from secondary tracks, the feed-down D^0 contributions coming from beauty hadron decays and the contaminations from secondary tracks and soft-pions.

5.2.3.1 Correction via Event Mixing technique

The correlation distributions $C^{peak}(\Delta\eta, \Delta\varphi)$ and $C^{SB}(\Delta\eta, \Delta\varphi)$ are corrected for the limited detector acceptance and detector spatial inhomogeneities using the event mixing technique. Structures in the angular correlation distribution, even for uncorrelated pair of particles, originate from the limited detector acceptance or angular inhomogeneities in the track reconstruction efficiency. In particular, these always produce a peak in the near-side.

Event pools	Values
zVtx bins:	
0	-10, -2.5
1	-2.5, 2.5
2	2.5, 10
Centrality or Multiplicity bins:	
0	0, 40
1	40, 65
2	65, 500

Table 5.3: Event pool setting.

Mixed-events are obtained by taking the D^0 meson candidates from the N^{th} event and the associated tracks from other preceding selected events. A schematic view of event mixing is shown in the Fig. 5.11. ALICE software framework is used to

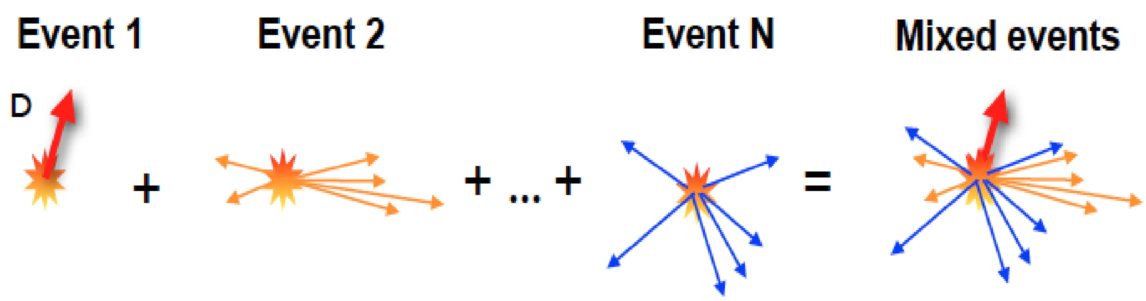

Figure 5.11: schematic diagram of event mixing.

generate mixed-event correlation distributions. Every processed event is stored in an "event pool" based on its topology. These so-called pools can be intended as sort of a matrix. The pools store events based on selection of multiplicity and primary vertex position. The setup for the pools used for this analysis on pPb data is shown in the table 5.3. Whenever a D^0 is found in an event, the pools get filled with events. As soon as the pool is ready (upon certain criteria on number of tracks and events), it starts mixing the events i.e correlate D^0 of N^{th} event with other events in that particular pool. Due to mixing of events, the distribution is expected to show no physical correlations and is used to estimate the effects of non-physical contributions to the physics we want to study. This originates from the finite pseudorapidity acceptance of the detector and the dead-zones in the detector (detector inhomoginities).

For an infinite pseudorapidity acceptance, the $\Delta\eta$ distribution will be flat. However, real detectors with finite acceptance, show a triangular shape which is not physical. Again due to detector dead-zones, the azimuthal distributions may consist of holes. This can produce an excess of correlations in the near-side of the $\Delta\varphi$ distribution. Therefore, in order to remove such non-physical influences from the physics correlations we want to study, the same event distributions are corrected by the mixed-event distributions.

In case of D^0-charged particle correlations, we generate the mixed-event distributions both for signal and sideband regions. Then the mixed-event distributions are rescaled by its average value in the range ($-0.2 < \Delta\varphi < 0.2$, $-0.2 < \Delta\eta < 0.2$). The normalization is done because the distributions contain by definition more entries than the same event. Then the same event correlation distributions are divided by the normalised mixed-event distributions (Equation 5.8).

$$\frac{d^2N^{corr}(\Delta\eta,\Delta\varphi)}{d\Delta\varphi d\Delta\eta} = \frac{\frac{d^2N^{SE}(\Delta\eta,\Delta\varphi)}{d\Delta\varphi d\Delta\eta}}{\frac{d^2N^{ME}(\Delta\eta,\Delta\varphi)}{d\Delta\varphi d\Delta\eta}} \cdot \frac{d^2N^{ME}(|\Delta\eta| < 0.2, |\Delta\varphi| < 0.2)}{d\Delta\varphi d\Delta\eta} \tag{5.8}$$

The top panel of Fig. 5.12 shows example of mixed-event distribution for signal and sideband region. Bottom panel shows the event mixing corrected signal and sideband regions. As stated in the previous section, after the event mixing correction the sideband method is applied to evaluate the signal peak correlation subtracting the background correlations below the mass peak.

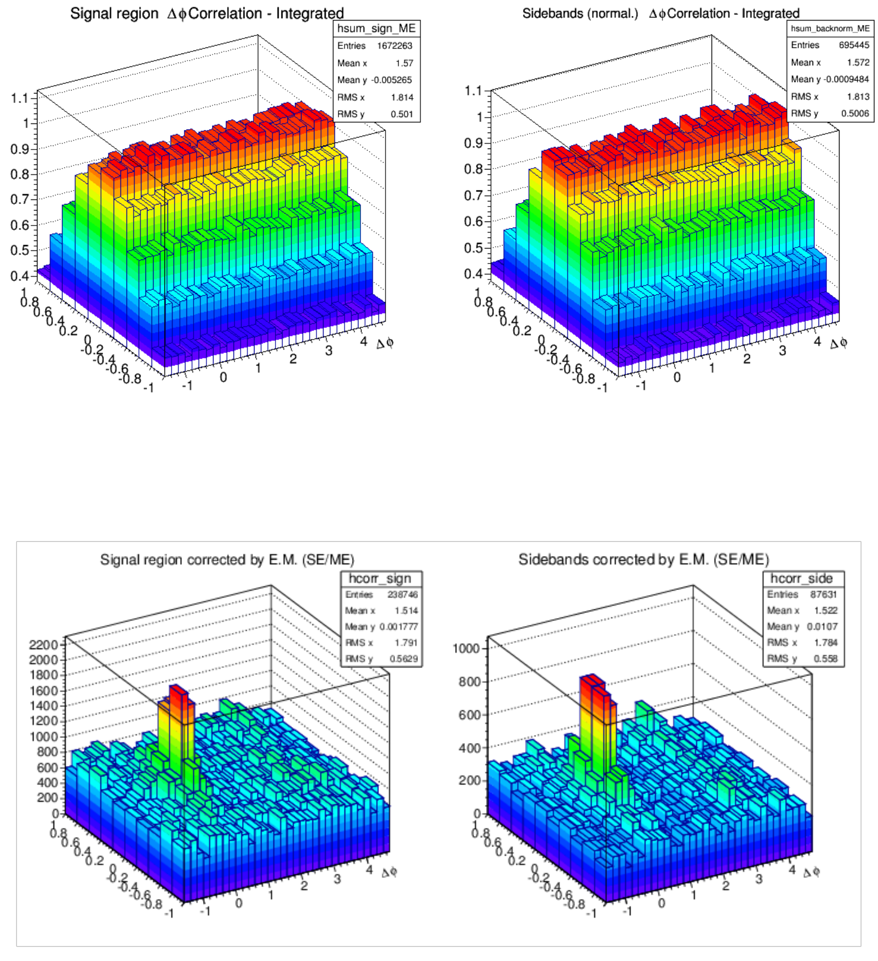

Figure 5.12: Examples of 2-dimensional ($\Delta\eta$, $\Delta\varphi$) correlation distributions between D^0 mesons and charged primary particles, for $5 < p_{\mathrm{T}}(\mathrm{D}^0) < 8$ GeV/c and $p_{\mathrm{T}}^{assoc} > 0.3$ GeV/c: (top) Mixed-event correlation for signal (left) and sideband (right) regions. (bottom) mix event corrected signal (left) and sideband (right) regions.

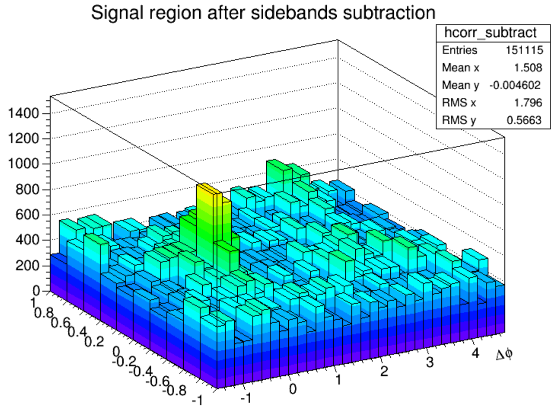

Figure 5.13: Background subtracted and mixed-event corrected 2-dimensional ($\Delta\eta$, $\Delta\varphi$) correlation distribution in the signal region.

Figure 5.13 shows the sideband corrected signal region correlation. It has been tested that by inverting the order of the event mixing correction and sideband subtraction, the correlated distributions remain same.

ALICE measures the charged particles in a pseudorapidity range of $|\eta| < 0.9$, but in this analysis the associated charged particles are taken in $|\eta| < 0.8$. Therefore, it is possible to extend the correlations to a $|\Delta\eta|$ value of 1.6. But as shown in the different figures of two-dimensional correlations, the analysis is limited to $|\Delta\eta| < 1.0$ since the study mainly focuses the jet-like correlation. Also, this is done to avoid the so-called "wing effect" which appears in large $\Delta\eta$ and the limited $\Delta\eta$ allows to reduce fluctuations due to lack of statistics at large $\Delta\eta$.

5.2.3.2 D^0 meson efficiency correction

The correlation distributions are corrected for trigger reconstruction and selection efficiency. The D^0 efficiency evaluation is discussed in the previous sections. The reconstruction efficiency of prompt D mesons is calculated as a function of p_{T} and event multiplicity. The dependency on the D^0 rapidity is neglected. The left panel

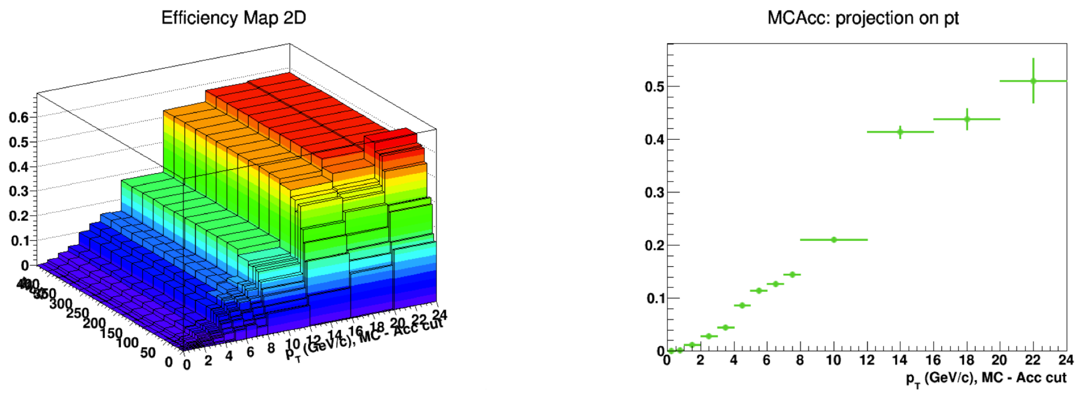

Figure 5.14: Prompt D^0 meson efficiency as a function of p_{T} and multiplicity (left) and p_{T} only (right).

of Fig. 5.14 shows two-dimensional reconstruction and selection efficiency map for prompt D^0 mesons as a function of multiplicity and p_{T} for minimum bias pPb Monte Carlo samples. The efficiency map is almost flat over large multiplicity and shows little dependence in the lower values of multiplicity in all p_{T} bins.

The p_{T} dependence of efficiency has a relevant effect on the correlation distributions. The p_{T} dependence of the trigger efficiency is corrected within each selected D^0 p_{T} bin. Since the final $\Delta\varphi$ correlation is normalized by number of trigger in each p_{T} bin, it is necessary to get efficiency corrected triggers for each p_{T} bin. To achieve this, D^0 invariant mass distributions are weighted by the inverse of the trigger reconstruction and selection efficiency in the same way as for correlation.

As discussed in the previous sections, the two types of efficiencies for D mesons (prompt and feed-down) are used. For correlations analysis the selection and reconstruction efficiency for prompt D^0 meson is used. The feed-down contribution of efficiency is used for the evaluation of the feed-down correction and for Monte Carlo "closure" test (see sections below).

5.2.3.3 Efficiency correction for associated charged particles

Along with trigger efficiency, correlation distributions are needed to be corrected for associated charged particle efficiency in each p_{T} bin. Tracking efficiency is important in order to check the reconstruction efficiency of tracks in the ITS and the TPC. The efficiency of charged particles has mild dependency on azimuthal angle φ but has strong dependency on track p_{T}.

The track reconstruction efficiency is usually estimated with simulated events. In this analysis ALICE "LHC13d3" Monte Carlo sample is used. The minimum bias events are generated using the HIJING event generator enriched with c and b quarks (using PYTHIA event generator). It is calculated as a function of the momentum of the track (p_{T}), pseudorapidity (η) and z-coordinate of the primary vertex (z_{Vtx}). All minimum bias events are taken without checking presence of D^0 in any event in order to gain higher statistics.

Left panel of Fig. 5.15 shows the two-dimensional efficiency map as function of p_{T} and η which is integrated over the z_{Vtx}. Like φ, a very mild dependence from the pseudorapidity is found in the $|\eta| < 0.8$ region. The binning of the efficiency map is chosen as fine as possible, especially in the low-p_{T} region and gradually border near high-p_{T} bins. Right panel of Fig. 5.15 shows η and z_{Vtx} integrated efficiency map as a function of p_{T}. The efficiency is flat in high-p_{T} range and a significant p_{T} dependence is found at low-p_{T}.

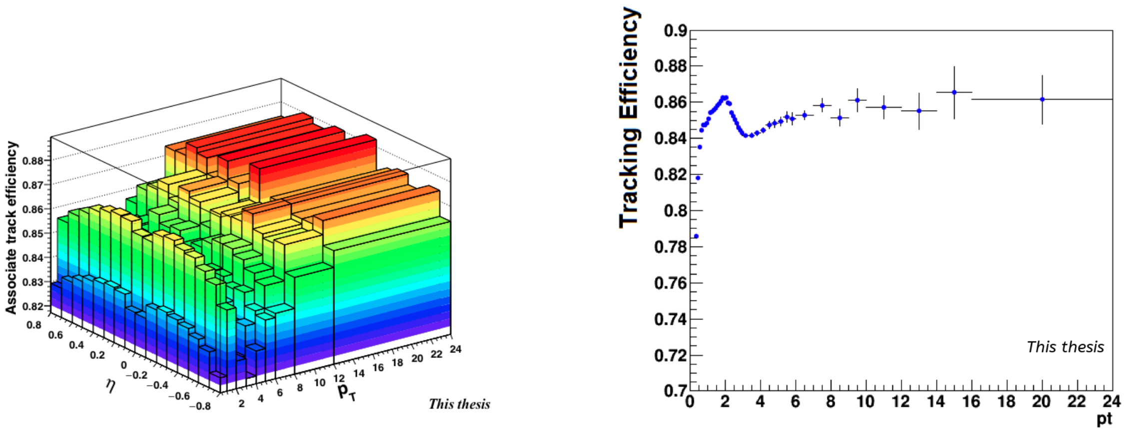

Figure 5.15: Single track efficiency as a function of p_{T} and η (left) and p_{T} only (right).

5.2.3.4 Beauty feed-down subtraction

A fraction of the reconstructed D^0 mesons consists of secondary D^0 mesons coming from B-meson decays. The topological cuts, applied to reject combinatorial background, select preferentially displaced vertices, yielding a larger efficiency for secondary D^0 mesons than for prompt D^0 mesons. In the previous sections it has been seen that the efficiencies are different for prompt and feed-down D^0 candidates. Therefore, it is necessary to remove feed-down contribution from inclusive D^0 mesons. The feed-down correction is applied after the two-dimensional correlation distributions are projected over $\Delta\varphi$ by integrating over $\Delta\eta$ in the interval $|\Delta\eta| < 1.0$. The contribution of feed-down D^0 mesons to the measured angular correlation is subtracted as follows [7]:

$$C_{prompt}(\Delta\varphi) = \frac{1}{f_{prompt}}\left[p_{prim} \cdot C_{inclusive}(\Delta\varphi) - (1 - f_{prompt}) C^{MC_{tempt}}_{feed-down}(\Delta\varphi)\right] \quad (5.9)$$

where, C_{prompt} and $C_{inclusive}$ are the per-trigger azimuthal correlation distributions before and after the feed-down subtraction. f_{prompt}, the fraction of prompt D^0 mesons, is evaluated on the basis of FONLL calculations of charm and beauty p_{T}-differential production cross sections [8] and on the reconstruction efficiencies of prompt and secondary D^0 mesons. It is calculated using Monte Carlo simulations [9] as:

$$f_{prompt} = 1 - (N^{\mathrm{D}^0,\overline{\mathrm{D}^0} feed-down\ raw} / N^{\mathrm{D}^0,\overline{\mathrm{D}^0}\ raw}) \tag{5.10}$$

with

$$N^{\mathrm{D}^0,\overline{\mathrm{D}^0} feed-down\ raw}|_{|y|<y_{acc}} = \frac{d\sigma^{\mathrm{D}^0,\overline{\mathrm{D}^0} fromB}_{FONLL}}{dp_{\mathrm{T}}}|_{|y|<0.5} \cdot \Delta y \Delta p_{\mathrm{T}} (Acc \times \epsilon)_{feed-down} \cdot BR \cdot L_{int} \tag{5.11}$$

The value of f_{prompt}, which depends on the D^0-meson species and varies as a function of p_{T}, is estimated to be in between 75% and 90%.

5.2.3.5 Correction for the contamination due to secondary particles (purity check)

Just like the D^0 candidates are contaminated by fake track pairs producing a large background, the associated charged particles can also be affected by secondary particles coming from long-lived strange hadrons or from interaction of particles from the detector material. Such contamination of secondary particles, can be tagged and removed by means of a distance of closest approach (DCA) from primary vertex cut.

A very stringent cut can not be applied on DCA due to the constraint over trigger meson daughter tracks. Hence, a residual contamination from secondary tracks may be accounted for correlation building.

The contaminations of secondary particles can be estimated using minimum bias Monte Carlo simulation based on HIJING (LHC13d3 sample) [10]. The left panel of Fig. 5.16 shows in 4 bins the primary or secondary tracks accepted or rejected for the integrated D^0 p_T range of 3-16 GeV/c. Right panel shows the ratio of correlation distributions with and without passing DCA cut. From the results, it can be concluded that the DCA cut helps in keeping the contamination of secondary tracks under 4%. A typical value of 0.036 for pPb data for the integrated D^0 p_T bins is written on the right panel of the figure. In all the D^0 p_T bins this ratio remains flat. The same check is repeated for other p_T thresholds/ranges of associated charged particles and a flat contamination is found. Therefore, to correct the data correlation

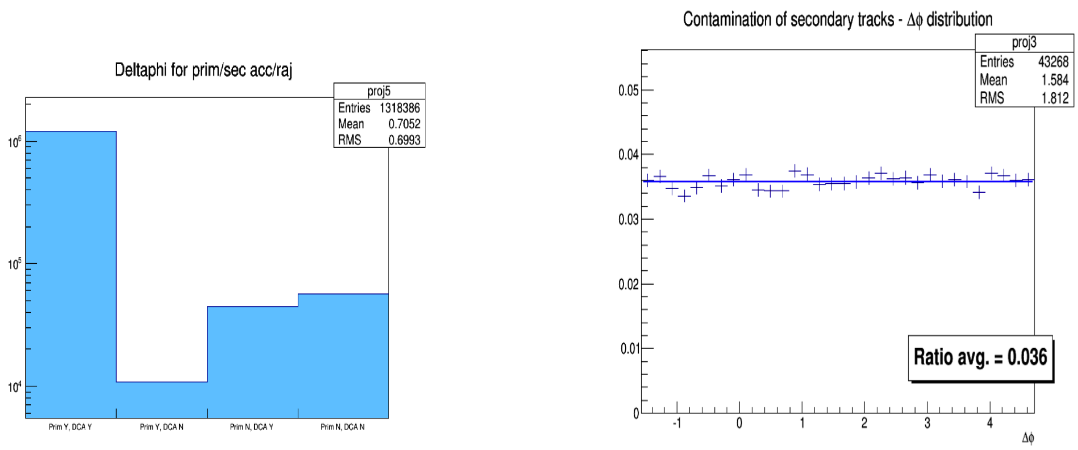

Figure 5.16: (Left) Number of primary/secondary tracks which are accepted/rejected by the DCA cut, for the integrated D^0 p_T bin. (Right) Ratio of correlations due to all tracks passing the quality cuts and of secondary tracks passing the DCA cut.

distributions, a global scale factor is applied by multiplying with the average purity (i.e., 1 minus the contamination value) to the correlation distributions.

5.2.4 Evaluation of systematic uncertainties

The D^0 meson-charged angular particle correlations analysis suffers from various systematics. The systematic uncertainties are coming from:

- D^0 meson yield extraction
- background subtraction
- D^0 topological cut efficiency
- associated track efficiency
- beauty feed-down subtraction
- residual contamination from secondary tracks
- soft-pions from D^* decays

The evaluations of all the systematics are discussed below.

5.2.4.1 Uncertainty related to D^0 meson yield extraction

The systematic uncertainty related to yield extraction is determined by varying the signal extraction procedure from invariant mass distribution. The standard way of getting D^0 yield is to integrate the Gaussian component of the mass fit in the signal region. The signal extraction technique is varied as:

- changing the background fit function (1st or 2nd order polynomial)

- changing the range or bin width in which the signal is extracted from the Gaussian fit
- reducing the range of invariant mass axis in which the fit of the data is evaluated
- extracting the yield via bin counting, based on counting the entries within 2σ of the peak after subtracting the background, instead of integrating the Gaussian fit function

By changing the yield extraction approach, both the yield (number of trigger D^0 mesons used for normalization of final $\Delta\varphi$ correlation distributions in each p_T bin) and the sideband correlation normalization factors are affected. The rest of the procedure to extract the angular correlation distribution is the same as in the standard analysis. This exercise yields a 10% systematic uncertainty for the yield extraction method for all p_T ranges.

5.2.4.2 Uncertainty related to background subtraction

In the standard Side-Band subtraction approach a sideband of $\pm 4\sigma$ on both side of the mass peak (signal region) is considered to estimate the sideband factor. This standard approach yields some systematic uncertainties due to the sideband factor. To estimate the background subtraction systematic uncertainty, the range of sidebands is varied w.r.t to standard one. Two different sideband definitions are used to modify the usual range of the sidebands:

- 4σ to 9σ from the centre of the peak

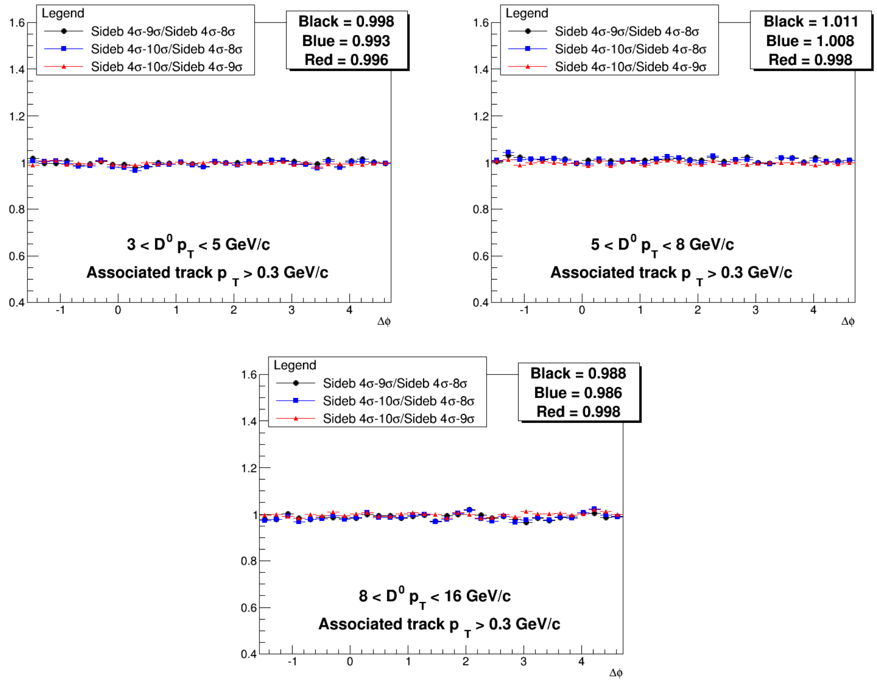

Figure 5.17: Ratio of correlation distributions obtained with standard sideband definition over correlation distributions with different ranges for sidebands, for different D^0 p_T bins and associated tracks $p_T > 0.3$ GeV/c. Other associated track p_T variations can be found here [11].

- 4σ to 10σ from the centre of the peak.

With these configurations of sideband ranges the azimuthal correlation distributions are obtained keeping rest of the procedure unchanged. As shown in Fig. 5.17 the ratios of the fully corrected azimuthal correlation distributions obtained with the standard sideband ranges and with different sideband definitions, are evaluated for all D^0 p_T bins. A ratio between the two new sideband definitions is also evaluated. From this study, a 5% systematic is assigned for the background subtraction independent of D^0 p_T and $\Delta\varphi$. It should be noted that due to invariant mass range constraint, the variation of range of sidebands are taken in such a way. It is not possible to go more on the left due to some structures present in the D^0 invariant mass distribution. A further study is done by varying the signal region width from $\pm 2\sigma$ (standard) to $\pm 1.5\sigma$ and this also gives a variation less than 5%.

5.2.4.3 Uncertainty related to D^0 topological cut efficiency

The extraction of D^0 meson signal through application of various topological selections can produce systematic uncertainty. To estimate this kind of systematic uncertainty, a cut variation approach is used where the correlations analysis is repeated by using different sets of topological selections to select the D^0 meson candidates. A set of loosened and tightened selections w.r.t the standard cuts are used. With the variation of cuts, the D^0 efficiency maps are computed separately. The efficiency maps for the loosened and tightened cuts are shown in the Fig. 5.18. By changing the selection cuts a significant variation of efficiency maps can be observed. With

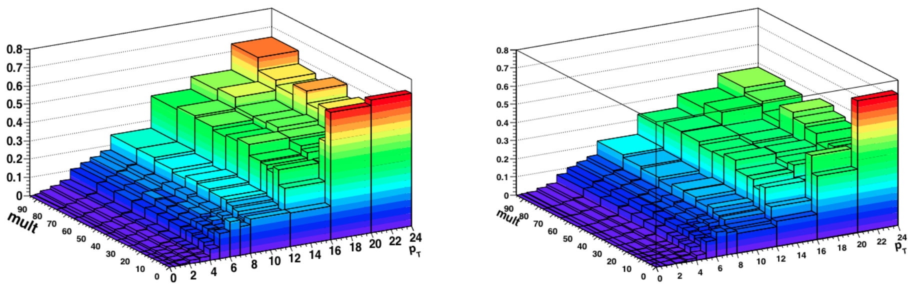

Figure 5.18: D^0 meson efficiency map as a function of multiplicity and p_T for tightened (left) and loosened (right) cut selections.

the variations of selection cuts of D^0 meson (standard/loosened/tightened), the fully corrected angular correlation distributions for different D^0 p_T intervals and for different associated charged particles p_T thresholds are extracted without changing the rest of the correlation procedure. Figure 5.19 shows the ratio of the correlation distributions obtained using the tightened and loosened selections over the results with the standard selection. From the study, a systematic uncertainty of 5%, without any variation in p_{T} and $\Delta\varphi$ is assigned.

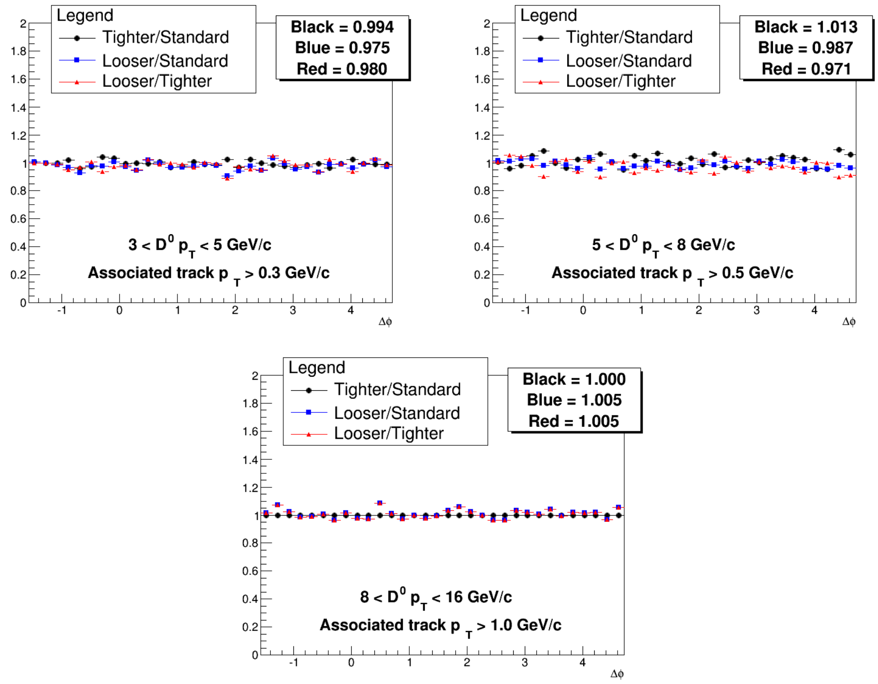

Figure 5.19: Comparison of the ratio of azimuthal correlation distributions for different cut selections on D^0 reconstruction, in different D^0 p_{T} bins and associated tracks $p_{\mathrm{T}} > 0.3$, 0.5, 1.0 GeV/c. Other trigger and associated track p_{T} variations can be found here [11].

5.2.4.4 Uncertainty related to associated track efficiency

The uncertainty on the correction for the associated charged particle reconstruction efficiency is assessed by varying the selection criteria applied to the reconstructed tracks. The standard selection cuts for associated charged particles is discussed in

Selection cuts	Default	TPC-only	ITS+TPC
Min. no. of ITS clusters	3	0	3
Min. no. of TPC clusters	70	70	70
ITS refit	No	No	Yes
TPC refit	Yes	Yes	Yes
DCA to primary vertex (along z)	1 cm	1 cm	1 cm
DCA to primary vertex (along xy)	0.25 cm	0.25 cm	0.25 cm
Requested hits in SPD	No	No	atleast 1

Table 5.4: Different track selection criteria for associated charged particles.

previous sections. A set of alternative cuts are defined for the associated tracks selection depending on the quality of reconstructed tracks for the TPC and the ITS detectors. The alternative track selections are:

- "TPC-only" selection i.e TPC tracks with no requests on the number of hits in the ITS with default minimum 70 clusters, TPC-refit and no ITS-refit
- "ITS+TPC" selection i.e at least 3 points in the ITS, ITS refit and a hit in atleast one SPD layer

The three sets of selections (standard, TPC-only and ITS+TPC) is listed in the table 5.4.

The Fig. 5.20 shows the single track efficiency maps for 3 sets of associated tracks filtering selections. With the various track selection definitions, the associated track efficiency maps are evaluated. The azimuthal correlations between D^0 mesons and charged particles are then weighted by associated track efficiency values for 3 different cases. Then the ratios of the azimuthal correlation distributions with different track selections over distributions with standard selection are evaluated.

Figure 5.21 shows the ratios of correlation distributions obtained using 3 different

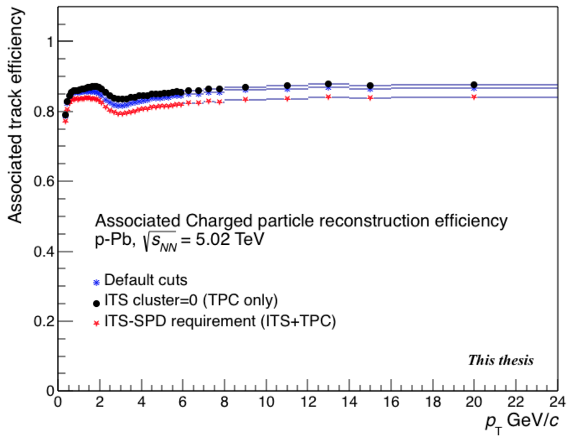

Figure 5.20: Associated charged particles efficiency map as a function of p_{T} for three different filtering selections; standard, TPC-only, ITS+TPC.

track filtering selections for 3 different D^0 p_{T} bins with the associated track p_{T} threshold of $p_{\mathrm{T}} > 0.3$ GeV/c. The ratios varies in a similar fashion with other associated charged particle p_{T} thresholds/ranges [11]. From the study of ratio of azimuthal correlation distributions for different associated tracks filtering selections, a $\pm 4\%$ systematic uncertainty is estimated without any variation in p_{T} and $\Delta\varphi$.

5.2.4.5 Uncertainty related to beauty feed-down subtraction

The uncertainty on the subtraction of the beauty feed-down contribution is quantified by generating the templates of feed-down azimuthal correlation distributions ($C^{MC_{tempt}}_{feed-down}$ $(\Delta\varphi)$ in Eq. 5.9), with different feed-down PYTHIA 6 tunes (subsection 5.2.5), and by considering the range of f_{prompt} values obtained by varying the prompt and feed-down D^0 meson p_{T}-differential production cross sections within FONLL uncertainty band, as described in subsubsection 5.2.3.4. The ratio of feed-down subtracted correlation distributions are obtained with the various sets

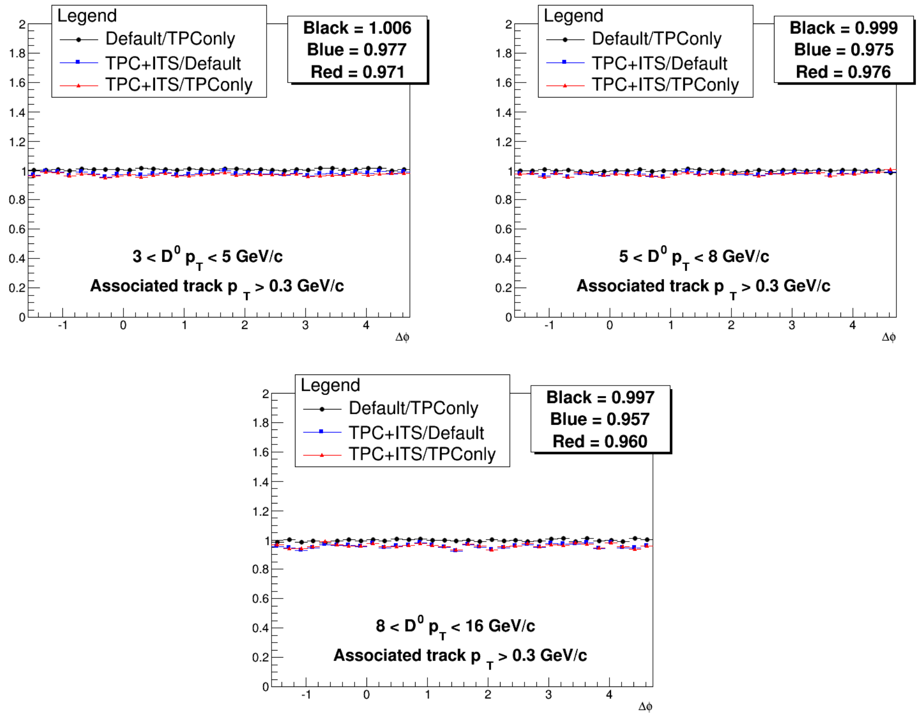

Figure 5.21: Ratio of correlation distributions obtained with different associated tracks filtering selections, for different D^0 p_T bins and associated tracks $p_T > 0.3$ GeV/c.

of f_{prompt} and Perugia tunes w.r.t to the standard choice (f_{prompt}, Perugia0 tune). It has been found that the effect of feed-down subtraction on the azimuthal correlation distributions is $\Delta\varphi$ dependent and remains within 8% for all D^0 p_T bins and associated track p_T ranges/thresholds.

5.2.4.6 Uncertainty related to residual contamination from secondary tracks

The contamination due to secondary tracks coming from strange hadrons and other sources is discussed in subsubsection 5.2.3.5. The uncertainty related to this can be estimated by repeating the analysis by varying the DCA cut in the x-y plane from 0.1 cm to 1 cm and and re-evaluating the purity of charged primary particles for each variation. Monte Carlo simulations are performed using the above mentioned values for the DCA cut. The level of the purity and the residual contamination from secondary tracks are evaluated for each case. The analysis is then repeated on data using the same set of DCA cuts on x-y plane. The correlation distributions are extracted for each set of DCA cuts keeping the residual correlation procedure as it is. The azimuthal correlations are multiplied by the purity values. Therefore, in order to estimate the uncertainty related to DCA cut variations, the ratio of azimuthal correlations with tighter DCA cut values over the loosest DCA cut value (1 cm) are evaluated. Figure 5.22 shows the ratio of correlation distributions for different DCA cuts for three D^0 p_T bins. The observed ratio is flat over $\Delta\varphi$ and in almost all the D^0 p_T bins . Hence eyeing on the ratio, a overall 3.5% systematic uncertainty is assigned for this.

5.2.4.7 Uncertainty related to soft-pions from D^* decays

Soft-pions are those which are produced during the decay of D^{*+} into D^0 ($D^{*+} \rightarrow D^0\pi^+$). The decay pions carry a small part of the mother D^{*+} momentum. Any possible contamination on the correlation analysis due to presence of such soft-pions can be estimated via Monte Carlo study and the contamination from D^{*+} decay pions is found to be below 1%. To estimate the uncertainty related to soft-pions removal on the correlation distributions, the analysis is performed with and without inclusion of soft-pions. The ratio of correlation distributions with and without soft-

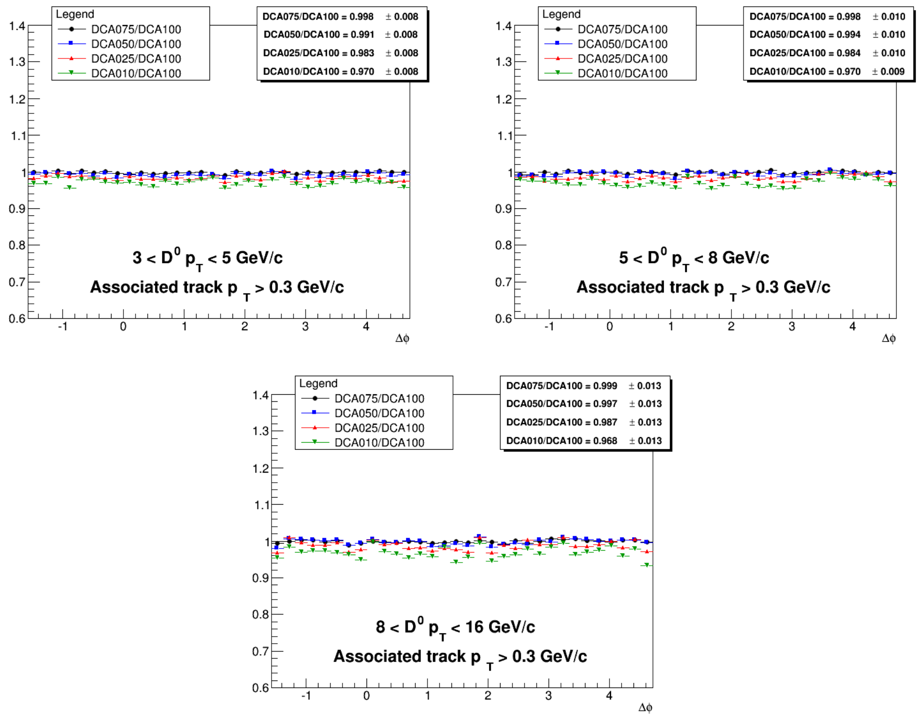

Figure 5.22: Ratio of azimuthal correlation distributions with tighter DCA cuts over standard one (1 cm) for three D^0 p_{T} bins with associated track $p_{\mathrm{T}} > 0.3$ GeV/c.

pions are found to be flat and hence no uncertainty is assigned for this.

5.2.5 Monte Carlo simulations: Closure test

Monte Carlo (MC) simulations are used to calculate the corrections for the azimuthal correlation distributions evaluated from data. The correlations analysis performed using Monte Carlo sample provide a compatibility check to the data. The Monte Carlo sample used for pPb collisions is LHC13d3.

- LHC13d3: This MC sample contains 41 million events simulated with HIJING v1.36 event generator [12]. At the generation level an event from a pPb collision, simulated with HIJING, is added on top of the PYTHIA event in order to enrich the sample with charm and beauty quarks. Particularly in pPb collisions at $\sqrt{s_{\rm NN}} = 5.02$ TeV the centre-of-mass frame is boosted in rapidity by $\Delta y_{NN} = 0.465$ in order to reproduce the rapidity shift of the reference frame of the nucleon-nucleon collision in the pPb collision system. Then the D^0 mesons are forced to decay in preferred decay channels. At the end, the generated particles are transported through the detector with the GEANT3 transport package [13].

A brief description of PYTHIA and HIJING event generators are given in the Appendix (section 8.1).

Prior to the feed-down subtraction, the whole analysis is performed both at the kinematic and reconstruction level using the charm-beauty enriched MC sample. At kinematic level, only the acceptance cuts are applied to trigger D^0 mesons and associated charged particles. At reconstruction level, the analysis is performed same as on data using topological selections, PID selections on D^0 mesons and track filtering cuts on associated charged particles, rejecting non-primary particles using DCA cut. In this case, only the true D^0 mesons are counted looking at the Monte Carlo truth (kinematic) event sample. Event mixing correction is applied on both kinematic and reconstruction level but no background subtraction is performed. Tracking efficiency and trigger efficiency corrections are applied only in the reconstruction level. The azimuthal correlation distributions are shown in Fig. 5.23 for kinematic level and in Fig. 5.24 for reconstruction level for D^0 mesons coming from different sources (charm, beauty etc) with associated track $p_{\rm T}$ threshold of 0.3 GeV/c.

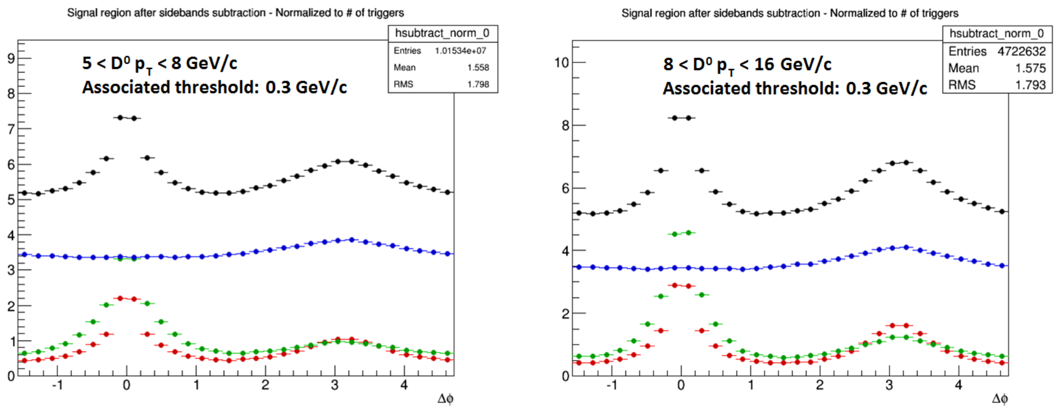

Figure 5.23: D^0-charged particle azimuthal correlation distributions obtained from Monte Carlo simulations, at kinematic level for 5-8 GeV/c and 8-16 GeV/c trigger ranges and with associated track p_T threshold of 0.3 GeV/c.

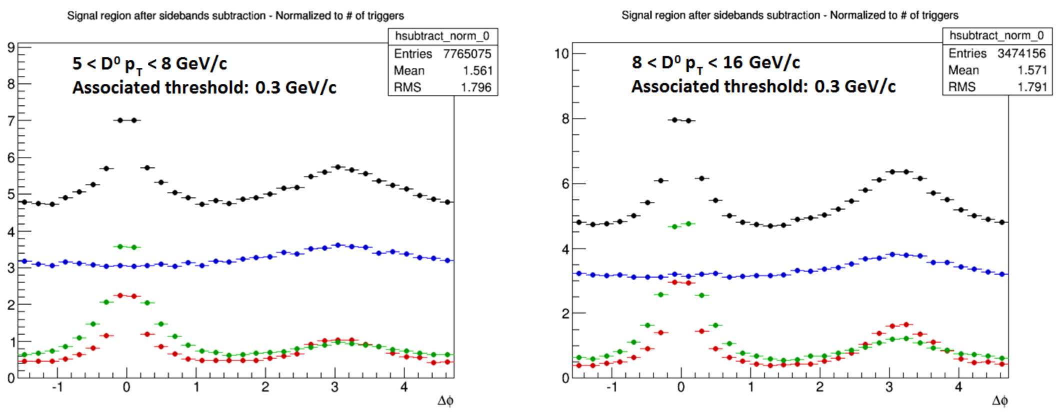

Figure 5.24: D^0-charged particle azimuthal correlation distributions obtained from Monte Carlo simulations, at reconstruction level for 5-8 GeV/c and 8-16 GeV/c trigger p_T ranges and with associated track p_T threshold of 0.3GeV/c.

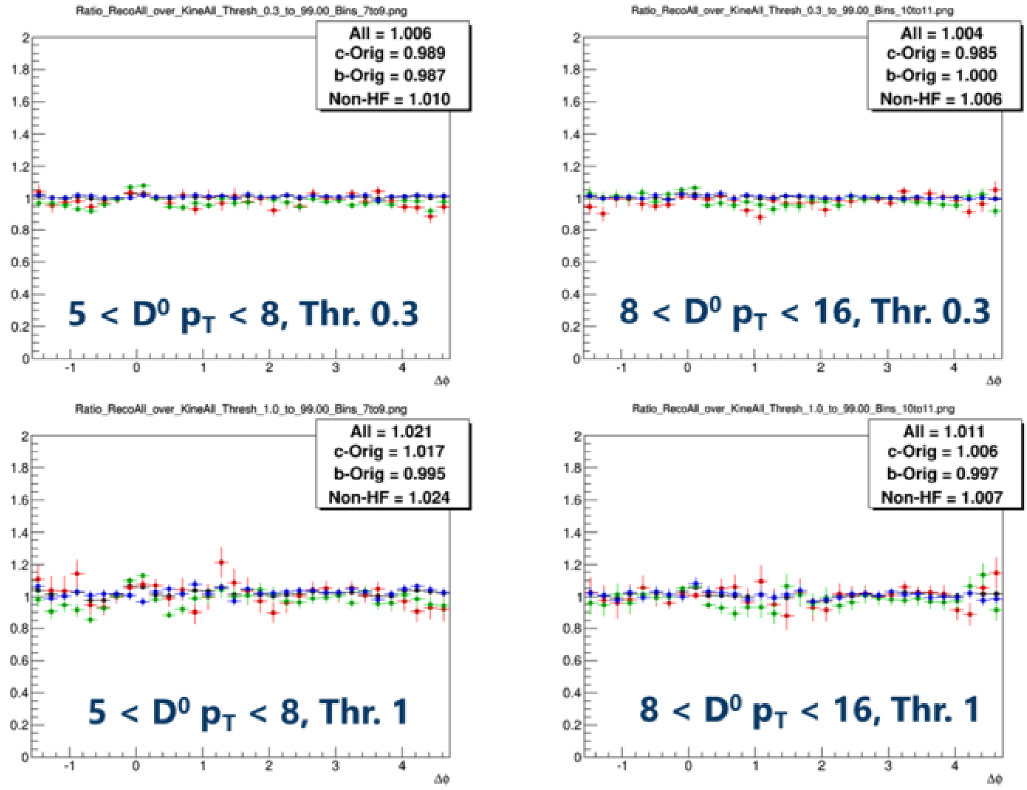

Figure 5.25: Ratios of fully corrected azimuthal correlation distributions at reconstructed level over azimuthal correlation distributions at kinematic level, in the two D^0 p_T bin, for the different associated track p_T ranges. Colors of different ratios correspond to different sources of D^0 as stated in the text.

Figure 5.23 and Fig. 5.24 show four types of correlations. Black points refer to the correlations using all D^0 particles coming from all sources normalized by all D^0 triggers. Red points correspond to azimuthal correlations using D^0 originated from charm fragmentation, normalized by c-D^0 triggers. Green points are for D^0 coming from beauty-hadron decays and normalized by b-D^0 triggers. Blue points refer to the correlations for the all D^0-hadrons from light quarks (non-heavy flavor), normalized by all D^0 triggers.

To check the compatibility between two types of results, kinematic and reconstructed, the ratios of fully corrected azimuthal correlation distributions at reconstruction level over kinematic level are evaluated for all the cases of different origins of D^0 and associated charged particles. The ratios shown in Fig. 5.25 are flat in $\Delta\varphi$ but depends on D^0 p_{T} bins. For prompt D^0 mesons (charm-origin), no effect is found but for feed-down D^0 mesons (beauty-origin), an overestimate of 2% in the near-side is found. It has been assumed that the source of this excess feed-down tracks in the near-side is due to a bias induced by the topological selection for the D^0 mesons.

Apart from this, different other closure studies are done by using efficiency for D^0 meson (with and without), efficiency for associated charged particles (with and without), even-mixing (with and without). The discrepancy still exists in the b-origin case in all these studies. Hence, a systematic uncertainty of -2% is assigned for $\Delta\varphi$-dependence of feed-down subtracted correlation distributions in the near-side.

5.2.6 Summary of systematic uncertainties

Table 5.5 is the summary of all the systematic uncertainties which affect the angular correlations between D^0 mesons and charged particles. The uncertainties can be correlated or uncorrelated in $\Delta\varphi$. The uncertainties arising from the feed-down subtraction and from Monte Carlo closure test are typically $\Delta\varphi$-uncorrelated systematic uncertainties. All the other contributions are correlated in $\Delta\varphi$ act as a scale uncertainty. No uncertainty has specific dependence on p_{T} of D^0 mesons or charged particles, except for the feed-down systematic uncertainty.

System	pPb
Signal, background normalization	$\pm 10\%$
Background $\Delta\varphi$ distribution	$\pm 5\%$
Associated-track reconstruction efficiency	$\pm 4\%$
Primary-particle purity	$\pm 3.5\%$
D-meson efficiency	$\pm 5\%$
Feed-down subtraction	up to 8%, $\Delta\varphi$ dependent
MC closure test	-2% (near-side)

Table 5.5: List of systematic uncertainties for the $\Delta\varphi$-correlation distributions between D^0 mesons and charged particles in pPb collisions.

5.2.7 Fitting of correlation distribution

In order to quantify the azimuthal correlations between D^0 mesons and charged particles, a fit procedure is performed. The fit function used in this analysis is composed of two Gaussians describing the "near-side" peak (mean fixed at $\Delta\varphi = 0$) and "away-side" peak (mean fixed at $\Delta\varphi = \pi$) and a constant term, describing the "baseline". The Gaussian functions are build with additional periodicity condition. The fit function is as below:

$$f(\Delta\varphi) = b + \frac{A_{NS}}{\sqrt{2\pi}\sigma_{fit,NS}} \; e^{-\frac{(\Delta\varphi)^2}{2\sigma^2_{fit,NS}}} + \frac{A_{AS}}{\sqrt{2\pi}\sigma_{fit,AS}} \; e^{-\frac{(\Delta\varphi-\pi)^2}{2\sigma^2_{fit,AS}}} \tag{5.12}$$

The integrals of the Gaussian terms, A_{NS} and A_{AS}, correspond to the per-trigger associated particle yields for the near (NS)-side and away (AS)-side peaks, respectively, while $\sigma_{fit,NS}$ and $\sigma_{fit,AS}$ quantify the widths of the correlation peak. The baseline b represents the physical minimum of the $\Delta\varphi$ distribution. In order to reduce the baseline fluctuations, b is fixed to the weighted average of eight points in the transverse region defined as $\pi/4 < \Delta\varphi < \pi/2$.

Note: For further reduction of statistical fluctuations, the azimuthal correlations are reflected in range 0< $\Delta\varphi < \pi$ as the symmetry is conserved. The fit of such reflected distributions still remains same with the same NS, AS and baseline measurements.

5.2.8 Systematic uncertainty related to fit procedure

To estimate the systematic uncertainty on the near-side peak associated yields and peak widths and on the baselines, the fit procedure is repeated with different approaches:

- instead of single Gaussian to fit the near-side peak, a double-Gaussian function is used
- without fixing the mean of the Gaussian functions
- baseline measurement procedure, with 2 or 4 points
- yield extraction using bin counting method
- moving upwards and downwards the data points by the corresponding value of the $\Delta\varphi$-uncorrelated systematic uncertainty

The main source of uncertainties sneaks through the baseline measurement as we assumed that the observed variation of $\Delta\varphi$ correlation in transverse region is mainly due to statistical fluctuations rather than its true physical trend.
For the baseline and the near-side yield the systematic uncertainties are calculated by summing the different values (from different approaches) in quadrature to the

$\Delta\varphi$-correlated systematics.

$$\sigma^{syst.}_{fit\ param} = \sqrt{Max(\Delta^{fit\ variation}, \Delta^{point\ shift})^2 + (\sigma^{correl}_{syst.})^2} \tag{5.13}$$

This is not done for the near-side width, since this parameter is not affected by the different normalization. The total uncertainties related to A_{NS}, σ_{NS} and baseline are listed in table 5.6 for D^0 p_T intervals 5-8 GeV/c and 8-16 GeV/c with associated track p_T, $0.3 < p_T^{assoc} < 1$ GeV/c and $p_T^{assoc} > 1.0$ GeV/c.

System	pPb	
Kinematic range	$5 < p_T(D^0) < 8$ GeV/c, $0.3 < p_T^{assoc} < 1$ GeV/c	$8 < p_T(D^0) < 16$ GeV/c, $p_T^{assoc} > 1$ GeV/c
NS yield	±17%	±12%
NS width	±3%	±3%
Baseline	±12%	±11%

Table 5.6: List of systematic uncertainties for near-side (NS) peak associated yield, near-side peak width, and baseline in pPb collisions, for two p_T ranges of D^0 meson and associated charged particles.

5.3 Results

In this section results from correlation analysis between D^0 mesons and charged particles will be discussed. The analysis is performed along with other two D mesons; D^+ and D^{*+}. As the correlations taking other two D mesons also give similar results, therefore the analysis is performed by averaging all the 3 correlation measurements at the end. This improves the statistical fluctuations. The technique of averaging the physics variables from analysis of different D mesons has been adopted in many analysis related to heavy-flavour by ALICE [14–18]. The results of azimuthal correlations between D^0 meson & charged particles and average D mesons & charged particles will be discussed in the following sections.

5.3.1 $\Delta\eta - \Delta\varphi$ correlations between D^0 mesons and charged particles

Figure 5.26 shows the fully corrected $\Delta\eta, \Delta\varphi$ correlation distributions calculated for the three p_T intervals $3 < p_T(D^0) < 5$ GeV/c, $5 < p_T(D^0) < 8$ GeV/c , $8 < p_T(D^0) < 16$ GeV/c and for associated p_T threshold/ranges of 0.3 GeV/c, 0.5 GeV/c and 1.0 GeV/c, 0.3 - 1.0 GeV/c. Figure 5.27 shows the one dimensional $\Delta\varphi$ correlation distributions in D^0 p_T range $8 < p_T(D^0) < 16$ GeV/c and in associated track p_T threshold of 0.3 and 1.0 GeV/c. The correlations distributions are fitted with the above mentioned fit function 5.12. The distributions are not corrected by feed-down correlation distributions. The correlations distributions are fitted well and near and away-side peaks are clearly visible. Figure 5.28 shows the results for fully corrected D^0 meson-charged particle azimuthal correlations distributions. Results are shown for 2 different D^0 p_T ranges with 3 different associated track $p_T > 0.3, 1$ GeV/c and $0.3 < p_T < 1$ GeV/c. As discussed earlier, the correlations distributions are evaluated in $[0, \pi]$ instead of full $\Delta\varphi$ range $(-\pi/2 < \Delta\varphi < 3\pi/2)$. This allows to reduce the impact of statistical fluctuations on the data points by a factor $1/\sqrt{2}$ assuming equal statistics for a pair of symmetric bins. A comparison among reflected distributions and distributions in the full range is shown in Fig. 5.29.

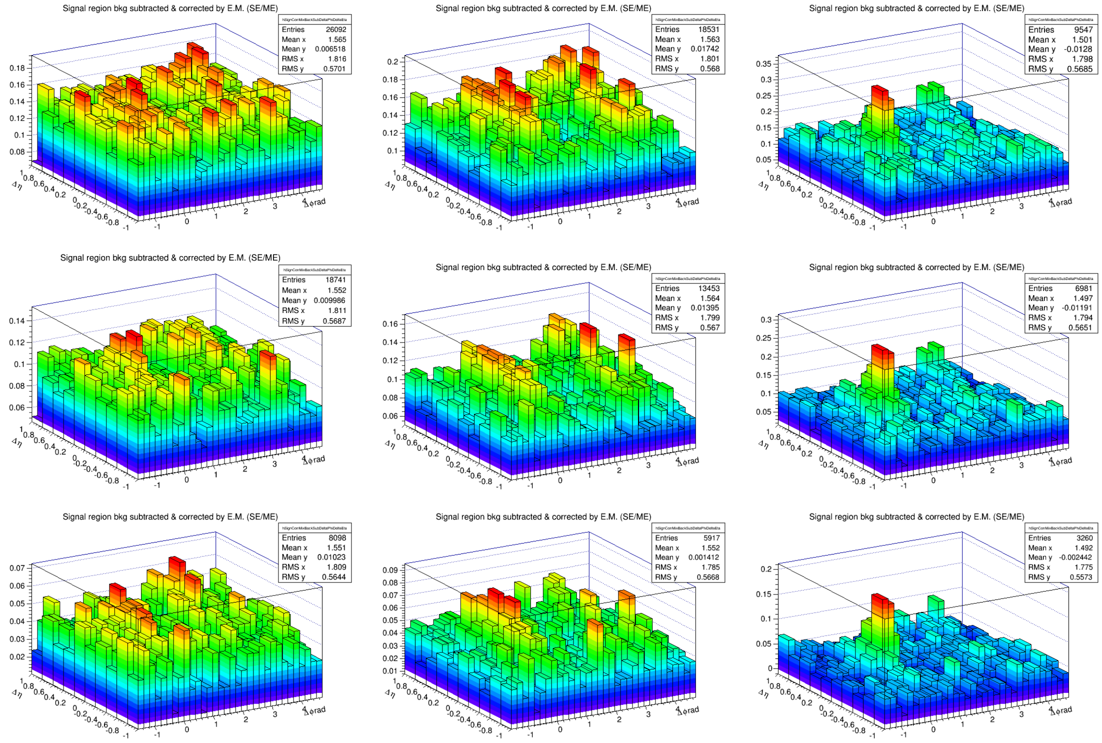

Figure 5.26: Fully corrected 2-dimensional $(\Delta\eta, \Delta\varphi)$ D^0-charged particle correlation distributions, in different D^0 p_T ranges, Low: $3 < p_T(D^0) < 5$ GeV/c, Mid: $5 < p_T(D^0) < 8$ GeV/c , High: $8 < p_T(D^0) < 16$ GeV/c for associated track p_T threshold of 0.3 GeV/c (upper row), 0.5 GeV/c (middle row) and 1.0 GeV/c (bottom row).

With the reflection in $\Delta\varphi$, the statistical fluctuations seem to be reduced and the baseline is shifted up.

5.3.2 Comparing three D mesons (D^0, D^+ and D^{*+}) correlation distributions

A comparative study between correlations distributions for three D mesons has been evaluated. Figure 5.30 shows the comparison of correlation distributions for three D

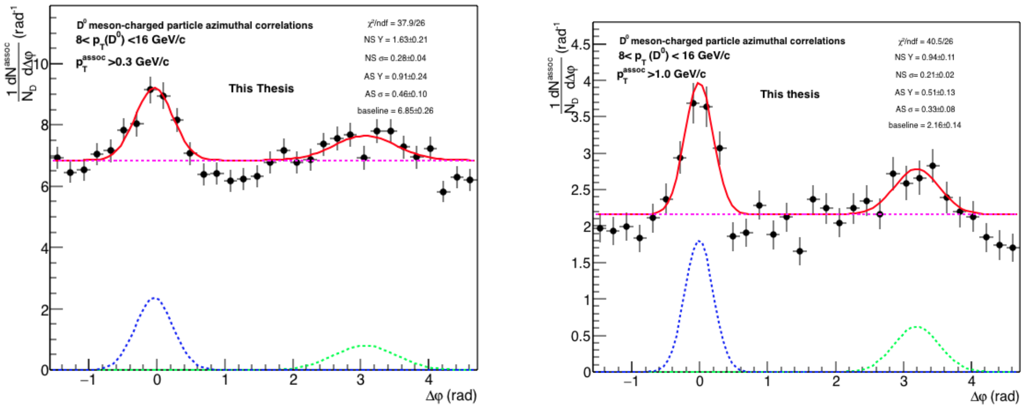

Figure 5.27: 1-dimensional $\Delta\varphi$ correlation distributions between D^0 mesons and charged particles in D^0 p_T bin $8 < p_T(D^0) < 16$ GeV/c and with associated track p_T threshold of 0.3 GeV/c (left) and 1.0 GeV/c (right). The distributions are fitted with standard fit function. The blue and green color dotted lines are the near-side and away-side Gaussian functions respectively.

mesons in two panels for p_T range of 8-16 GeV/c with associated track p_T threshold of 0.3 GeV/c. The correlation distributions in the full $\Delta\varphi$ range $(0-2\pi)$ are shown in left panel. Right panel consists with the reflected plots $(0-\pi)$ for the same kinematic ranges of trigger and tracks. From this figure a direct comparison of correlations distributions among three D mesons can be observed. The distributions obtained with the three D meson species are compatible within uncertainties. The comparison is also done for other D meson p_T ranges and for different p_T ranges/thresholds of associated tracks [11].

5.3.3 Average of D^0, D^+ and D^{*+}

The azimuthal correlations for the three D mesons (D^0, D^+ and D^{*+}) are found to be compatible within the the statistical and systematic uncertainties. It is considered

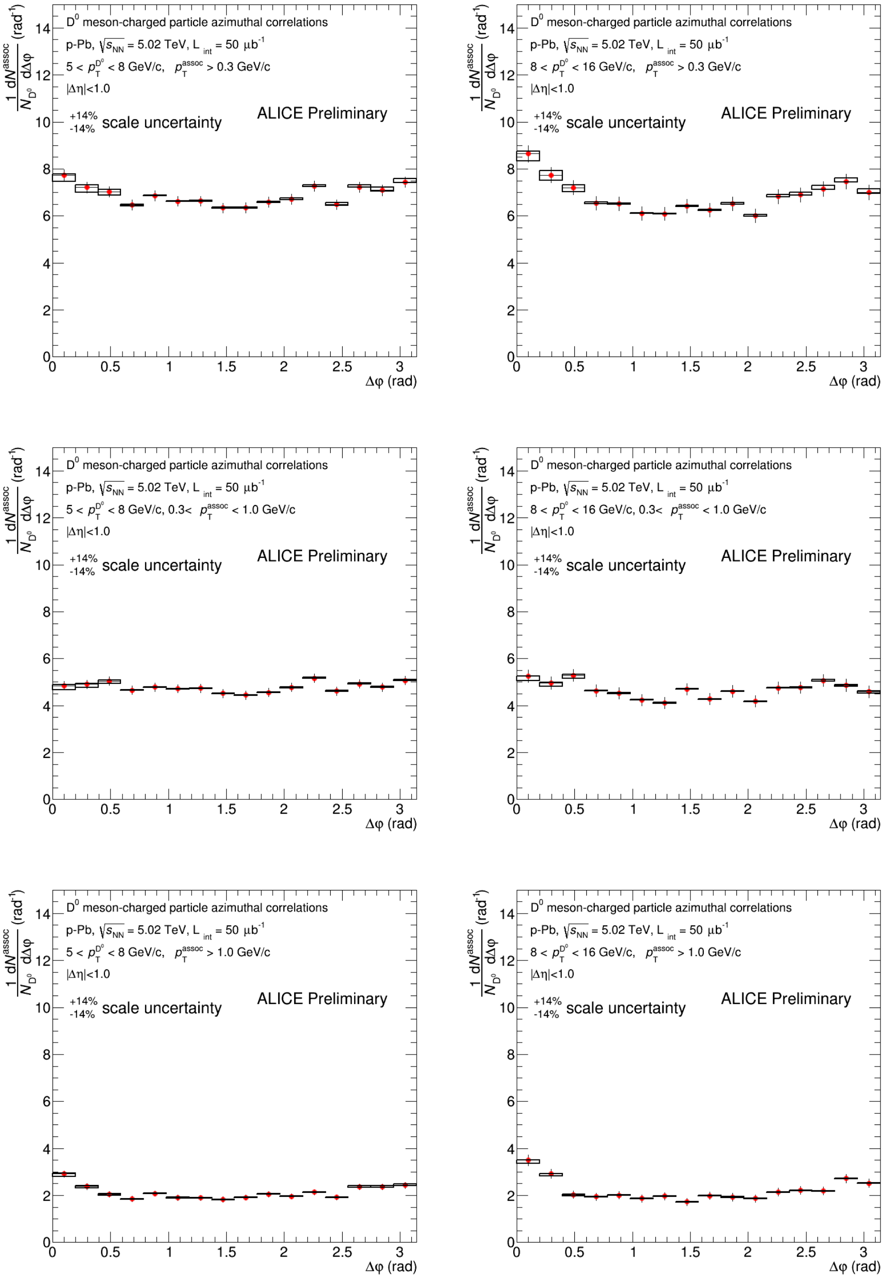

Figure 5.28: Fully corrected $\Delta\varphi$ distributions of D^0-charged particle azimuthal correlations, in D^0 p_T bins (Column-Left: $5 < p_T(D^0) < 8$ GeV/c, Column-Right: 8 $< p_T(D^0) < 16$ GeV/c) and associated tracks p_T ranges (top-row: > 0.3 GeV/c, middle-row: 0.3 to 1 GeV/c, bottom-row: >1.0 GeV/c).

.

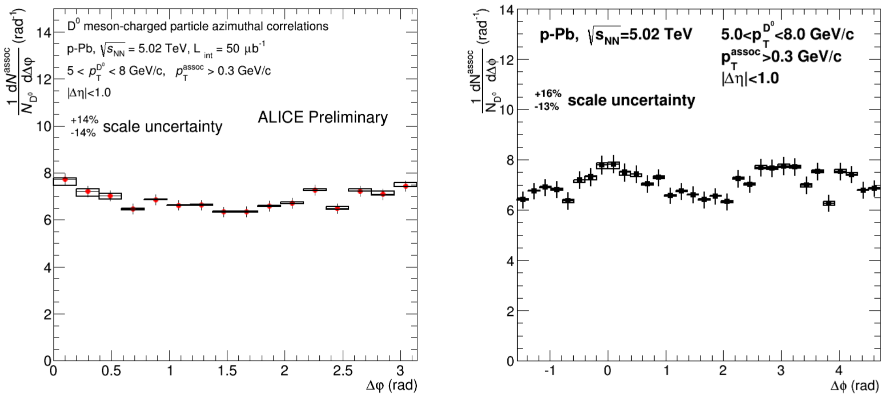

Figure 5.29: Example of comparison of full range (0 - 2π) and reflected (0 - π) azimuthal correlation distributions for D^0 p_T range $5 < p_\mathrm{T}(\mathrm{D}^0) < 8$ GeV/c with associated track p_T threshold of 0.3 GeV/c.

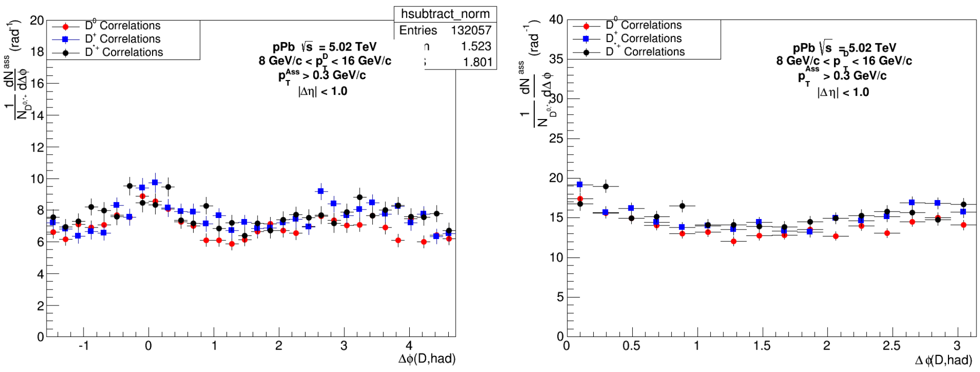

Figure 5.30: Example of comparison of azimuthal correlation distributions for three D mesons in the p_T range of 8-16 GeV/c with associated track p_T threshold of 0.3 GeV/c in full $\Delta\varphi$ range (left) and in reflected range (right).

that there is no visible difference in the correlations observed in Monte Carlo simulations also. Therefore, a weighted average of the azimuthal correlation distributions of D^0, D^+ and D^{*+} is performed in order to reduce the overall uncertainties:

$$\Big\langle \frac{1}{N_D}\frac{dN^{assoc}}{d\Delta\varphi}\Big\rangle_{D-mesons} = \frac{\sum_{i=meson} w_i \frac{1}{N_D}\frac{dN_i^{assoc}}{d\Delta\varphi}}{\sum_{i=meson} w_i}, \qquad w_i = \frac{1}{\sigma^2_{i,stat.} + \sigma^2_{i,uncorr.syst.}} \tag{5.14}$$

The uncorrelated systematic uncertainty and the statistical uncertainty on the average are then recalculated according to:

$$\sigma^2 = \frac{\sum_{i=meson} w_i \sigma_i^2}{\sum_{i=meson} w_i} \tag{5.15}$$

For $\sigma_i^2 = 1/w_i$ the equation 5.15 coincides with the standard formula giving the uncertainty on a weighted average.

The uncertainty from the $\Delta\varphi$-correlated uncertainty sources to the average systematic uncertainty is calculated via error propagation on the formula of the weighted average, Eq. 5.14:

$$\sigma = \frac{\sum_{i=meson} w_i \sigma_i}{\sum_{i=meson} w_i} \tag{5.16}$$

The uncertainties on the associated track reconstruction efficiency, the contamination from secondary tracks, the feed-down subtraction, the Monte Carlo closure test are considered fully correlated among the mesons, while those deriving from the yield extraction, the background subtraction, and the D meson reconstruction & selection efficiency are treated as uncorrelated.

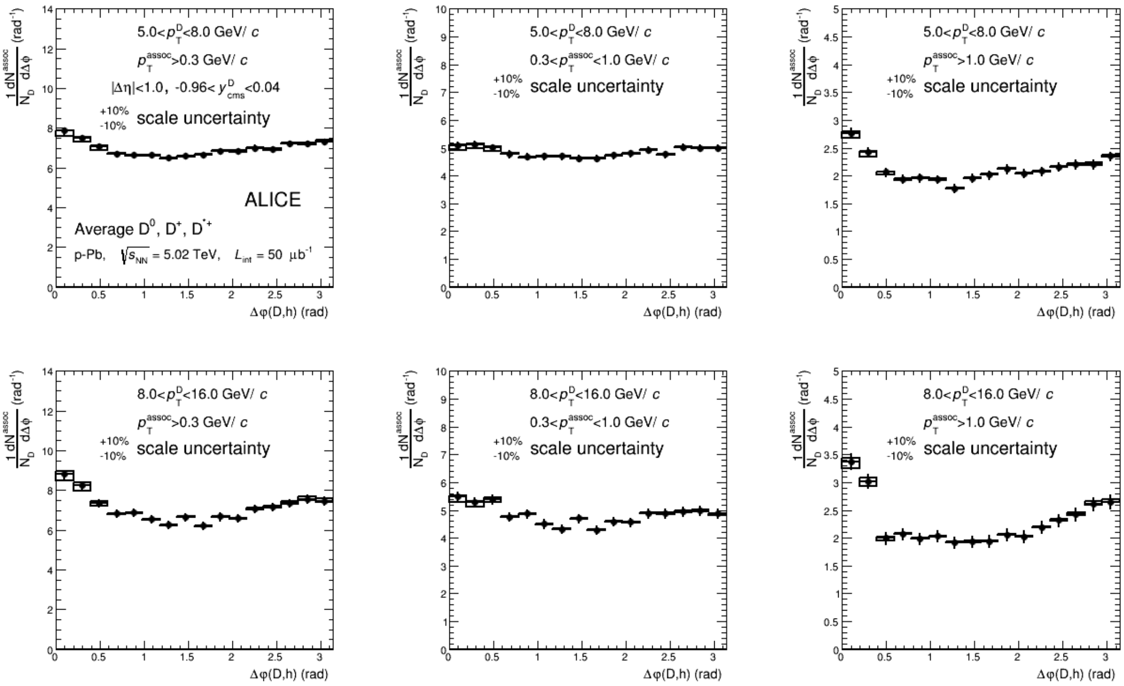

Figure 5.31: Azimuthal correlation distributions between average of D^0, D^+ and D^{*+} and primary charged particles in the D meson p_T ranges $5 < p_T(D) < 8$ GeV/c and $8 < p_T(D) < 16$ GeV/c, with associated track $p_T > 0.3$ GeV/c, $p_T > 1$ GeV/c and $0.3 < p_T < 1$ GeV/c.

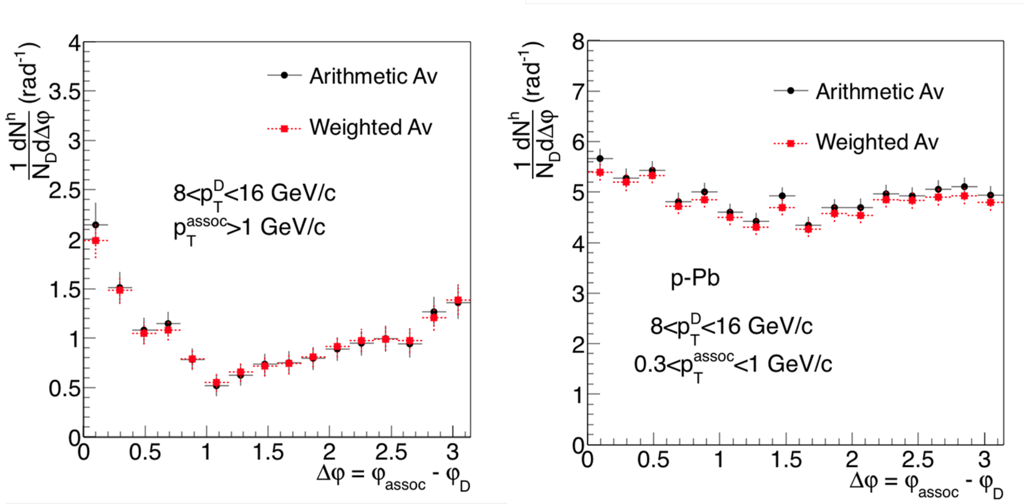

Figure 5.32: Comparison of weighted and arithmetic averages D meson-charged particle azimuthal correlations with associated track $p_{\mathrm{T}} > 0.3$ GeV/c, $0.3 < p_{\mathrm{T}} < 1$ GeV/c in the D meson p_{T} range $8 < p_{\mathrm{T}}(\mathrm{D}) < 16$ GeV/c.

Figure 5.31 shows the average of D^0, D^+ and D^{*+} azimuthal correlations with associated track $p_{\mathrm{T}} > 0.3$, 0.5, 1 GeV/c and in the D meson p_{T} ranges $5 < p_{\mathrm{T}}(\mathrm{D}) < 8$ GeV/c and $8 < p_{\mathrm{T}}(\mathrm{D}) < 16$ GeV/c. A rising trend of the height of the near-side peak with increasing D meson p_{T} is observed. In order to achieve the reliability of this weighted average approach, a straight-forward arithmetic average has been computed for all three mesons which of course does not depend on any assumption. Figure 5.32 shows the comparative results of these two approaches for evaluating the averages for D meson in $8 < p_{\mathrm{T}}(\mathrm{D}) < 16$ GeV/c and with associated track $p_{\mathrm{T}} > 0.3$ GeV/c, $0.3 < p_{\mathrm{T}} < 1$ GeV/c. The results are found to be compatible for the selected kinematic ranges though the arithmetic average shows higher statistical uncertainties. Hence, the weighted average approach has been validated and further computations will be done with this method.

5.3.3.1 Computation of near-side yields, near-side widths and baselines as a function of D meson p_{T}

For the computation of near-side yield, near-side width and baseline, the correlation distributions are fitted with two Gaussian functions (with means fixed at 0 and π) plus a constant, with a periodicity condition applied on the fit (Eq. 5.12).

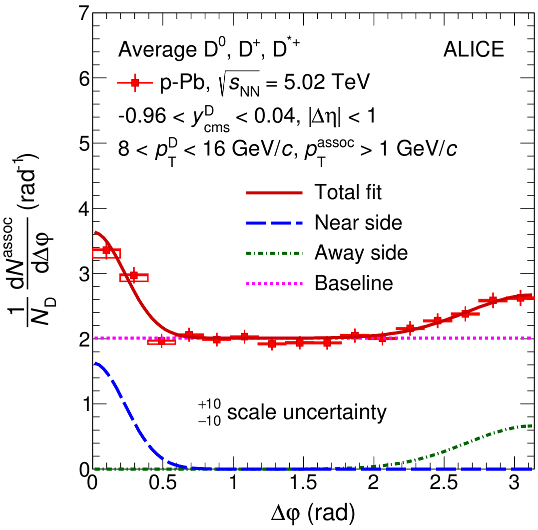

Figure 5.33: Example of fit to the azimuthal correlation distributions, for the average of the three D-mesons in $5 < p_{\mathrm{T}}(\mathrm{D}) < 8$ GeV/c and $p_{\mathrm{T}}^{assoc} > 1$ GeV/c.

Figure 5.33 shows example of fit function on the average D meson-charged particle correlation distribution reflected in the range 0 to π in D meson p_{T} range $5 < p_{\mathrm{T}}(\mathrm{D}) < 8$ GeV/c and with $p_{\mathrm{T}}^{assoc} > 1$ GeV/c, providing values of χ^2/NDF close to unity. The red, blue, green, magenta color lines show the total fit, near-side Gaussian (dashed line), away-side Gaussian (dashed-dotted line) and constant baseline (dotted line) functions respectively. The statistical uncertainties are shown as error bars. The $\Delta\varphi$-uncorrelated systematic uncertainties are shown as boxes, while the part of

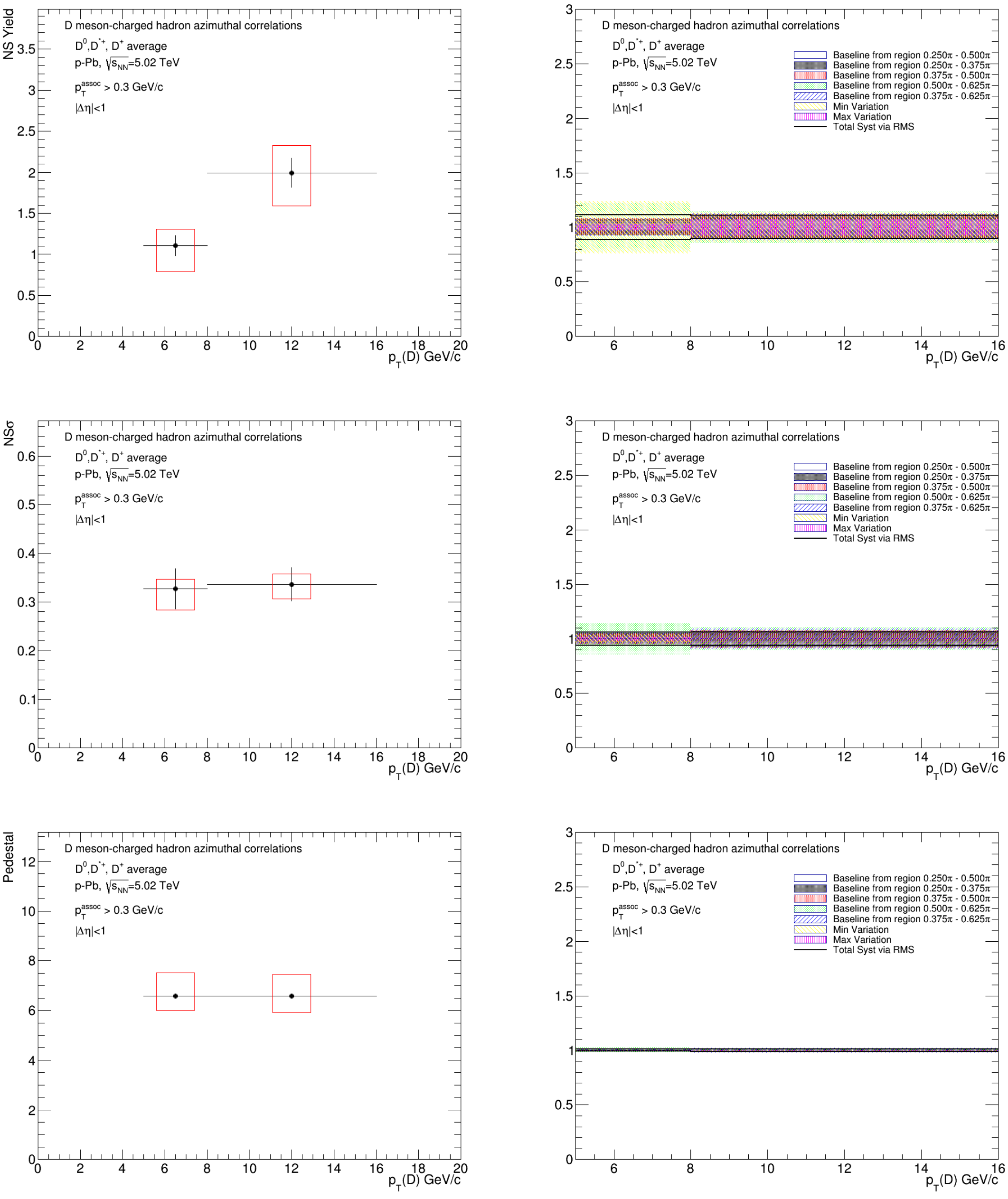

Figure 5.34: (left column) Near-side yield, near-side width and height of the baseline extracted from fit to the azimuthal correlation distributions for $p_{\mathrm{T}}^{assoc} > 0.3$ GeV/c. (right column) The corresponding systematic uncertainties coming from the variation of the fit procedure.

systematic uncertainty correlated in $\Delta\varphi$ is shown in text (scale uncertainty).

The measurements of parameters like near-side associated yield, near-side width and baseline are performed from the fit procedure described here subsection 5.2.7. The near-side yields are calculated by integrating the near-side Gaussian after baseline subtraction. The left column of Fig. 5.34 shows the near-side associated yield, width and, the height of the baseline (pedestal) for the average correlation distributions as a function of D p_{T} with $p_{\mathrm{T}}^{assoc} > 0.3$ GeV/c. The corresponding plots in the right column explain the systematic uncertainty of the considered observables from the variation of the fit procedure (see here subsection 5.2.7). The near-side widths and baselines show no relevant p_{T} dependence and a hints of an increasing trend with p_{T} for the near-side yield is observed.

5.3.3.2 Comparison of data and Monte Carlo simulations

The measured angular correlation distributions are compared to simulation results obtained with the event generators PYTHIA 6.4.25 [19] (the Perugia-0, Perugia-2010, and Perugia-2011 tunes [10, 20]), PYTHIA 8.1 (tune 4C, including MPI and color reconnection) [21], POWHEG [22] coupled to PYTHIA (Perugia-2011 tune), and EPOS 3 [23]. In the simulations done with $\sqrt{s_{\mathrm{NN}}} = 5.02$ TeV, the centre-of-mass frame is boosted in rapidity by $\Delta y_{NN} = 0.465$ in the proton going direction in order to reproduce the rapidity shift of the reference frame of the nucleon-nucleon collision in the pPb collision system. A brief descriptions of different event generators are given in section 8.1.

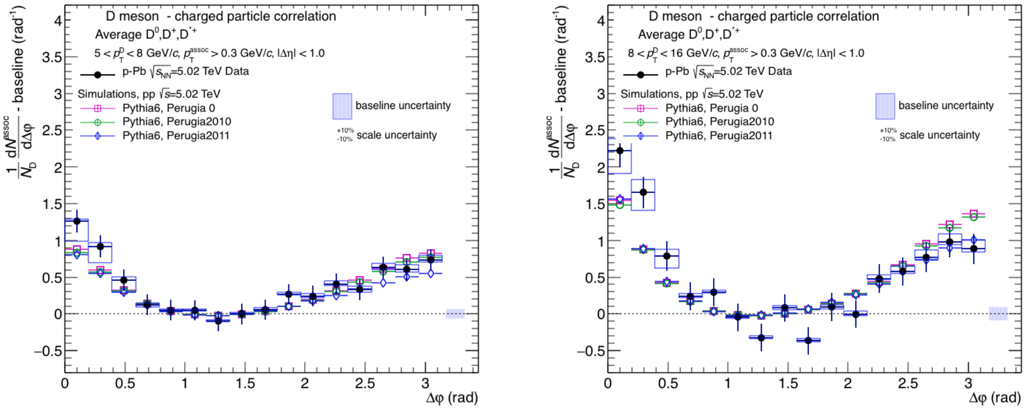

Figure 5.35: Comparison of $\Delta\varphi$ azimuthal correlation distribution, obtained from data and simulations (PYTHIA, with three tunes), in the different kinematic ranges analyzed.

Figure 5.35 shows the comparison of the average azimuthal correlation distributions measured in pPb collisions with expectations from simulations performed with PYTHIA in different tunes after the baseline subtraction. In case of the simulations, the baseline is estimated at the minimum of the azimuthal correlation distributions as the statistical fluctuations are negligible. The uncertainty related to the baseline definition is negligible and not displayed in the figures. The distributions obtained with the different tunes, do not show significant differences in the near-side. In the away-side, the PYTHIA 6 tunes Perugia 0 and Perugia 2010 tend to have higher correlation values for $p_{\mathrm{T}}^{assoc} > 0.3$ GeV/c, compared to the other simulation results. All the considered Monte Carlo simulations describe, within the uncertainties, the data in the whole $\Delta\varphi$ range. However, a hint of a more pronounced peak in the near-side in data compared to the models is present for D mesons with $8 < p_{\mathrm{T}} < 16$ GeV/c for $p_{\mathrm{T}}^{assoc} > 0.3$ GeV/c [7]. Similar comparison is done for other event generators [7].

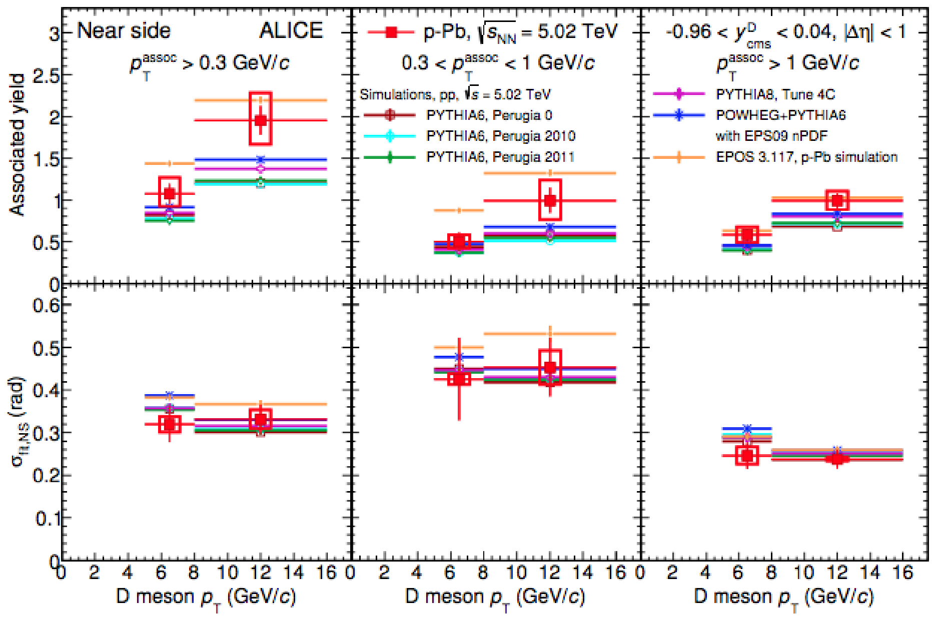

Figure 5.36: Comparison of near-side peak associated yield (top row) and near-side peak width (bottom row) values measured in pPb collisions at $\sqrt{s_{\rm NN}}$= 5.02 TeV with the expectations from simulations performed with different Monte Carlo event generators. Statistical and systematic uncertainties are shown as error bars and boxes, respectively [7].

Figure 5.36 shows the comparison of associated yield (A_{NS}) and width ($\sigma_{fit,NS}$) in the near-side peak of the averaged azimuthal correlation distributions measured in pPb collisions. The values are compared with the expectations from simulations performed with PYTHIA in different tunes and POWHEG+PYTHIA, PYTHIA 8 and EPOS 3. The simulations obtained with EPOS 3 provide a better description of the near-side yields for D mesons with $8 < p_{\rm T} < 16$ GeV/c. At lower D-meson $p_{\rm T}$ a better agreement is obtained with PYTHIA and POWHEG+PYTHIA simulations. The width of the near-side peaks, shown in the second row of the same figure and the simulation outputs are compatible within measured uncertainties.

5.3.3.3 Comparison of *pp* and *pPb* data results

The D meson charged particle angular correlations analysis is also evaluated for *pp* at $\sqrt{s}$= 7 TeV in ALICE PWGHF-HFCJ group. Since *pp* collisions are always taken as a reference for coherent binary nucleon-nucleon collisions, the study of angular correlations between D meson and charged particles in *pPb* collisions is compared with *pp* collisions.

Figure 5.37 shows the $\Delta\varphi$ distributions after the subtraction of the baseline for *pp* at $\sqrt{s}$= 7 TeV (black points) and *pPb* at $\sqrt{s_{\mathrm{NN}}}$= 5.02 TeV (red points). The results obtained for the two collision systems are compatible within uncertainties. According to simulations of *pp* collisions performed with PYTHIA 6 (Perugia-0, -2010, and -2011 tunes), the different centre-of-mass energies and the slightly different D meson rapidity ranges of the two measurements should induce variations in the baseline subtracted azimuthal correlation distributions smaller than 7% in the near- and away-side regions. Such difference is well below the current level of uncertainties [7].

The comparisons of associated yields (A_{NS}) and widths ($\sigma_{fit,NS}$) in the near-side peak of the averaged D meson-charged particle azimuthal correlation distributions are shown in Fig. 5.38 for the two collisional systems *pp* and *pPb* as a function of D meson transverse momentum (p_{T}(D)). The top row of Fig. 5.38 shows that the near-side peak associated yields increase with p_{T}(D) for both the collisional systems and are compatible within the uncertainties for all the associated track p_{T} ranges. The bottom row of the same figure describes the near-side peak width ($\sigma_{fit,NS}$) for

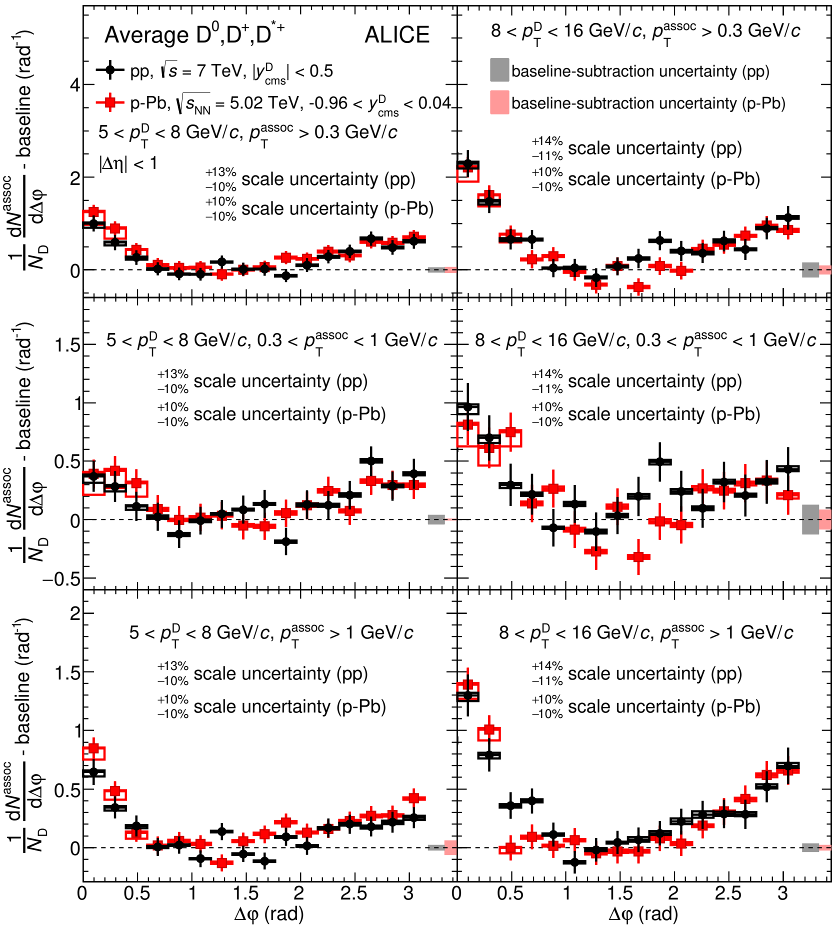

Figure 5.37: Average of D^0, D^+ and D^{*+} azimuthal correlations in pp (red) and pPb (blue) with D meson p_T ranges $5 < p_\mathrm{T} < 8$ GeV/c and $8 < p_\mathrm{T} < 16$ GeV/c, for the three regions of associated track p_T [7].

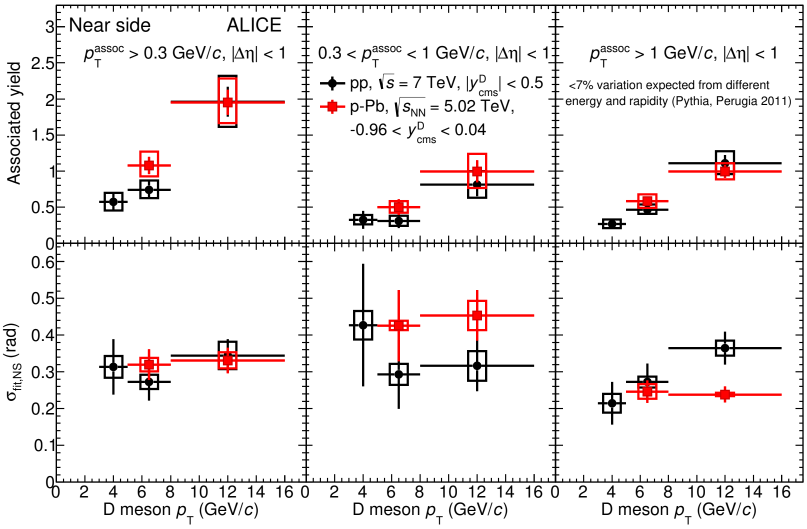

Figure 5.38: Comparison of the near-side peak associated yield (top row) and peak width (bottom row) between pp and pPb collisions as a function of $p_{\mathrm{T}}(\mathrm{D})$, for $p_{\mathrm{T}}^{assoc} >$ 0.3 GeV/c (left column), 0.3< p_{T}^{assoc} < 1 GeV/c (middle column), and $p_{\mathrm{T}}^{assoc} > 1$ GeV/c (right column). Statistical and systematic uncertainties are shown as error bars and boxes, respectively [7].

pp and pPb data. Although for $p_{\mathrm{T}}^{assoc} > 0.3$ GeV/c the near-side peak width does not depend on D meson p_{T}, the current level of uncertainty does not allow us to quantify the dependence of near-side peak width on D meson and associated track p_{T}. The measurements of near-side yields and widths suffer from the impact of baseline uncertainty which is expected to be significantly reduced in future with larger statistics [7].

5.3.4 Summary and Conclusion

In this thesis the measurement of angular correlations between D^0 mesons (trigger particles) and unidentified charged primary particles (associated particles) in proton-lead (pPb) collisions is presented. The analysis has been performed using the ALICE detector at the LHC. The ALICE analysis framework is used for this study. The analysis tools and softwares were developed for pp data analysis and is then extended for pPb.

The azimuthal correlation analysis between D^0 meson and charged particles is studied in three different D^0 meson transverse momentum intervals, $3 < p_{\mathrm{T}}^{\mathrm{D}^0} < 5$ GeV/c, $5 < p_{\mathrm{T}}^{\mathrm{D}^0} < 8$ GeV/c, and $8 < p_{\mathrm{T}}^{\mathrm{D}^0} < 16$ GeV/c and for associated charged particles transverse momentum $p_{\mathrm{T}}^{assoc} > 0.3$ GeV/c, $p_{\mathrm{T}}^{assoc} > 0.5$ GeV/c, $p_{\mathrm{T}}^{assoc} > 1.0$ GeV/c and in the sub-range $0.3 < p_{\mathrm{T}}^{assoc} < 1$ GeV/c.

For this analysis the Inner Tracking System (ITS), Time Projection Chamber (TPC), Time of Flight (TOF) and V0 detectors are used. Overall 100 million minimum bias events corresponding to an integrated luminosity of about $L_{int} = 50\ \mu b^{-1}$ has been studied. Events with a reconstructed primary interaction vertex within $\pm$ 10 cm from the centre of the detector along the beam line are considered. For pPb collisions, the center-of-mass reference frame of the nucleon-nucleon collision is shifted in rapidity by $\Delta y_{NN} = 0.465$ in the proton going direction with respect to the laboratory frame, due to the different per-nucleon energies of the proton and the lead beams.

D^0 mesons are reconstructed via the decay channel $\mathrm{D}^0 \rightarrow \mathrm{K}^-\pi^+$ which has a branching ratio of $(3.88 \pm 0.05)\%$. The D^0 candidates are built by combining the tracks with $|\eta| < 0.8$ and $p_{\mathrm{T}} > 0.3$ GeV/c coming from the secondary vertex. ALICE ITS has an extremely good precision of finding secondary decay vertices. A set of topological selections were applied on the daughter tracks to reduce the background for the measurement of D^0 yield. The associated charged particles are defined by all unidentified primary charged particles with $p_T^{assoc} > 0.3$ GeV/c and with $|\eta| < 0.8$ except for the D^0 daughters. A minimum "distance to closest approach" (DCA) cut is applied to reject the secondary tracks.

The D^0 mesons are then correlated with the charged particles in the above specified p_T ranges. The analysis consists of various corrections viz. side-band correction, trigger and track efficiency correction, mixed-event correction and beauty feed-down correction. Various types of systematics uncertainties are also evaluated. The $\Delta\varphi$ correlations show visible peak at $\Delta\varphi = 0$ and π for all the p_T ranges of D^0 and associated tracks. A parallel analysis for the other two D mesons (D^+ and D^{*+}) is done by other co-analyzers. The results from analysis of D^+ and D^{*+} as trigger particles show nice compatibility within the uncertainty with this analysis. Hence, to reduce the influence of statistical and systematic uncertainties, the weighted average of the correlation distributions of different D meson species is evaluated. The average D^0, D^+, D^{*+} correlations are computed for those specific p_T ranges of trigger and associated tracks.

A comparison of the fully corrected azimuthal correlations for both D^0 only and average of three D mesons were compared with different Monte Carlo simulated events. For *pPb* study LHC13d3 Monte Carlo sample is used where the events are simulated using HIJING event generator on top of PYTHIA. The outcomes of the comparisons between data and Monte Carlo show a substantial agreement within the measured uncertainties.

In order to extract the physical quantities, like the baseline height of the correlation distributions, the yield and the width of the near-side peak, a fit procedure is adopted with proper function. The distributions were fitted with two Gaussian functions for near- and away- side peaks and a constant for baseline. The near-side yield and width are evaluated from the fit after baseline subtraction. The dependency of these quantities on the D meson p_{T} is evaluated. The results show an increase of near-side yield with D meson p_{T} for different associated track p_{T} ranges. The analysis suffers from baseline uncertainties hugely due to lack of statistics. For pPb, a constant v_2 is added for the baseline measurements.

The analysis is also compared with pp data at $\sqrt{s} = 7$ TeV. A good agreement between pp and pPb correlations is found within the measured uncertainties. From Monte Carlo study it is found that the different centre-of-mass energies and the slightly different D-meson rapidity ranges of the two measurements induce variations in the baseline subtracted azimuthal correlation distributions smaller than 7% in the near- and away-side regions which is well below the uncertainty level of current analysis. Due to large statistical fluctuations it was not possible to extend the analysis in large $\Delta\eta$ region where any possible ridge-like structure could possibly be explored. Study of azimuthal correlations using heavy-flavor decay electrons as trigger particle by ALICE heavy-flavor group, showed a double ridge structure in pPb collisions at $\sqrt{s_{\mathrm{NN}}} = 5.02$ TeV. Also any kind of azimuthal anisotropy (flow) could be explored with correlation analysis in heavy-flavor sector. For the current analysis, the statistical fluctuations on the correlation results and, as a consequence, the uncertainties on the physical observables extracted by fitting the distributions do not allow us to explore any possible cold nuclear matter effects.

Bibliography

[1] ALICE Analysis Notes, D meson production in pPb collisions at $\sqrt{s_{\rm NN}} = 5.023$ TeV, ANA-1747.

[2] K. A. Olive et al., PDG Collaboration, Chin. Phys. **C38**, 090001 (2014).

[3] B. Abelev et al., ALICE Collaboration, JINST, 9 (11), P11003 (2014).

[4] E. Bruna et al., ALICE Note, ALICE-INT-2009-018 (2009).

[5] B. Abelev et al., ALICE Collaboration, JHEP**01**, 128 (2012).

[6] Measurements of D-hadron azimuthal correlations with ALICE at the LHC, Fabio Colamaria, CERN-THESIS-2014-036.

[7] J. Adam et al., (ALICE Collaboration), Eur. Phys. J. C 77 (2017) 245.

[8] M. Cacciari, M. Greco, and P. Nason, JHEP**05**, 007 (1998).

[9] B. Abelev et al., ALICE Collaboration, JHEP**01**, 128 (2012).

[10] P. Z. Skands, The Perugia tunes, arXiv:0905.3418 [hep-ph].

[11] ALICE Analysis Notes, D-hadron correlations in pPb collisions at $\sqrt{s_{\mathrm{NN}}} = 5.02$ TeV, ANA-1555.

[12] X. N. Wang and M. Gyulassy, Phys. Rev. **D44**, 3501-3516 (1991).

[13] R. Brun, F. Carminati, and S. Giani, CERN Program Library Long Write-up W5013 (1994).

[14] B. Abelev et al., ALICE Collaboration, JHEP**01**, 128 (2012).

[15] B. Abelev et al., ALICE Collaboration, JHEP**09** 112 (2012).

[16] B. Abelev et al., ALICE Collaboration, PRL **111**, 102301 (2013).

[17] B. Abelev et al., ALICE Collaboration, Phys. Rev. **C90**, 034904 (2014).

[18] B. Abelev et al., ALICE Collaboration, PRL **113**, 232301 (2014).

[19] T. Sjöstrand, S. Mrenna, and P. Z. Skands, JHEP**05**, 026 (2006).

[20] P. Z. Skands, Phys. Rev. **D82**, 074018 (2010).

[21] T. Sjöstrand, S. Mrenna, and P. Z. Skands, Comput. Phys. Commun. 178, 852-867 (2008).

[22] P. Nason, JHEP**11**, 040 (2004).

[23] H. J. Drescher, M. Hladik, S. Ostapchenko, T. Pierog, and K. Werner, Phys. Rept. 350, 93-289 (2001).

Chapter 6

Study of small systems with simulated events

In this chapter, the results from Monte Carlo simulated events using EPOS 3 and PYTHIA 8 models will be discussed. The results are composed of multiplicity dependent charged particle production and two-particle angular correlations using D meson triggers and unidentified hadron triggers in pPb collisions at $\sqrt{s_{\rm NN}}$ = 5.02 TeV using EPOS 3 event generator with and without hydrodynamical evolution & in pp collisions at $\sqrt{s}$ = 7 TeV using PYTHIA 8 event generator with and without color reconnection (CR)

6.1 Study of high-multiplicity pPb events using EPOS 3 model

Our analysis of the minimum-bias ALICE data of pPb collisions at $\sqrt{s_{\mathrm{NN}}} = 5.02$ TeV in terms of D meson-charged particle azimuthal correlations (presented in chapter 5) reiterates the absence of cold nuclear matter effects in pPb collisions at the LHC. This observation and also the unexpected features in high-multiplicity pPb events as already discussed in details in section 1.4, prompted us to extend the study of D meson-charged particle azimuthal correlations to high-multiplicity events. However, due to lack of sufficient data statistics for such study, we depend on the simulated events, generated with the EPOS 3 code (briefly described in the section 8.1). The EPOS 3 code with hydrodynamic evolution has been successful in explaining most of the significant features of pPb data [1]. Using the EPOS 3 code, we have generated 18 million minimum-bias pPb events at $\sqrt{s_{\mathrm{NN}}} = 5.02$ TeV, with the in-built (3 + 1D) viscous hydrodynamic evolution followed by hadronic evolution allowing re-scattering before the freeze-out of particles through standard Cooper-Frye procedure. We have also generated 10 million amount of minimum-bias pPb events with the EPOS 3 code without hydrodynamic. These events without hydrodynamic evolution do not reproduce the data in terms of the basic observables. As for example, the identified particle spectra as obtained by ALICE, cannot be reproduced from the pPb events at $\sqrt{s_{\mathrm{NN}}} = 5.02$ TeV, generated by EPOS 3 code without hydrodynamic evolution. We obtain the invariant yield spectra for the identified charged particles, $\pi^{\pm}$, $K^{\pm}$ and p, $\bar{p}$ for different centrality classes (the detail of the centrality estimation has been given below) from the EPOS 3 generated events and plot the spectra

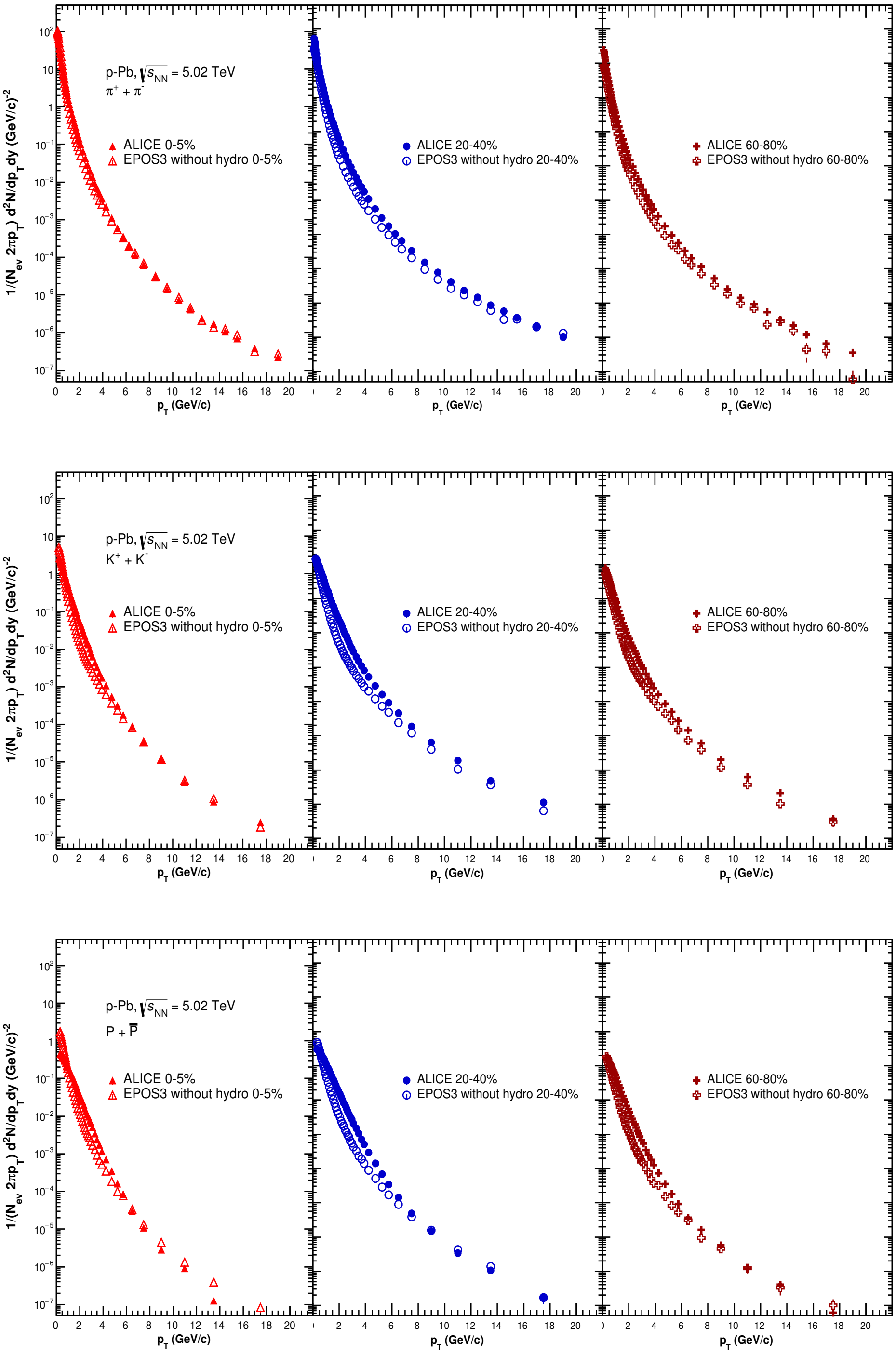

Figure 6.1: The multiplicity dependent invariant yields of pions (top), kaons (middle) and protons (bottom) in pPb collisions at $\sqrt{s_{\mathrm{NN}}} = 5.02$ TeV, measured by ALICE [2], are compared with the simulated events from the EPOS 3 without hydrodynamic evolution [1].

in Fig. 6.1, for pions (top), kaons (middle) and protons (bottom) respectively along with the respective spectra measured by ALICE, for representative centrality classes (similar comparative study on identified spectra with the EPOS 3 generated events with hydrodynamic evolution has been presented below). As can be seen from the Fig. 6.1, the data cannot be reproduced by non-hydro EPOS 3 code and so we skip the presentation of the detail analysis of these non-hydro events.

Although, the uniqueness of the heavy-flavor particles as probe and the versatility of the two-particle angular correlations have already been discussed in chapter 3 and in chapter 2, respectively, for the convenience of the readers, we briefly discuss all these topics in this section also.

6.1.1 Heavy-flavor mesons: The probe

Because of their large masses, the production of HF-quarks (charm and bottom) predominantly takes place in the hard scattering of partons (fusion of gluons at the LHC energies) during the primordial stage of ultra-relativistic heavy-ion collisions and has remote possibility in the successive stages (including from the jet-medium interactions) of the evolution of the expanding partonic medium that reaches the thermalized QGP state before hadronization. Most of the heavy quarks, produced in heavy-ion collisions thus witness the entire evolution of the QGP medium. Also, due to the large momentum transfer in the hard partonic interactions, the production cross sections of heavy-quarks are calculable in the perturbative QCD approach. While defusing through the medium, made of the light quarks and gluons, the heavy quarks experience radiative and collisional energy loss that is reflected in the spectra of the final state HF-mesons. The heavy flavor mesons thus make unique direct probe for studying the properties of the QGP-medium, in terms of the collective flow and the jet-quenching. The HF-meson (the D-meson) has already played a significant role in characterizing the medium formed in $PbPb$ and pPb collisions at the LHC energies. ALICE has reported suppression of high-p_{T} D-mesons [3] in $PbPb$ collisions at $\sqrt{s_{\mathrm{NN}}} = 2.76$ TeV. Also, the D-mesons have been found to have medium induced collective flow [4] in $PbPb$ collisions at $\sqrt{s_{\mathrm{NN}}} = 2.76$ TeV. ALICE has measured the nuclear modification factor, R_{pPb}, for D-mesons yields [5] and the relative yields of D-mesons as a function of relative charged particle multiplicity [6] in pPb collisions at $\sqrt{s_{\mathrm{NN}}} = 5.02$ TeV. The R_{pPb} measurement, revealing very small CNM effects for $p_T \geq 3$ GeV/c, confirmed that the suppression of high-p_{T} D-mesons [3] in $PbPb$ collisions at $\sqrt{s_{\mathrm{NN}}} = 2.76$ TeV is predominantly due to the charm energy loss in the medium.

The "ridge" structure in high-multiplicity events of pPb collisions [7–10], as observed in light-flavor two-particle angular correlation study, has been suggested to be due to either collectivity [11] or the gluon saturation [12]. Though, the collectivity in the high-multiplicity pPb events at the LHC energy is largely accepted, this new study of multiplicity dependent azimuthal correlations of HF-mesons and charged particles in pPb events could shed further light, in this context.

6.1.2 Two-particle angular correlations: The analysis tool

The two-particle angular correlation function is characterized by the $\Delta\eta, \Delta\varphi$ distribution (where $\Delta\eta$ and $\Delta\varphi$ are the differences in the pseudorapidity (η) and azimuthal angle (φ) of the two particles) of per-trigger particle yield of associated charged particles and is given by:

$$\frac{1}{N_{trig}}\frac{d^2N^{assoc}}{d\Delta\eta d\Delta\varphi} = B(0,0) \times \frac{S(\Delta\eta,\Delta\varphi)}{B(\Delta\eta,\Delta\varphi)} \tag{6.1}$$

where N_{trig} is the number of trigger particles in the specified $p_T^{trigger}$ range.

The function S($\Delta\eta, \Delta\varphi$) is the differential measure of per-trigger distribution of associated hadrons in the same event, i.e,

$$S(\Delta\eta,\Delta\varphi) = \frac{1}{N_{trig}}\frac{d^2N^{assoc}_{same}}{d\Delta\eta d\Delta\varphi} \tag{6.2}$$

The same event distribution functions are corrected for the random combinatorial background and effects due to the limited acceptance by dividing the raw same event distribution function by the mixed event background distribution, where trigger and associated particles are paired from two different events of similar multiplicity.

The background distribution function B($\Delta\eta, \Delta\varphi$) is defined as:

$$B(\Delta\eta,\Delta\varphi) = \frac{d^2N^{mixed}}{d\Delta\eta d\Delta\varphi} \tag{6.3}$$

where N^{mixed} is the number of mixed event pairs.

The factor B(0,0) in Eq. 6.1 is used to normalize the mixed event correlation function such that it is unity at ($\Delta\eta, \Delta\varphi$)=(0,0). Finally, the acceptance corrected correlation function is determined by scaling the same event distribution function, $S(\Delta\eta, \Delta\varphi)$ by the inverse of the normalized background distribution function, $B(\Delta\eta, \Delta\varphi)/B(0, 0)$.

The two-particle azimuthal correlations function is a versatile analysis tool that, depending on the $|\Delta\eta|$ and the p_{T}-ranges for the trigger and the associated particles, addresses several sources of correlations in multiparticle production. Of the correlations, interested for this study, this analysis tool provides an useful alternate to the direct jet-reconstruction method for studying the jet properties, indicating the jet-medium interactions. Also, the correlated emission of particles from collective, and so the thermalized, medium can be identified and extracted.

The "short-range" ($|\Delta\eta| \sim 0$) two-particle azimuthal angle correlations are dominated by high-p_{T} jets, produced back-to-back in hard QCD scattering. The jet correlations are reflected in $|\Delta\varphi|$ - distribution. The jet-induced per-trigger hadron-pair yields from the same jet populate at $|\Delta\varphi| = (|\varphi_{trigger} - \varphi_{assoc.}|) \sim 0$. The pair yields from away-side jets show up at $|\Delta\varphi| = (|\varphi_{trigger} - \varphi_{assoc.}|) \sim \pi$. Due to the fragmentation process and several medium effects, the back-to-back short-range jet correlations get smeared, affecting the away-side structure. The near-side short-range jet-like correlations, however, can carry clearer information on jet-medium interactions and the p_{T}-differential, bulk-subtracted per-trigger correlated yields may be helpful in characterizing the medium.

On the other hand, for the correlated emission of particles from collective medium, the two-particle azimuthal angle correlations in the "long-range" ($|\Delta\eta| \gg 0$) give rise to structure in both the near-side and the away-side. While the away-side structure may have contribution from correlations due to momentum conservation and other effects, the near-side structure of the two-particle azimuthal angle correlations in the long-range is considered to be free from other effects and attributed to the formation of collective medium. In relativistic heavy-ion collisions, the per-trigger pair yields with small $|\Delta\varphi|$ over a wide range of $|\Delta\eta|$ (long-range), result a "ridge" structure in the constructed correlation functions. The "ridge" structure also appears in high-multiplicity pp [13–16] and pPb [7–10] collisions at the LHC. In the absence of medium formation, one does not expect significant structure in the near-side of the long-range two-particle angular correlation functions, as the jets and resonance decays contribute in the short-range only. The appearance of "ridge" is primarily a low p_{T} or soft-particle phenomenon. In the high-multiplicity pPb data [8], the "ridge" structure has been found to be most prominent in the $1<p_T<2$ GeV/c, while the structure diminishes in the higher p_{T}-range.

The particles in the intermediate p_{T} range, between the "hard" and the "soft" ones, originate from mixed sources and usually has contributions from the "soft" as well as from the "hard" particles. Also, particles from the recombinations or coalescence of quarks are likely to contribute in this p_{T}-range. In this context, it may be noted that the enhanced baryon to meson ratio in this intermediate p_{T}-range at the LHC, as observed in central collisions of both the $PbPb$ [17] and pPb, [18] is attributed to the radial flow and the hadronization by the recombination of quarks, rather than fragmentation of quarks. The quark recombination model explains [19] the baryon to meson ratio in the p_{T}-range up to 5 GeV/c. The correlation functions obtained from the two-particle angular correlations study is quantified in terms of per-trigger yields. In the considered p_{T}-range, therefore, all the triggers in the short-range correlation functions do not necessarily come from hard jet-like triggers. The contributions to the triggers from sources other than the hard-scattered ones in the jet-like correlation functions causes "trigger dilution". This effect has already been exhibited in a study [20] with the EPOS 3 generated events with the identified hadron triggers and unidentified charged associated particles. It has been shown that while both the pion and proton triggers get diluted with increasing centrality, the rate of dilution is more for protons. The increased rate of dilution for proton triggers with multiplicity has been attributed to the larger rate of increase of the soft proton triggers due to radial flow. In the context of the jet-like correlations study, however, one expects D-meson triggers to remain unaffected or less affected by the trigger dilution due to the fact the charm quarks are predominantly produced in the primordial hard scattering and, also, the large relaxation time for the heavy-quarks causes delay in acquiring the medium induced radial flow.

6.1.3 Event generation by EPOS 3

The most important aspect of the EPOS 3 simulation code for particle production at the LHC energy is probably the similar treatment adopted in $proton - proton$, $proton - nucleus$ and $nucleus - nucleus$ collisions, which facilitate understanding the observed feature of collectivity in the high-multiplicity pp and pPb events at the LHC vis-a-vis the exhaustively studied collective phenomena in relativistic $nucleus - nucleus$ collisions. In this model, an elementary scattering of partons give rise to parton ladder of pomeron. Each parton ladder may be considered as a longitudinal color field or a flux tubes, carrying transverse momentum of the hard scattering. The flux tubes expand and at some stage get fragmented into string segments of quark-antiquark pairs. In high energy high-multiplicity pp, $p - nucleus$ and $nucleus - nucleus$ events, many elementary parton-parton scatterings produce a large number of flux tubes and eventually high local string-segment density. The high energy of string segments and / or high local string-segment density (above a critical value) constitute the bulk matter, forming a medium. The string segments, inside the bulk matter, which do not have enough energy to escape, get thermalized and undergo hydrodynamical expansion following (3 + 1D) viscous hydrodynamic evolution followed by hadronic evolution allowing re-scattering before the freeze-out of the "soft" (low p_{T}) hadrons take place through standard Cooper-Frye procedure. The string segments produced inside the bulk matter, close to the surface, by picking up quark-antiquark from the thermalized matter and have enough energy to escape, form jets with the jet-hadrons mostly in the "intermediate" p_{T}-range. The string segments from outside the bulk matter hadronize by Schwinger's mechanism and escape as "high" p_{T} jet-hadrons.

In view of the particular topic of interest for this work, the production mechanism of heavy quark and subsequently the HF-mesons in the EPOS 3 framework will be worth discussing at this point. According to the initial conditions of the EPOS 3, the heavy quarks may be produced [21] in the initial stage, whenever the massive quark - antiquark production is possible, following the same general procedure, as discussed above, through fragmentation of flux tubes or the parton ladders, formed in elementary scattering of partons. In multiple scattering in the EPOS framework, many parton ladders are produced, while each of the parton ladders contributes in production of the charm as well as the light quarks leading to the production of D-mesons and light hadrons. However, the low momentum string segments containing the charm quark-antiquark pairs, unlike the low energy string segments of the light quarks, do not contribute to the formation of the hydrodynamically expanding bulk matter, and rather give rise to the formation of D-mesons in the low p_{T}-range. Also, in EPOS 3, no interaction between the heavy quarks and the bulk thermalized matter is implemented [21]. So, in the existing EPOS 3 code, there is no way that the low-p_{T} D-mesons exhibit any collective behaviour. This is in contrast to the conventional QGP scenario, where the hard scattered charm quarks, through collisional and radiative energy loss during their passage in the thermalized partonic medium, get themselves thermalized, resulting $v_2(p_{\mathrm{T}})$ for the D-mesons, similar to that for the light hadrons in the "low"-p_{T}-range.

The particles in the "intermediate" p_{T}-range in the EPOS framework, however, come from the jet-hadrons produced from the string segments which carry the collective property of the thermalized bulk matter as well as enough energy to escape it. So, even in the given EPOS 3 framework, the D-mesons originating from the initial hard processes in the intermediate p_{T}-range are likely to carry the collective property of the bulk fluid, like the other light hadrons. With these considerations, to explore the collective nature of the high-multiplicity pPb events at the LHC energy in terms of the long-range two particle angular correlations of the D-mesons, in the intermediate p_{T}-range, and the charged particles, we have generated 10 million minimum-bias pPb events at $\sqrt{s_{\mathrm{NN}}} = 5.02$ TeV, using the EPOS3.107 code.

To make this centrality-dependent study of the simulated events more like data analysis by the experiments, for the centrality estimation, we follow the technique, identical to the one followed by ALICE. Also, we validate the generated events by reproducing the available centrality-dependent ALICE measurements which are relevant to the type of analysis we aim to carry out.

6.1.4 Centrality estimation

The multiplicity or the centrality dependent studies of pPb data by the ALICE have been carried out in different event classes identified with a range of multiplicities. The event classes are obtained either from the signal amplitude in the VZERO detector in the backward rapidity region ($2.8<\eta<5.1$) or from the reconstructed tracklets from the Silicon Pixel Detector (SPD) in the mid-rapidity $|\eta|< 1.0$. For the centrality estimation from the VZERO detector, the minimum-bias events are divided into several event classes, defined as fraction of the analyzed event sample, based on the cuts on the total deposited charge in the VZERO detector in the Pb-going direction. The deposited charge on the VZERO detector is proportional to the multiplicity of the charged particle in the covered pseudorapidity interval.

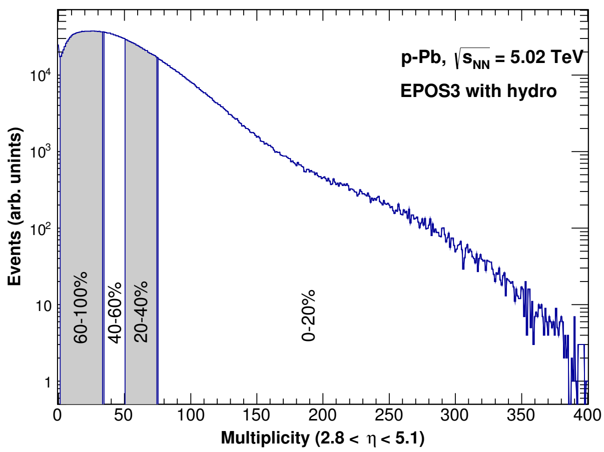

Figure 6.2: Centrality selection for the EPOS 3 generated events from the VZERO-A acceptance [6] of ALICE set-up.

For this analysis with the simulated events, for the centrality selection, we consider the charged particle multiplicity in the lead-going direction in the same pseudorapidity region of 2.8<η_{lab}<5.1, which is the acceptance of the respective VZERO detector in the ALICE set-up. We take into account the asymmetric pPb collisions, where the nucleon-nucleon center-of-mass system moves in the direction of the proton beam corresponding to a rapidity of y_{NN} = - 0.465, resulting the laboratory reference interval $|y_{lab}|$<0.5 shifting of the centre-of-mass rapidity coverage of - 0.96 <y_{cms}< 0.04. In Fig. 6.2, we have shown the fractions of multiplicity distributions as the centrality selection obtained from EPOS 3 minimum-bias events.

6.1.5 Relative yields of D-meson as a function of relative charged particle multiplicity

ALICE has measured [6] the D-meson yields as a function of centrality estimated from VZERO detector in the backward rapidity region (2.8<η<5.1) and also from the reconstructed tracklets in the mid-rapidity $|\eta|$< 1.0. The ALICE measurement of average relative yields of D-mesons, $(d^2N_D/dydp_T)$ / $\langle d^2N_D/dydp_T\rangle$ as a function of relative charged particle multiplicity $(dN_{ch}/d\eta)$ / $\langle dN_{ch}/d\eta\rangle$, measured with both the methods of the centrality estimation, for different p_{T} bins, 1 to 2, 2 to 4, 4 to 8 and 8 to 12 GeV/c have been well reproduced [6] by the EPOS 3.116. We have generated events by using the EPOS 3.107. It is important to match the multiplicity dependent D-meson yields with the events generated by EPOS 3.107 also. We analyze the simulated events and match the ALICE measurement of the relative yields of D-mesons as a function of relative multiplicity, estimated from the pseudo-rapidity coverage of the VZERO acceptance. Here, in Fig. 6.3, we present the centrality or equivalently the multiplicity dependence of relative D-mesons yields

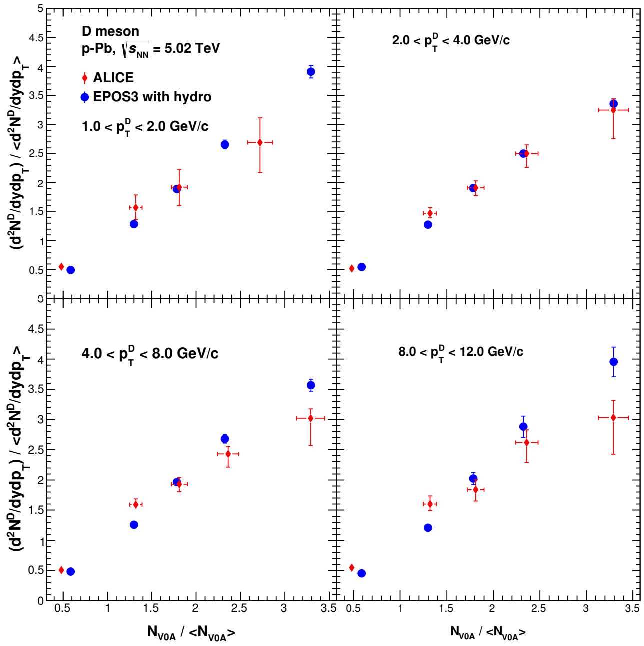

Figure 6.3: Average relative D-meson yields as a function of the relative V0A multiplicity ($N_{V0A}/ < N_{V0A} >$) in different p_T(D) intervals.

for four p_T-bins, 1 to 2, 2 to 4, 4 to 8 and 8 to 12 GeV/c, as obtained from the EPOS 3 generated events along with those measured by the ALICE. The EPOS 3 reasonably reproduces the measured multiplicity dependence of relative D-meson yields in pPb collisions at $\sqrt{s_{NN}} = 5.02$ TeV.

6.1.6 Multiplicity dependent invariant yields of identified charged particles

Having the EPOS 3.107 generated events validated by matching the EPOS 3.116 and ALICE measurement of relative D-mesons yields as a function of relative charged particle multiplicity, before studying the D-mesons charged particles azimuthal correlations with the EPOS 3 generated events, it will be relevant to see how the generated events describe the measured multiplicity dependent yields of the charged particles. ALICE has measured [2] invariant yields of identified charged particles, $\pi^{\pm}$, $K^{\pm}$ and p, $\bar{p}$ for different centrality classes of events. We obtain the invariant yield spectra for the identified charged particles for the centrality classes from the EPOS 3 generated events and plot the spectra in Fig. 6.4, along with the respective spectra measured by ALICE. As can be seen in the Fig. 6.4, the invariant yields of identified charged particles in different centrality classes obtained from EPOS 3 match well with those measured by ALICE [2]. The EPOS 3 generated event-sample thus reproduces the multiplicity dependent yields for D-meson and identified charged particles in pPb collisions at $\sqrt{s_{\rm NN}}$ = 5.02 TeV successfully and can now be analyzed in terms multiplicity dependent D-meson charged particle azimuthal correlation functions.

6.1.7 Short-range jet-like correlations

To study the short-range, jet-like correlations in the produced particles in high energy collisions, the two-particle azimuthal correlations is studied in $|\Delta\eta| \sim 0$ with high $p_T^{trigger}$. In this study of the centrality dependent short-range ($|\Delta\eta|< 1$) or jet-like correlations we choose three $p_T^{trigger}$-ranges: 3 to 5, 5 to 8 and 8 to 16 GeV/c for the D-meson triggers and $p_T^{associated}$ >0.3 GeV/c or 1 GeV/c for the associated charged particles, as has been studied with the ALICE minimum-bias data.

The bulk-subtracted per D-triggered correlated yields as obtained from the EPOS

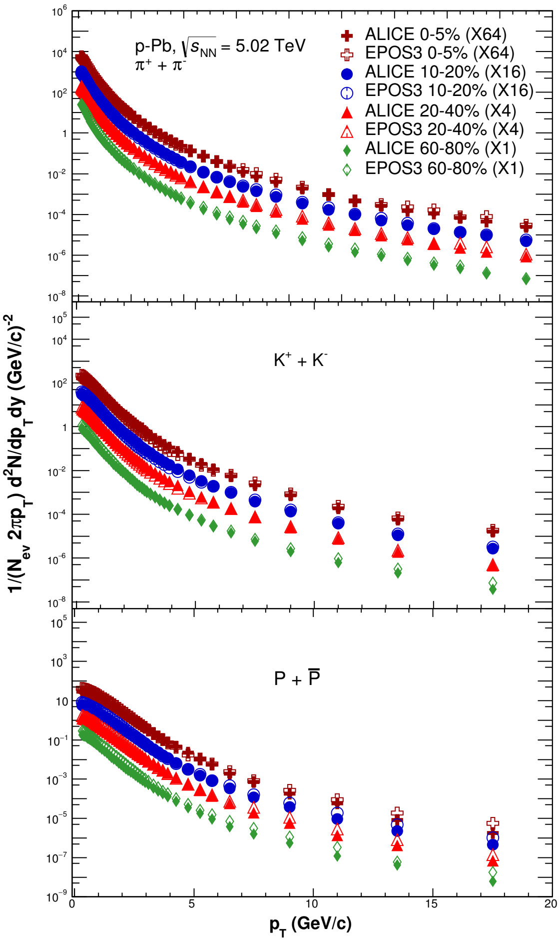

Figure 6.4: The multiplicity dependent invariant yields of identified charged particles in pPb collisions at $\sqrt{s_{\mathrm{NN}}} = 5.02$ TeV, measured by ALICE [2], are compared with the simulated events from the EPOS 3 event generator with hydrodynamical evolution.

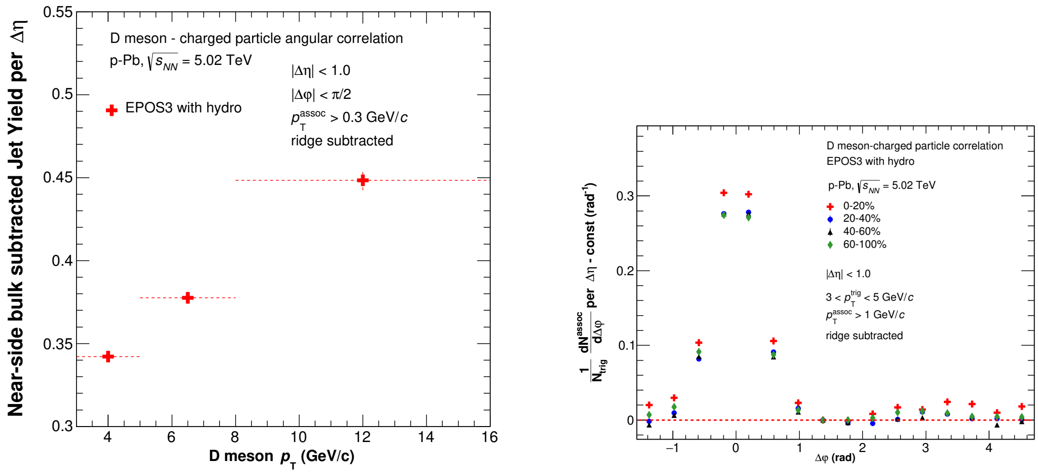

Figure 6.5: (Left) Minimum bias per D-meson triggered correlated yields, in $|\Delta\eta|<1$ in different $p_T^{trigger}$ ranges, 3 to 5, 5 to 8 and 8 to 16 GeV/c and in the $p_T^{associated}$ threshold, $p_T^{assoc} > 0.3$ GeV/c. (Right) $\Delta\varphi$ projection in $|\Delta\eta|<1$ for different centrality bins of EPOS 3 generated pPb collisions at $\sqrt{s_{\rm NN}} = 5.02$ TeV in the $p_T^{trigger}$ range, 3 $<p_T<$ 5 GeV/c and in the $p_T^{associated}$ range, $1<p_T<$ $p_T^{trigger}$ GeV/c.

3 generated minimum bias events as function of $p_T^{trigger}$ are presented in the left panel of Fig. 6.5. As has been observed by the ALICE for minimum-bias events [22], the computed yields using EPOS 3 simulated events are increasing with the D-meson $p_{\rm T}$ ($p_T^{trigger}$). The centrality dependence of bulk-subtracted per D-triggered $\Delta\varphi$ distributions integrated over $|\Delta\eta|<1$ is shown in the right panel of Fig. 6.5. Clearly visible near-side peaks are observed for all the centrality bins.

To compare the effect of the so-called trigger dilution [20], we construct the hadron - charged particle correlation functions in the same $|\Delta\eta|$-range and the $p_T^{trigger}$ range, 3 to 5 GeV/c, that falls within the considered $p_T^{trigger}$-range of the study where the trigger dilution has been shown to be effective for proton and pion triggers. We compare the near-side bulk-subtracted per-trigger correlated yields for the D-charged particle & the hadron-charged particle correlations for different centrality

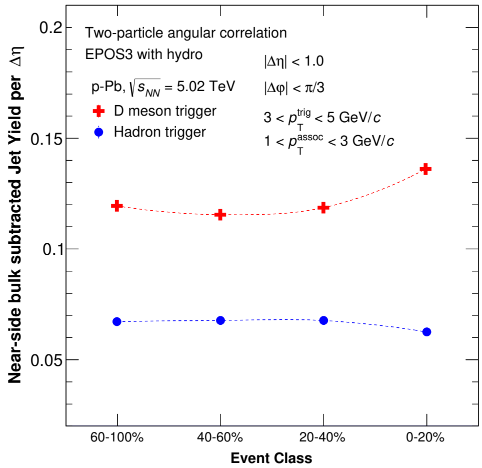

Figure 6.6: Comparison of bulk-subtracted jet-yields obtained from the correlation distributions taking trigger particles as D-mesons and charged hadron in the $p_T^{trigger}$ range, $3 < p_T < 5$ GeV/c and in the $p_T^{associated}$ range, $1 < p_T < 3$ GeV/c for different centrality bins of EPOS 3 generated pPb collisions at $\sqrt{s_{\mathrm{NN}}} = 5.02$ TeV. The dotted lines connect the points to show the trend of the centrality-dependences.

classes of the pPb collisions (Fig. 6.6). As revealed in the Fig. 6.6, while the trigger dilution indeed affects the light-flavoured hadron-triggers, the phenomenon does not affect the D-meson triggers.

6.1.8 Long-range ridge-like correlations

In case of formation of collective medium, the long-range two-particle angular correlations of "soft" particles ideally exist over the entire $|\Delta\eta|$-range. The effect, however, gets submerged by the dominant jet-like correlation in the short-range ($|\Delta\eta| \sim 0$). On the other hand, the ridge-like, bulk correlations appear prominent in the long $|\Delta\eta|$-range, ($|\Delta\eta| \gg 0$) where jet-like short-range correlations are almost absent. At the LHC, ALICE, CMS and ATLAS have studied [7–9] the centrality dependent long-range two-particle correlations of charged particles in pPb collisions at $\sqrt{s_{\mathrm{NN}}} = 5.02$ TeV. These experiments, however, have followed different definition and methodology of extracting per-trigger correlated yields in different $|\Delta\eta|$-range, depending on the detector acceptance. The basis of selection of event classes are different for different experiments. The ranges of $p_T^{trigger}$ and $p_T^{associated}$ also do not match. Because of these differences, though all these studies by different experiments reveal the ridge-like structure in the high-multiplicity pPb events, quantifying the per-trigger correlated yields, the results cannot be compared on the same footing. In this work, for the centrality dependent long-range, D-mesons charged particles angular correlations study with the simulated events, we choose the same $|\Delta\eta|$-range and similar p_{T}-ranges (to start with), as used by the CMS experiment in revealing [8] the ridge-like structure in the near-side long-range azimuthal correlations for charged particles in pPb data at $\sqrt{s_{\mathrm{NN}}} = 5.02$ TeV. This helps us to qualitatively compare our study with existing results from similar analysis, in terms of the $\Delta\varphi$ distributions of the per-trigger yields.

So, for the study of the D-mesons and charged particles angular correlations in the long-range, we consider $2 <|\Delta\eta|< 4$. The CMS experiment has studied multiplicity (N_{track}) - dependent near-side, long-range angular correlations for charged particles in pPb collisions at $\sqrt{s_{\mathrm{NN}}} = 5.02$ TeV in different p_{T}-intervals, 0.1 to 1, 1 to 2, 2 to 3 and 3 to 4 GeV/c, with the same p_{T}-ranges for both the triggers and the associated particles. The study revealed most prominent ridge-like structure in the high-multiplicity events in the 1 to 2 GeV/c p_{T}-interval. The ridge-like structure diminishes with higher p_{T} and nearly disappears in the p_{T}-interval 3 to 4 GeV/c.

We first construct the long-range two-particle azimuthal correlations for the hadrons and the charged particles in the simulated events for the same centrality classes as estimated and described in the beginning of this article for the p_{T}-intervals 1 to 2, 2 to 3 and 3 to 4 GeV/c. The per-trigger correlated yield, projected onto $\Delta\varphi$ and subtracted by the $Yield_{|\Delta\varphi=1.0}$ (the per-trigger correlated yield at $\Delta\varphi = 1.0$) for 2 $<|\Delta\eta|<$ 4 for different centrality bins are obtained and shown in the the left panel of Fig. 6.7. The centrality dependence of the correlated yield as a function of $\Delta\varphi$ for different p_{T}-intervals in the simulated events reveals similar feature as observed in the two-particle azimuthal correlations of the charged particles with the CMS data [8]: the ridge-like structure is most prominent in the 1 to 2 GeV/c p_{T}-range and in the most central events, while it gradually decreases with increasing p_{T}.

Next, we construct the long-range two-particle azimuthal correlations for D-mesons and charged particles from the simulated events for the same centrality classes and in the same p_{T}-intervals 1 to 2, 2 to 3 and 3 to 4 GeV/c. The per-trigger correlated yields, in the long-range, are projected onto $\Delta\varphi$ for different centrality bins. The $\Delta\varphi$ distributions are plotted in the right panel of Fig. 6.7. As depicted in the right panel of the Fig. 6.7, the centrality dependent correlated yield as a function of $\Delta\varphi$ in the simulated events in the considered p_{T} intervals do not really show the features as observed in case of two-particle correlations of hadrons and charged particles. The non-appearance of the ridge-like structure in the "low" p_{T}-range appears consistent in view of the production of the heavy-quarks and their non-interaction with fluid in the EPOS 3 framework. Also, the collective property of light charged particles in the QGP-like medium is usually exhibited up to 3 GeV/c.

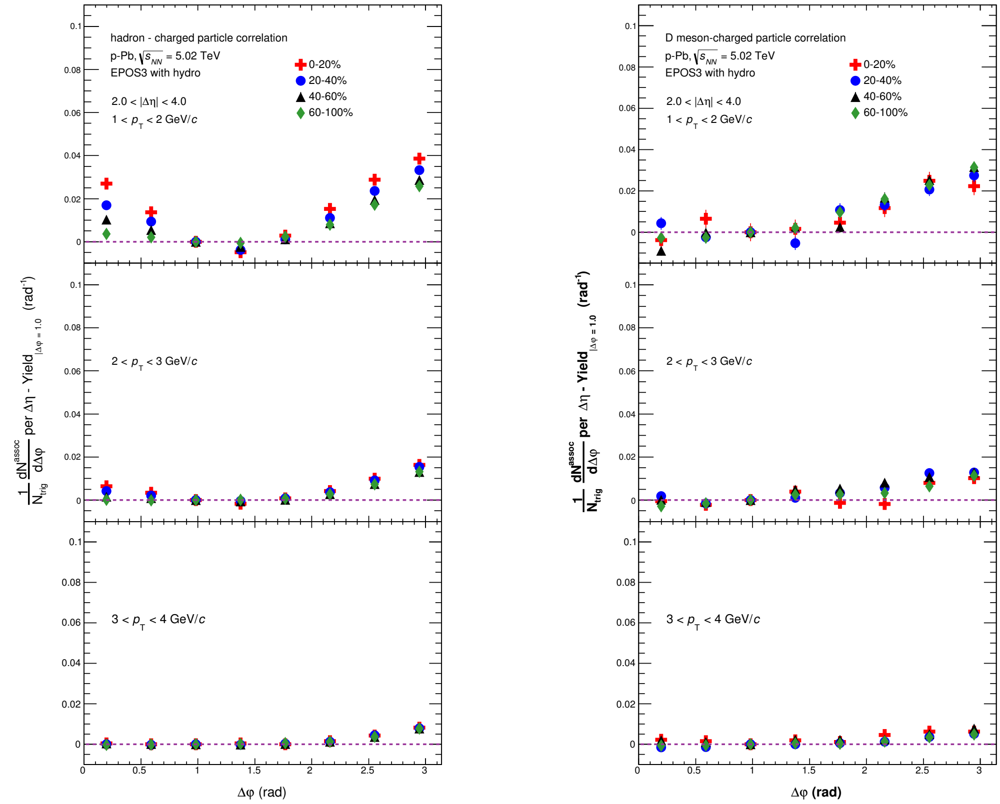

Figure 6.7: The centrality dependence of $\Delta\varphi$ distributions in the long-range $2 < \Delta\eta < 4$ for two-particle azimuthal correlations taking hadrons (left) and D-mesons (right) as trigger particles, for different centrality classes and in different kinematic ranges of the same $p_T^{trigger}$ and $p_T^{associated}$.

At this point, we recollect that ALICE has measured [4] significant positive v_2 (comparable in magnitude to the light-flavored charged hadrons v_2) of the D-mesons in the 2 $<p_T<$ 6 GeV/c range, in 30 - 50 % centrality class of $PbPb$ collisions at $\sqrt{s_{\rm NN}}$ = 2.76 TeV. The ALICE result and the fact that the measured v_2 of light charged particles at RHIC and LHC are usually observed to have the positive v_2 up to the $p_{\rm T}$-range of about 3 GeV/c, prompt us to consider respective $p_{\rm T}$-ranges for D-mesons and the charged particles for studying collectivity in terms of the long-range two-particle angular correlations. Incidentally and also importantly, as argued in the subsection 6.1.5, the D-mesons in the intermediate $p_{\rm T}$-range, in the EPOS 3 approach, inherently carry the collective property of the bulk fluid. It may also be noted that the modulations in the $\Delta\varphi$ distributions of the two-particle angular correlations actually represent the cumulative effects due to the v_2 and it's higher harmonics which, for the long-range correlations, can be factorized as the $v_n(p_T^{trigger})v_n(p_T^{associated})$. We construct the long-range two-particle azimuthal correlations for the D-mesons and the charged particles for 2 $<|\Delta\eta|<$ 4, 3 $<p_T^{trigger}<$ 5 GeV/c and 1$<p_T^{associated}<$ 3 GeV/c from the simulated events in the selected centralities. In the considered $p_{\rm T}$-ranges, the long-range two-particle azimuthal correlations of D-mesons and charged particles indeed reveal a prominent ridge-like structure in the most central event-class, as has been depicted in Fig. 6.8 and Fig. 6.9.

The appearance of the ridge-like structure in the long-range two-particle angular correlations of the D-mesons, in the intermediate $p_{\rm T}$-range, and charged particles in the high-multiplicity EPOS 3 generated pPb events reflects the collective property of the D-mesons, developed due to the fluid-jet interactions in the EPOS 3 framework.

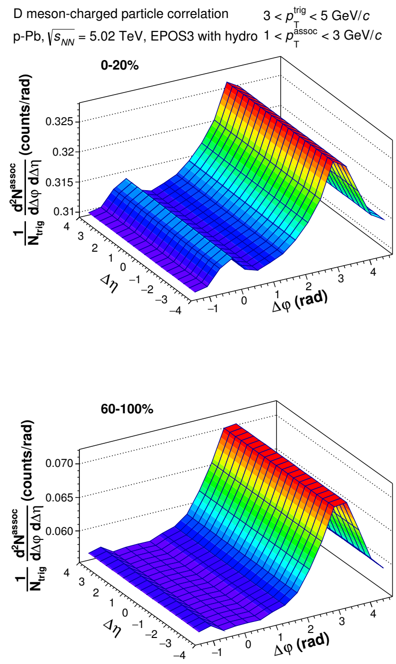

Figure 6.8: Two particle $\Delta\eta - \Delta\varphi$ correlation function for 3 $<p_T^{trigger}<$ 5 GeV/c and 1 $<p_T^{associated}<$ 3 GeV/c with D-meson as trigger particles for the hydrodynamic-EPOS 3 generated pPb collisions at $\sqrt{s_{\rm NN}}$ = 5.02 TeV in 0 - 20 (top) and 60 - 100 (bottom) per cent central event classes.

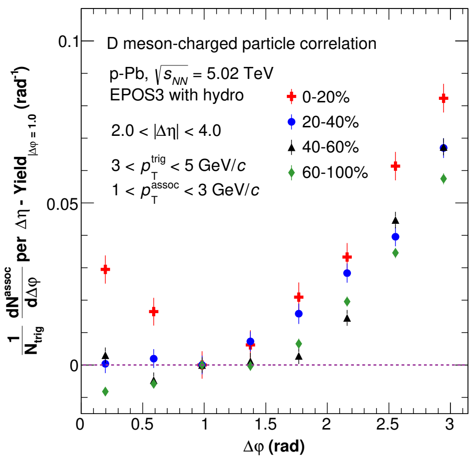

Figure 6.9: The centrality dependence of per-trigger $\Delta\varphi$ distributions in the long-range (2 $<\Delta\eta<$ 4) as obtained from D mesons-charged particles azimuthal correlations, for 3 $<p_T^{trigger}<$ 5 GeV/c and 1$<p_T^{associated}<$ 3 GeV/c.

6.1.9 Summary and Conclusion

The study of two-particle angular correlations using D meson triggers in the short-range ($|\Delta\eta| < 1.0$) with the EPOS 3 generated events reveals that the near-side per-trigger correlated yields are increasing with the D meson p_{T}. The results from the simulated events qualitatively reproduce the ALICE data of D meson-charged particle angular correlations in minimum-bias pPb collisions at $\sqrt{s_{\mathrm{NN}}} = 5.02$ TeV. With the validation of the EPOS 3 generated events in the minimum-bias case, we proceed for the multiplicity dependent two-particle angular correlations using both D meson and light hadrons as trigger particles. The comparison of results show the so-called trigger dilution effect for the hadron triggers. However, for the D-meson triggers not only the trigger dilution is absent, the per-trigger correlated yield increases with centrality.

In the context of the observed collective property of the D-mesons, further discussions on our analysis of EPOS 3 generated high-multiplicity pPb events vis-a-vis the measured v_2 of D-mesons by the ALICE in $PbPb$ collisions [4] or by the STAR in $AuAu$ collisions [23] and the prescribed mechanisms of development of collective properties in particles carrying the primordial heavy quarks, according to the quark coalescence models or the EPOS 3 model, will be worth discussing.

The ALICE has measured [4] non-zero v_2 in $PbPb$ collisions at $\sqrt{s_{\mathrm{NN}}} = 2.76$ TeV for $2 < p_T < 6$ GeV/c. The Ref. [4] has briefed two major mechanisms which could cause collective behaviour of the D-mesons. In the low ($p_T < 3$ GeV/c) and intermediate ($3 < p_T < 6$ GeV/c) p_{T}-ranges, the D-mesons are formed from the coalescence of the

c-quark and the thermal light-quark, inheriting the collective properties from the light-quark content. In the higher p_{T}-range, the path-length dependent in-medium energy loss due to the medium-induced gluon radiation and elastic collisions may give rise to the collective behaviour.

In a very recent study [23] on the v_2 of D-mesons in $AuAu$ collisions at $\sqrt{s_{\mathrm{NN}}} =$ 200 GeV by the STAR collaboration at the RHIC, the D-mesons have been found to exhibit similar collective behaviour as the light hadrons, in terms of $v_2(p_{\mathrm{T}})$ in the range, 1 $<p_T<$ 6 GeV/c. In contrast to the collective property of D-mesons in the intermediate p_{T}-range in the high-multiplicity pPb events at the LHC energy, as revealed from this analysis, the STAR data show the mass-ordering of $v_2(p_{\mathrm{T}})$, including the D-mesons, in the low p_{T} ($<$ 2 GeV/c) range also. At RHIC, the D-mesons, along with the light hadrons, follow a common trend of v_2, scaled with number of constituent quarks, as a function of scaled transverse kinetic energy. It may be noted that the so-called "number of constituent quark" (NCQ) - scaling is explained [24] by the quark coalescences model.

According to the quark coalescence models [25, 26], as a result of charm-medium interactions during the passage of the heavy quarks through the QGP-like medium, a significant number of low and intermediate momentum charm-quarks coalesce with the constituent light-quarks, carrying the collective expansion characteristics of the thermalized partonic medium. The collective property of the light-quark thus get carried forward to the D-meson, giving rise to the collective features in observables related to the D-mesons at low ($p_T<$ 3 GeV/c) and intermediate (3 $<p_T<$ 6 GeV/c) p_{T}-ranges. As the momentum of the D-mesons, with constituent quarks of unequal masses, is mostly contributed by the heavy charm-quark, the constituent light-quark has to have low momentum and low v_2 [27, 28], resulting slower development of collective features with the p_{T}.

In the present study, the $p_T^{trigger}$, 3 to 5 GeV/c falls within the category of the so-called "intermediate" p_{T}-range. The particles in the intermediate p_{T}-range, between the "hard" and the "soft" ones, come from mixed sources of particle production, including: a) the ones originating from the hadronization through recombinations or coalescence of quarks inside a thermal medium, according to the quark coalescence models, or b) the jet hadrons, produced inside a thermalized fluid through breaking of flux tubes into segments by the quarks, carrying the fluid properties, according to the EPOS model. Though the quark coalescence models and the EPOS 3 model take different theoretical approaches in explaining the particle production mechanism in the relativistic heavy-ion collisions, for both the hydrodynamic models, the collective properties of the hadrons in the intermediate-p_{T} ranges are generally imparted by the thermalized partonic medium through its constituents, carrying the properties of the fluid.

So, in accordance with either of the discussed models, the appearance of a ridge-like structure in the long-range two particle angular correlations of D-mesons, in the intermediate-p_{T} range, and charged particles, indicates the formation of thermalized partonic medium in the high-multiplicity pPb events at the LHC energy.

6.2 Study of high-multiplicity pp events at the LHC energies up to the intermediate-p_{T} range

The conventional models of particle production in relativistic proton-proton (pp) collisions have been reasonably successful in explaining the pre-LHC data by considering different approaches for different ranges of transverse momentum (p_{T}) of the produced particles. The production of high-p_{T} particles from the high energy parton-parton interactions is theoretically calculable in pQCD approach, and so the data can be described fairly well by most of these models. In the non-perturbative regime, as the production mechanism of low and intermediate-p_{T} ($p_{\mathrm{T}} < 2$ GeV/c) particles is not that well understood because of lack of proper theoretical tools, several empirical formalisms have been adopted in different models to match the data. The LHC pp data came with a surprise when none of the prevailing models of particle production in pp collisions could describe the features of high-multiplicity events, particularly in the low and intermediate-p_{T} range. The failures indicate that the considered physics mechanisms in these models for the particle production in the non-perturbative regime are not sufficient.

As discussed in section 1.4, the pQCD-inspired multiparton interaction (MPI) model along with the color reconnection (CR) scheme as implemented in the Monte Carlo code, PYTHIA 8 has come up with an alternate explanation to the observed flow-like collective behaviour of the final-state particles in high-multiplicity pp events [30]. According to the CR scheme, the multiparticle production in high-multiplicity events results from a large number of overlapped MPIs. The overlapped partons from individual MPIs get connected by color strings, and the partons cannot hadronize independently. The collective hadronization of reconnected partons from the overlapped MPIs takes place through a string fragmentation process. The effect of a transverse boost of the reconnected partons is manifested in the observed [30] flow-like dependence of $< p_{\mathrm{T}} >$ on N_{ch}. It is worth noting here that the CR mechanism explains the data including the high-p_{T} ($p_{\mathrm{T}} < 10$ GeV/c) particles, while the signals of hydrodynamic collectivity are seen [15] up to the intermediate-p_{T} ($p_{\mathrm{T}} < 2$ GeV/c) range. It is, therefore, important to study the responses of color reconnection up to the intermediate-p_{T} range only, for a better understanding of the relative effect of the collective hadronization due to color reconnection on the intermediate-p_{T} phenomena in high-multiplicity pp events. In view of above, a comprehensive study on the comparison between the data and the MPI model, with and without color reconnection, in terms of several features of the multiparticle production up to the intermediate-p_{T} range in high-multiplicity pp events will be presented here.

6.2.1 Results and Discussions: PYTHIA 8 simulated events for pp collisions at $\sqrt{s} = 7$ TeV

In this context the MPI based event generator PYTHIA 8 tune 4C (see section 8.1) including color reconnection scheme is used. Using the tuned simulation code, 10 million minimum bias pp events at $\sqrt{s} = 7$ TeV for each of the options, with and without CR have been generated. We have analyzed the generated event samples in terms of transverse momentum (p_{T}) and two-particle angular correlations, with appropriate kinematic cuts and conditions, to compare with several hydrodynamic

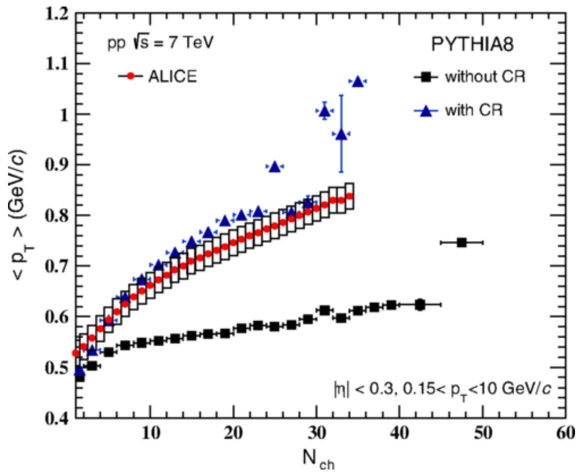

Figure 6.10: Average transverse momentum, $< p_{\mathrm{T}} >$, as a function of charged particle multiplicity, N$_{ch}$, as measured by ALICE [30] is compared with the simulated events from PYTHIA 8 Tune 4C event generator with and without CR.

flow-like effects as observed in the LHC experiments in pp collisions at $\sqrt{s}$ = 7 TeV. For the authenticity of the generated events, at first we have reproduced the ALICE published charged particle multiplicity (N$_{ch}$) dependent mean transverse momentum ($< p_{\mathrm{T}} >$) distribution for both with and without CR. The Fig. 6.10 shows that the PYTHIA 8 with color reconnection reproduces the data successfully for the kinematic range $p_{\mathrm{T}} < 10$ GeV/c and $|\eta| < 0.3$.

6.2.2 Transverse Momentum (p_{T}) / Mass (m_{T})

6.2.2.1 $< N_{ch} >$ dependent $< p_{\mathrm{T}} >$ for identified charged particles up to intermediate-p_{T}

The reasonable success of the MPI model in explaining the N_{ch}-dependence of $< p_{\mathrm{T}} >$ of unidentified charged particles up to the p_{T}-range of 10 GeV/c, encourages us to see how the MPI model with color reconnection fits into the nature of the multiplicity dependence of $< p_{\mathrm{T}} >$, obtained from the measured spectra of identified charged particles up to the intermediate p_{T}-range. We select subsamples, defined with $< N_{tracks} >$, from the generated event sample for studying the N_{ch}-dependence of $< p_{\mathrm{T}} >$ for the identified charged particles in the same kinematic range as measured by the CMS experiment [31,32]. The $< N_{tracks} >$ for each of the event classes has been obtained by taking the mean of the true-track multiplicities of events in the respective event class. For simplicity $< N_{tracks} >$ is written as N_{ch} here.

The Fig. 6.11 shows that the CR causes increase in $< p_{\mathrm{T}} >$ of the charged particles in the simulated events, for $N_{ch} > 40$. Also, the increase in $< p_{\mathrm{T}} >$ has a N_{ch}-dependence. However, the effect of the CR remains far from matching the measured N_{ch}-dependence of N_{ch} for the identified charged particles in the given kinematic ranges and multiplicities. The wide mismatch between CMS data and the simulated events, in terms of N_{ch}-dependence of $< p_{\mathrm{T}} >$, prompts us to compare the identified charged particle spectra from the data and the simulated events.

6.2.2.2 Identified charged particle spectra

The p_{T}-spectra of the produced particles contain information on temperature as well as transverse expansion of a thermalized medium, if formed. The temperature related information should ideally be reflected by the low-p_{T} particles (usually < 2 GeV/c, as has been considered in heavy-ion collisions).

The slope of the transverse mass (m_{T})-spectra for identified charged particles that

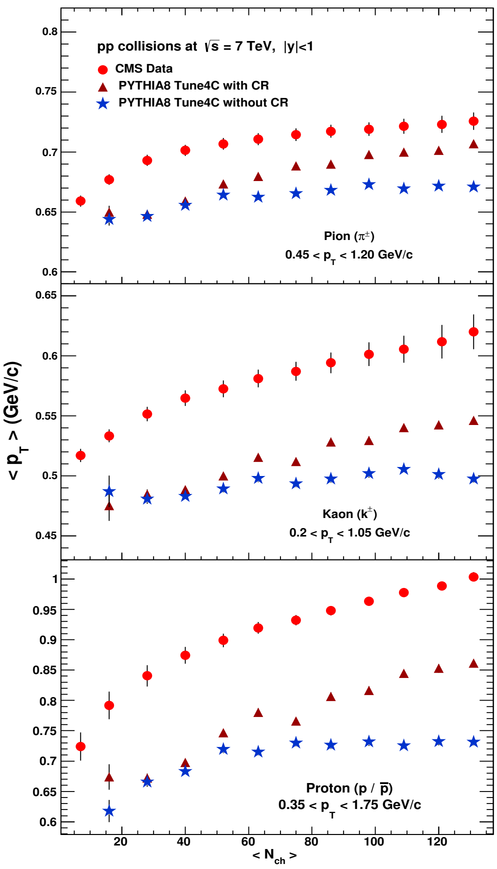

Figure 6.11: Average transverse momentum, $< p_{\mathrm{T}} >$ for the identified charged particles in pp collisions at $\sqrt{s} = 7$ TeV, as a function of mean charged particle multiplicity for several event classes. The CMS data [31, 32], have been compared with simulated events from PYTHIA 8 Tune 4C event generator with and without CR [33].

can be obtained from the $p_{\rm T}$-spectra (for a particle of mass m, $m_{\rm T} = ({\rm m}^2 + p_{\rm T}^2)^{1/2}$), is used for comparing thermal states of the system. The $m_{\rm T}$-spectra corresponding to low-$p_{\rm T}$ particles are usually satisfactorily fitted with the exponential function of the form:

$$\frac{dN}{m_T dm_T} = C.exp\big(-\frac{m_T}{T_{effective}}\big) \tag{6.4}$$

where $\mathrm{T}_{effective}$, known as the inverse slope parameter, contains information about the temperature as well as of the effect due to transverse expansion of the system. Increase in the inverse slope parameter, $\mathrm{T}_{effective}$ with mass, m, for the most commonly measured identified charged particles ($\pi^{\pm}$, $\mathrm{K}^{\pm}$, p and $\bar{p}$), that has been observed in heavy-ion [34, 35] and recent proton-lead collisions [36] at the LHC is a well known phenomenon, attributed to the collective flow of the medium formed in the collision.

By fitting the $m_{\rm T}$-spectra data of identified charged particles obtained from the overlapped range ($0.475 < p_{\rm T} < 1.025$ GeV/c) of the $p_{\rm T}$-spectra at $\sqrt{s} = 7$ TeV as measured [32] by the CMS experiment, the inverse slope parameter $\mathrm{T}_{effective}$ can be obtained. The increase of $\mathrm{T}_{effective}$, as shown in the Fig. 6.12, with the mass of identified charged particles for event classes of high $< N_{ch} >$ reiterates the finding of collective medium in high-multiplicity pp events. Comparing the mass ordering for different multiplicity classes, we note that, the data show relatively large increase in the inverse slope parameters from the multiplicity class of $< N_{ch} > = 120$ to $< N_{ch} > = 131$.

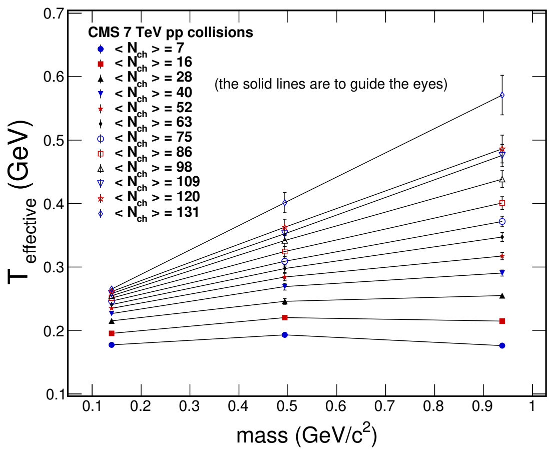

Figure 6.12: The inverse slope parameter $T_{effective}$ as a function of mass of identified charged particles ($m_{\pi^\pm} = 0.14$, $m_{K^\pm} = 0.495$, $m_{p(\bar{p})} = 0.938$ GeV/c^2) produced in pp collisions [31, 32] at $\sqrt{s} = 7$ TeV. $< N_{ch} >$ is the mean multiplicity of the charged particles representing event classes [33].

To compare the measured spectra with those from the simulated pp events, we initially chose the event class of the highest multiplicity, identified by $< N_{ch} > = 131$. In Fig. 6.13 the identified charged particle spectra as a function of the transverse mass for $\pi^\pm$, $K^\pm$and p & $\bar{p}$, obtained from the measured $p_{\rm T}$-spectra [31,32] and from the simulation with and without CR for $0.475 < p_{\rm T} < 1.025$ and for the multiplicity class of $N_{ch} = 131$, are plotted.

We fit the spectra with the exponential function not for the temperature estimation but just for a quantitative comparison of the spectra from the experiment and the simulation in terms of the inverse slope parameter. From the fit values (table 6.1), it has been found that while the high-multiplicity pp data exhibit mass ordering of inverse slope parameter of the $m_{\rm T}$- distributions, the simulated PYTHIA events, with or without CR, do not exhibit such mass-ordering.

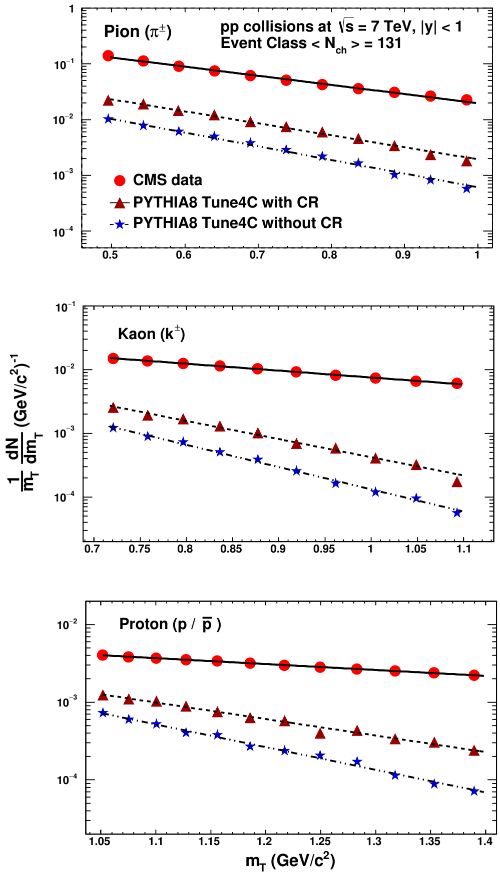

Figure 6.13: m_T -spectra for identified charged particles as obtained from the CMS data. The data are compared with the simulated events using PYTHIA 8 Tune 4C event generator with and without CR.

6.2.3 Two-particle angular correlations

6.2.3.1 The correlation function

The observed limitation of the MPI with color reconnection in explaining the N_{ch}-dependence of $< p_{\mathrm{T}} >$ for the identified charged particles with $p_{\mathrm{T}} < 2.0$ GeV/c

Identified Particles	Data		With CR		Without CR	
	T_{eff}	$\frac{\chi^2}{NDF}$	T_{eff}	$\frac{\chi^2}{NDF}$	T_{eff}	$\frac{\chi^2}{NDF}$
	$\langle N_{ch} \rangle = 131$					
$\pi^{\pm}$	0.265 $\pm$0.002	5.432	0.202 $\pm$0.001	28.224	0.177 $\pm$0.001	28.180
$K^{\pm}$	0.401 $\pm$0.016	0.084	0.152 $\pm$0.002	6.612	0.124 $\pm$0.001	3.313
$(p, \bar{p})$	0.571 $\pm$0.031	0.039	0.204 $\pm$0.004	2.596	0.148 $\pm$0.003	2.327

Table 6.1: The inverse slope parameters of the exponential fits to the m_T-spectra of $\pi^{\pm}$, $K^{\pm}$ and p & $\bar{p}$ for the multiplicity class $\langle N_{ch} \rangle = 131$ for CMS experiment [31,32] and PYTHIA 8 Tune 4C with and without CR.

leads us to think that the model may not really provide an alternate explanation to the features, considered to be due to the hydrodynamic collectivity. We, therefore, proceed to check the responses of the model to the analysis in terms of the two-particle angular correlations giving rise to "long-range near-side correlated yields", a measure of correlations that is attributed to the formation of collective medium. It has been discussed in section 1.4 that recent data results on two-particle angular correlations study from various LHC experiments has put a strong backbench for the collectivity in high-multiplicity pp [37] or pPb collisions by extracting the anisotropy coefficient v_2. While the mass ordering of $v_2(p_{\mathrm{T}})$ for the identified charged particles has been observed [38], the p_{T}-dependence of v_2, similar to that observed in the pPb and the $PbPb$ collisions, has also been revealed [39]. It may be worth mentioning at this point that these v_2-related features have been explained [40] in an alternate approach in the IP-Glasma model, based on Color Glass Condensate, followed by the Lund string fragmentation algorithm of PYTHIA. However, we continue to contrast the MPI model, as implemented in the default PYTHIA, with and without CR.

The basic definition and construction of two-particle angular correlations are discussed in chapter 2. In relativistic heavy-ion collisions, the "long-range" ($|\Delta\eta| >> 0$) two-particle azimuthal angle correlations have been attributed to the formation of collective partonic medium. The per-trigger pair yields with small $|\Delta\varphi|$ over a wide range of $|\Delta\eta|$ (long-range), result in a "ridge" structure in the constructed correlation functions. The "ridge" structure also appears in the high-multiplicity *pPb* and *pp* events at the LHC as discussed in section 1.4. The analysis [15] of the LHC *pp* data in terms of the correlated yields as a function of $|\Delta\varphi|$ reveals that the long-range "ridge"-structure at $|\Delta\varphi| \sim 0$ increases with multiplicity of *pp* events. Here in terms of the two-particle angular correlations, we focus on the "ridge-like" correlations only and choose to contrast the MPI model with the published results.

6.2.3.2 Extraction of long-range near-side correlated yields

For an optimum comparison with the experimental results on multiplicity-dependent correlation analysis, in terms of the near-side correlated yield in the long-range, the generated minimum bias events, with and without the CR scheme, at $\sqrt{s} = 7$ TeV have been divided into different multiplicity classes following the criteria adopted in Ref. [15]. The multiplicity classes and the total number of events analyzed in each class are given in table 6.2:

2-dimensional $\Delta\eta - \Delta\varphi$ correlation functions, shown in Fig. 6.14 (left) are evaluated using PYTHIA 8 simulated events with CR. The same event (top), mixed

Multiplicity bin	No. of events (in million)	
	with CR	without CR
$2 \leq N_{ch} < 35$	6.1	5.4
$35 \leq N_{ch} < 90$	2.3	2.2
$90 \leq N_{ch} < 110$	0.2	0.4
$N_{ch} \geq 110$	0.8	0.6

Table 6.2: Multiplicity classes and the corresponding number of simulated events used for the correlation analysis.

event (middle) and mixed event corrected (bottom) two-particle correlations are shown for particle transverse momentum $1.0 < p_{\mathrm{T}} < 2.0$ GeV/c and $|\eta| < 2.4$. A simple visible expression of mixed event corrected correlations suggests that there is no such long-range correlations in PYTHIA 8 with CR mechanism.

For the long-range correlations, the 2-dimensional correlation functions are then projected onto the $|\Delta\varphi|$ axis for $2.0 < |\Delta\eta| < 4.0$. Fig. 6.14 (right) shows the multiplicity dependent 1-dimensional $\Delta\varphi$ distribution as extracted by the CMS experiment in pp collisions at $\sqrt{s} = 7$ TeV together with the results of the PYTHIA events of similar multiplicity and identical range of particle transverse momentum.

It is clear from the Fig. 6.14, for both the simulated event classes (with and without CR), that the $\Delta\varphi$-distributions in $\Delta\varphi \sim 0$ are close to zero for low multiplicity events, in agreement with the data. The distributions obtained from the high-multiplicity simulated events, including those generated by invoking the CR, continue to coincide with zero, contradicting the data.

The comparison of the multiplicity dependence of long-range near-side correlations between the data and the simulated events is better represented in terms of the long-range near-side correlated yields. To reduce the statistical fluctuations

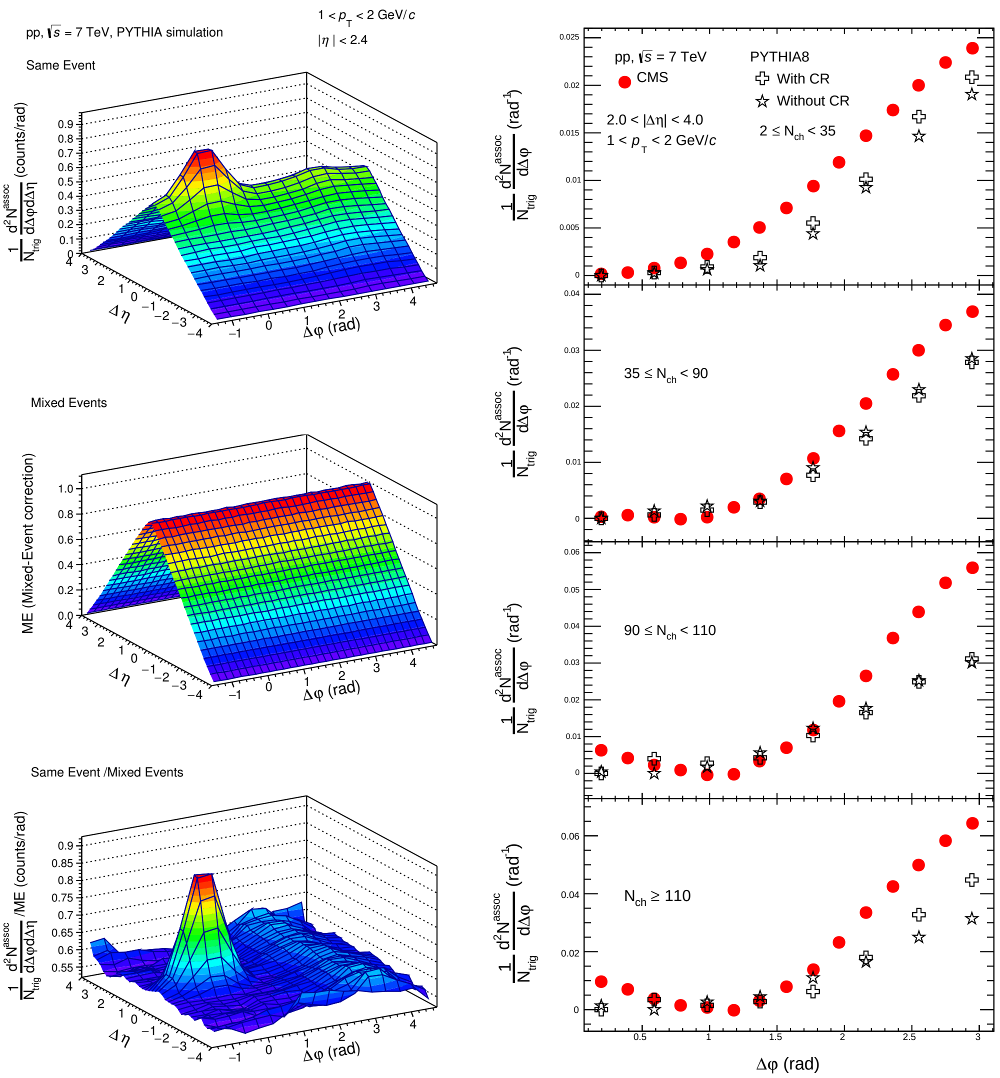

Figure 6.14: (Left) Representation of 2-dimensional $(\Delta\eta, \Delta\varphi)$ two-particle angular correlations using PYTHIA 8 CR scheme. (Right) 1-dimensional $\Delta\varphi$ projection for the region of ridge-like correlations from the data [15] and for the simulated events by PYTHIA with and without CR.

in baseline estimation, conventionally, the one-dimensional correlation distribution over the entire 2π range is reflected / folded in to $0 < \Delta\varphi < \pi$.

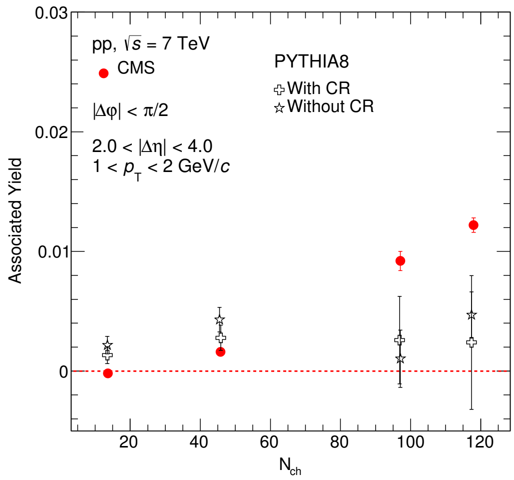

Figure 6.15: Comparison of multiplicity dependent near-side ridge-like correlated yields for the CMS data and simulated PYTHIA events.

The baseline for calculating the correlated correlated yield is considered here as a straight-line parallel to the $\Delta\varphi$ axis that passes through the point of minimum yield. The long-range correlated yield above the baseline is calculated by the bin counting method. The near-side long-range correlated yields as calculated from the PYTHIA generated events are plotted in Fig. 6.15 along with the results from data, obtained from [15]. It is worth discussing at this point that the calculation of yields above the baseline is very sensitive to the statistics. So, instead of quantitative comparison between the yields from data and the simulation, we prefer to compare the relative trend of multiplicity-dependent yields.

6.2.4 Summary and Conclusion

The study aims to contrast the MPI model with the multiparticle production data of high-multiplicity pp events in the intermediate-p_{T} range, that carries information of the collective medium, if any, formed in the collisions.

In terms of the p_{T}-distributions and related observables, the analysis reveals that the N_{ch} dependence of $< p_{\mathrm{T}} >$ for identified charged particles up to the intermediate-p_{T} range in simulated events do not match the data. Though the CR scheme gives a boost to the $< p_{\mathrm{T}} >$ of the identified particles for $N_{ch} > 40$, it is not enough to describe the data. In the lower range of N_{ch}, the CR has no effect on $< p_{\mathrm{T}} >$.

The CR in the MPI model also fails to describe the existing mass ordering of inverse slope parameter of the identified charged particle spectra for the high-multiplicity pp events in data. The MPI model, by invoking the CR scheme also, cannot describe the "ridge-like" structure in the two-particle angular correlations in the high-multiplicity pp data.

Hence, this study reveals that the color reconnection does not provide full explanation of the collective feature in pp collisions. In the high-multiplicity pp events, the model cannot account for the flow-like effects in the intermediate-p_{T} ($p_{\mathrm{T}} < 2$ GeV/c) range, where the hydrodynamic models appear to be convincing.

Bibliography

[1] K. Werner et al., Phys. Rev. **C89**, 064903 (2014).

[2] J. Adam et al., Phys. Lett. **B760**, 720–735 (2016).

[3] B. Abelev et al., ALICE Collaboration, JHEP **09**, 112 (2012).

[4] B. Abelev et al., ALICE Collaboration, Phys. Rev. Lett. **111**, 102301 (2013).

[5] B. Abelev et al., ALICE Collaboration, Phys. Rev. Lett. **113**, 232301 (2014).

[6] B. Abelev et al., ALICE Collaboration, JHEP **08**, 1 (2016).

[7] B. Ablev et al., ALICE Collaboration, Phys. Lett. **B719**, 29 (2013).

[8] S. Chatrchyan et al., CMS Collaboration, Physics Letters **B718**, 795 (2013).

[9] G. Aad et al., ATLAS Collaboration, Phys. Rev. Lett. **110**, 182302 (2013).

[10] B. Ablev et al., ALICE Collaboration, Phys. Lett. **B 728**, 25(2014).

[11] P. Bozek, Phys. Rev. **C85**, 014911 (2012).

[12] K. Dusling and R. Venugopalan, Phys. Rev. **D87**, 094034 (2013).ref001

[13] V. Khachatryan et al., CMS Collaboration, J. High Energy Phys. JHEP09, 091 (2010).

[14] G. Aad et al., ATLAS Collaboration, Phys. Rev. Lett. **116**, 172301 (2016).

[15] V. Khachatryan et al., CMS Collaboration, Phys. Rev. Lett. **116**, 172302 (2016).

[16] V. Khachatryan et al., CMS Collaboration, arXiv: 1606.06198v1 [nucl-ex] (2016).

[17] B. Ablev et al., ALICE Collaboration, Phys. Lett. **B736**, 196 (2014).

[18] B. Ablev et al., ALICE Collaboration, Phys. Lett. **B728**, 25 (2014).

[19] R. Fries, B. Muller, C. Nonaka, S. Bass, Phys. Rev. Lett. **90**, 202303 (2003).

[20] D. Sarkar, S. Choudhury and S. Chattopadhyay, Phys. Lett. **B760**, 763 (2016).

[21] K.Werner et al., arXiv:1602.03414v1 [nucl-th] (2016).

[22] J. Adam et al., ALICE Collaboration, arXiv:1605.06963v1 [nucl-ex].

[23] L. Adamczyk et al., STAR Collaboration, arXiv: nucl-ex/1701.06060v2.

[24] J. Adam et al., STAR Collaboration, Phys. Rev. **C72**, 014904 (2005).

[25] D. Molnar, S.A. Voloshin, Phys. Rev. Lett. **91**, 092301 (2003).

[26] V. Greco, C. M. Ko and P. Levai, Phys. Rev. **C68**, 034904 (2003).

[27] V. Greco, C. M. Ko and R. Rapp, Phys. Lett. **B595**, 202 (2004).

[28] Z. Lin and D. Molnar, Phys. Rev. **C68**, 044901 (2003).

[29] P. Gossiaux, Proceedings of the Quark Matter - 2017.

[30] B. Abelev et al., ALICE Collaboration, Phys. Lett. **B727**, 371 (2013).

[31] V. Khachatryan et al., CMS Collaboration, Euro. Phys. J. **C72**, 2164 (2012).

[32] The Durham HepData Project, http://hepdata.cedar.ac.uk/view/ins1123117.

[33] Somnath Kar et al., Phys. Rev. **D95**, 014016.

[34] Bearden, I. G. et al., NA44 Collaboration. Phys. Rev. Lett. **78**, 2080 (1997).

[35] Xu, N. Prog. Part. Nucl. Phys. **53**, 165-182 (2004).

[36] S. Chatrchyan et al., CMS Collaboration, Eur. Phys. J. **C74**, 2847 (2014).

[37] V. Khachatryan et al., CMS Collaboration, Phys. Lett. **B765**, 193 (2017).

[38] V. Khachatryan et al., CMS Collaboration, arXiv: 1606.06198v1 [nucl-ex] (2016).

[39] G. Aad et al., ATLAS Collaboration, Phys. Rev. Lett. **116**, 172301 (2016).

[40] B. Schenke, S. Schlichting, P. Tribedy and R. Venugopalan, Phys. Rev. Lett. **117**, 162301 (2016).

Chapter 7

Outlook

The summary and conclusions are already discussed at the end of chapter 5 and chapter 6 for the results presented in this thesis. Here we will briefly discuss some future perspectives for the analysis done using ALICE data and for the simulated events.

7.1 Angular correlations between D^0 mesons and charged particles using ALICE data: Outlook and future perspectives

Along with the ALICE *pp* and *pPb* Run I data, the correlation analysis between D^0 mesons and charged particle were also carried out with the ALICE 2011 *PbPb* data but no feasible correlations, even in central collisions (0-10% centrality class) with 1.6 $\times 10^7$ events, were found. The current setup of ALICE detector could not provide enough precision for such correlations study. The main difficulty was with very low signal/background ratio (S/B) of D^0 mesons. Hence, a substantial statistical fluctuation in the $\Delta\varphi$ distribution kills any physical correlation structure. It is also estimated that even Run-II *PbPb* data at higher energy $\sqrt{s_{\mathrm{NN}}} = 5.5$ TeV where the statistics will increase by a factor up to 10 w.r.t Run-I data, will not be able to provide enough feasibility to the correlation analysis.

With the ALICE upgrade, after the Long Shutdown 2 (LS2) (expected for 2018-2019) and improvement of ITS tracking and vertexing performance, an increase of the S/B ratio by a factor up to 10 for the D^0 meson reconstruction is expected. Hence, a possibility of D meson-charged particle correlations can be carried out for Run-III *PbPb* data with better precesion.

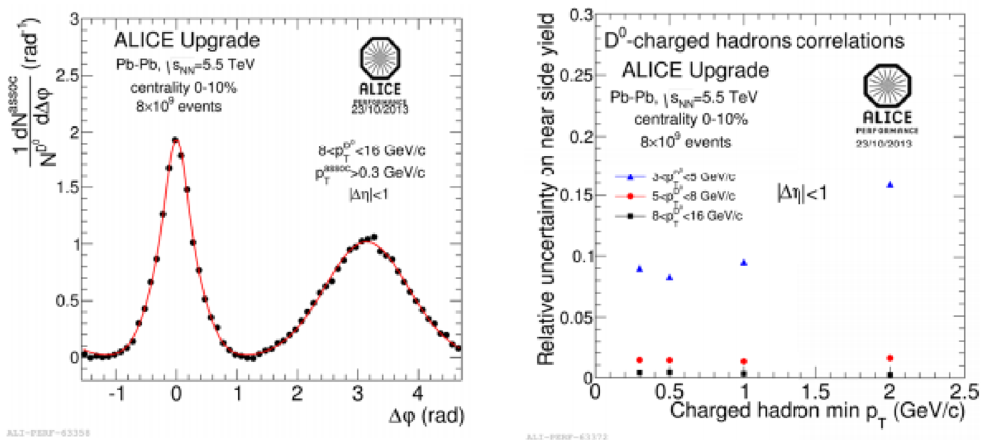

Figure 7.1: (Left) Estimated D^0-charged particle azimuthal correlation distribution in 0-10% central *PbPb* collisions from Monte Carlo simulations with the upgraded ALICE detectors for $8 < p_{\mathrm{T}}(D^0) < 16$ GeV/c range with $p_{\mathrm{T}}^{assoc} > 0.3$ GeV/c after the subtraction of the baseline. (Right) Estimates for the statistical uncertainty of the near-side yields as a function of p_{T}^{assoc} in *PbPb* after the ALICE upgrade

Looking forward to future analysis in higher energy and with higher statistics, a Monte Carlo based simulation study is performed for central (0-10%) $PbPb$ collisions using a template of correlation distributions from PYTHIA. An example of D^0-charged particle correlation distribution is shown in the left panel of Fig. 7.1. In the right panel the relative uncertainty on near-side peak yield is shown as a function of charged particle p_T. The uncertainties are expected to be small with the upgrade.

7.2 Study of small systems with simulated events: Outlook and future perspectives

pPb **collisions:**

We have studied the centrality or the multiplicity dependence of the long-range two-particle angular correlations for the D-mesons and charged particles, produced in EPOS 3-generated pPb events at $\sqrt{s_{\rm NN}} = 5.02$ TeV.

The ridge-like structures (in $2 < |\Delta\eta| < 4$), as revealed by the LHC experiments in the pPb data in the long-range, two-particle angular correlations of "soft" charged particles, is absent in the D-mesons charged particles angular correlations in the similar p_T-ranges in the EPOS 3 generated events. The observation is in accordance with the limitation of the EPOS 3 code, in the present form, that does not provide interaction between the initially produced heavy quarks and the thermalized bulk matter.

In high-multiplicity EPOS 3-generated pPb events, a prominent ridge-like structure appears in the long-range two-particle angular correlations of D-mesons and charged particles, with the D-mesons in the intermediate p_{T}-range, ($3 < p_T^{trigger} < 5$ GeV/c and the charged particles in $1 < p_T < 3$ GeV/c, within the respective p_{T}-ranges where the final state particles exhibit hydrodynamic collectivity through positive v_2 in the relativistic nucleus-nucleus collisions. The ridge-like structure, revealed by this study with the D-meson triggers in the intermediate p_{T}-range in the EPOS 3 generated high-multiplicity events, if confirmed by the data, will reiterate the possibility of the formation of thermalized partonic medium in the high-multiplicity pPb collisions.

On the absence of ridge-like structure in two-particle angular correlations of D-mesons and charged particles in the low p_{T}-range, it must be mentioned here, that the developers of the EPOS code have very recently started working on the coupling of the dynamics of heavy quark with the EPOS 3 model, as has been reported in the Quark Matter 2017 conference. The issue of the interactions between the heavy quarks and the fluid medium in the EPOS3 framework is an important aspect that is to be taken care of. Our results may be useful in tuning the model. We have communicated our results to the developers of the code.

***pp* collisions:**

Our study on possible alternate explanation to the hydro-like features in high-multiplicity events, in terms of the pQCD inspired Multiple Parton Interactions (MPI) along with the color reconnection mechanism, as implemented in the PYTHIA 8, explicitly brought out the limitation of the model. Now, there are several other studies available in the literature which corroborate our findings. On the other hand, one must also appreciate that the smaller size and the shorter life-time of the system, expected to be produced in high-multiplicity pp collisions even according to the hydro-based models, is not really conducive for the medium to get thermalized. Nevertheless, very strong indications of collective properties in multi-particle productions in the high-multiplicity events of the small systems clearly indicates that the age-old understanding of the particle productions in high energy pp and pPb collisions needs to be thoroughly reviewed. Our study belongs to the initial identification of the problem and, obviously, there remains a lot of studies to be undertaken in different theoretical approaches to get a clear renewed picture of particle production in pp collisions in the post-LHC era.

Chapter 8

Appendix

8.1 Event generators

The event generators are bunch of software libraries used to simulate the high energy collisions through Monte Carlo (MC) methods. The Monte Carlo methods are stochastic techniques, meaning, they are based on the use of random numbers and probability statistics to investigate problems. Often, the event generators are used as “black box” without knowing what is happening inside. They are extensively used for theoretical predictions as well as in data analysis. Together with the detector simulations, they can provide real event scenarios with the detector acceptance and efficiency measurement. The main parts of event generators while simulating a high energy collision (hadronic or nucleonic) are following:

- Initial-state component building

- Initial-state showers
- Initial-state hard scattering
- Hard and soft processes
- In-medium energy loss, collectivity (for heavy-ion)
- Final-state showers
- Hadronization and further decays
- Underlying Events

There are many event generators designed to simulate high energy collisions, such as PYTHIA (formerly PYTHIA/Jetset), HERWIG, ISAJET, SHERPA, GiBUU, HIJING, AMPT, GENIE, EPOS etc. For the analysis described in this thesis, PYTHIA, HIJING, POWHEG and EPOS event generators are used. A brief description will be given in the following sections.

8.1.1 PYTHIA

The PYTHIA event generator is used to simulate high-energy particle physics events. It describes the collisions between the elementary particles like $e^{\pm}, p, \bar{p}$. It combines perturbative QCD and different phenomenological models to address different aspects such as hard and soft interactions, parton distributions, multiparton interactions, initial- and final-state parton showers, fragmentation etc [1]. Originally PYTHIA was written in FORTRAN 77 programming language. From 2007 releases, it is converted to C++ with the version PYTHIA 8. Both FORTRAN and C++ components are merged at the end.

Different steps or the event generation flow of PYTHIA events are shown in the Fig. 8.1. In the first step, two beams are coming towards each other. The distribution

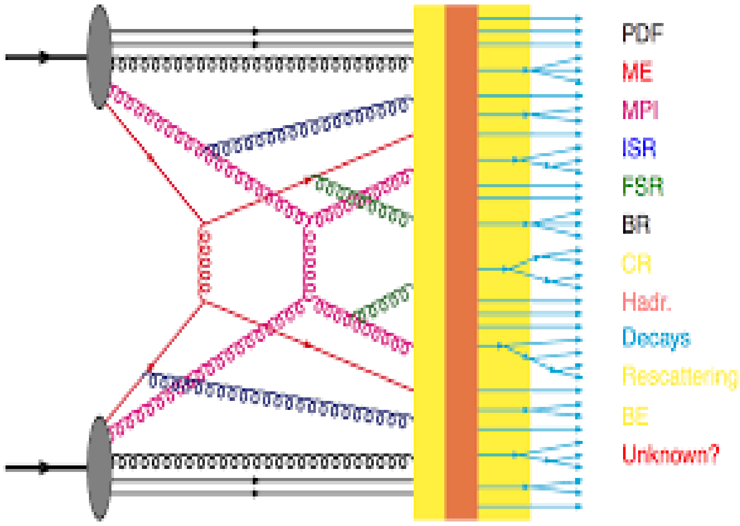

Figure 8.1: A schematic diagram of PYTHIA event generation with different steps.

of different partons of the two beams can be characterized by the corresponding parton distribution functions (PDFs) $f_i(x, Q^2)$ which is defined as the probability of finding a parton i with the momentum fraction x of the total momentum of the beam particle probed at a momentum scale Q^2. Since the PDFs can not be derived from first principles, PYTHIA uses parameterizations of experimental data. There are different PDFs available from high-energy lepton–hadron and hadron–hadron collision measurements. In each beam, partons may go through interactions which is called "initial-state shower". Two incoming partons then undergo hard interactions (e.g qg$\rightarrow$qg, gg$\rightarrow$qg, qg$\rightarrow$qγ etc.) [2] and this produces outgoing partons. The interactions may produce resonances and there could be multiple interactions. The non-interacted partons are called beam remnants. Semi hard processes may also occur. PYTHIA includes all such processes. Using perturbative QCD, the total cross section of initial hard scattering between incoming partons can be defined.

After this the outgoing partons undergo series of branching into partons. At the end the outgoing partons fragment to colorless hadrons due to QCD confinement which is called hadronization. Since the hadronization is still un-clear, PYTHIA uses phenomenological approach, the so-called Lund string fragmentation model. After the hadronization, some hadrons may decay further. A complete event in PYTHIA stores all the information for the produced hadrons.

There two main PYTHIA versions available are PYTHIA 6 [1] and PYTHIA 8 [3]. PYTHIA 6.4 version consists of 3 tunes Perugia-0, Perugia-2010, and Perugia-2011. The Perugia-2010 tune includes a modification in the amount of final-state-radiation and high-z fragmentation. In PYTHIA 8 version, several improvements in multiparton interactions are introduced and also includes color reconnection mechanism. In this thesis, at different stages, PYTHIA simulated events are used in the AliRoot framework.

8.1.1.1 PYTHIA 8 tune 4C and Color Reconnection

The multiparton interation (MPI) based PYTHIA tune 4C [4] is the latest and successful tune for LHC energies. It includes also color reconnection mechanism which became popular after reproducing the ALICE data in terms of $< p_{\mathrm{T}} >$ as function of N_{ch} giving a possible explanation to the observed flow-like behaviour of high-multiplicity pp data at $\sqrt{s} = 7$ TeV.

Color reconnection (CR) is a microscopic process where final state partons are connected by color strings, in such a way that the total string length becomes as

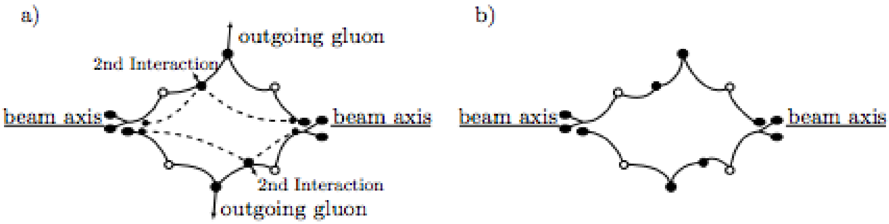

Figure 8.2: The color reconnection mechanism in the string fragmentation model. The outgoing partons which are color connected to the projectile and target remnants (continuous lines) are reconnect with the partons in the second hard scattering (in dashed lines) (a). Color reconnected string (b).

short as possible [5]. So the fragmentation of two independent hard scatterings get dependent. The string connected final state partons follow the movement of the partonic end points. Such induced movements of strings produces a common boost in the fragmentation. With CR two partons from independent hard scattering at mid-rapidity can color reconnect and make a large transverse boost (Fig. 8.2).

8.1.2 HIJING

In high energy heavy-ion collisions it is expected that the majority of the particles produced via parton scattering will originate from hard or semi-hard (with p_{T} of few GeV/c) processes. HIJING (**H**eavy **I**on **J**et **IN**teraction **G**enerator) [6] Monte Carlo model was developed by M. Gyulassy and X. N. Wang using heavy-ion results as input to study the role of mini jets in pp, pA and AA collisions. It combines with the Dual Parton Model, Lund FRITIOF and perturbative QCD processes from PYTHIA. It validates data by understanding the interplay between different soft and hard QCD processes in heavy-ion collisions. HIJING delivers particle spectra, back-to-back two-particle correlations successfully for AA and pA collisions. Multiple minijet production and a model for jet quenching to study the high-p_{T} observables are included. In this thesis, for the ALICE data analysis, pPb collisions are simulated using AliRoot HIJING on top of PYTHIA with a boost in the pseudorapidity of $\Delta y_{NN} = 0.465$.

8.1.3 POWHEG

The POWHEG [7] is an acronym which stands for: **P**ositive **W**eight **H**ardest **E**mission **G**enerator. The POWHEG simulation code is based on NLO calculations in the Shower Monte Carlo (SMC) programs making use of the POWHEG method [8]. In the POWHEG method the hardest emission is generated with NLO accuracy at first and independently from the subsequent parton shower. Earlier only leading order (LO) calculations as implemented in the context of general purpose SMC programs, were used as basic tool for simulating real experiments. The SMC programs did not exhibit the NLO accuracy which become important in precision measurement. With the POWHEG program many features are implemented at the next to leading-logarithmic level. The POWHEG program is build to produce positive-weighted events and it does not depend on the Monte Carlo program used for subsequent showering. It can easily be interfaced to any modern shower generator. It has been interfaced to HERWIG and PYTHIA. Up to now, the POWHEG method, in the context of hadron colliders, has been applied to ZZ pair hadroproduction, heavy-flavour production, Drell-Yan vector boson production, Higgs boson production via gluon fusion etc. [9, 10].

8.1.4 EPOS

The event generator EPOS is an acronym which stands for: **E**nergy conserving multiple scattering; **P**artons, parton ladders and strings; **O**ff shell remnants; **S**aturation. While PYTHIA is based on the "factorization approach", EPOS is based on "Parton-based Gribov-Regge theory" [11] which by construction is a multiple scattering theory. It also combines the eikonalized parton model. To exhibit the interaction between the incoming partons, idea of theoretical object like Pomerons are implemented. EPOS is a real event generator where multiple interactions are based on a quantum formalism. EPOS uses a parton model where each binary interaction is represented by a parton ladder. These parton ladders may be considered as quasi-longitudinal color field, conveniently treated as relativistic strings or string fragments. There can be two types of parton ladders. The open ones are for inelastic collisions and closed ones are for elastic collisions. A significant part of the theory implemented in EPOS model is the off-shell remnants. The beam remnants can possibly take part in the collision process enhancing the particle yield.

The version EPOS 3 (used in this thesis) takes the advantage of full (3 + 1D) viscous hydrodynamical calculations followed by hadronic cascade, unlike any other event generator. The hydrodynamical evolution is done event by event. An important new aspect of EPOS is the separation of collision zones into the "core" and "corona" regions [12], based on the string densities at earlier times of the collision. The high energy density region (i.e., above a certain critical string density) is termed as "core" where hadronization is done by imposing radial flow for all hadron species. Hence, the core undergoes a full collective expansion producing QGP in heavy-ion collisions. The low string density region is coined as "corona", where particle production is done as like in pp scattering. The contribution of corona decreases with increasing centrality and the relative core-corona distribution depends on hadron types. At the end the color objects are fragmented into hadrons and for the hadronization EPOS uses the standard Cooper-Frye procedure where equilibrium hadron distributions are applied.

The EPOS generator aims at reproducing a large range of LHC observables like multiplicity, jets or collective behaviour. It is a well suited simulation model to describe collisions at LHC and the higher energies. So far it is quite successful in explaining LHC data for different collisions systems in different energies [12, 13].

Bibliography

[1] PYTHIA, Torbjorn Sjöstrand, Stephen Mrenna, Peter Skands, JHEP**05** 026 (2006).

[2] J. F. Grosse-Oetringhaus, Ph.D. thesis, University of Munster, Germany, (2009).

[3] T. Sjöstrand, S. Mrenna, and P. Z. Skands, Comput. Phys. Commun., 178 pp. 852-867 (2008).

[4] R. Corke and T. Sjöstrand, JHEP**03**, 032 (2011).

[5] A. Ortiz Velasquez et al., Phys. Rev. Lett. **111**, 042001 (2013).

[6] HIJING, Xin-Nian Wang and Miklos Gyulassy, Phys. Rev. **D44**, 3501 (1991).

[7] P. Nason, JHEP**11**, 040 (2004).

[8] S. Frixione et al., arXiv:hep-ph/0709.2092,

[9] C. Oleari, The POWHEG BOX, arXiv:1007.3893v1.

[10] Simone Alioli, Paolo Nason, Carlo Oleari, Emanuele Re, JHEP**06**, 043 (2010).

[11] H. J. Drescher et al., Physics Reports 350, 93-289 (2001).

[12] Klaus Werner, Phys. Rev. Lett. **98**, 152301 (2007).

[13] T. Pierog, Iu. Karpenko, J. M. Katzy, E. Yatsenko, and K. Werner, Phys. Rev. **C92**, 034906 (2015).